ASME
SETTING THE STANDARD

Transactions of the ASME, Journal of Fluids Engineering
(ISSN 0098-2202) is published monthly by
The American Society of Mechanical Engineers,
Three Park Avenue, New York, NY 10016.
Periodicals postage paid at New York, NY
and additional mailing offices.
POSTMASTER: Send address changes to Transactions of the
ASME, Journal of Fluids Engineering, c/o THE AMERICAN
SOCIETY OF MECHANICAL ENGINEERS,
22 Law Drive, Box 2300, Fairfield, NJ 07007-2300.
CHANGES OF ADDRESS must be received at Society
headquarters seven weeks before they are to be effective.
Please send old label and new address.

Journal of Fluids Engineering

Published Monthly by ASME

VOLUME 131 • NUMBER 10 • OCTOBER 2009

RESEARCH PAPERS

Flows in Complex Systems

Fundamental Issues and Canonical Flows

Multiphase Flows

(Contents continued on inside back cover)

This journal is printed on acid-free paper, which exceeds the ANSI Z39.48-1992 specification for permanence of paper and library materials. ♾™
♻ 85% recycled content, including 10% post-consumer fibers.

(**Contents continued**)

Journal of Fluids Engineering **Volume 131, Number 10** **OCTOBER 2009**

TECHNICAL BRIEFS

The ASME Journal of Fluids Engineering is abstracted and indexed in the following:

Applied Science & Technology Index, Chemical Abstracts, Chemical Engineering and Biotechnology Abstracts (Electronic equivalent of Process and Chemical Engineering), Civil Engineering Abstracts, Computer & Information Systems Abstracts, Corrosion Abstracts, Current Contents, Ei EncompassLit, Electronics & Communications Abstracts, Engineered Materials Abstracts, Engineering Index, Environmental Engineering Abstracts, Environmental Science and Pollution Management, Excerpta Medica, Fluidex, Index to Scientific Reviews, INSPEC, International Building Services Abstracts, Mechanical & Transportation Engineering Abstracts, Mechanical Engineering Abstracts, METADEX (The electronic equivalent of Metals Abstracts and Alloys Index), Petroleum Abstracts, Process and Chemical Engineering, Referativnyi Zhurnal, Science Citation Index, SciSearch (The electronic equivalent of Science Citation Index), Shock and Vibration Digest, Solid State and Superconductivity Abstracts, Theoretical Chemical Engineering

An Experimental Investigation of the Flow Fields Within Geometrically Similar Miniature-Scale Centrifugal Pumps

Daniel Kearney
Mem. ASME
Stokes Institute,
University of Limerick,
Limerick, Ireland
e-mail: daniel.kearney@ul.ie

Ronan Grimes
Mem. ASME
e-mail: ronan.grimes@ul.ie

Jeff Punch
Mem. ASME
e-mail: jeff.punch@ul.ie

CTVR,
Stokes Institute,
University of Limerick,
Limerick, Ireland

Flow fields within two miniature-scale centrifugal pumps are measured and analyzed to facilitate an understanding of how scaling influences performance. A full-scale pump, of impeller diameter 34.3 mm and blade height 5 mm, and a half-scale version were fabricated from a transparent material to allow optical access. Synchronized particle-image velocimetry (PIV) was performed within the blade passage of each pump. Pressure-flow characteristics, hydrodynamic efficiencies, and high-resolution flow field measurements are reported for six rotational speeds over a Reynolds number range 706–2355. Fluidic phenomena occurring in the impeller passage at both pressure and suction surfaces are identified. Efficiencies are evaluated from direct measurement to be between 10% and 44% and compared with inner efficiencies calculated from the PIV data. Hydrodynamic losses as a percentage of overall efficiency increase from 12% to 55% for $2355 \leq Re \leq 706$. *Slip factors, in the range 0.92–1.10, have been derived from velocimetry data.* [DOI: 10.1115/1.3176985]

1 Introduction

Consumer demands for high-performance, small-scale information, and communication technologies have driven the need for thermal management solutions. In some applications, component-level heat fluxes are currently approaching the limits of conventional forced air cooling—see Ref. [1], for example—and alternative technologies are now under consideration. The evolution of data centers, moreover, is placing an increasing demand on efficient thermal solutions to counteract growing energy costs. It is evident in literature that there is a lot of research activity addressing liquid cooling, much of which concentrates on primary heat removal from the system level components to the cooling liquid. Garimella et al. [2] highlighted the lack of research invested in the other aspects of liquid cooling systems, for example, pumping, interconnection and facility for hot plugging, fluid reservoirs, and secondary heat exchange. The scope of this paper is an investigation of the hydrodynamic performance of miniature centrifugal pumps designed for electronics cooling applications.

Singhal et al. [3] compiled a state-of-the-art review of micropumping technologies suitable for microchannel coolers. A range of pumping techniques from mechanical, electro-, and magnetokinetic, phase change, and miscellaneous were assessed with reference to their performance, size, potential for miniaturization, power requirements, and suitability for electronics cooling applications. Quantitative performance was examined in terms of the maxima of flow rate per unit area and back pressure. Rotary micropumps exhibited reasonable performance in comparison with other techniques, although their potential for miniaturization was noted to be moderate, primarily due to the risk of stiction occurring at small scales. Many of the novel micropumps in development fail to achieve the required cooling flow rates for contemporary solutions and are not currently cost effective. Current micropump technologies, as demonstrated by Matteucci et al. [4], Lei et al. [5], Ahn et al. [6], are often application specific and unsuitable liquid cooling applications, which require modularity.

Most contemporary liquid cooled electronics systems use rotary pumps, and these are predominantly centrifugal in configuration. Centrifugal pumps offer advantages in terms of cost, established motor drive technology, and uniformity of flow. Relatively, little work has been conducted on miniaturizing centrifugal pumps for small-scale thermal management applications. In particular, these miniature-scale centrifugal pumps appear to be designed for ease of manufacture with little attention to the optimization of hydrodynamic performance. It is evident that miniature rotary pumps will continue to be deployed in liquid cooling systems for the medium term and that performance improvements will be required as heat loads increase and available space diminishes.

One of the primary challenges in the miniaturization of pump design is prediction of performance. At larger scales, the pump scaling laws can be used with a high degree of confidence to predict variations in pump performance with size and speed. As scale is reduced, however, Reynolds number is reduced, and below a critical Reynolds number significant reductions in hydrodynamic efficiency can occur, invalidating the pump scaling laws, as reported by Day et al. [8] and Lorenz and Smith [9]. There is a need for velocimetry data to investigate the fluidic phenomena, which influence hydrodynamic losses at low Reynolds numbers.

Particle-image velocimetry (PIV) data for miniature-scale pumps were reported by Sankovic et al. [7] for an impeller diameter of 35 mm. Hardware limitations restricted the analysis of velocity flows within the interblade area to an interrogation region of 64×64 pixels, however, which corresponds to a vector-to-vector distance of not less than 500 μm. The data presented in this paper for a similar scale feature vector field resolutions as fine as 60 μm with each data set comprising 150 images. Much research was conducted on investigating qualitative imagery in the impeller passage and volute region at varying scales of macroscale centrifugal pumps—for example, Refs. [10–12]. However,

Contributed by the Fluids Engineering Division of ASME for publication in the JOURNAL OF FLUIDS ENGINEERING. Manuscript received November 14, 2008; final manuscript received June 1, 2009; published online September 11, 2009. Assoc. Editor: Juergen Kompenhans. Paper presented at the 2008 ASME Heat Transfer, Fluids, Energy, Solar, and Nano Conferences (HTFESN 2008), Jacksonville, FL, August 10–14.

this macroscale work was carried out on pumps of diameter scale between 5.5 and 14 times greater than those considered in this paper.

The objective of this paper is to investigate the flow fields within two miniature-scale centrifugal pumps in order to understand how scaling influences pump performance. This paper focuses on pumps whose size is appropriate to modern day electronics cooling applications, where space is one of the primary constraints. A full-scale pump, of impeller diameter 34.3 mm and blade height 5 mm, and a half-scale version were fabricated from a transparent material to allow optical access. Pressure-flow characteristics and high-resolution flow field measurements were recorded for a range of rotational speeds. Rotational speeds were selected within the torque range of the dc motor driving the impeller and in the range of realistic operational flow rates for a typical cooling system. Velocity vectors were evaluated for each flow field at three operating points and compared with conventional pump theory. The data were plotted nondimensionally to investigate points of similitude. Evolution of the theoretical velocity triangles moving from inlet to discharge were compared with the experimental data and the findings are discussed in the context of efficiency degradation and increasing hydrodynamic losses at decreasing Reynolds numbers. Fluidic phenomena occurring in the impeller passage at both pressure and suction sides of the impeller blades are identified. The authors believe that this is the first comparative study that includes a detailed analysis of both qualitative and quantitative flow fields of pumps at this scale.

2 Scaling Groups

The conventional scaling laws for centrifugal pumps, as outlined by Stepanoff [13], allow comparison of the performance of pumps of varying scale working with a range of liquids. Dimensionless flow, pressure, and Reynolds number are defined, respectively, as follows:

$$\Phi = \frac{Q_v}{\omega D^2 h} \tag{1}$$

$$\Psi = \frac{\Delta P}{\rho \omega^2 D^2} \tag{2}$$

$$\mathrm{Re} = \frac{Q_v}{\nu D} \tag{3}$$

This study investigates a constant viscosity fluid at a range of Reynolds numbers determined by varying rotational speed and scale.

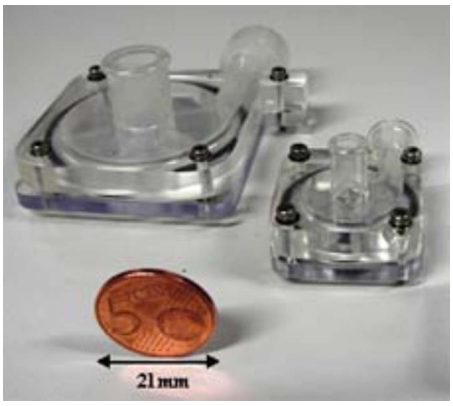

Fig. 1 Transparent centrifugal pumps

Table 1 Pump geometry and nominal flow conditions

Geometry		Pump A	Pump B	Units
Inlet diameter	D_1	10.0	5.0	mm
Outlet diameter	D_2	34.3	17.15	mm
Blade height	h	5.0	2.5	mm
Number of blades	z	6	6	–
Inlet blade thickness	t_1	2.0	1.0	mm
Outlet blade thickness	t_2	3.0	1.5	mm
Axial blade clearance	c	1.0	0.5	mm
Inlet blade angle	α_1	85	85	deg
Outlet blade angle	α_2	72	72	deg
Blade curvature radius	R_b	25.0	12.5	mm
Rotational speed	rpm	3400	8000	rpm
Maximum flow rate at zero pressure rise and nominal speed	$Q_{v\,\max}$	8	2.65	l/min
Maximum pressure rise at zero flow rate and nominal speed	$\Delta P_{\max}$	22.4	29.6	kPa

3 Experimentation

This section comprises a detailed description of the experimental apparatus, an overview of the performance characterization procedure, and considerations for the application of PIV, including details of the experimental procedure.

3.1 Apparatus. The details of the pumps and the hydrodynamic characterization system are presented in Secs. 3.1.1–3.1.3.

3.1.1 Pumps. The experimental characterization was carried out on two custom-made transparent centrifugal pumps (Fig. 1) whose dimensions are specified in Table 1 and illustrated in Fig. 2. The pump casings were manufactured from clear polished polyurethane with a refractive index of approximately 1.4. The transparency allowed full-field PIV within the impeller region. The original geometry of the pump impeller was based on the commercially available CSP MAG centrifugal pump. The pumps were powered by a brushless motor (Maxon EC-max 22) controlled by a servo amplifier (4-Q-EC DES 50/5) with data sampling in accordance with the following standards: ISO 2859, MIL STD 105E, and DIN/ISO 3951. This controller allows instantaneous

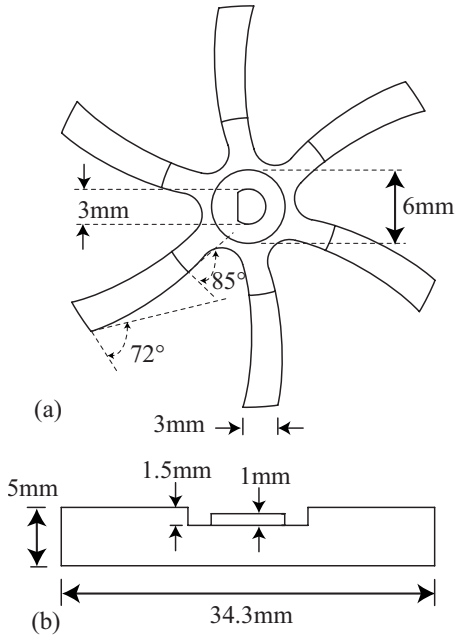

Fig. 2 Pump A impeller geometry where (*a*) represents a plan view and (*b*) represents a lateral view

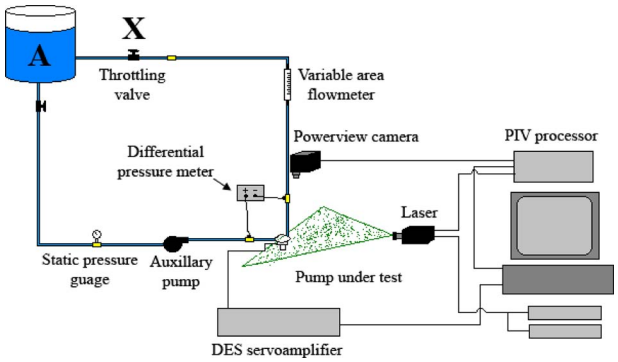

Fig. 3 Hydrodynamic test bed (to EN ISO 5198:1998) with velocimetry

speed and torque read out at a frequency of 20 Hz through a graphic user interface. Instantaneous shaft power was also recorded using a Hall sensor within the motor in order to evaluate hydrodynamic efficiency. The motor torque output was then calculated by multiplying the current output by the specific torque constant for the motor. The frictional effect due to the sealing gland was less than 1% of the no-load torque and considered to be negligible.

3.1.2 Hydrodynamic Test Bed. The experimental facility was used to measure pressure-flow characteristics for the full-scale and half-scale pumps for a range of rotational speeds. Water was used as the working fluid. Figure 3 is a schematic diagram of the measurement system for this experiment, designed in accordance with EN ISO 5198:1998 [14]. A 5 l reservoir positioned at a height of 200 mm above the pump provided sufficient static pressure within the flow loop to prevent any potential for cavitation to occur in either the auxiliary or the test pumps. The reservoir featured an unsealed open top in order to allow access for seeding the flow. The piping used was PVC drawn tubing with an internal diameter of 9.5 mm and with a surface roughness of 1.5 μm. This material allows better optical access than conventional transparent media. Pressure differentials across the pumps were measured by a wet/wet differential pressure transducer (GE Druck PDCR 4170 high performance) with a range −35 kPa to ±35 kPa connect to a digital pressure indicator (Druck DPI 280). The transducer has an accuracy of ±0.08% best straight line maximum, which at full scale corresponds to a measurement uncertainty of ±28 Pa. Two variable area flow meters connected in parallel—model RAQN (flow rate range 1.7–17 l/min and adheres to the VDI 3153 standard class 4) and Dwyer minimaster (0.25–2.5 l/min with an accuracy of ±4% of full scale)—were used to obtain the full measurement range required for the pump characterization. Flow rates were read directly from the graduated scales on the rotameters. Volumetric flow rate and pressure rise were varied in the test bed using a throttling valve with a low loss coefficient and an auxiliary pump as indicated in the schematic.

3.1.3 Performance Characterization Procedure. Pump characterization was carried out on the full-scale and half-scale pumps using the following procedural steps.

1. The selected pump was run at the characterization speed for an initial warm up period of 4–5 min in the hydrodynamic test bed. This ensured the removal of any air bubbles in the system and a uniform steady state flow through the system prior to data acquisition.
2. The ball valve (shown at position X in Fig. 3) was then closed and the pressure reading was taken at zero flow. The corresponding output torque current reading at the pump shaft was recorded simultaneously.

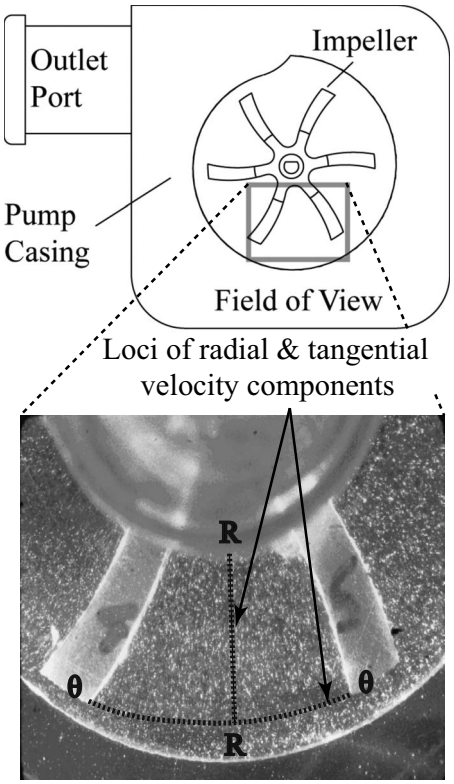

Fig. 4 Pump A with impeller blades (4 and 5) in PIV measurement position 90 deg anticlockwise of the outlet

3. The valve was opened in increments to reduce the pressure rise across the pump. At each increment, pressure rise, flow rate, and torque were measured.
4. When the valve was fully opened, the auxiliary pump was used to overcome system impedance within the test bed in order to allow characterization over the full performance range to the zero pressure rise condition.

Each test condition adhered to these procedural steps for pump A at 2200 rpm, 2800 rpm, and 3400 rpm and pump B at 4000 rpm, 6000 rpm, and 8000 rpm.

3.2 PIV Experimentation. The new wave research Nd-YAG Minilase III laser used for the PIV in this experiment has a 532 nm wavelength. The images from the pump were captured by a TSI PowerView Plus 2MP PIV camera (model 630057) connected to a PC via a PIV processor as detailed in Fig. 3. The PIV analysis was carried out using TSI's INSIGHT 3G software program. The software controlled the laser pulse durations, light intensity, the camera frame rate, and calculated the particle displacements. It also enabled postprocessing of the corresponding A and B images subsequent to capture removing background noise and reducing reflections. Tracer particles were chosen based on the following ideal criteria: consistent flow tracking, no fluid alterations, or settling during test. The TSI silver-coated hollow glass spheres selected had a diameter range between 8 μm and 12 μm with density index of 1.65.

A common region of interest (Fig. 4) was observed for each experimental condition and a corresponding time-averaged velocity flow field was computed. Each data set comprises 150 image pairs taken at the midpoint of the blade height in each case. The laser sheet thicknesses in pump A and pump B were approximately 2 mm and 0.9 mm, respectively. Pump rotation was synchronized with the PIV data acquisition system ensuring all data were recorded in an identical impeller segment. Synchronization was accomplished by triggering the PIV acquisition system with

Table 2 PIV processing parameters

PIV parameters	Pump A	Pump B	Units
Laser sheet thickness	2	1	mm
Actual particle size	8–12	8–12	μm
Length per pixel	10.16	7.57	μm
Resolution	1600×1200	1600×1200	pixel
Interrogation size	32×32	32×32	pixel
Time between images	10	10	μm

the Hall sensor output at the impeller shaft. This yielded PIV data sets, which were recorded between identical impeller blades throughout the experiments. PIV parameters are outlined in Table 2.

The fluid flow region within the blade passage was divided into an array of interrogation areas. Each interrogation area consisted of 32×32 pixels. The interrogation areas were individually analyzed using the following plug-in grid engines—the Nyquist grid, the Gaussian peak engine, and the fast Fourier transform (FFT) correlator. The Nyquist grid engine operates with a 50% interrogation overlap fitting a Nyquist sampling criteria. A single filter pass using a Gaussian peak in conjunction with the FFT correlator removed any spurious vectors from the data. A validation procedure was also performed on the data within the measured range. A second recursive evaluation of the PIV data produced an interrogation region of 16×16 pixels achieving vector-to-vector spacing of 80 μm and 60 μm for pump A and pump B, respectively.

3.2.1 PIV Experimentation Procedure. All PIV measurements presented here were obtained at or close to the best efficiency point (BEP) of the pumps at a nondimensional flow coefficient Φ equal to 0.04. Table 3 defines the actual flow conditions for each velocimetry test condition including comparison with maximum efficiency value.

1. The auxiliary pump was run at constant speed for 4–5 min in to achieve steady state through the hydrodynamic test bed.
2. A sufficient concentration of seeding as quantified by Reithmuller et al. [14] was added to the reservoir at position A and stirred until a homogeneous mixture of fluid and tracer particles was observed passing throughout the system.
3. The flow was throttled by partially closing valve X until the pressure reading was at the required specific flow coefficient.
4. The pump rotational speed was recorded, and a 3 min delay was allowed in order to attain steady state for this condition prior to recording any PIV data.
5. 150 PIV image pairs were recorded and an analysis was conducted on the corresponding blade passages between the impeller blades as illustrated in Fig. 4.

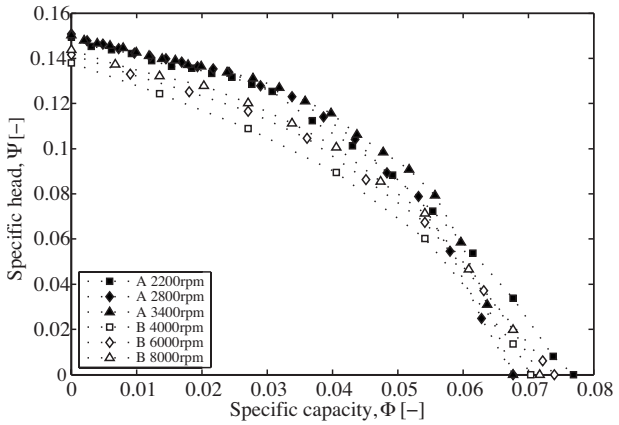

Fig. 5 Nondimensional pressure-flow curves as a function of operational speed (uncertainty of $\Phi = \pm 5-20\%$ and $\Psi = \pm 0.8\%$)

4 Results and Discussion

In this section, the hydrodynamic characteristics of both pumps are presented and discussed in conjunction with the measured PIV data. One- and two-dimensional velocity profiles are also presented and the findings are discussed in conjunction with the Euler velocity triangles.

4.1 Hydrodynamic Characterization. Figure 5 illustrates the nondimensional pressure-flow performance of each pump at various operating points. It is clear that the characteristics do not scale completely with inferior performance for the smaller scale pump. Moreover, performance degrades at lower speeds. This anomaly in ideal agreement with conventional pump theory is further highlighted in Fig. 6 with the decrease in hydrodynamic efficiency with decreasing speed and geometric scale. Figure 7 illustrates the decreasing maximum hydrodynamic efficiency as a function of reducing Reynolds number for the range of test conditions. Hydrodynamic efficiency is a ratio of fluid power and mechanical shaft power:

$$\eta_{\text{hydro}} \frac{\Delta P \cdot Q_v}{T\omega} \tag{4}$$

Fluid power is represented as the product of pressure rise and volumetric flow rate. Shaft power input is presented as the product of input torque and rotational speed. Equation (4) was used to calculate efficiency from measured values of pressure differential, flow rate, torque, and rotational speed. Decreasing efficiency with scale is one of the primary inhibiting factors for the usage of rotary pumps at reduced scales [15]. Some possible reasons for this decrease in performance are drawn from a qualitative analysis of the velocimetry data in the next section.

Table 3 Pump flow conditions for velocimetry test data including maximum efficiency values for comparison

Pump	rpm	$\eta_{\max}$ (%)	η (%)	Q_v (l/min)	Φ	Ψ	Re
A	3400	44	44	5.00	0.04	0.12	2355
	2800	43	42	3.50	0.04	0.11	1884
	2200	37	36	2.50	0.04	0.11	1413
B	8000	34	34	1.50	0.04	0.10	1413
	6000	23	23	1.00	0.04	0.10	942
	4000	10	10	0.75	0.04	0.90	706

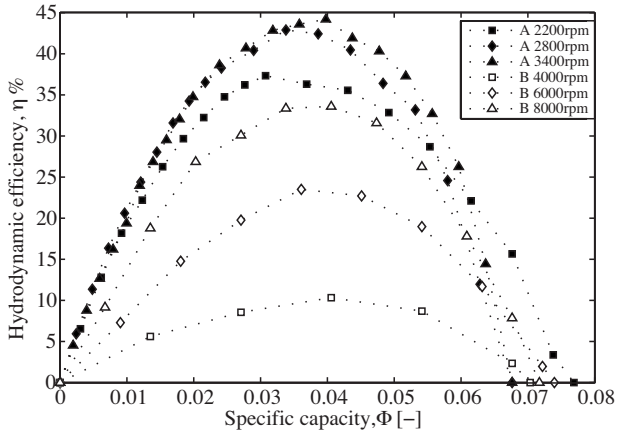

Fig. 6 Efficiency curves of test pumps as a function of operating speed (uncertainty of $\Phi = \pm 5-20\%$; $\eta = \pm 5.08-20.02\%$)

4.2 Two-Dimensional Velocity Flow Fields. Figure 8 illustrates synchronized relative velocity flow fields for each of the six test conditions where $\Phi = 0.04$ (Table 3). The rotation of the impeller is anticlockwise and the tangential velocity of the impeller is subtracted from the measured local fluid velocities to obtain their relative component. In all cases, it is evident that the flow patterns deviate from the ideal channel-style flow parallel to the blades. Four flow features are evident: secondary flow, incident flow, out-of-plane flow, and dead zones. These are discussed in Secs. 4.2.1–4.2.4.

4.2.1 Secondary Flow. A noteworthy feature recognized in these figures is the presence of secondary flow. Secondary flow occurs as the fluid is deflected toward the impeller axis and results in a decrease in the centrifugal force. This finding was also found in work by Choi et al. [16] on pumps of diameter four times greater than those investigated here. Similar transient fluid dynamic phenomena are also highlighted in the miniature-scale range. Tsukiya et al. [17] illustrated the development of secondary flows in the passage of a miniature-scale centrifugal pump of diameter 80 mm and an exit angle of 67 deg. The secondary flows within this pump were found to develop as a result of adverse flow phenomenon at the suction surface of the blade. Figure 8(*f*) illustrates secondary flow development in the region corresponding to coordinates (2.6,5) to (5.9,5), from upper center to lower center at the impeller exit at the lowest Reynolds number condition under test. This secondary cross flow (flow moving from pressure to suction side) is likely to be a contributing factor to reduced efficiency in the smaller scale pump as it is not congruent with the diffusing blade and deviates from an ideal channel-style flow. The absolute tangential velocity of the fluid V_θ is reduced as a result of this secondary flow and hence the overall hydrodynamic efficiency is reduced.

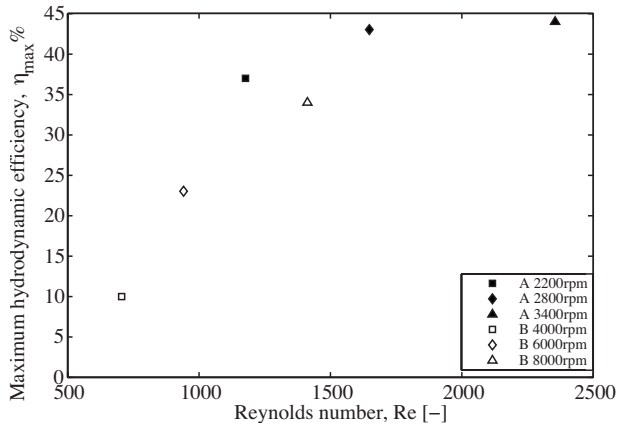

Fig. 7 Decreasing maximum hydrodynamic efficiency as a function of Reynolds number (uncertainty of $\eta = \pm 5.08-20.02\%$; $\mathrm{Re} = \pm 5.01-20\%$)

4.2.2 Incident Flow. At the inlet to the blade passage in all six cases presented, it is evident that flow is incident onto the leading edge of the blade, as vectors point diagonally down and to the left. Incident flow creates local zones with decelerated flow. Redesigning the blade's leading edge such that it is aligned with this relative inlet flow direction would be likely to improve the performance of the pump. The radial flow direction (i.e., inwards or outwards relative to blade inlet) at the impeller exit is of significance as it influences the flow rate of the pump. The flow through the impeller passage (through-flow) shows contrasting direction with scale. Figures 8(*a*)–8(*c*) display regions of through-flow migrating from pressure side to the suction side. At the suction side, however, this flow becomes more complex at the blades' trailing edge. This flow feature does not appear to scale as it is not present to the same degree in pump B. In contrast, the predominant flow path in pump B is from suction side to exit pressure side as outlined in Figs. 8(*d*)–8(*f*) at coordinates (6,5) to (2,2).

4.2.3 Out-of-Plane Flow. Investigating a centrifugal pump in a similar manner, Choi et al. [16] deduced that leakage flow within the measured plane may interact with flow in adjacent planes and thus illustrate a complex three-dimensional flow pattern. Each measurement plane is subjected to an averaging of the local velocity by the PIV algorithm as outlined previously. There is an apparent three-dimensional flow occurring at the suction side of pump A for each rotational speed investigated, as highlighted in Fig. 8(*b*). Flow tends to move toward the suction side and away from the pressure side of the rotating blade. It is inferred that this may be due to out-of-plane flow caused by the presence of a "horseshoe" vortex pair acting in a radial direction. The researches of Sumer et al. [18] and Gulich [19] illustrate the formation of this vortex when flow on the hub decelerates on approaching the impeller leading edge. The blockage caused by the blade and stagnating fluid results in the liquid being displaced from the wall laterally into the channel forming a horseshoelike vortex, as illustrated in Fig. 9. This vortex is illustrated throughout Figs. 8(*a*)–8(*c*) by the movement of two flow regimes: one flow regime moves toward the suction side of the blade and another away from the pressure side. The vortex in pump B occupies a smaller percentage area of the blade passage than pump A (Figs. 8(*a*)–8(*c*)); however, there is evidence of flow toward the suction side in Figs. 8(*d*)–8(*f*) at (7.5,3). The measurement plane in pump B at 8000 rpm indicates a zone of reduced flow and thus may be recording closer to the vortex center. Since the measurement plane is located at the blade midpoint in each case, it is conjectured that the position of vortex may displaced at higher rotational speeds. Reducing the width of the leading edge would reduce the fluid stagnation zone, thus preventing fluid separation and the development of this vortex at reducing scale. Sudden expansion of the impeller area can result in sharp deceleration of the flow, separation, and shock losses adjacent to the blade [19]. These losses encourage the development of a vortex and reduce radial outflow, thus decreasing hydrodynamic efficiency.

4.2.4 Dead Zones. Zones of reduced flow or "dead zones" are a prominent feature observable in each flow field. Figures 8(*a*) and 8(*d*) illustrate examples of large regions of retarded flow within the blade passage in each scale of pump. In pump A this can be observed at coordinates (8,8) and again in pump B located at (6.6,3). In pump A these dead zones are also observed in isolated areas in the blade passage at increased rotational speeds—Fig. 8(*b*) coordinates (7,8.5) and Fig. 8(*c*) coordinates (9,9). Throughout pump B, however, these zones of reduced or stagnant

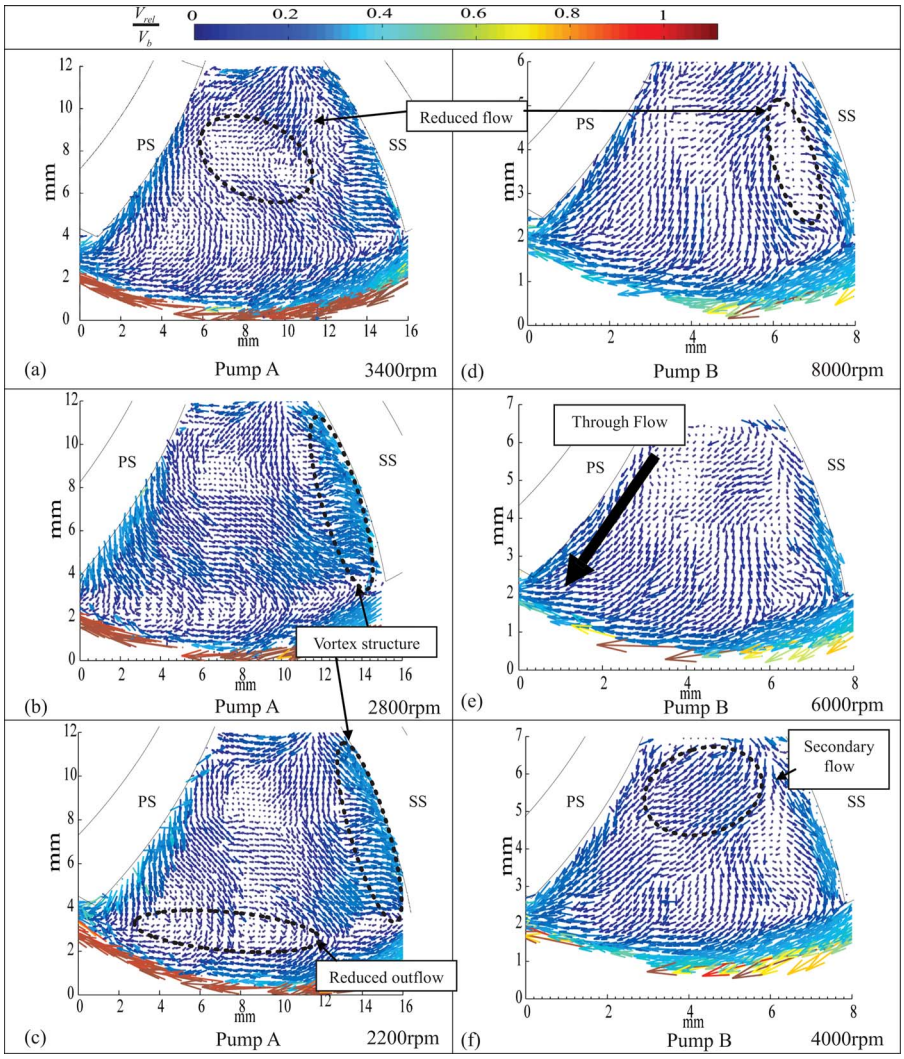

Fig. 8 Relative velocity flow fields normalized with respective blade speeds V_{rel}/V_b

relative flow can be observed adjacent to the suction side of the blade. It is conjectured that the dead zones on the suction side of pump B correlate with the measurement of the center of the horseshoe vortex. The center of the vortex may be directly in the measurement plane leading to the measurement of a dead zone at the center of the vortex on the suction side. This finding is consistent in Figs. 8(*a*)–8(*c*) for pump B. The percentage area covered by these stagnant zones at this scale is greater than those of pump A, a geometrically similar pump of twice the dimension. The net reduced flow in the radial direction correlates to a reduced flow rate within the pump and thus to a reduced overall hydrodynamic efficiency. This observation is consistent with relative flow fields discovered in macroscale work by Pedersen et al. [11] and Tsukiya et al. [17].

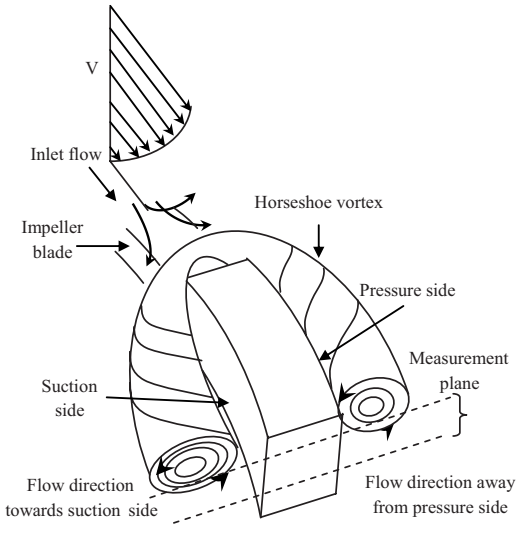

Fig. 9 Formation of a horseshoe vortex pair

Analyzing the velocity blade profiles within the blade passages at the midplane has identified some mechanisms of loss. The PIV data are recorded over a region of approximately 40% of the blade height; some averaging is implicit and, in addition, some other features may exist away from the measurement region. It is speculated, however, that it is unlikely these mechanisms of loss occur at each plane about the midpoint due to the sensitivity of the velocimetry technique to boundary layer development. This is discussed in more detail in Sec. 4.3. In addition to these four features, there are other flow patterns evident within the pumps which vary. It is likely that these features, as mechanisms of loss, diminish the efficiency of the pumps, particularly at lower Reynolds numbers.

4.3 One-Dimensional Velocity Profiles. In this subsection the PIV data, from each of the operating conditions, at selected radial and circumferential loci illustrated in Fig. 4 are compared

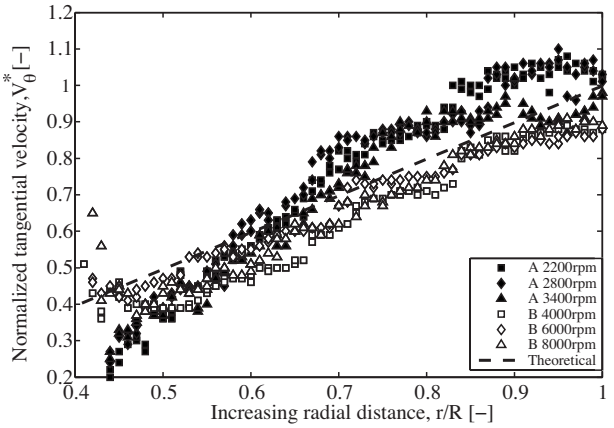

Fig. 10 Average tangential velocity normalized with blade tip speed V_θ/V_b as a function of increasing radial distance (r/R)

with the measured values extracted from the hydrodynamic characterization. The one-dimensional velocity data are also compared with Euler velocity vectors calculated from direct measurements.

Figure 10 illustrates the absolute tangential velocity V_θ normalized with blade velocity V_b as a function of increasing nondimensional radial distance (r/R) for each operating point. The graph is composed of 180 averaged velocity data points taken along radial line $R-R$ as defined in Fig. 4. The whirl velocity component increases as it extends toward the blade impeller tip for each Reynolds number, a finding that conforms to conventional pump theory. For any given operating condition, the pressure rise across a pump is proportional to the tangential component of velocity. It is notable that the highest velocity vectors are recorded for the three test conditions of the large-scale pump, an indication of its superior pressure rise in comparison with the small-scale pump. It is also apparent that the average velocity for the lower rpm values of pump A exceeds that of the blade tip speed at $0.6 \leq r/R \leq 0.8$. It is hypothesized that this phenomenon may be attributed to the measurement of a horseshoe vortex pair acting in the radial direction. Furthermore, it is conjectured that the two-dimensional flow fields illustrate the flow vectors for both these conditions acting in a normal direction to the blade suction surface.

Figure 11 presents time-averaged absolute tangential velocities extracted along arc θ-θ, shown in Fig. 4, plotted as a function of circumferential angle at the impeller outlet for each test condition.

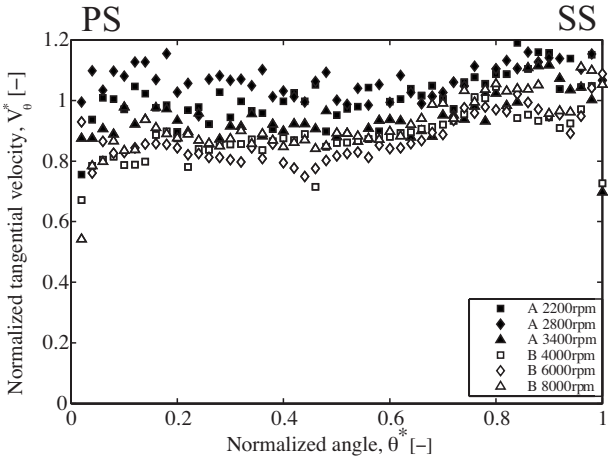

Fig. 11 Average tangential velocity normalized with blade tip speed V_θ/V_b at each degree along a circumferential blade tip arc θ-θ at $r/R=1$ as a function of normalized passage angle θ/θ_{bp}

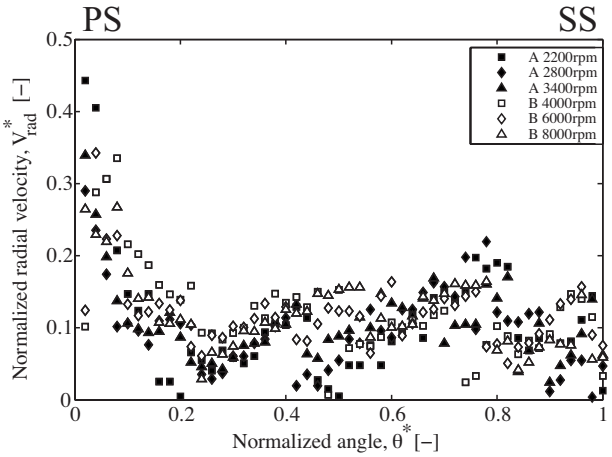

Fig. 12 Radial velocity component normalized with blade tip speed V_{rad}/V_b at each degree along a circumferential blade tip arc θ-θ at $r/R=1$ as a function of normalized passage angle θ/θ_{bp}

The angle θ is measured from pressure side to suction side. Each degree is represented by a data point, which is time-averaged data over 150 images. The fluid velocity approaches that of the blade in all cases and in conjunction with Figs. 8(*b*), 8(*c*), and 10, higher velocity components can be seen at the suction side of the rotating impeller. The nondimensional data collapse with a variance of between 0.03% and 1.58% from unity. With reference to Table 3, the pressure coefficients vary for each test condition and this variation in V_θ is responsible for the measured differences in Ψ.

Figure 12 illustrates nondimensional plots of radial velocity (V_{rad}/V_b) as a function of normalized angular position for both scales of pump at three rotational speeds. These six conditions span Reynolds numbers ranging from 706–2355. Each data set is taken at the blade midheight and at blade trailing edge, $r/R=1$, for each respective pump. The key features to note in this graph are a reduced exiting velocity along a circumferential arc θ-θ at the impeller tip ($r/R=1$) moving from pressure side to suction side of the passage and higher exiting radial velocity at the pressure side of the rotating blade. All qualitative imagery (see Fig. 8) demonstrates a degree of decreased through-flow in the center of the blade passage and this is most prominent in the large pump for the measurements at 2200 rpm and 2800 rpm. This finding corresponds with the plotted data in Fig. 10 where the predominant

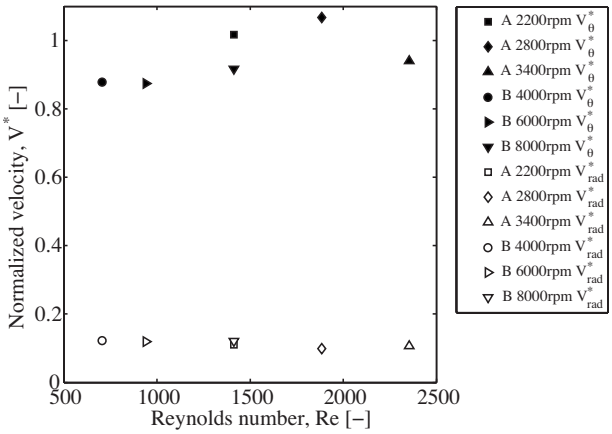

Fig. 13 Average normalized absolute tangential V_θ/V_b and radial velocity components V_{rad}/V_b for a circumferential blade tip arc θ-θ at the blade tip $r/R=1$ as a function of Reynolds number

flow occurs on the pressure side of the blade passage.

In Fig. 13, the tangential and radial velocity measurements, which were presented in Figs. 11 and 12 are spatially averaged and plotted against Reynolds for all of the points and both pumps. The normalized tangential velocity V_θ^* and radial velocity V_{rad}^* are extracted from averaged data points over the blade span of 50 deg along arc θ-θ at $r/R=1$ for each test condition. The main trend evident in Fig. 13 is one of decreasing tangential velocity, by approximately 20%, with reducing Reynolds number—with the exception of the largest Reynolds number value. For any operating condition, pressure rise across a pump is proportional to the absolute tangential component of velocity. It can be observed that the nondimensional radial velocity component is almost uniform in each test: this is expected, as all tests were run at the same specific flow coefficient, $\Phi=0.04$. For comparison, hydrodynamic efficiency was also computed from Eq. (4) based on the measured one-dimensional averaged velocity components as follows:

$$\Delta P = \bar{V}_\theta \cdot \bar{V}_b \cdot \rho \tag{5}$$

$$Q_v = \bar{V}_{\text{rad}} \cdot \bar{V}_b \cdot \rho \tag{6}$$

The radial velocity component V_{rad} is directly proportional to volumetric flow rate Q_v and is a measure of the through-flow in the impeller passage. Consequently, as the flow coefficient was the same for all of the cases investigated, it can be seen from Fig. 13 that the spatially averaged nondimensional radial velocity for each test condition is the same. The absolute tangential component of velocity V_θ therefore is a measure of overall pump efficiency.

Figure 14 shows hydrodynamic efficiency—evaluated from Eq. (4)—expressed as a function of Reynolds number. Similar trends are evident in the measured and calculated efficiencies, an indication that the quantitative velocity data are consistent with the measured performance characteristics of the pumps. The discrepancy in magnitude is likely to be due to the frictional losses within the pump volute and pipe losses between the pressure tappings including expansion and contraction at inlet and at exit as described by Van den Braembussche [20]. The merit in understanding inner hydrodynamic efficiencies allows optimization of the impeller geometry and serves as a guide to pump performance. Furthermore, the difference between inner and overall pump efficiency values quantifies the frictional losses associated with specific geometry and the relative increase in these hydrodynamic losses with decreasing Reynolds number and scale. Examining the discrepancy in magnitude expressed as a percentage of overall efficiency indicates an overall increase in hydrodynamic losses from 12% to 55% for decreasing Reynolds numbers in the range 2355–706. Figure 14 also plots an approximate measure of boundary layer development inside the pump in order to examine efficiency degradation with decreasing Reynolds number. Theoretical boundary layer development δ_{cl} is plotted for a characteristic chord length at blade tip. Conventional flat plate boundary layer theory is applied to this analysis and boundary layer growth is represented by

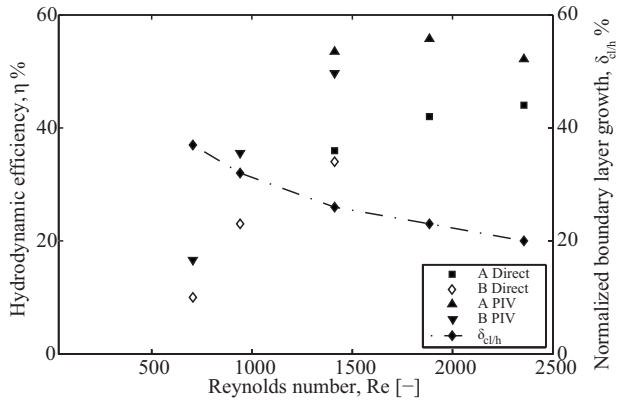

Fig. 14 Hydrodynamic efficiency and normalized boundary layer development δ_{cl}/h as a function of Reynolds number for pumps A and B

$$\delta_{\text{cl}} = \frac{5x}{\sqrt{\text{Re}_L}} \tag{7}$$

where the Reynolds number Re_L is calculated using a characteristic chord length and the mean radial flow velocity in the blade passage at that location. This velocity is expressed by the following equation:

$$\bar{V}_{\text{rad}} = \frac{Q_v}{6A_{\text{bp}}} = \frac{Q_v}{[\pi D - t]h} \tag{8}$$

At the lowest Reynolds numbers, the boundary layer engulfs 80% of the overall passage height. In the PIV measurements, the light sheet thickness of the measurement plane occupied a total of 40% of the blade height and therefore a significant portion of the boundary layer is included in the measurement area. The boundary layer reduces the effective area of the passage and increases the value of the expected mean velocity. The PIV data are sensitive to the alignment of the light sheet as the light sheet spans such a large proportion of the boundary layer. This is likely to represent a source of error in the velocity measurements as the PIV data represent an integrated measurement over a control volume equivalent to 40% of the overall passage height. However, the fluid velocity is not constant as it passes from inlet to exit in the pump volute unlike for flat plates. Continuity of mass dictates the fluid velocity reduces as it moves toward the blade tip. Boundary layer growth increases at lower flow velocities; thus its influence becomes more apparent in the measure of the velocimetry data at lower Reynolds numbers. Hodson [21] stated that at low Reynolds numbers the boundary layers tend to be laminar and separate readily in regions of increased pressure (or reduced velocity), giving rise to dead zones and increased hydrodynamic losses. This finding can be referred to the decreasing efficiency of the pumps at reducing Reynolds number.

4.3.1 Euler Velocity Triangles. The direction of the relative velocity component throughout the blade passage is of significant importance in determining the efficiency of the pump. In an idealized flow, the relative velocity of the fluid exiting the pump blade passage will be aligned with the blade trailing edge. In reality, however, the flow deviates from the blade orientation and the amount by which it deviates is indicative of the loss generated, as it results in a reduction in the outlet swirl and hence pressure rise. In order to assess the deviation, velocity triangles are evaluated at discharge for both PIV data (see Fig. 13) and the measured performance characteristics. The absolute velocity component is represented by the following trigonometric expression:

$$V_{\text{abs}} = \sqrt{V_{\text{rad}}^2 + V_b^2 + V_{\text{rad}}^2 \tan^2\theta + 2V_b V_{\text{rad}} \tan\theta} \tag{9}$$

The average radial and whirl (V_{rad} and V_θ) components are used to construct the PIV velocity triangles according to the relationship outlined in Eq. (9). (Graphically Eq. (9) can be represented by Fig. 15.) Considering the directly measured data, the average radial velocity component was calculated from Eq. (8). Figures 16(*a*) and 16(*b*) illustrate a comparison between the velocity triangles calculated from PIV data representing flow at the blade trailing edge and inferred from the measured volumetric flow rate. The PIV velocity triangles facilitate a direct comparison between the data plotted in Fig. 13 and the behavior of an inviscid fluid at this measured flow rate. The variation in scale between the PIV velocity triangles and those constructed from overall bulk measurements is due to the higher centerline velocity in the measured plane. Large absolute components of velocity are evident in Fig. 16 for pump A at both 2800 rpm and 2200 rpm. The local absolute velocities exceed the blade velocity at $r/R=1$ resulting in a negative deviation angle ζ. The deviation angle in Figs. 16(*a*) and

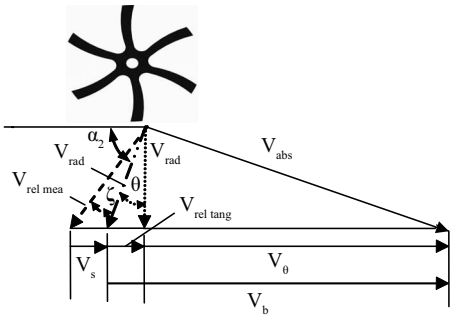

Fig. 15 Euler velocity triangle illustrating velocity components

16(*b*) in either positive or negative direction from blade outlet angle correlates with the degree of slip within the flow at the blade trailing edge. A contrary finding in the small-scale pumps can be observed in Fig. 16(*b*), which features a positive deviation angle that extends the relative component in the opposite direction. The magnitude of these deviation angles is presented in Figs. 16(*a*) and 16(*b*), quantifying the deviation of the real flow from the blade outlet angle. Slip factors ranging from 0.92 to 1.10 are evaluated using the slip factor definition as illustrated in Eq. (10) where a slip factor equal to one represents blade-congruent flow.

$$\sigma = 1 - \frac{V_s}{V_b} \tag{10}$$

V_s is defined as the magnitude of slip as illustrated in Figs. 16(*a*) and 16(*b*). A slip factor greater than 1 indicates fluid moving faster than blade velocity and is also representative of incongruent flow behavior. The slip factor represents a reduction in the capability of the miniature-scale pump to transfer energy and is indicative of hydrodynamic loss. Incorrect blade alignment with the incident flow causes separation and undesirable flow structures to occur in the pump. Increasing the backward curvature of the blade angle at inlet and discharge to match the relative flow outlet angle would reduce hydrodynamic loss through the blade passage and improve pumping performance.

5 Conclusions

In this paper, an experimental and theoretical investigation of the pumping performance of geometrically similar flow fields within miniature-scale centrifugal pumps is reported. The following conclusions can be drawn.

- The performance characteristics for the each test pump were characterized and the maximum hydrodynamic efficiencies were evaluated to be in the range 10–44% for Reynolds numbers between 2355 and 706.
- The relative velocity flow fields of two centrifugal pumps of geometrical similitude have been analyzed at varying operational speeds: dead zones, regions of secondary flow, out-of-plane flow, and reduced outflow are features, which were identified as contributing to fluidic loss. It is conjectured that a radial horseshoe vortex pair may exist at the pressure and suction side of the blade in both pumps.
- PIV data have been used quantitatively to calculate maximum inner hydrodynamic efficiencies, and this has been found to vary with Reynolds number in a similar manner to the efficiencies calculated from the hydrodynamic characteristics. However, the magnitude of the efficiencies calculated from the PIV is higher than that calculated from the measured values due to frictional losses within the pump and the pipe and contraction and expansion of the fittings in the pipe network.
- Evaluating inner efficiency using velocimetry quantifies frictional losses associated with specific geometry and highlights the increase in these hydrodynamic losses with decreasing Reynolds number and scale. The hydrodynamic losses expressed as a percentage of overall efficiency increase from 12% to 55% for decreasing Reynolds numbers in the range 2355–706.
- Boundary layer thickness within the pumps has been estimated to extend over 80% of the blade passage height covering part of the PIV measurement region. Integrating the velocity data in a measured control volume of fluid over the pump passage height that is significantly influenced by a boundary layer yields an apparent higher hydrodynamic performance than the measured values.
- The outlet angle of the impeller is not aligned with the cor-

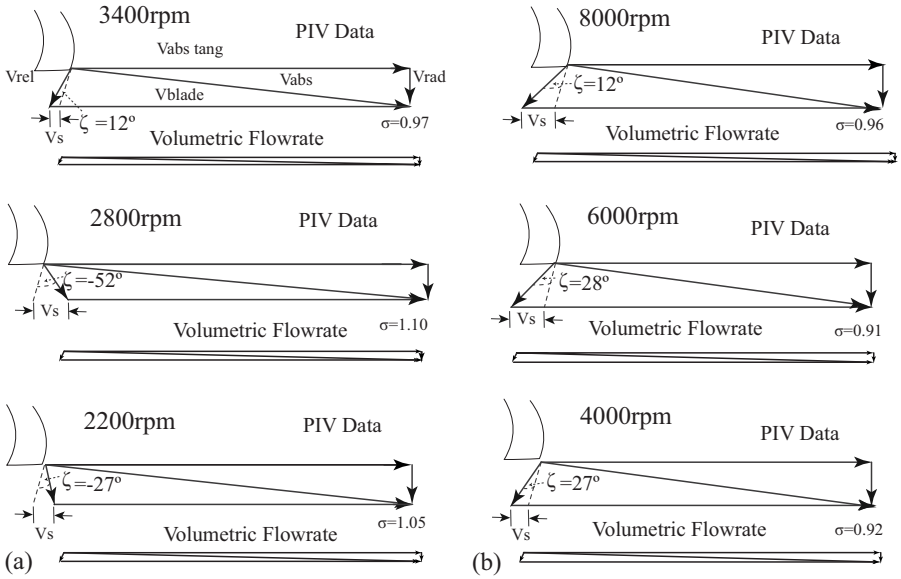

Fig. 16 Velocity triangles constructed from PIV data and overall measured data illustrated in (*a*) for pump A and (*b*) for pump B

responding incident flow within both scales of pump, as evident by slip factors in the range 0.92–1.10. An incorrect blade angle, at both inlet and outlet, is thought to be a large contributing factor to suboptimal hydrodynamic performance of both pumps. Increasing the backward curvature of the blade angle at inlet and discharge to match the relative flow angle would improve pumping performance and reduce hydrodynamic loss throughout the blade passage.

This study suggests that for geometrically similar pumps the flow fields differ considerably as the scale is reduced. Although examining macroscale flow fields can be useful in identifying flow structures, it is not a reliable predictor of flow regimes at reducing scale. Velocimetry data within the blade passage have enabled the identification of loss mechanisms within the flow, the quantification of overall hydrodynamic losses, and the measurement of incongruent flow at the impeller discharge. Thus, an improved understanding of the hydrodynamic behavior of miniature-scale centrifugal pumps has been gained, providing a basis for future improvements to their design.

Future studies should consider the use of three-dimensional stereo PIV to accurately quantify complex flow within the pump. The measurement of the third velocity component will account for any perspective error associated with the current velocimetry technique and accurately measure the magnitude of out-of-plane flow.

Acknowledgment

The author would like to acknowledge the financial support of Enterprise Ireland through the Industry Led Research Program in Power Electronics. The involvement of J.P. is supported by Science Foundation Ireland under Grant No. 03/CE3/I405.

Nomenclature

Symbol Description Unit

A = area (m^2)
D = impeller diameter (m)
L = characteristic length (m)
P = pressure rise (Pa)
Q = flow rate (m^3/s)
R = impeller radius (m)
Re = Reynolds number
T = shaft torque (nm)
V = time-averaged velocity (m/s)
Z = number of blades
c = axial blade clearance (m)
g = acceleration due to gravity (m/s^2)
h = blade height (m)
r = local radial distance (m)
rpm = rotational speed
t = blade thickness (m)
x = nominal distance (m)

Greek Symbols

Δ = difference
Φ = specific volumetric flow rate
Ψ = specific pressure rise
α = blade angle (deg)
δ = boundary layer thickness (m)
ζ = deviation angle (deg)
η = efficiency
θ = angle (deg)
ν = kinematic viscosity (m/s^2)
ρ = density of water (kg/m^3)
σ = slip factor
ω = rotational speed (rad/s)

Superscript

* = normalized

Subscripts

L = characteristic length scale
abs = absolute
b = blade
bp = blade passage
cl = chord length
max = maximum
rad = rad
rel = relative
rel mea = measured relative component
rel tang = relative tangential
s = slip
v = volumetric
x = local distance
θ = absolute tangential
1 = inlet
2 = outlet

References

[1] Rodgers, P., Eveloy, V., and Pecht, M., 2005, "Extending the Limits of Air-Cooling in Microelectronic Equipment," Keynote Presentation, Proceedings of the IEEE EuroSIME, pp. 695–702.
[2] Garimella, S. V., Joshi, Y. K., Bar-Cohen, A., Mahajan, R., Toh, K. C., Carey, V. P., Baelmans, M., Lohan, J., Sammakia, B., and Andros, F., 2002, "Thermal Challenges in Next Generation Electronic Systems—Summary of Panel Presentations and Discussions," IEEE Trans. Compon. Packag. Technol., **25**(4), pp. 569–575.
[3] Singhal, V., Garimella, S. V., and Raman, A., 2006, "Microscale Pumping Technologies for Microchannel Cooling Systems," Appl. Mech. Rev., **57**(3), pp. 191–221.
[4] Matteucci, M., Perennes, F., Marmiroli, B., Miotti, P., Vaccari, L., Gosparini, A., Turchet, A., and Di Fabrizio, E., 2006, "Compact Micropumping System Based on LIGA Fabricated Microparts," Microelectron. Eng., **83**, pp. 1288–1290.
[5] Lei, K. F., Law, W. C., Suen, Y.-K., Li, W. J., Yam, Y., Ho, H. P., and Kong, S.-K., 2007, "A Vortex Pump-Based Optically-Transparent Microfluidic Platform for Biotech and Medical Applications," Proc. Inst. Mech. Eng., Part H: J. Eng. Med., **221**, pp. 129–141.
[6] Ahn, C. H., and Allen, M. G., 1995 "Fluid Micropumps Based on Rotary Magnetic Actuators," Micro Electro Mechanical Systems MEMS'95, Proceedings, IEEE.
[7] Sankovic, J. M., Kadambi, J. R., Mehta, M., 2004, "PIV Investigations of the Flow in the Volute of a Rotary Blood Pump," ASME J. Fluids Eng., **126**, pp. 730–734.
[8] Day, S. W., Lemire, P., Flack, R. D., and McDaniel, J. C., 2003, "Effect of Reynolds Number on Performance of a Small Centrifugal Pump," Fourth ASME/JSME Joint Fluids Engineering Conference, Jul. 6–11.
[9] Lorenz, M., and Smith, W. A., 2002, "Rotodynamic Pump Scaling," ASAIO J., **48**, pp. 419–430.
[10] Dong, R., Chu, S., and Katz, J., 1992, "Quantitative Visualization of the Flow Within the Volute of a Centrifugal Pump. Part B: Results and Analysis," ASME J. Fluids Eng., **114**, pp. 396–403.
[11] Pedersen, N., Larsen, P. S., and Jacobsen, C. B., 2003, "Flow in a Centrifugal Pump Impeller at Design and Off-Design Conditions—Part 1: Particle Image Velocimetry (PIV) and Laser Doppler Velocimetry (LDV) Measurements," ASME J. Fluids Eng., **125**, pp. 61–72.
[12] Paone, N., Reithmuller, M. L. and Van den Braembussche, R. A., 1989, "Experimental Investigation of the Flow in the Vaneless Diffuser of a Centrifugal Pump by Particle Image Displacement Velocimetry," Exp. Fluids, **7**, pp. 371–378.
[13] Stepanoff, A. J., 1957, *Centrifugal and Axial Flow Pumps: Theory, Design and Application*, 2nd ed., Wiley, New York.
[14] EN ISO 5198:1998, 1999, "Centrifugal, Mixed Flow and Axial Pumps—Code for Hydraulic Performance Tests—Precision Class."
[15] Reithmuller M. L., Raffel, M. R., Kompenhans, J., Carosone, F., Cenedese, A., Bruker, Ch., *Particle Image Velocimetry, 2003* (Lecture Series 1996–2003), Von Karman Institute for Fluid Dynamics.
[16] Choi, Y.-D., Nishinao, K., Kurokawa, J., and Matsui, J., 2004, "PIV Measurement of Internal Flow Characteristics of Very Low Specific Speed Semi-Open Impeller," Exp. Fluids, **37**, pp. 617–630.
[17] Tsukiya, T., Taenka, Y., Tatsumi, E., and Takano, H., 2002, "Visualization Study of Transient Flow in the Centrifugal Blood Pump Impeller," ASAIO J., **48**, pp. 431–436.
[18] Sumer, B. M., Christiansen, N., and Fredsøe, J., 1997, "The Horseshoe Vortex and Vortex Shredding Around Vertical Wall-Mounted Cylinder Exposed to Waves," J. Fluid Mech., **332**, pp. 41–70.
[19] Gulich, J. P., 2008, *Centrifugal Pumps*, Springer-Verlag, Berlin.
[20] Van den Braembussche, R. A., 2006, "Flow and Loss Mechanisms in Volutes of Centrifugal Pumps," *Design and Analysis of High Speed Pumps*, pp. 12-1–12-26. Educational Notes RTO-EN-AVT-143, Paper 12. Neuilly-sur-Seine, France: RTO. Available from: http://www.rto.nato.int/abstracts.asp
[21] Hodson H. P., 2006, *Boundary Layers in Turbomachines* (Lecture Series 1991–2006), Von Karman Institute for Fluid Dynamics.

Pressure Fluctuation Prediction of a Model Kaplan Turbine by Unsteady Turbulent Flow Simulation

Shuhong Liu
State Key Laboratory of Hydro Science and Hydraulic Engineering,
Tsinghua University,
Beijing 100084, China

Shengcai Li[1]
WIMRC,
University of Warwick,
Coventry CV4 AL, UK
e-mail: S.Li@warwick.ac.uk

Yulin Wu
State Key Laboratory of Hydro Science and Hydraulic Engineering,
Tsinghua University,
Beijing 100084, China

While larger and larger turbines are being developed, hydraulic stability has become one of the key issues for their performance assessments. An accurate prediction of their pressure fluctuations is vital to the success of new model development. In this paper, we briefly introduced the method, i.e., the three-dimensional unsteady turbulent flow simulation of the complete flow passage, which we used for predicting the pressure fluctuations of a model Kaplan turbine. In order to verify the prediction, the model turbine was tested on the test rig at the Harbin Electric Machinery Co., Ltd. (HEC), China, which meets all the international standards. Our main findings from this numerical prediction of pressure fluctuations for a model Kaplan turbine are as follows. (1) The approach by using 3D unsteady turbulent flow including rotor-stator interaction for the whole flow passage is a feasible way for predicting model turbine hydraulic instability. The predicted values at different points along its flow passage all agree well with the test data in terms of their frequencies and amplitudes. (2) The low-frequency pressure fluctuation originating from the draft tube is maximal and influences the stability of the turbine operation mostly. The whole flow passage analysis shows that the swirling vortex rope in the draft tube is the major source generating the pressure fluctuations in this model turbine. (3) The second harmonic of the rotational frequency $2f_n$ is more dominant than the blade passing frequency Zf_n in the draft tube. This prediction, including the turbulence model, computational methods, and the boundary conditions, is valid either for performance prediction at design stage and/or for operation optimization after commissioning.
[DOI: 10.1115/1.3184025]

Keywords: Kaplan turbine, turbulent flow simulation, unsteady flow, pressure fluctuation prediction

1 Introduction

Zhang [1] pointed out that the physical origin of the spontaneous unsteady flow under off-design conditions was identified as due to the absolute instability feature of the swirling flow in the draft tube conical inlet, which either occupied a large portion of the inlet and caused a strong helical vortex rope at small flow rate condition, or started midway and caused a breakdownlike vortex bubble, followed by weak helical waves at large flow rate conditions. It was worth emphasizing that the axial-flow velocity profiles in the inlet played a key role in the absolute instability/convective instability characters of the swirling flow.

Rheingans [2] was the first person who studied this important phenomenon and suggested an empirical equation to estimate the frequency of the vortex train in the draft tube, that is

$$f = f_n/c$$

where f_n is rotating frequency of turbine, and c is a constant between 3.2 and 4.0.

Recently, much more studies have been performed experimentally and numerically, showing that the low-frequency pressure fluctuation in the draft tube possesses a frequency of 0.15–0.33 times the runner's rotating frequency, and that this pressure fluctuation is mainly induced by the flow at the area near the inlet of the draft tube.

Among those numerical approaches for turbine flow analysis, the three-dimensional unsteady turbulent flow simulation is one of the most important developments. Ruprecht et al. [3,4] was the first to attempt to numerically simulate the complete flow of a Francis turbine including the rotor-stator interactions. As to partial flows, many studies have been done. For example, using large eddy simulation (LES), Skotak [5] modeled the unsteady flow of a helical vortex in the turbine draft tube. Sick et al. [6] and Paik and Sotiropoulos [7] performed the unsteady flow simulation in the elbow type draft tube and compared their results with test data. Muntean et al. [8] did an analysis for the flow in the spiral case and the distributor of a Kaplan turbine, acquiring information on channel vortex at different operation conditions.

In order to predict the hydraulic stability performance, we need to simulate the three-dimensional unsteady turbulent flow throughout the complete flow passage of this model Kaplan turbine. By using the software FLUENT and the simulation approach developed by Liu et al. [9], the pressure fluctuations at different sampling points along the flow passage have been predicted based on the calculations. For validating the approach, a thorough model test has been performed on the test rig at the Harbin Electric Co.

2 Numerical Prediction

2.1 Parameters of Model Kaplan Turbine and Computational Domain. The model turbine is developed for scaling up to a prototype Kaplan turbine with the following specifications: De-

[1]Corresponding author.

Contributed by the Fluids Engineering Division of ASME for publication in the JOURNAL OF FLUIDS ENGINEERING. Manuscript received May 19, 2008; final manuscript received April 14, 2009; published online September 18, 2009. Assoc. Editor: Chunill Hah.

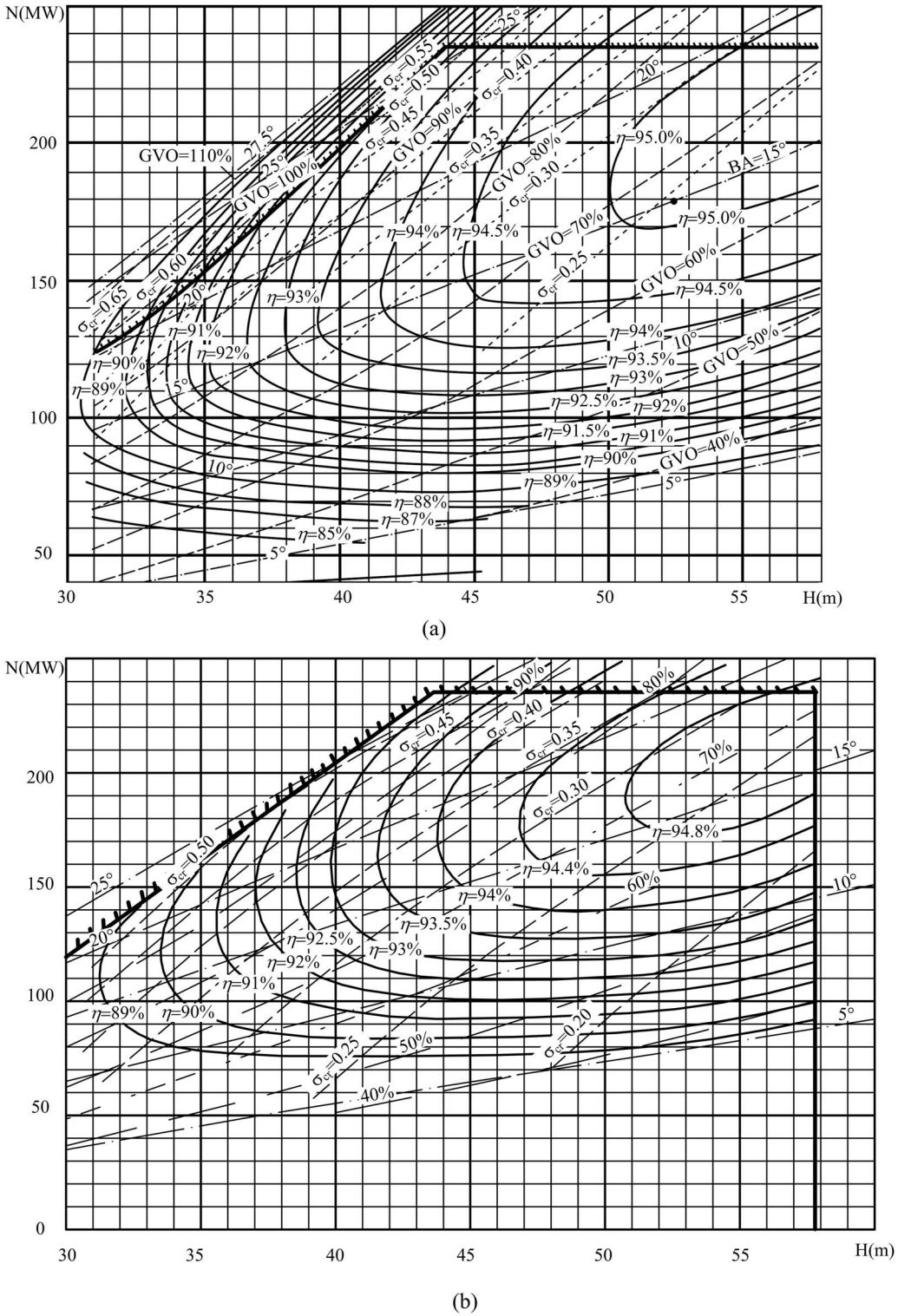

Fig. 1 Operation performances of the prototype turbine: (*a*) test, and (*b*) prediction by steady flow simulation (GVO-guide vane opening, BA-blade angle, η-efficiency, σ_a-cavitation number)

sign head $H_r=47$ m; runner diameter $D_1=8$ m; rated speed $n=107$ rpm; number of guide vanes $Z_0=24$, and number of runner blade $Z=6$. Its operation performances are shown in Fig. 1, in which Fig. 1(*a*) is the model test data and Fig. 1(*b*) is the steady flow simulation results. Both of them are scaled up to the prototype by using similarity laws.

Prior to prediction, a three-dimensional steady turbulent simulation has been conducted, which will then enable the numerical prediction using the 3D unsteady turbulent flow simulation. The computational domain covers the complete flow passage starting from the inlet of the spiral casing throughout the stay vanes, guide vanes, and runner to the outlet of draft tube (Fig. 2), including the flow interactions between the stationary guide vanes and the runner, and between the runner and the draft tube.

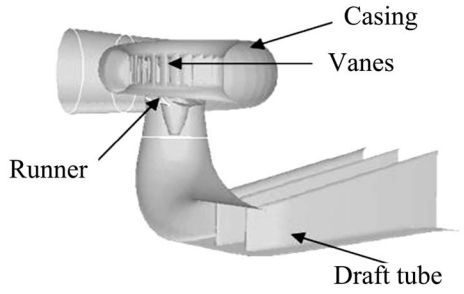

Fig. 2 Flow passage of the Kaplan turbine

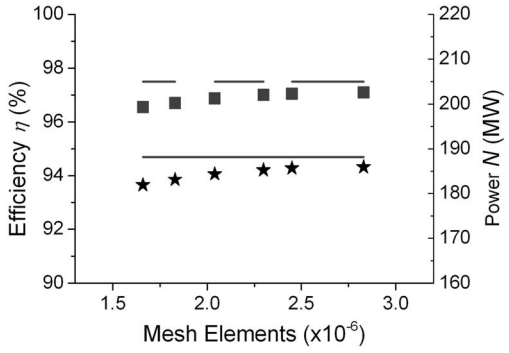

Fig. 3 *N* and η versus mesh elements; (–■–) calculated power, (– –) tested power, (--★--) calculated efficiency, and (——) tested efficiency

2.2 Mesh Scheme. Owing to the complexity of the computational domain, the unstructured tetrahedron mesh has been employed because of its fine adaptability [10]. For interfaces between the guide vanes and the runner, and between the runner and the draft tube, slip meshes have been adopted to count for these two rotor-stator interactions. Those meshes on both sides of the interface are slipping toward each other, and the crunodes may not be consistent, but it is essential to ensure that their velocity components are consistent after interpolation, as well as their pressure and flow flux after integration.

To test the grid independence, several mesh schemes were employed for the steady flow simulation of the model Kaplan turbine. After more than 1500 iterations, all calculations reached to convergent solutions. In Fig. 3, the comparison of the predicted prototype's efficiency and power with the test results indicates that if the mesh elements are more than 2.5×10^6 the simulation will be good enough for this study though the higher ones would be better in particular for unsteady flow analysis.

A mesh with 2,578,000 elements and 543,000 crunodes were finally employed for the whole flow passage and the detailed mesh information for each component were listed in Table 1. After the test run, this mesh was fine enough to satisfy $y^+<200$ near the wall and to obtain the required features of pressure fluctuations. As far as only the amplitudes and dominant frequencies are concerned, the above mesh density should serve the purpose of this study well in terms of revealing the main features of the pressure fluctuation. Other detailed information, such as boundary layer flow etc., is not an objective for this paper.

Table 1 Mesh scheme of each part in the passage

	Casing and vanes	Runner	Draft tube
Crunodes	171,000	254,000	118,000
Mesh	813,000	1,204,000	561,000

Computational parameters for the model turbine are listed in Table 2, which are related to the rated operating point of the prototype Kaplan turbine.

2.3 Turbulence Model and Numerical Methods. The incompressible continuity equation and Reynolds time averaged N–S equation have been used to simulate the flow through the turbine passage, and the renormalization group (RNG) $k-\varepsilon$ double equation turbulence model has been employed to close the equations [11]. The governing equations are as follows.

The continuity equation

$$\frac{\partial \overline{u_j}}{\partial x_j}=0 \tag{1}$$

The momentum equation

$$\rho\frac{\partial \overline{u_i}}{\partial t}+\rho\overline{u_j}\frac{\partial \overline{u_i}}{\partial x_j}=\rho F_i-\frac{\partial \overline{p}}{\partial x_i}+\mu\frac{\partial^2\overline{u_i}}{\partial x_j\,\partial x_j}-\rho\frac{\partial}{\partial x_j}(\overline{u_i'u_j'}) \tag{2}$$

where

$$-\rho\overline{u_i'u_j'}=\mu_t\left(\frac{\partial \overline{u_i}}{\partial x_j}+\frac{\partial \overline{u_j}}{\partial x_i}\right)-\frac{2}{3}\left(\rho k+\mu_t\frac{\partial \overline{u_i}}{\partial x_i}\right)\delta_{ij}$$

The RNG $k-\varepsilon$ double equations

$$\rho\frac{Dk}{Dt}=\frac{\partial}{\partial x_j}\left(\alpha_k\mu_{\text{eff}}\frac{\partial k}{\partial x_j}\right)+2\mu_t\overline{S}_{ij}\frac{\partial \overline{u_i}}{\partial x_j}-\rho\varepsilon \tag{3}$$

$$\rho\frac{D\varepsilon}{Dt}=\frac{\partial}{\partial x_j}\left(\alpha_\varepsilon\mu_{\text{eff}}\frac{\partial \varepsilon}{\partial x_j}\right)+2C_{1\varepsilon}\frac{\varepsilon}{k}\nu_t\overline{S}_{ij}\frac{\partial \overline{u_i}}{\partial x_j}-C_{2\varepsilon}\rho\frac{\varepsilon^2}{k}-R \tag{4}$$

where $\overline{S_{ij}}=(\partial\overline{u_i}/\partial x_j+\partial\overline{u_j}/\partial x_i)$, $\mu_{\text{eff}}=\mu_t+\mu$, and $\mu_t=C_\mu k^2/\varepsilon$.

The additional term R

$$R=\frac{C_\mu\rho\eta^3(1-\eta/\eta_0)}{1+\beta\eta^3}\frac{\varepsilon^2}{k} \tag{5}$$

where $\eta=Sk/\varepsilon$, $\eta_0=4.38$, $C_\mu=0.0845$, $\beta=0.012$, $C_{1\varepsilon}=1.42$ (original in the model), $C_{2\varepsilon}=1.68$, $\alpha_k=1.0$, and $\alpha_\varepsilon=0.769$. Among these constants used in the turbulence model, a properly chosen value of $C_{1\varepsilon}$ is essential for improving the prediction of the pressure fluctuation. In the present simulation, $C_{1\varepsilon}=1.45$ was selected based on our preliminary computations.

The finite volume method has been adopted for space discretization and the second-order universal implicit mode has been used in the temporal space. The second-order central difference has been adopted for the source and diffusion terms of the governing equations and the second-order upwind difference has been adopted for the convection term.

The time step (TS) of 0.001 s was used for the unsteady flow simulation. At each time step, the SIMPLEC method is used to

Table 2 Computational parameters for the model Kaplan turbine

Angle of blade ψ (deg)	Opening of guide vanes A_0 (mm)	Prototype head H_p (m)	Unit speed n_{11} (rpm)	Unit flow rate Q_{11} (l/s)	Rotational speed n (rpm)	Test head H (m)
15	20	52.2	118.6	805	1267.9	14

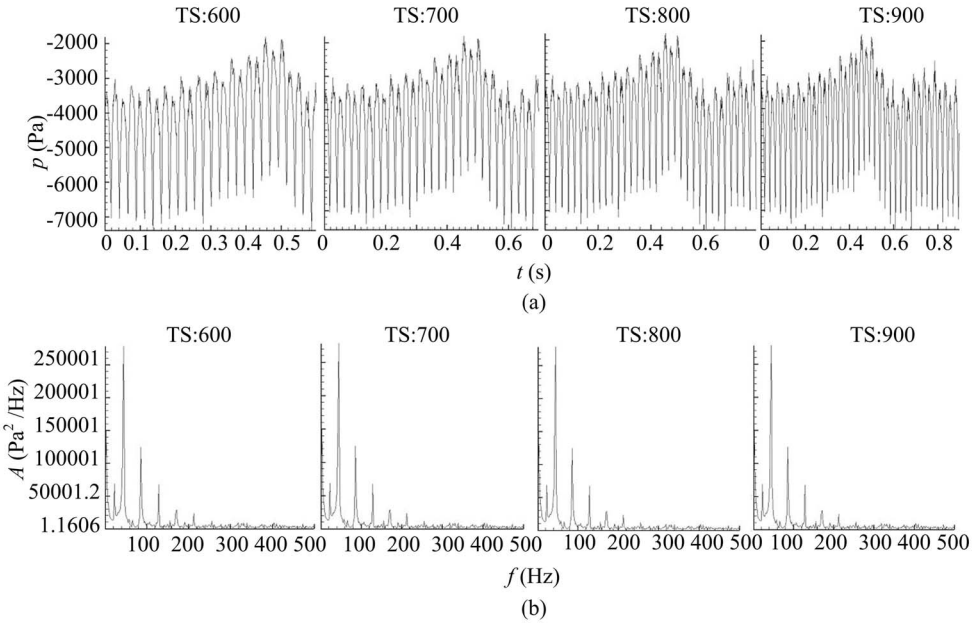

Fig. 4 Calculated pressure fluctuations at the inlet of the draft tube (TS): (*a*) pressure variation with time, and (*b*) pressure fluctuation spectrum

solve the discretized equations. When it converges, the calculation will proceed to the next time step, meanwhile the mesh of the runner will rotate to a new position.

2.4 Boundary Conditions and Number Independence of Time Step. The boundary conditions for the steady flow computation are as follows. On the inlet of the spiral casing the static pressure equals the test head with velocity normal to inlet boundary. The initial value of the inlet velocity is determined by the flow rate.

On the outlet of the draft tube the pressure is determined by the tail water level. To satisfy the flow continuity condition, correction to the outlet velocity distribution should be made to off-set the flow rate difference between the inlet and the outlet during the calculation process.

It is assumed that in the normal direction of the boundaries except for the inlet boundary, gradients of k and ε are zero. The wall function is employed for the vicinity of the fixed wall, and the no-slip boundary condition is applied too. For rotating boundary of runner, the boundary is moving at a velocity equal to tangent velocity of the runner periphery.

For unsteady flow calculation, the results of the steady flow calculation are taken as the initial flow field for the complete flow passage. With the time step of 0.001 s and the runner rotating speed of 1267.9 rpm, the runner of the model turbine will rotate in an angle of 7.61 deg for each time step.

The pressure measuring sensors used for the model Kaplan turbine and the prototype hydraulic turbine have the specifications as follows:

- Accuracy: $\pm 0.075\%$ of the full measuring range
- Dynamic character: delay time T_d=4.5 ms
- Sampling frequency: 220 Hz
- Output: 4–20 mA
- Measuring range: 0.3 MPa (in this study)

The sampling rate of 220 Hz used in the experiments allows us to observe pressure fluctuations up to the 10th harmonic of the rotational frequency.

For numerical prediction, calculations have been conducted up to more than the 20th harmonic. This range covers all the pressure fluctuation components interested, including the rotor-stator interactions, which is below the 30th harmonic. The time step of 0.001 s is small enough for achieving the 20th harmonic compared with the test sampling.

The total number of time step for a complete simulation is 900. In order to verify that the calculation is independent of the number of time step, simulations for different time steps of 200, 300, 400, 500, 600, 700, 800, and 900 have been tested. The resultant spectrum of the pressure fluctuations for 600, 700, 800, and 900 steps are almost identical, as shown in Fig. 4. Therefore, the simulation with time steps more than 600 can capture the main features (frequencies and amplitude) of the pressure fluctuations occurring in the flow passage of the model turbine for various operating conditions.

Figure 5 shows the locations where pressure measuring is taken for the tests of the model turbine. The sampling points for numerical simulations are also selected identically. As shown in the figure, they are located before and after the stay vanes, in front of the runner, beneath the runner at a distance of $0.3D_1$, at the inlet of the draft tube ($-X$ and $-Y$ points), and at the front wall of the draft tube elbow.

3 Analysis and Discussion

The predicted fluctuations for the model turbine, both their waveforms and frequency spectra in the fast Fourier transform (FFT), as shown in Fig. 6, have revealed essential information about the hydraulic instability of the model Kaplan turbine. Table 3 shows the pressure fluctuation spectrum data and main frequencies at various locations. Pressure variations with time (i.e., t =0.4 s, 0.5 s) in three sections (S_1, S_2, and S_3) are plotted in Fig. 7.

The source of the pressure fluctuations, their occurrence in the entire flow passage can all be identified from the calculation results [12].

At this particular operation condition for which the prediction calculation has been made, the rotating frequency of the turbine shaft is f_n=21.13 Hz. There is a component of the pressure fluctuations at a low frequency of f=3.48 Hz has been predicted, which is 0.165 times of the rotating frequency. Its amplitude reaches maximum at the front wall of the draft tube elbow (Point

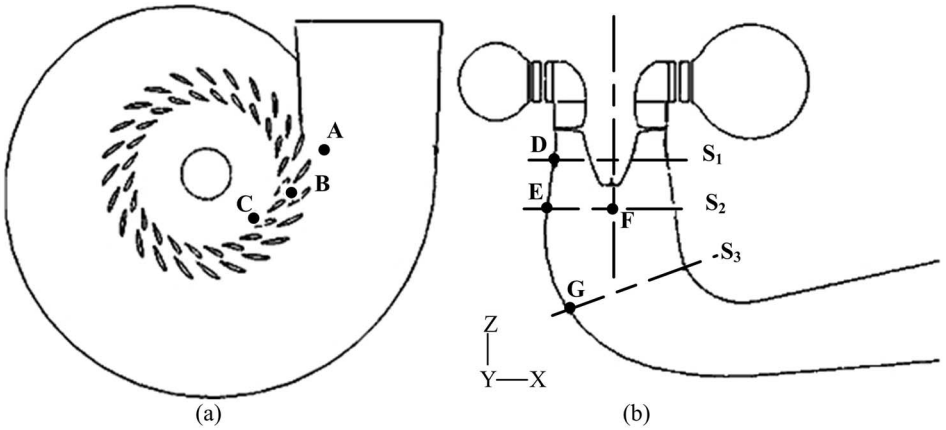

Location of recording points and sections

A: Point before stay vanes	F: Point at inlet of draft tube (-*Y*)
B: Point after stay vanes	G: Point at front wall of draft tube elbow
C: Point after guide vanes	S_1: Section beneath runner exit at a distance of $0.3D_1$
D: Point at $0.3D_1$ below center of runner	S_2: Section at inlet of draft tube
E: Point at inlet of draft tube (-*X*)	S_3 :Section at draft tube elbow

Fig. 5 Locations where the numerical and experimental sampling for the pressure fluctuations were taken: (*a*) plan view and (*b*) side view

G). This fluctuation propagates toward upstream with its amplitude decaying. This component, we believe, originated from the swirling rope in the draft tube.

Low frequency fluctuations are of special interest because they can propagate up to the whole water conduit, causing structural vibration of the power plant. It is also likely to induce the electric power surge of the grid through the coupling, with the generator subject to their frequency characteristics. For dual regulated Kaplan turbines, on-cam operation sets both the guide vane opening and the runner blade angle in such combination that no significant runner outlet swirl and draft tube surge are generated.

The component of $f=23.4$ Hz is approximately equal to the rotating frequency f_n, with its own highest amplitude appearing at locations underneath the runner exit at a distance of $0.3D_1$ and at the inlet section of the draft tube. It propagates upstream and downstream with its amplitude decaying gradually. This component is produced by the rotation of the turbine.

There are also another two higher harmonic components being predicted: the second $f=45.3$ Hz and the fourth $f=86.0$ Hz, which are the largest and the second largest harmonic frequencies in the draft tube. Their highest amplitudes appear at the inlet section of the draft tube, which we believe are attributed to the swirling of the nonuniform pressure distribution in this section (referring to S_2 in Fig. 7). It propagates upstream and downstream with amplitudes decaying. Also the second harmonic of the rotational frequency at inlet of the draft tube ($f=45.3$ Hz obtained from test, and $f=42.3$ Hz from calculation) is more dominant than the blade passing frequency,[2] $Zf_n=126.8$ Hz (tested $f=125.8$ Hz and calculated 128.8 Hz) in the draft tube. This second harmonic frequency in the draft tube is created by the two rotating low pressure areas (referring to S_2 in Fig. 7).

The fluctuation component of $f=128.8$ Hz (6th harmonic) reaches its highest amplitude underneath the runner and decreases quickly while propagating downstream. The components of $f=171.6$ Hz, $f=213.4$ Hz, and $f=302.9$ Hz (8th, 10th, and 14th harmonics) are also predicted but their amplitudes are small.

The location where the highest amplitude sampled is believed to be the origin of the fluctuation. As analyzed by hydraulic impedance approach, this location is featured as a diffuser whose hydraulic impedance[3] is extremely high. This high impedance implies that a small flow rate oscillator (unsteadiness) will induce an extremely high pressure fluctuation there. That is, it serves well as an oscillation exciter. For details, see Refs. [13,14].

In this simulation, because the turbulent unsteady flow simulation is applied to predict the turbine pressure fluctuation under noncavitation conditions, the hydraulic impedance in the pressure variation plays an essential role not others such as wall friction, Reynolds and viscous stresses, etc. The hydraulic compliance is mainly represented by the cavitation compliance in the draft tube[4] if the flow is cavitated there. However, for this noncavitated flow analysis the compliance effect is negligible.

For the location before the stay vanes (Point A), the fluctuation component with a frequency of 0.165 times of the rotating frequency (i.e., $f=3.48$ Hz) is the strongest, as shown in Table 3. Since this low-frequency fluctuation propagates throughout the whole system as we mentioned before, it possesses a feature of the

[2]The excitation frequency, which is equal to the rotation speed multiplied by the number of runner blades, is defined as the blade passing frequency. Owing to the interaction of the runner blades with the guide vanes, higher frequencies of up to k folds of the blade passing frequency can be generated, with k being typically between 1 and 2 for hydraulic turbines. For this turbine, it is equal to $f=126.8$ Hz, if $k=1$. The pressure fluctuation component, with the highest amplitude at the front-runner and in the downstream of the runner, has k value of 4, which is the guide vane number ($Z_0=24$) divided by the runner blade number ($Z=6$). The component is produced by the rotor-stator interaction.

[3]The hydraulic impedance $Z(x)$ is a complex-valued function in a fluid system, which is defined as the ratio of the complex head $H(x)$ to the complex discharge $Q(x)$ at a particular point in the system ($Z(x)=H(x)/Q(x)$).

[4]It is defined as $-\partial V_{vap}/\partial NPSE$, where V_{vap} is the cavitation volume in the draft tube, and $NPSE$ is the net positive suction head of the turbine. V_{vap} can be predicted using the cavity flow calculation in the flow passage of the turbine by using cavity two-phase flow (compressible flow) simulation.

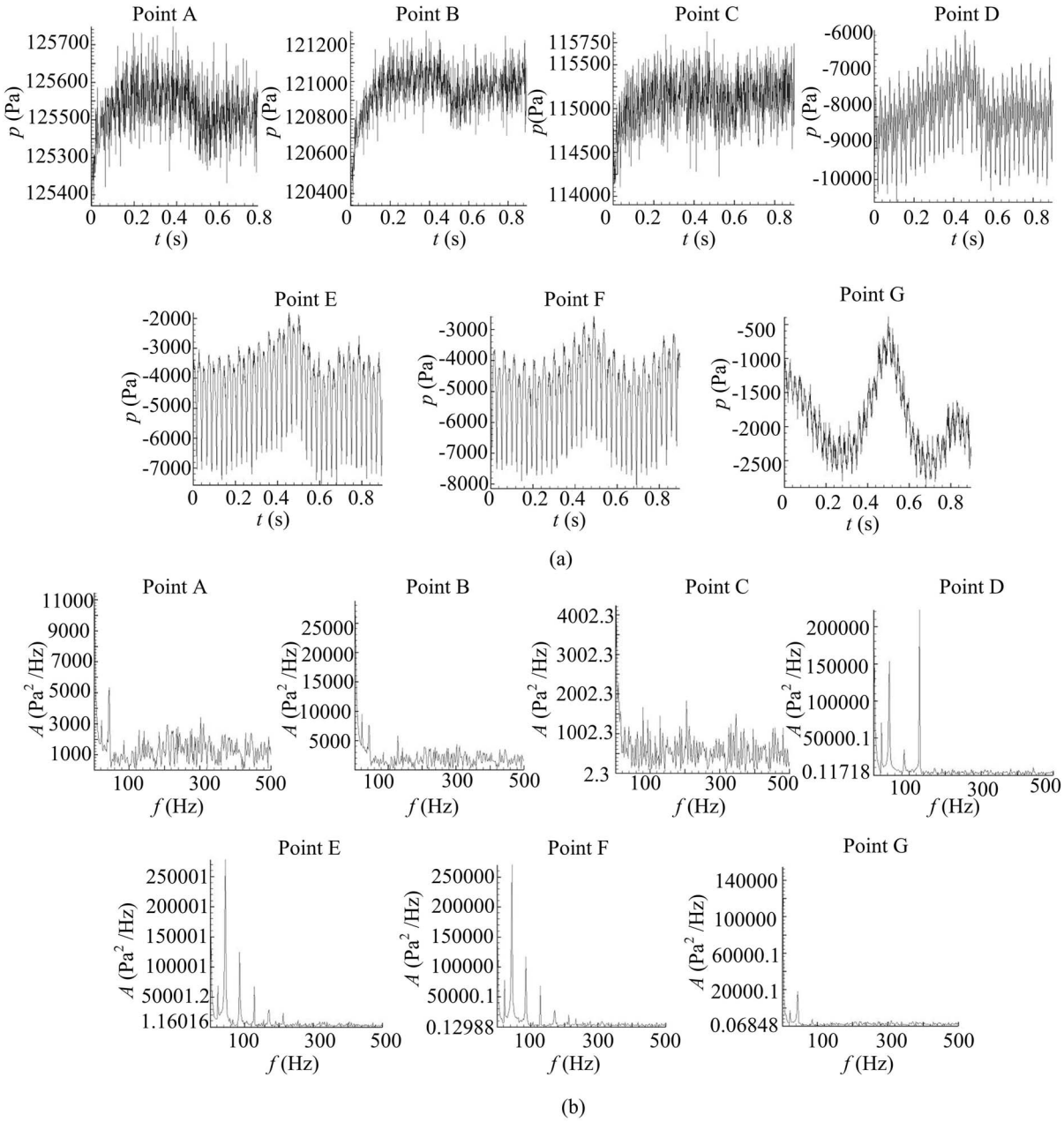

Fig. 6 Predicted pressure fluctuations at various sampling locations of the model turbine flow passage: (*a*) pressure variation with time, and (*b*) pressure fluctuation spectrum (FFT)

Table 3 Pressure fluctuation spectrum and main frequencies at various locations

	Fluctuation frequency (Hz)				
	f=3.48	f=23.4	f=45.3	f=86.0	f=128.8
Spectrum at point A (Pa^2/Hz)	11,400	3,200	5,400	1,900	2,600
Spectrum at point B (Pa^2/Hz)	28,700	9,500	7,400	3,000	5,600
Spectrum at point C (Pa^2/Hz)	42,300	8,000	9,200	7,500	14,400
Spectrum at point D (Pa^2/Hz)	126,000	70,300	153,000	34,300	222,300
Spectrum at point E (Pa^2/Hz)	150,000	68,500	277,900	124,500	67,300
Spectrum at point F (Pa^2/Hz)	133,800	77,600	269,600	116,700	67,600
Spectrum at point G (Pa^2/Hz)	174,300	17,000	38,000	7,500	1,700

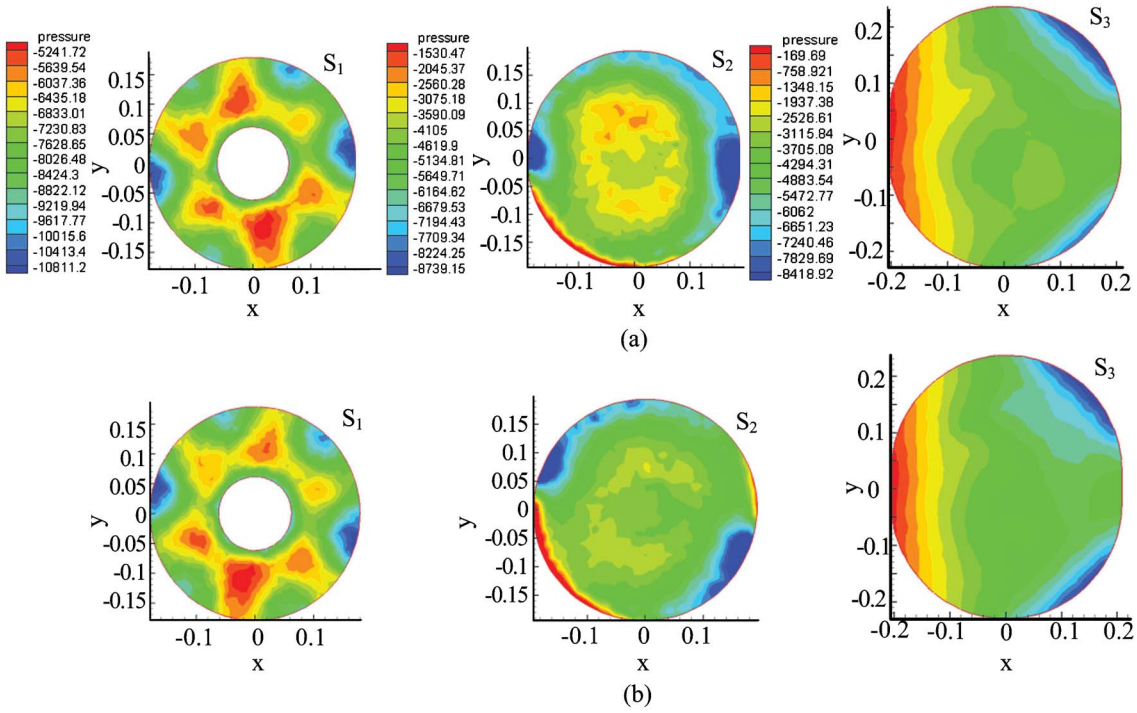

Fig. 7 Predicted pressure variations with time at various locations of the model turbine: (*a*) $t=0.4$ s, and (*b*) $t=0.5$ s

system instability. The second strongest component is the 2nd harmonic with a frequency of $f=45.3$ Hz, which comes from the entrance of the draft tube.

For the location after the stay vanes (point B), the fluctuation components are almost the same as those before the stay vanes, but a little larger than those at point A.

For the location after the guide vanes and before the runner (point C), the component with a frequency ($f=3.48$ Hz) of 0.165 times of the rotating frequency is also the strongest, as shown in Table 3. The second strongest is the 6th harmonic ($f=128.8$ Hz), which is transmitted from the location underneath the runner exit. Referring to S_1 in Fig. 7, there are six spike-shaped pressure variations, which rotate at the runner rotating speed. It is presumably relevant to the blade number.

For the location underneath the runner (point D), the strongest component has a frequency of $f=128.8$ Hz (i.e., the 6th harmonic), which is also a blade number related component. The second strongest component is the 2nd harmonic ($f=45.3$ Hz), which is induced by the nonuniform pressure distribution featured with two high pressure areas at the entrance of the draft tube. The third strongest one is the component with a frequency of 0.165 times of the rotating frequency ($f=3.48$ Hz) as mentioned before.

For the location at the entrance of draft tube, two pressure sampling points named as $-X$ (point E) and $-Y$ (point F) are listed in Table 3. For both points, the components of the 2nd harmonic with frequency of $f=45.3$ Hz have largest amplitudes, which originated from the nonuniform pressure distribution as explained before. The second strongest component has a frequency of 0.165 times of the rotating frequency ($f=3.48$ Hz).

For the location at the front wall of draft tube elbow (point G), there are two large fluctuation components with frequencies of $f=3.48$ Hz and $f=45.3$ Hz have been predicted.

4 Comparison With the Model Turbine Test

In order to validate the numerical predictions, the model turbine has been tested on the test rig at the Harbin Electric Machinery Co., Ltd. (HEC).

4.1 Model Turbine Test. The experimental observation of pressure the fluctuations of this model Kaplan turbine has been conducted on the rig, as shown in Fig. 8. Its main specifications are as follows: maximum head of 100 m, maximum flow rate of 1.2 m^3/s, runner diameter of 300–500 mm, power of the torque meter of 400 kW, rotating speed of the torque meter of 300–1800 rpm, power of driving pump of 2×400 kW, capacity of the flow rate calibrator of 120 m^3, capacity of the reservoir of 750 m^3, and maximum error of the efficiency test of $<\pm0.25\%$.

4.2 Experimental Uncertainty. This test rig offers high mea-

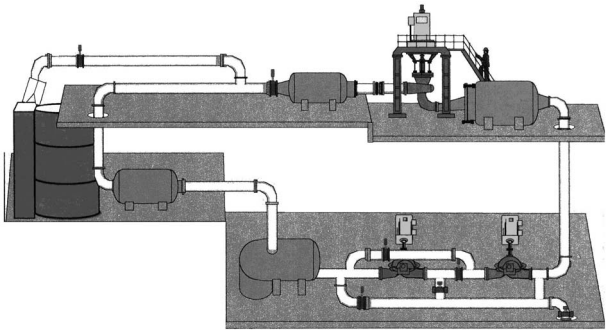

Fig. 8 The international standard test rig at HEC (courtesy of HEC)

Table 4 Measurement accuracy

Parameters	Measuring range	Uncertainty (%)
Flow rate Q (m^3/s)	0–1.0	±0.2
Head H (m)	0–2.07	0.075
Force on arm K (E pound)	0–1000	±0.02
Angular speed ω	0–3000	±0.05

Table 5 Comparison of the frequencies and relative amplitudes at various locations

		Low ($<f_n$) $\Delta H'/H$ (%)	1st (f_n) $\Delta H'/H$ (%)	2nd ($2f_n$) $\Delta H'/H$ (%)	4th ($4f_n$) $\Delta H'/H$ (%)	6th ($6f_n$) $\Delta H'/H$ (%)	Pressure fluctuation at time domain $\Delta H'/H$ (%)
System frequency	C	f=3.2 Hz	f=21.3 Hz	f=42.3 Hz	f=84.2 Hz	f=125.8 Hz	
	T	f=3.48 Hz	f=23.4 Hz	f=45.3 Hz	f=86.0 Hz	f=128.8 Hz	
Point A	C	0.142	0.195	0.353	0.289	0.413	0.67
Point B	C	0.226	0.337	0.414	0.363	0.607	0.89
Point C	C	0.274	0.268	0.461	0.574	0.973	1.56
Point D	C	0.473	0.916	1.88	1.23	3.8	4.10
	T	1.40	1.50	3.0	1.5	4.1	4.80
Point E	C	0.516	0.90	2.53	2.34	2.11	4.03
	T	2.0	1.60	4.4	3.6	2.0	5.14
Point F	C	0.49	0.963	2.96	2.26	2.11	4.01
	T	1.60	1.60	4.5	3.5	2.0	5.10
Point G	C	0.55	0.45	0.94	0.57	0.33	1.10
	T	3.0	0.50	1.3	0.5	0.2	3.18

(Calculated: C; tested: T)

suring accuracies, as shown in Table 4.

As to the pressure measurement, high accuracies have been achieved by employing precision measuring systems. The water pressure at the draft tube is measured by a pressure transducer (type 3051TA1A2B21A). Its measuring range is 0–200 kPa with a precision of 0.075%. The pressure fluctuations are recorded by transducers (type 112A22) with sensitivity of 100 mV/psi and linearity of $\leq$1%FS.

4.3 Comparison With Test Data. The predicted fluctuations have been compared against the data obtained from the test, as shown in Table 5. The comparison has been made for (a) fluctuation components ranging from the system's low frequency throughout the rotating frequency and its higher harmonics, and (b) their relative amplitude ($\Delta H'/H$)[5] for each sampling location.

The technical information such as dominant frequency and its location(s) is essential for the development of new turbines and the safe operation of the commissioned turbines. It is particularly important to those turbine systems[6] where the middle part of the system (including section S_1 and Point D) is not buried in concrete and prone to internal flow-induced vibrations. Therefore, pressure transducers are often mounted for monitoring the conditions there. For the acceptance test of the model turbine, conditions in section S_1, such as the relative amplitudes $\Delta H/H$, etc. (in particular at the sampling point D), are used for the assessment of hydraulic instability of the model turbine. This is why we compared these attributions of the fluctuations.

From the comparison made between the test results and the calculations, as shown in Table 5, the following can be seen:

(1) A good agreement is achieved in general for harmonic frequencies.
(2) The amplitudes of the components coincides well at Point D underneath the runner at a distance of $0.3D_1$.
(3) In the draft tube, there are some discrepancies in respect to amplitude comparisons in particular for sections S_2 and S_3. This discrepancy may partially be attributed to the inconsistency of the testing conditions of the tail water level in the suction tank. During the calculations, it is treated as constant but in reality the draft tube of the model turbine is supported by frame and subject to vibrations.
(4) The main frequencies at each section agree well. For instance, at section S_1, the dominant frequency is the blade passing frequency and in the draft tube the second harmonic frequency becomes the dominant one as shown consistently by both the calculations and model tests.
(5) The predicted fluctuation before the runner is relatively small, so are the experiment data, and therefore, have been omitted from the test report provided by HEC.

The good agreement between the test data and calculation results indicates the validity of this calculation method for predicting hydraulic stability during the design stage of the model turbine.

5 Conclusions

The following remarks can be drawn.

(1) The approach using three-dimensional unsteady turbulent flow, including rotor-stator interaction for the whole flow passage, is a feasible way for predicting the model turbine hydraulic instability. The predicted values at different points along its flow passage all agree well with the test data in terms of their frequencies and amplitudes.
(2) The low-frequency (3.48 Hz) pressure fluctuation originating from the draft tube is maximal and influences the stability of the turbine operation mostly. The whole flow passage analysis shows that the swirling vortex rope in the draft tube is the major source generating the pressure fluctuations in this model turbine.
(3) In the draft tube, the 2nd harmonic of the rotational frequency $2f_n$ (that is f=45.3 Hz obtained from test and f =42.3 Hz from calculation) is more dominant than the blade passing frequency f_nZ.
(4) The conclusive prediction obtained through this numerical work strongly indicates that the turbulence model, computational methods, and boundary conditions employed are appropriate for the purpose of pressure fluctuation prediction for model Kaplan turbines.
(5) This method can be further extended to predict the hydraulic instabilities of prototype turbines whose off-design operations often cause severe low-frequency fluctuations.
(6) This prediction is an effect approach, which can be used either at the design stage for performance prediction and/or after commissioning for operation optimization.

Acknowledgment

The research is support by the Chinese National Foundation of Natural Science (Contract No. 90410019); and the Research Exchange with China and India by the Royal Academy of Engineering (UK) (Grant No. R. ESCM 3027).

[5]It is defined as the ratio of the maximum amplitude in time history with 97% reliability to the effective head.

[6]This is a common practice in most power stations.

In addition, the second author (S. Li) also acknowledges the EPSRC's WIMRC (UK) financial support (Grant Nos. R. ESCM 9001 and R. ESCM 9004) and the Chinese Open Grant (Grant No. SKlhse-2006-E-01) by the State Key Laboratory of Hydro Science and Hydraulic Engineering.

References

[1] Zhang, R.-K., Mao, F., Wu, J.-Z., Chen, S.-Y., Wu, Y.-L., and Liu, S.-H., 2009, "Characteristics and Control of the Draft-Tube Flow in Part-Load Francis Turbine," ASME J. Fluids Eng., **131**(2), p. 021101.

[2] Rheingans, W. J., 1940, "Power Swing in Hydroelectric Power Plants," Trans. ASME, **62**, pp. 171–184.

[3] Ruprecht, A., Heitele, M., and Helmrich, M., 2000, "Numerical Simulation of a Complete Francis Turbine Including Unsteady Rotor/Stator Interactions," *Proceedings of the 20th IAHR Symposium on Hydraulic Machinery and Systems*, Charlotte, NC, Paper No. CFD-S03.

[4] Ruprecht, A., Helmrich, T., and Scherer, T., 2002, "Simulation of Vortex Rope in a Turbine Draft Tube," *Proceedings of the 22nd IAHR Symposium on Hydraulic Machinery and Systems*, Lausanne, Swiss, Paper No. A86-HEYGMGJF.

[5] Skotak, A., 2000, "Of the Helical Vortex in the Turbine Draft Tube Modeling," *Proceedings of the 20th IAHR Symposium on Hydraulic Machinery and Systems*, Charlotte, NC, Paper No. CFD-S07.

[6] Sick, M., Dörfler, P., Sallaberger, M., Lohmberg, A., and Casey, M., 2002, "CFD Simulation of the Draft Tube Vortex," *Proceedings of the 22nd IAHR Symposium on Hydraulic Machinery and Systems*, Lausanne, Swiss, Paper No. A31-KZYRFXJV.

[7] Paik, J., and Sotiropoulos, F., 2004, "Numerical Simulation of Flow in a Hydroturbine Draft Tube Using Unsteady Statistical Turbulence Models," *Proceedings of the 22nd IAHR Symposium on Hydraulic Machinery and Systems*, Stockholm, Sweden, Paper No. A10(1).

[8] Muntean, S., Balint, D., and Susan-Resiga, R., 2004, "3D Flow Analysis in the Spiral Case and Distributor of a Kaplan Turbine," *Proceedings of the 22nd IAHR Symposium on Hydraulic Machinery and Systems*, Stockholm, Sweden, Paper No. A10(2).

[9] Liu, S. H., Shao, Q., and Yang, J. M., 2004, "Unsteady Turbulent Simulation of Three Gorges Hydraulic Turbine and Analysis of Pressure in the Whole Passage," Journal of Hydroelectric Engineering, **23**(5), pp. 97–101.

[10] Hassan, O., Probert, E. J., Morgan, K., and Weatherill, N. P., 2000, "Unsteady Flow Simulation Using Unstructured Meshes," Comput. Methods Appl. Mech. Eng., **189**(4), pp. 1247–1275.

[11] Yakhot, V., and Orszag, S. A., 1986, "Renormalization Group Analysis of Turbulence. I: Basic Theory," J. Sci. Comput., **1**(1), pp. 3–51.

[12] Zhang, L., Wu, W. Z., and Wu, Y. L.., 2002, "Prediction of Pressure Fluctuation Through Francis Turbine," Journal of Large Electric Machine and Hydraulic Turbine, **5**, pp. 34–38.

[13] Li, S. C., 1992, "Pressure Fluctuations in Cavitating Draft-Tube Flows," The Writer Annual Meeting of the American Society of Mechanical Engineers, Anaheim, CA, Vol. FED 136, pp. 1–6.

[14] Li, S. C., Zuo, Z. G., Liu, S. H., Wu, Y. L., and Li, S., 2008, "Cavitation Resonance," ASME J. Fluids Eng., **130**, p. 031302.

Aerodynamic Forces on Multiple Unit Trains in Cross Winds

Christopher J. Baker

Mark Sterling
e-mail: m.sterling@bham.ac.uk

School of Civil Engineering,
University of Birmingham,
Edgbaston, Birmingham B15 2TT, UK

This paper describes the results of wind tunnel tests that were carried out to measure the aerodynamic characteristics of an electrical multiple unit (EMU) vehicle in a cross wind. The measurements were made on a 1/30 scale model of the Class 365 EMU in a simulation of the natural wind. The time histories of surface pressures were measured at a large number of points over the vehicle from which the aerodynamic characteristics and force coefficients were determined. This paper describes the complex fluctuating pressure field over the vehicle, through a consideration of the mean and fluctuating pressure coefficients and their spectra, and through a proper orthogonal decomposition analysis, which identifies the major modes of this distribution. The mean, fluctuating, and extreme aerodynamic side and lift forces are also discussed. It is shown that the flow pattern around the vehicle is dominated by large windward roof corner pressure fluctuations.
[DOI: 10.1115/1.3222908]

Keywords: cross winds, train pantographs, train aerodynamics

1 Introduction

In recent years there has been a substantial amount of research carried out to investigate the effects of high winds on trains in different parts of the world—in the U.K. [1,2], France [3], Japan [4], and Germany [5]. These investigations have been driven by the realization that modern, high speed trains are at risk of overturning in high wind conditions, and indeed a number of such accidents have been reported in recent years in Japan, China, Belgium, and Switzerland [6]. While these accidents have occurred for relatively narrow gauge tracks, there is clearly a need to develop methods for the assessment of the safety risk of new trains and track infrastructures. Such methods involve the determination of the aerodynamic forces and moments either through the use of wind tunnel tests [7,8] or through the use of CFD calculations [9], together with a calculation of the development of overturning moments as the train passes through a simulated wind field of some sort. Draft codes of practice outlining such calculations have recently been produced [10,11].

While the overturning issue is undoubtedly of importance, there are other effects of high cross winds on trains, such as the loss of ride quality due to wind enhanced vibrations of the suspension, infringement of the "kinematic envelope" that defines the notional maximum train movement from its normal position, which is used to design clearances through stations, dust dispersion from trains in high winds [12], and the problem of pantograph sway, i.e., excessive displacements between the current collection device (the pantograph) and the overhead wire that supplies the electrical current. The results presented in this paper arise out of a project to investigate this last phenomenon. To determine the overall pantograph sway for any particular vehicle, then some knowledge of the overall aerodynamic forces and moments on the vehicle are required. The vehicle perceived to be particularly at risk to such effects in the U.K. was the Class 365 multiple unit four car commuter train. Wind tunnel tests were therefore carried out to measure these forces through the use of integrated surface pressure measurements, and pantograph sway calculations were carried out [13]. However, the data obtained in the experiments were of a fundamental nature and it was clear that fuller analysis of this data could enable a physical insight to be gained into the nature of the flow field around the train. Such an analysis is presented in this paper.

Before proceeding the limitations of these experiments need to be made clear. They were carried out on a stationary model train in a simulated atmospheric boundary layer. Thus the relative movement of the vehicle to the ground is not modeled. At higher vehicle speed the train will "see" a wind field that is very considerably different to that simulated (because of the vectorial addition of the train speed and the wind speed will change the effective wind angle and lower the effective turbulence intensity). Thus the experimental setup presented here can only be regarded as a rather limited representation of reality. That being said, the modeling of the stationary train situation is realistic and the overall effect of a stationary ground plane on the side force is small (see Refs. [14,15] for further details).

The wind tunnel tests are first described in Sec. 2. Section 3 then describes the pressure coefficient distributions around the train for a range of yaw angles (the angle between the wind direction and the train axis). The unsteady pressure coefficients are also considered through an analysis of the pressure coefficient standard deviations and spectra. Section 4 describes the results of a proper orthogonal decomposition (POD) analysis of the pressure coefficient data and reveals the major fluctuating flow modes throughout the yaw angle range. Section 5 then presents the aerodynamic forces and moments on the vehicle (essentially an integration of the pressure coefficients presented in Sec. 3). The mean, standard deviations, spectra, and extreme values of the force coefficients are presented. Section 6 examines the force coefficient data further and considers in detail the instantaneous peak values and the corresponding pressure distributions, which give rise to these forces. Finally, conclusions are presented in Sec. 7.

2 The Wind Tunnel Measurements

The experiments were carried out using a 1/30 scale model of a Class 365 electrical multiple unit, mounted statically in a simulation of the atmospheric boundary layer in the RWDI Anemos environmental wind tunnel. This has a working section of $15 \times 2.4 \times 1.8$ m^3 and the boundary layer is simulated using standard upstream grid and roughness methods. A photograph of the vehicle in the wind tunnel is shown in Fig. 1 and the grids and roughness elements can be clearly seen. Note that the roughness elements are placed in close proximity to the train model, a fact which will be seen to have some significance in what follows. In order to model

Contributed by the Fluids Engineering Division of ASME for publication in the JOURNAL OF FLUIDS ENGINEERING. Manuscript received February 26, 2009; final manuscript received August 5, 2009; published online September 18, 2009. Edtior: Joseph Katz.

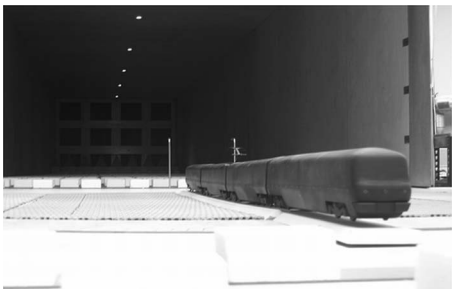

Fig. 1 The Class 365 EMU wind tunnel model

conditions relevant to the U.K., the model was placed on a scaled representation of the track formation and consequently was 17 mm higher than the wind tunnel floor. Figure 2 shows the simulated atmospheric boundary layer measured at the model position at the center of the wind tunnel turntable, together with the "target" profile for a $\frac{1}{30}$ scale boundary layer with a full-scale surface roughness length of 0.03 m, corresponding to a rural environment [16], measured at the model position using standard hot wire anemometry techniques. The velocities $(U(z))$ are normalized with the measured velocity at 3 m equivalent full-scale height $(U(3))$ and the heights above the wind tunnel floor z are normalized with a nominal reference height of 3 m, which is somewhat less than the train height of 4 m. Up to normalized values of height of 2–3 m, the simulation can be seen to be reasonable. Figure 3 shows the corresponding turbulence intensity simulation, together with the target value. The turbulence intensity $I(z)$ is defined as the ratio of the turbulence level $\sigma_U(z)$ to the mean velocity $U(z)$, although for the sake of clarity the results are shown as the ratio of $I(z)$ to $I(3)$. In general the agreement between the simulation and the target

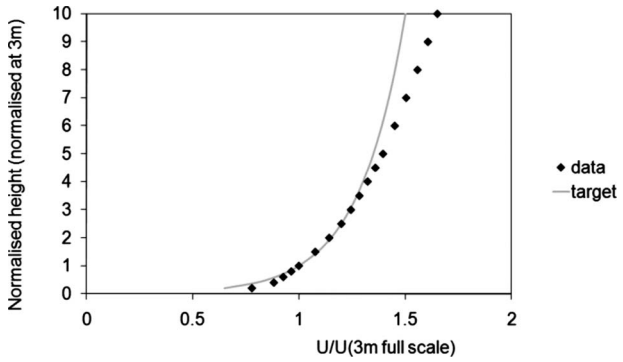

Fig. 2 The simulated velocity profile and target value for a full-scale surface roughness=0.03 m

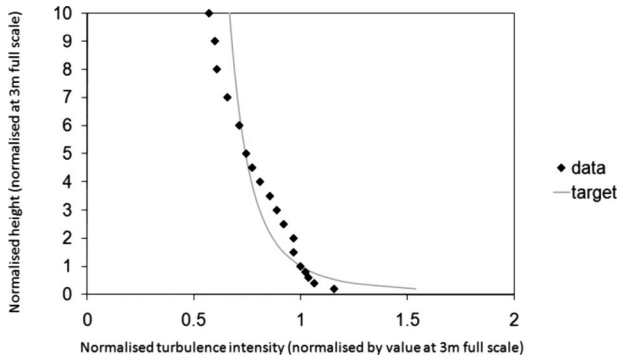

Fig. 3 The simulated turbulence intensity profile and target value for a full-scale surface roughness=0.03 m

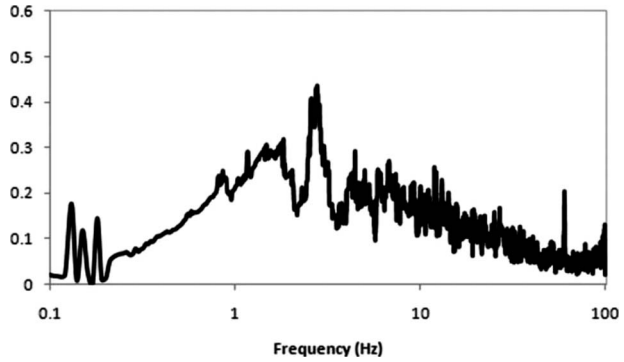

Fig. 4 The simulated velocity spectrum at z=100 mm (3 m full scale) plotted in normalized form (spectral density ×frequency/variance)

can be seen to be reasonable and similar to those obtained in other such atmospheric boundary layer tests. Figure 4 shows a velocity power spectrum, measured at 3 m (full-scale equivalent) above the ground. As with all the spectra presented in this paper, this is plotted in the normalized form of spectral density $S_U \times$ frequency n/variance $\sigma_U{}^2$. It can be seen to be of the expected form with an energy peak in the midfrequency range. The turbulent length scale ${}^xL_U$ was obtained by integrating the autocorrelation function corresponding of streamwise velocity measured at a full-scale equivalent height of 3 m above the ground. The value of this parameter was around 15 m (full-scale equivalent), which is somewhat lower than the likely full-scale value of around 50 m. Such a scale mismatch is not uncommon in atmospheric boundary layer simulations and it is generally accepted that if the length scales are greater than around three times the model height, as in this case, they can be regarded as adequate. The model was placed in the open section of the wind tunnel at a distance of 15 m from the fans, which resulted in blockage ratios varying between 2% and 5% for yaw angles between 15 deg and 90 deg. No blockage correction was applied.

The wind tunnel forces and moments were measured on two vehicles of the train—the leading vehicle and the trailing vehicle with the pantograph. The results presented in this paper will be for the leading vehicle only. However, additional analysis has indicated that the results presented below are generally applicable to the trailing vehicle as well. Measurements were made of the fluctuating surface pressure at approximately 100 pressure tappings (Honeywell, UK, DC005NDC4) on each vehicle, using a 256 channel pressure transducer system sampled every 0.002 s. Previous work that has measured train force coefficients using such a method and compared the results to force balance measurements has indicated that this number of tappings is adequate [17]. The notation that was used to describe the pressure positions is presented in Fig. 5. Essentially the tappings are numbered one to 14 on each loop, with loop B being at the front of the leading car, and loop H being at the rear of the leading car (note that "loop A" was a single pressure tapping at the train nose). Force time histories were then obtained by integration of the pressure field over the surface of the vehicle. This integration effectively assumed that the tributary area of each pressure tapping extended to half the distance to the next pressure tapping in each direction. The resulting forces on the train surface were then resolved into the horizontal and vertical directions to obtain the side force S (normal to the train axis, and positive in the downwind direction) and the lift force L (normal to the train axis and positive in the vertical direction). Values of the rolling moment about various axes were also found, but are not presented here as such values are essentially weighted values of the more fundamental side and lift forces.

In what follows the pressures and forces will be presented in standard coefficient form. The pressure coefficients are defined as

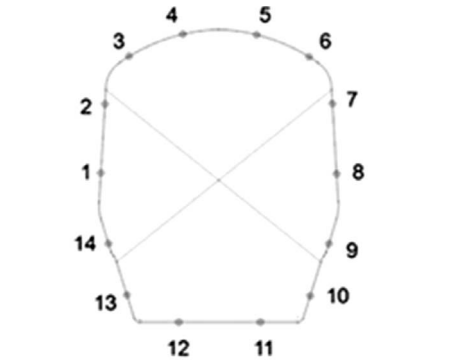

(a) Pressure tap identification

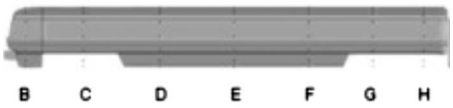

(b) tapping loop distribution

Fig. 5 Pressure tapping notation: (*a*) pressure tap identification and (*b*) tapping loop distribution

$$C_p = (p - p_r)/0.5\rho U(3)^2 \quad (1)$$

where p is the surface pressure, p_r is the reference pressure measured at train height using an upstream reference probe and calibrated against the pressure at the center of the turn table, and ρ is the density of air (taken as 1.2 kg/m^3). The side and lift force coefficients are defined as

$$C_s = S/0.5\rho A U(3)^2 \quad (2)$$

$$C_L = L/0.5\rho A U(3)^2 \quad (3)$$

where A is the reference side area (=70 m^2). The results will be presented for a variety of yaw angles ψ (the angle between the train axis and the wind tunnel velocity, which was set simply by rotating the vehicle relative to the flow direction). The pressure coefficient values are repeatable to within $\pm 5\%$ and the force coefficient values to within $\pm 5\%$. All experiments were carried out at a reference velocity $U(3)$ of 6.88 m/s, giving a Reynolds number based on train height of 5.9×10^4. The power spectra of the above quantities will also be presented. As with the wind spectrum, these will all be plotted in a normalized form $S_p n/\sigma_p{}^2$, $S_{CS} n/\sigma_{CS}{}^2$, and $S_{CL} n/\sigma_{CL}{}^2$.

A small number of flow visualization tests were carried out using standard smoke flow techniques. These tests had to be carried out at very low wind tunnel velocities to enable the smoke to be seen, and the high levels of turbulence within the flow made the observations difficult. In effect all that these tests demonstrated were large scale separations in the lee of the vehicle, which are of course only to be expected. These results will thus not be discussed further.

3 Pressure Distributions

Figure 6 shows an illustrative plot of the mean pressure distribution on tapping loop E at a yaw angle of 90 deg (i.e., the wind perpendicular to the train). This distribution is typical of much of the data and shows a positive pressure on the front face, a large suction over the windward roof corner and smaller suctions over the rest of the roof and on the leeside. This is of course similar to the pressure distribution observed over low rise buildings.

Figure 7 shows the variation in the mean pressure coefficient distribution on all the tapping loops around the leading car for the complete yaw angle range. Each figure shows the contours of surface pressure distribution for a particular yaw angle. It can be seen that in general the pressure coefficients are similar to those shown in Fig. 6 for all but the lowest yaw angle. They are positive and reasonably uniform over the windward face of the vehicle (windward wall), with a large suction on the roof of the vehicle (roof) and a smaller suction on the leeward (leeward wall) and underside of the vehicle. The suction tends to increase toward the front of the vehicle and as the yaw angle increases. The large pressure gradients between the windward wall and the roof are suggestive of a flow separation over the windward roof corner of the vehicle. At the lower yaw angle of 15 deg the pressure coefficient, unsurprisingly, shows little variation along and around the vehicle.

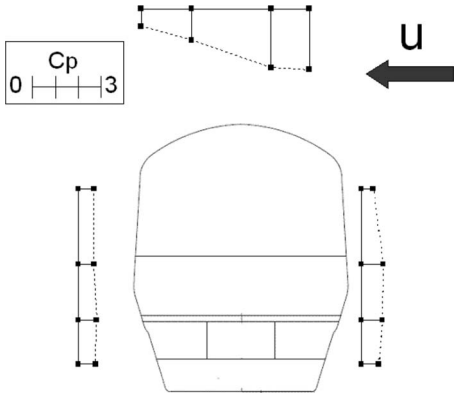

Fig. 6 Pressure coefficient distribution at 90 deg yaw on loop E (solid line represents datum, dotted line represents the pressure coefficient, and negative values are between the datum and the train sketch)

Figure 8 shows the variation in the standard deviation of the pressure coefficient, presented in a similar format. Large values of this parameter indicate significant fluctuations in the pressure time history and thus significant unsteadiness in the flow around the vehicle. Small values indicate a relatively steady flow area. It can be seen that, in general, the standard deviations are highest at the windward leading edge of the roof (tappings 3 and 4), indicating major unsteadiness in the roof windward corner separation. There can be seen to be a small increase in this parameter as the yaw angle increases, and the values closest to the front of the train are a little higher than those to the rear. It can thus be concluded from these plots that the dominant flow mechanism is some sort of unsteady separation close to the windward edge of the roof, which becomes of increasing significance as the yaw angle increases.

Figure 9 shows the power spectra of the pressure coefficients for yaw angles of 45 deg and 90 deg. Tap 1 (on the windward wall) shows a peak at around 4 Hz, similar to that shown in Fig. 4 for the oncoming wind velocity. Tap 3, near the windward corner, however, shows a large peak at a lower frequency of approximately 2 Hz, although there is some indication of a further peak around 4 Hz. These peaks also exist on tap 5, which is situated further over the roof. These results suggest that the fluctuations on the windward wall follow the upstream velocity fluctuations, while there are some further mechanisms of unsteadiness present over the windward corner and roof. It can be conjectured that the 2 Hz peaks in these regions are caused by the "flapping" of a separated shear layer over the vehicle roof.

Figure 10 illustrates the probability distributions for the pressure data relating to the time series analyzed in Fig. 9. The vertical axis in Fig. 10 represents the standard deviation of the relevant distribution $\sigma_p(i)$ multiplied by the associated probability $p(i)$. Also shown in Fig. 10 is the probability distribution relating to a normal distribution with a corresponding similar variance. Corresponding data relating to the standard deviation, skewness, and kurtosis are given in Table 1. Figure 10(*a*) illustrates that the

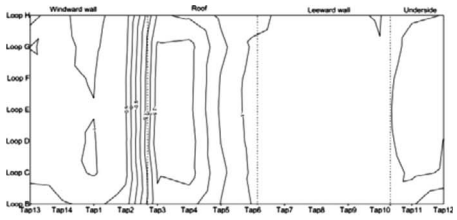

(a) 90 yaw

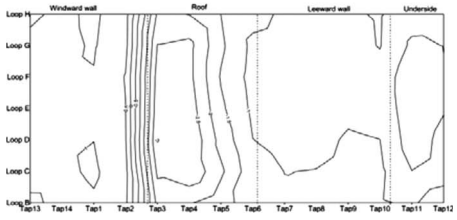

(b) 75 yaw

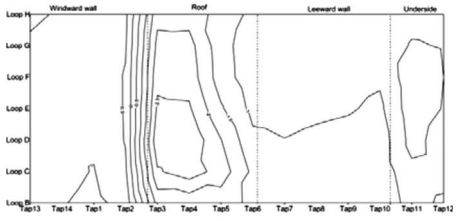

(c) 60 yaw

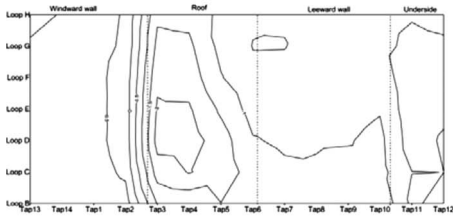

(d) 45 yaw

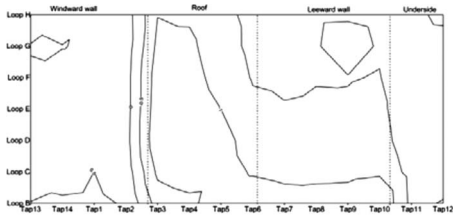

(e) 30 yaw

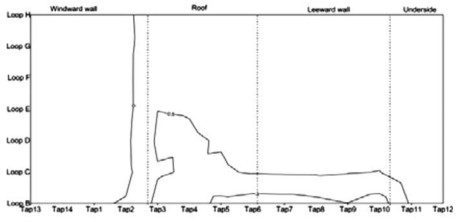

(f) 15 yaw

Fig. 7 Mean pressure coefficients on the leading car

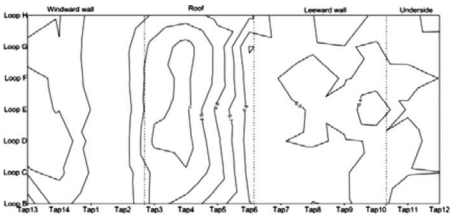

(a) 90 yaw

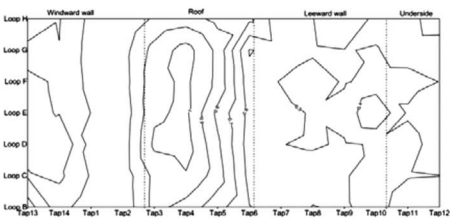

(b) 75 yaw

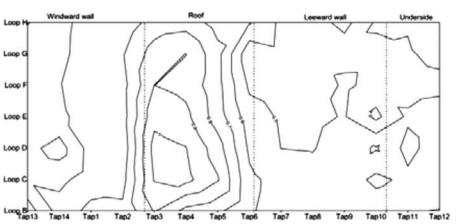

(c) 60 yaw

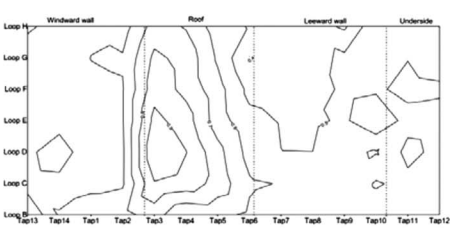

(d) 45 yaw

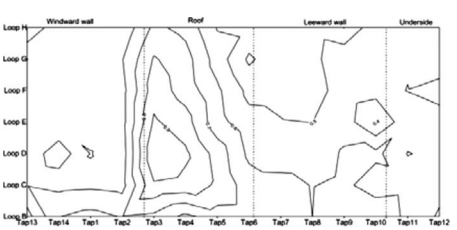

(e) 30 yaw

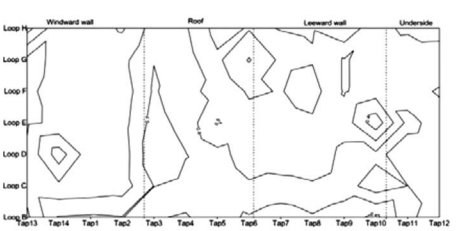

(f) 15 yaw

Fig. 8 Standard deviation of the pressure coefficients on the leading car

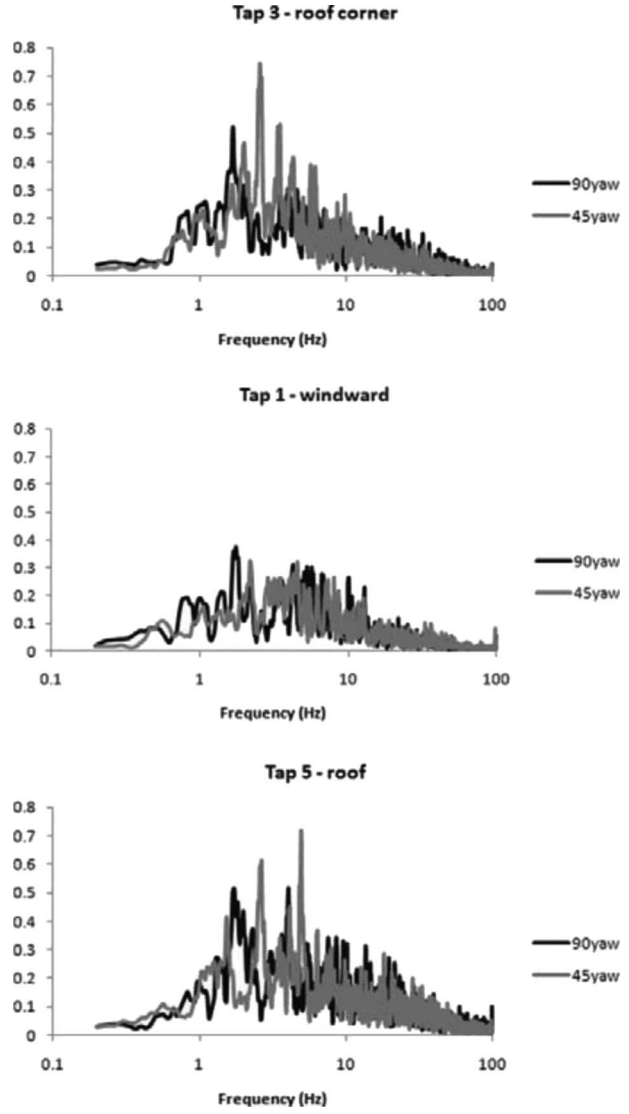

Fig. 9 Pressure coefficient spectra on the leading car (loop E) plotted in normalized form (spectral density ×frequency/variance)

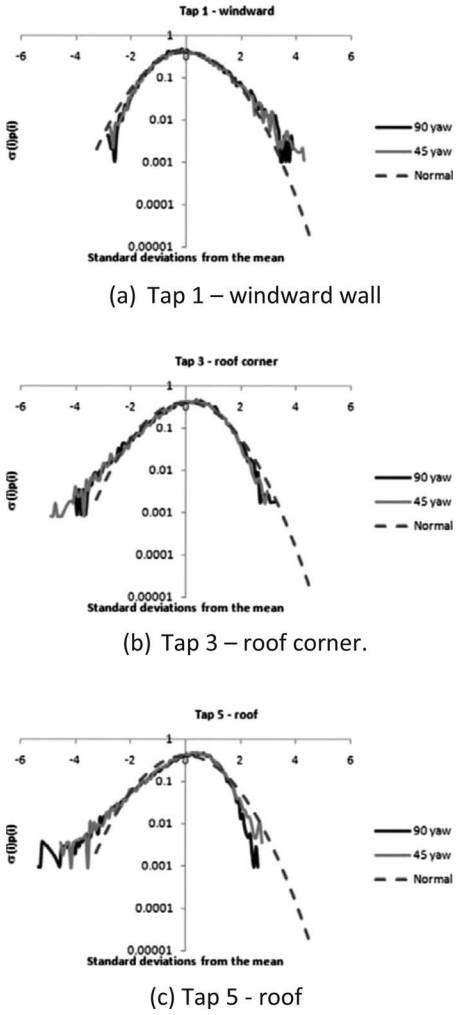

Fig. 10 Probability distributions for the pressure time series data shown in Fig. 9: (*a*) tap 1-windward wall, (*b*) tap 3-roof corner, and (*c*) tap 5-roof

probability distributions on the windward wall have a slight positive skewness and to a large extent can be approximated by a normal distribution. This again suggests that pressure fluctuations in this region follow the upstream velocity fluctuations. At the extreme tails of the distribution this approximation is somewhat questionable and may have implications in terms of the extreme side force experienced by the train. This point will be examined in Sec. 6. Figures 10(*b*) and 10(*c*) indicate negative values of skewness. The standard deviation (Table 1) is largest for tap 3, as would be expected from the data illustrated in Fig. 8. Again, a normal distribution appears to be able to approximate the probability distributions reasonably well over a range equivalent to at least three standard deviations from the mean, although the negative skewness indicates the higher probability of high suction peaks for these tappings, which is again consistent with the pressure standard deviations and spectral analysis described above.

4 POD Analysis

In this section the results of a POD analysis of the pressure coefficient data set out in Sec. 3 are presented. Details of this analysis are not presented here since it is simply set out for a similar situation (the flow around a low rise building) in Refs. [18,19] to which the reader is referred for full details. Essentially the POD analysis makes the assumption that the time history of the fluctuating surface pressure field can be split into a number of independent (and orthogonal) modes, each with a different spatial distribution across the surface of the vehicle and with different time variations. These modes are obtained from the covariance of the cross-correlation matrix of all the fluctuating pressures at all the measurement points, with the eigenvectors of the matrix representing the spatial distribution of each mode, and the square of the eigenvalues representing the energy within each mode. From this information the time histories of each mode can be reconstructed.

Now previous work using this technique on low rise buildings has indicated that usually only a small number of modes are responsible for most of the fluctuating energy, and that physical causes can plausibly be assigned to these major energetic modes. The latter point needs to be approached with a degree of circumspection; however, since to some degree the mode shapes will be fixed by the condition of orthogonality that is applied.

Table 2 shows the cumulative energy distribution of the top 10 modes for the complete yaw angle range. It can be seen that depending on yaw angle, the first mode contributes between 43% and 64% of the total fluctuating energy, the second between 10% and 18%, and the top 10 modes account for between 84% and 92% of the total. Figure 11 shows the eigenvector distribution for the mode 1. Similar to the results illustrated in Fig. 8, the most

Table 1 Standard deviation, skewness, and kurtosis values relating to pressure coefficient data shown in Fig. 10

	90 deg yaw			45 deg yaw		
	Tap 1	Tap 3	Tap 5	Tap 1	Tap 3	Tap 5
σ_p	0.709	0.982	0.774	0.570	0.932	0.648
Skewness	0.433	−0.456	−0.934	0.370	−0.575	−0.759
Kurtosis	0.354	0.513	1.740	0.294	1.102	1.537

energetic distributions are for yaw angles of 30 deg, 45 deg, 60 deg, 75 deg, and 90 deg. It can be seen that the eigenvectors are maximum around the windward edge of the roof, and can plausibly be assigned to the windward corner separation described in Sec. 3. It would appear that for loop D, about a third of the way from the front of the leading vehicle, these fluctuations extend on to the windward face of the vehicle. Figure 12 shows a similar plot for mode 2. It can be seen that this is positive on the windward wall, significantly negative over the roof of the vehicle, and negative to a lesser extent elsewhere. This pattern mirrors that of the mean pressure distribution in Fig. 7, and suggests that this mode physically represents fluctuations caused by quasisteady effects. If this identification of modes is valid, then the fact that the roof separation mode is more energetic than the primary quasisteady mode is of interest, since the reverse is usually true for low rise buildings (see Refs. [18,19]). Figure 13 shows the eigenvectors for mode 3. Here the interpretation is more difficult, and it may be that the patterns do not represent a particular physical flow mechanism, or that they represent different flow mechanisms at different yaw angles. For yaw angles of 30 deg, 45 deg, 75 deg, and 90 deg the patterns are similar, although of different intensities, with an asymmetric mode shape. For 60 deg the mode shape is similar, but the high and low values of eigenvectors have been reversed.

Figure 14 shows the spectra from the time histories of modes 1 to 3 for two yaw angles (45 deg and 90 deg). It can be seen that the spectrum for mode 1 appear to peak at approximately 2–5 Hz, whereas the peak for modes 2 and 3 occurs at approximately 2–3 Hz. There also appears to be a more pronounced high frequency cutoff for mode 1, i.e., at approximately 10 Hz. It is not altogether straightforward to explain these spectra in terms of the physical causes for the modes outlined above, although the higher frequency peak for mode 1 may be as a result of a windward corner flow separation. A comparison with the velocity spectrum in Fig. 4 also suggests that mode 2 could reflect the oncoming wind, and thus represents quasisteady pressure fluctuations over the vehicle. Once again the mode 3 spectrum is not easily interpretable, and seems to resemble some sort of combination of the mode 1 and 2 spectra.

5 Force Coefficients

Figure 15 shows that the variation in the time average force coefficients with respect to yaw angle. The side force coefficient magnitudes are similar to those obtained in wind tunnel tests on other trains (see Ref. [19] for example), but the lift force coefficients are significantly higher than previously observed. It is conjectured that this is because the undertrain gap on the Class 365 is significantly smaller than for most of the vehicles previously studied, and thus much of the flow will go over the train, with a greater reduction in roof pressure and thus a greater lift. However, it is known that lift coefficients show a great sensitivity to a number of effects, and it may be that these high coefficients are a result of, for example, the simulated wind tunnel floor roughness in the near vicinity of the vehicle. Figure 16 shows the standard deviations for the side σ_{CS} and lift force coefficients σ_{CL}. These fluctuations are more or less constant over the yaw angle range, despite the increase in the mean coefficients. This implies that the ratio of the standard deviations to the mean values will increase significantly as the yaw angle decreases. Figure 17 shows the corresponding spectra for yaw angles of 45 deg and 90 deg. It is clear that these spectra do not show the peaks that are apparent in the individual pressure tapping and POD mode spectra, indicating that these local peaks are effectively filtered out in the integration of surface pressures to obtain the side and lift forces. The falloff in these spectra at higher frequencies is also apparent, which is due to the lack of correlation of small scale pressure fluctuations over the vehicle. This point is also discussed at length in Ref. [20], where an in depth analysis on the measured aerodynamic admittances is reported.

6 Analysis of Peak Loading Events

6.1 Force Coefficients. Figure 18 illustrates the variation in the instantaneous side force coefficient for three different yaw angles. Discrete, peak events are noticeable in Fig. 18 for all of the yaw angles shown. Brief details relating to such variations can also be inferred from Table 3. In Table 3, CoV represents the coefficient of variation, which for the current purposes is defined

Table 2 Cumulative energy by POD mode expressed in terms of the variance

Mode	15 deg yaw	30 deg yaw	45 deg yaw	60 deg yaw	75 deg yaw	90 deg yaw
1	63.5	49.5	49.0	43.0	43.3	42.6
2	73.3	68.2	64.5	60.5	58.0	59.2
3	79.1	74.1	71.4	68.4	66.7	68.0
4	83.4	79.0	76.4	73.0	71.4	71.8
5	85.3	81.4	78.8	76.0	74.8	74.9
6	87.0	83.4	80.7	78.1	77.1	77.0
7	88.5	84.7	82.1	79.9	79.2	79.0
8	89.9	86.0	83.4	81.5	80.7	80.7
9	91.2	87.1	84.6	82.8	82.2	82.2
10	92.0	88.1	85.5	83.9	83.5	83.5

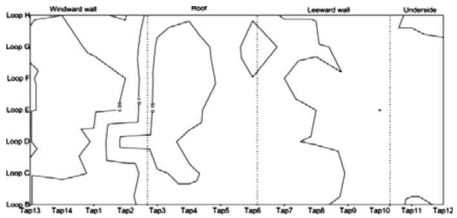

(a) 90 yaw

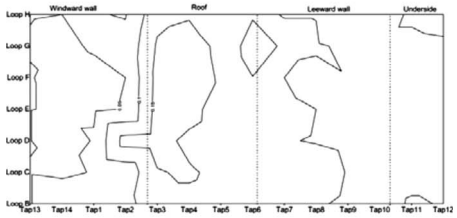

(b) 75 yaw

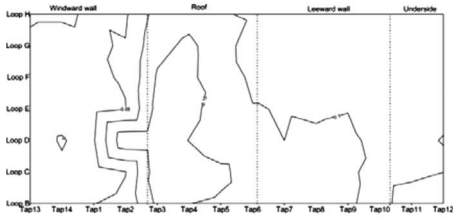

(c) 60 yaw

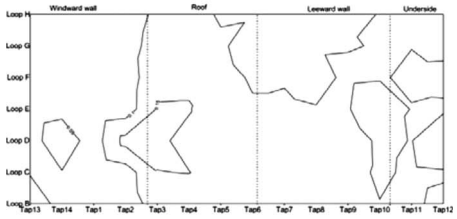

(d) 45 yaw

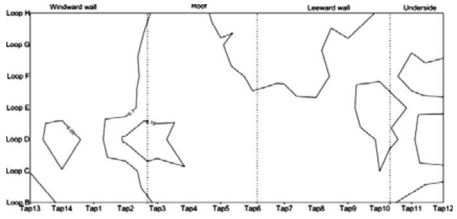

(e) 30 yaw

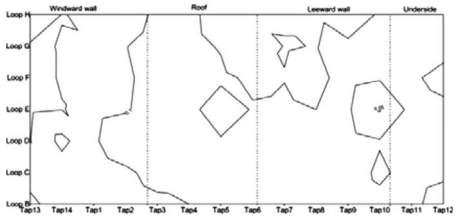

(f) 15 yaw

Fig. 11 Pressure coefficient POD mode 1 on the leading car

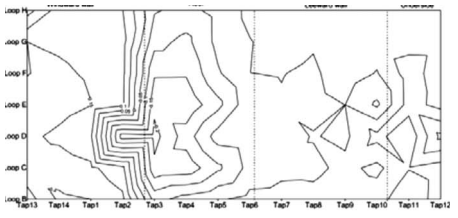

(a) 90 yaw

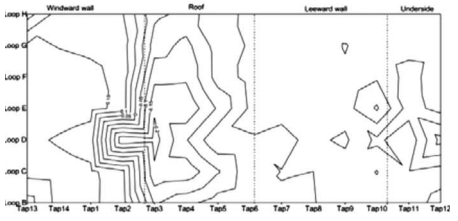

(b) 75 yaw

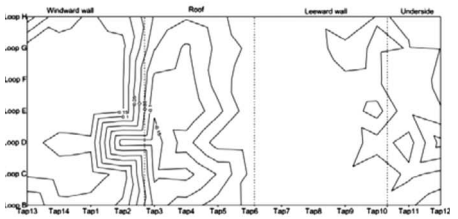

(c) 60 yaw

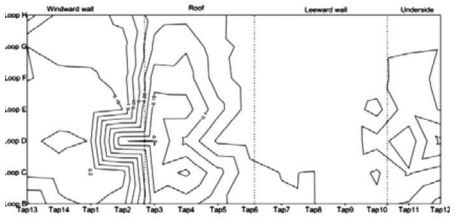

(d) 45 yaw

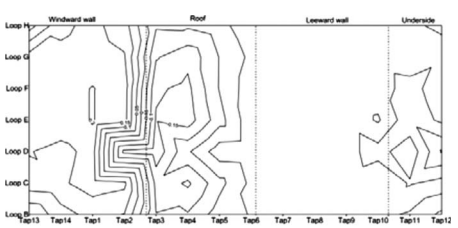

(e) 30 yaw

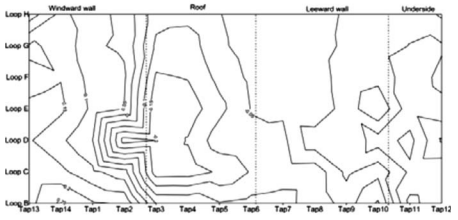

(f) 15 yaw

Fig. 12 Pressure coefficient POD mode 2 on the leading car

as the standard deviation divided by the mean. In all cases it can be observed that the CoV decreases as the yaw angle increases, which is in keeping with the results of Figs. 15 and 16. The data illustrates positive values of skewness irrespective of yaw angles, which suggests that more positive peak values of this coefficient would be expected to occur, compared with a normally distributed parameter. It is interesting to note that for each yaw angle, the value of skewness corresponding to the side force coefficient is

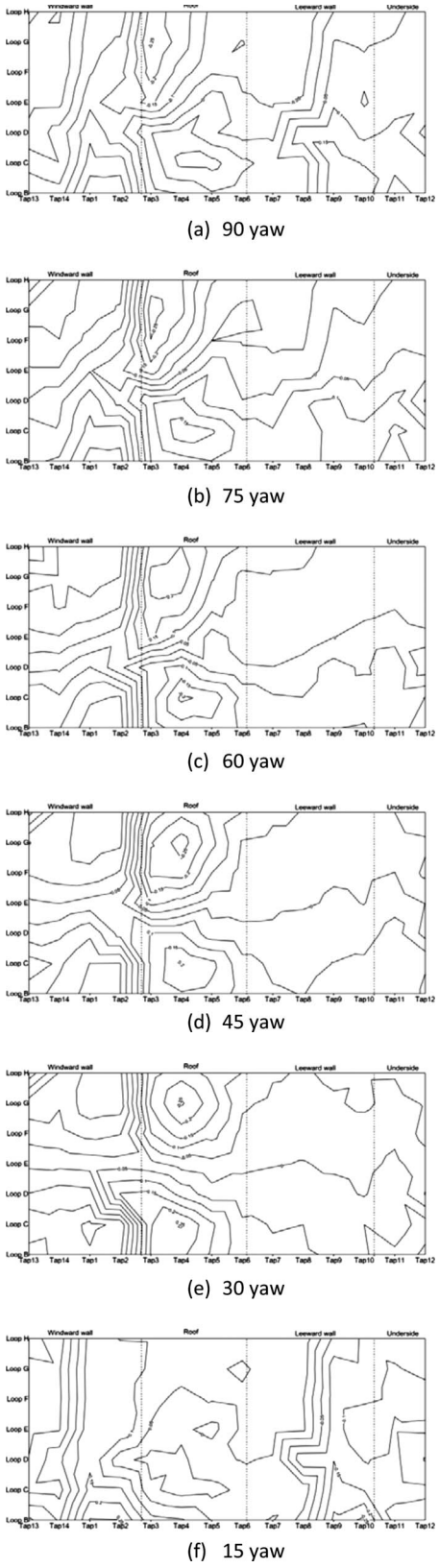

Fig. 13 Pressure coefficient POD mode 3 on the leading car

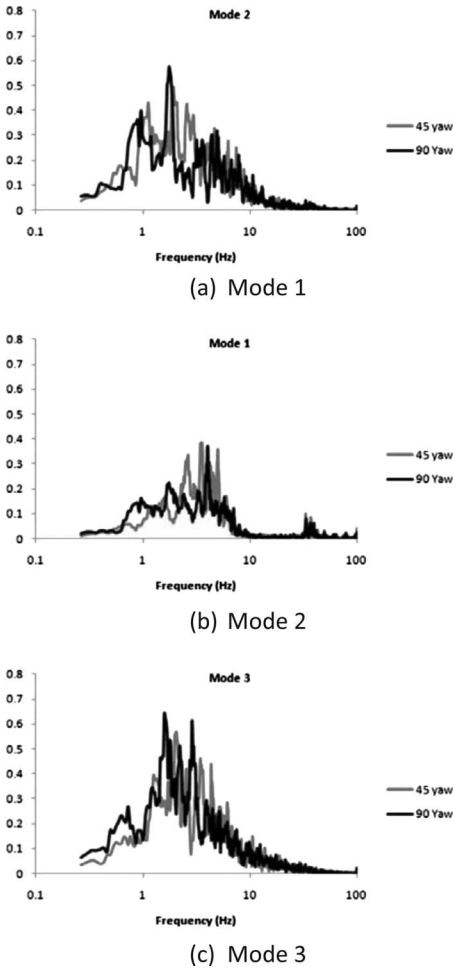

Fig. 14 Pressure coefficient mode spectra plotted in normalized form (spectral density×frequency/variance): (*a*) mode 1, (*b*) mode 2, and (*c*) mode 3

larger than the corresponding values for the other parameters. This trend can also be observed in the values of kurtosis, with peak values of this parameter occurring for a yaw angle of 30 deg. Values of kurtosis are significantly greater that zero, indicating that the data is more peaked than a normal distribution, i.e., leptokurtic.

Figure 19 indicates the cross-correlation coefficients between the side and lift force coefficients with respect to the yaw angle. In general, it can be observed that the correlation coefficient increases as the yaw angle increases, with maximum values occurring between yaw angles of 60 deg and 90 deg. These relatively low values suggest that the fluctuations in the side and lift force coefficients are not due to one single physical flow mechanism that affects both parameters, but that a number of independent flow mechanisms exist. These are likely to be the windward roof

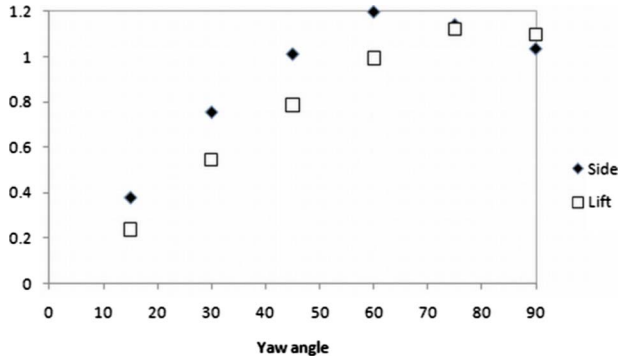

Fig. 15 Mean force coefficients for the leading car

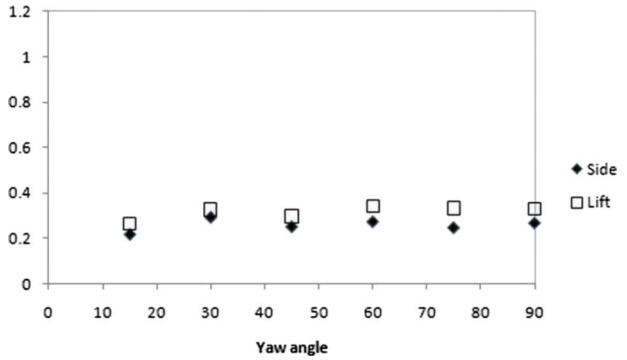

Fig. 16 Standard deviations of the force coefficients for the leading car

corner separation that will mainly affect the lift force and the upstream buffeting that will mainly affect the side force. Figure 20 illustrates a plot of the instantaneous values of the lift coefficient (vertical axis) together with the corresponding value of the instantaneous side force coefficient (horizontal axis). The degree of scatter shown is obvious and suggests that the flow is only correlated in an average sense. It is clear that the peaks in the side force do not occur at the same time as the peaks in the lift force and vice versa. The large degree in scatter can perhaps be attributed to the non-Gaussian behavior of the side and lift force coefficients (Fig. 21). In Fig. 21, the data have been plotted in a semilogarithmic form to enable the differences at the extremes of distributions to be observed easier. In this figure, the normal line indicates a Gaussian (or normal) distribution. It is acknowledged that each different yaw angle has a different value of standard deviation and as such there should be a family of curves illustrating different normal distributions. However, the differences in standard deviation are sufficiently small as to not be noticeable in Fig. 21; hence, only one line is shown. The trends in Fig. 21 support the findings outlined in Table 3 and indicate that the side force coefficient exhibit non-Gaussian behavior irrespective of the yaw angle. Figure 21 highlights that the major differences occur on the right hand side tail of the distribution. This has important implications and suggests that peak values will occur more frequently and may be larger in magnitude than suggested by a normal distribution. This is perhaps not too surprising since localized peak wind velocities can be attributed to coherent structures present in the wind [21] and it is these structures that will in part yield large values of the side force coefficient. Furthermore, organized features such as flow separation and delta wing type vortices [22] can occur over bluff bodies and will play a large role in determining the localized and overall lift forces. In order to examine the behavior of the peak force coefficients, two identical filters were applied to the data, as illustrated in Fig. 20. The first filter was applied to the side force coefficient data and identified instances where this coefficient was greater than or equal to the 99.67th percentile, which represents an equivalent full-scale time of 3 s. The corresponding values of the side and lift force coefficients were extracted and are illustrated in Fig. 22. The second filter was the same as the first but applied in the reverse order, i.e., maximum values of the lift force coefficient were noted and the corresponding values of the side force coefficient were extracted (Fig. 23).

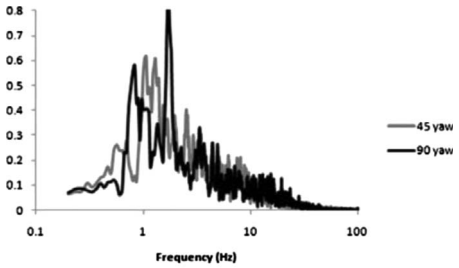

(a) Side force coefficient

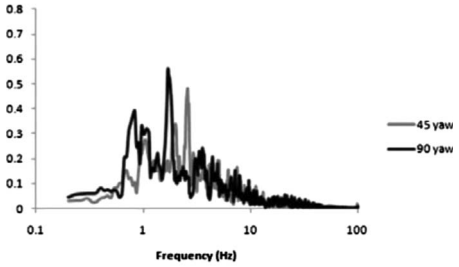

(b) Lift force coefficient

Fig. 17 Force coefficient spectra for the leading car plotted in normalized form (spectral density×frequency/variance): (*a*) side and (*b*) lift force coefficients

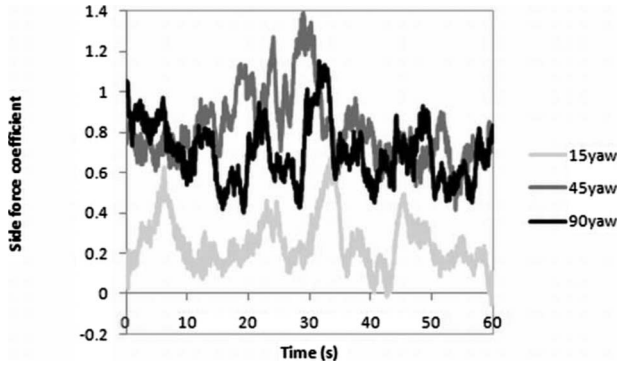

Fig. 18 An illustration of the variation in the side force coefficient on car A with respect to yaw angle (NB the time has been expressed in terms of full-scale equivalent time)

These figures illustrate that there is a considerable degree of scatter between the peak lift and side force coefficient values, i.e., relatively large values of the side force coefficient can occur when the lift force coefficient is large or small (e.g., Fig. 23(*e*)). Peak values of the cross-correlation coefficient for the extreme events occur at around 45 deg yaw and in general rapidly decrease either side of this yaw angle (see Table 4). The values in Table 4 have been obtained by calculating the correlation coefficient of the side and lift force coefficients corresponding to the data obtained by applying the above mentioned filter on the side force data. The scatter associated in the peak values suggests that different flow mechanisms are responsible for the peak forces that arise on the train, i.e., the peak values cannot be attributed to one single flow mechanism. This point will be explored further in Sec. 6.2 when the pressure distributions are examined in detail.

6.2 Pressure Distributions Associated With Extreme Events. Employing the filter outlined above resulted in 50 instances for each yaw angle, where the instantaneous side force coefficient was greater than or equal to the 99.67th percentile value. The ensemble average pressure distributions for these peak events are shown in Fig. 24. As the yaw angle decreases it can be observed that the center of pressure for the side force moves toward the front of the vehicle. In addition, with the exception of the data corresponding to a 15 deg yaw angle there is also a region of high suction over the roof of the vehicle. It is also noticeable that the magnitude of the pressure exerted on the windward face and roof of the vehicle for a yaw angle of 15 deg is significantly less than all other yaw angles. This is consistent with the results presented in Fig. 23(*f*). A large region of negative pressure extends over the leading edge of the roof when the flow is perpendicular to the vehicle (Fig. 24(*a*)). This suggests that on average there is a

Table 3 Force coefficient data (CoV=standard deviation/mean)

	Side coefficient			Lift coefficient		
Yaw	CoV	Skewness	Kurtosis	CoV	Skewness	Kurtosis
15	0.581	0.745	0.963	1.113	0.204	0.206
30	0.391	1.134	2.605	0.600	0.561	1.173
45	0.250	0.957	1.559	0.378	0.443	0.653
60	0.230	0.962	1.396	0.345	0.686	0.998
75	0.218	0.505	0.379	0.298	0.261	0.225
90	0.260	0.861	0.842	0.300	0.564	0.629

large degree of flow separation at this particular yaw angle. As the yaw angle increases, the length of this separation zone decreases but there are instances where the localized pressure is more negative. This possibly suggests a switch in the flow structure from a separated structure to a delta wing type vortex.

Figure 25 indicates the ensemble average pressure distributions corresponding to the peak lift force events. The results are somewhat similar to the corresponding ensemble average side force events shown in Fig. 24, i.e., as the yaw angle decreases from 90 deg to 30 deg the high suction region over the leading edge of the roof moves toward the front of the vehicle with the largest magnitudes occurring for a yaw angle of 60 deg. Furthermore, the center of positive pressure on the windward face of the vehicle moves toward the front and peaks at a yaw angle of 30 deg.

In Secs. 3–5, reference has been made to the variability of the peak data. In order to explore this further the time at which the maximum and minimum values of lift force coefficient corresponding to the peak values of side force coefficient were noted and the instantaneous pressure distributions corresponding to these times are illustrated in Figs. 26 and 27. The results in Fig. 26 follow similar trends to those indicated in Fig. 24, i.e., there is an increase in the side force as the yaw angle decreases from 90 deg to 30 deg. Large suctions are apparent for the 45 deg yaw and 60 deg yaw cases, which are not evident in the ensemble average (Figs. 24(*c*) and 24(*d*)). This supports the earlier findings that the separation zone over the roof of the vehicle is highly unsteady and that possible different flow mechanisms are occurring. In general, the higher lift force coefficients arise as a result of larger and more intensive negative pressures occurring over the roof of the vehicle. It is noticeable from both Figs. 26 and 27 (and from the smoke flow visualization experiments which are not reported here) that

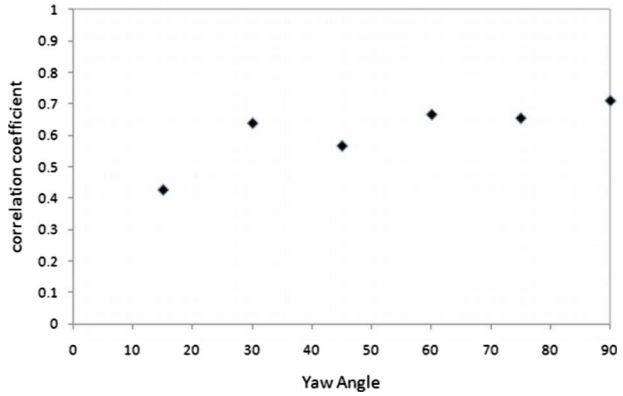

Fig. 19 Overall cross-correlation force coefficient with respect to the yaw angle ($c_s \times c_l$).

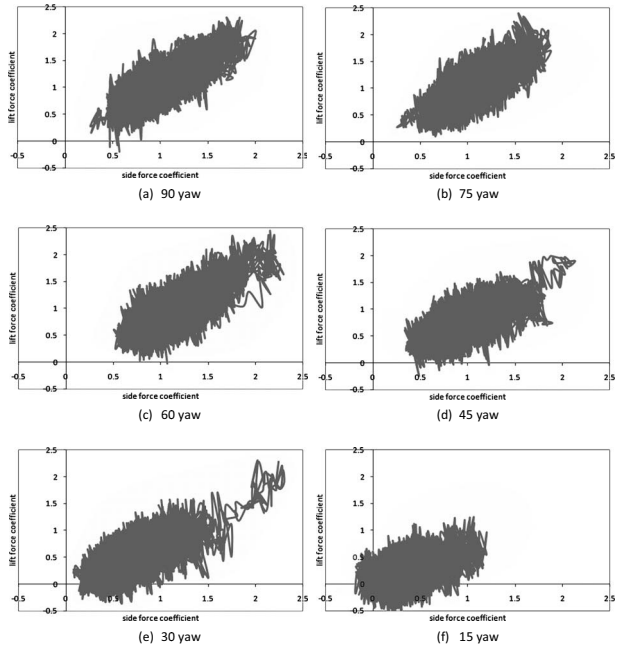

Fig. 20 Instantaneous plots of the lift force coefficient versus the side force coefficient for a range of yaw angles.

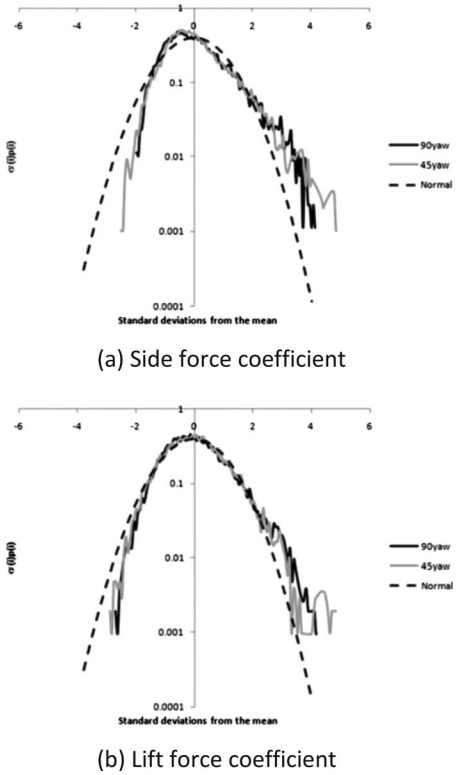

Fig. 21 Probability distributions relating to the force coefficient time series: (*a*) side and (*b*) lift force coefficients

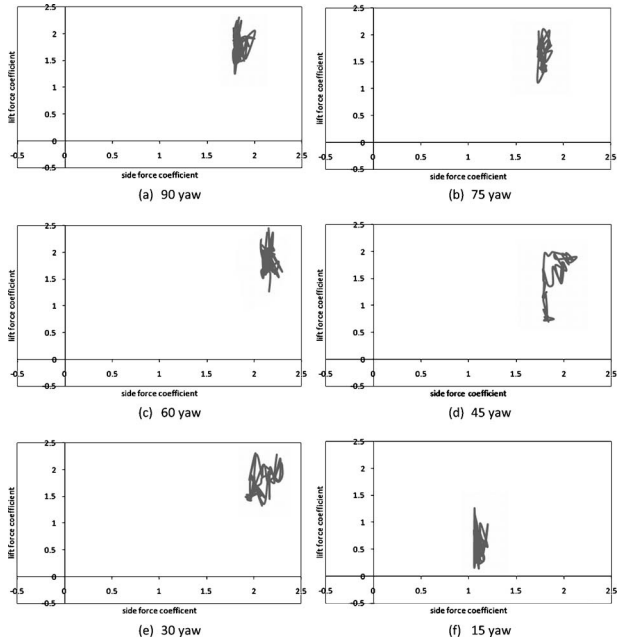

Fig. 22 99.67th percentile filter applied to the side force coefficient data

there is very little underbody flow. This ensures that the mean and maximum values of the lift force coefficient are higher than those reported elsewhere for different trains (e.g., see Ref. [7]). Figure 27 illustrates that when the side force coefficient attains peaks values but the corresponding lift force coefficient is small the region of negative pressure on the roof of the train is reduced in size and magnitude. Finally, Figs. 26 and 27 indicate that the maximum values of the side force arise mainly as a result of the stagnation zone occurring on the windward face of the train, i.e., there is little negative pressure close to the leeward wall.

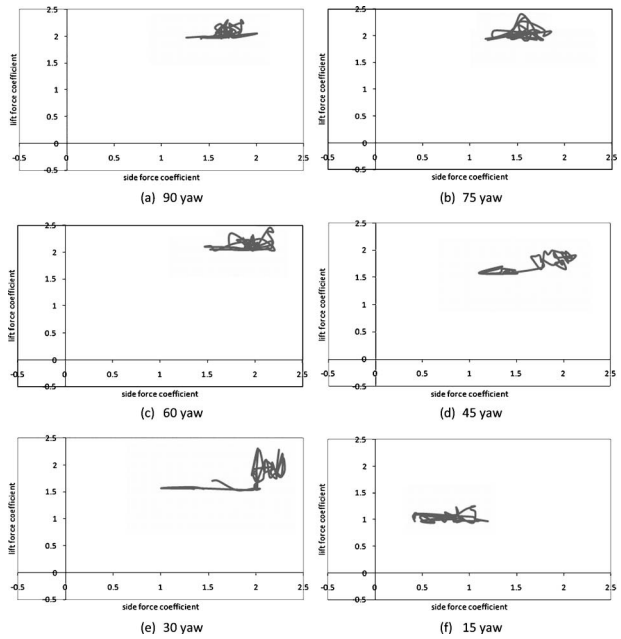

Fig. 23 99.67th percentile filter applied to the lift force coefficient data

Table 4 Cross-correlation values between force coefficients for the peak events

Yaw	Trigger applied to side force coefficient	Trigger applied to lift force coefficient
15	−0.137	0.100
30	0.448	0.575
45	0.632	0.748
60	−0.109	0.212
75	0.140	−0.007
90	0.124	0.440

7 Conclusions

From the work described in Secs. 2–6, the following conclusions can be drawn:

- The use of distributed pressure tappings over a vehicle model provides a great deal of information on the nature of the flow field, and can be successfully integrated to obtain force and moment coefficients.
- The mean pressure coefficients over the vehicle are similar to those that would be found around a typical low rise building.
- The dominant fluctuating flow mechanism is the unsteadiness in the flow around the roof windward corner, associated with some types of separated flow. The energy in this fluctuation is at a lower frequency than the energy in the oncoming wind.
- A POD analysis reveals that the dominant mode reflects the windward roof corner separation, while the second model reflects the unsteadiness in the oncoming flow.
- The coefficient of variation (standard deviation/mean) for both the side and lift force coefficients increases as the yaw angle decreases. This can possibly be attributed to the formation of delta wing vortices occurring over the roof of the vehicle, resulting in stronger but more intermittent flow structures. This view is supported by the analysis of the pressure data shown in Figs. 24–26.
- The skewness and kurtosis values (Table 3), in conjunction with the probability distributions of Fig. 21, indicate non-Gaussian behavior in both the lift and side force coefficients. In particular there is evidence to suggest that the positive peak values of these parameters will occur more frequently when compared with a normally distributed parameter.
- The overall value of the lift force coefficient is greater than what might have been reasonably expected when compared with similar measurements on different trains [7]. This has been attributed to the fact that there appears to be very little underbody flow during the peak events (Figs. 24–26).
- The overall correlation coefficient for the instantaneous values of the side and lift force coefficients has been shown to vary with respect to the yaw angles. It has been observed that there is a significant degree of scatter of this parameter and that during peak events relatively low values of the lift force coefficient can occur when the side force coefficient is high and vice versa. This has implications for the rolling moment about the leeward rail, which is an important measure of train stability and a combination of both the lift and side forces.

Nomenclature

A = full-scale equivalent reference area (m^2)
C_L = lift force coefficient
C_p = pressure coefficient
C_S = side force coefficient

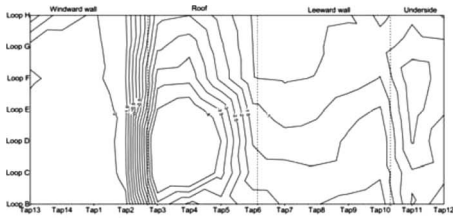

(a) 90 yaw

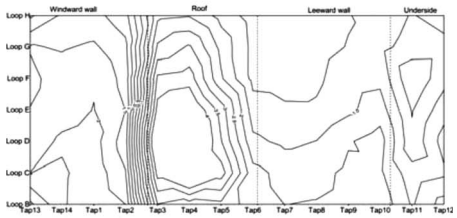

(b) 75 yaw

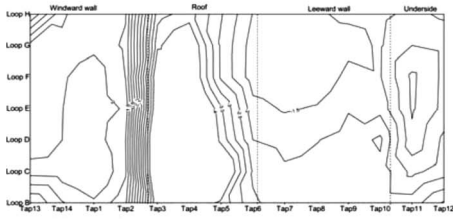

(c) 60 yaw

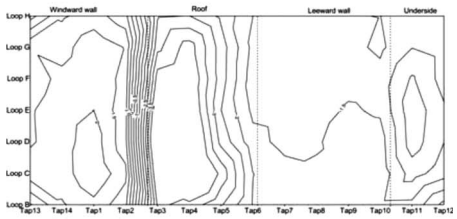

(d) 45 yaw

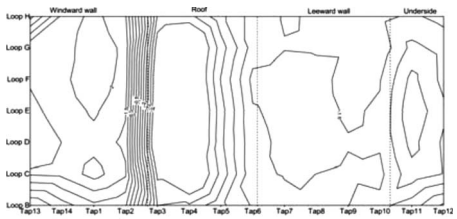

(e) 30 yaw

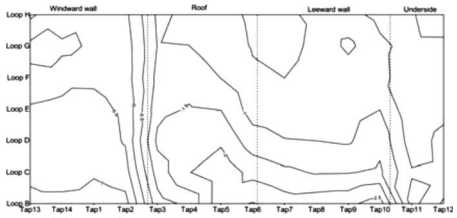

(f) 15 yaw

Fig. 24 Ensemble average pressure distribution corresponding to a side force peak event

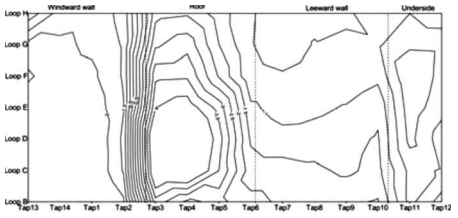

(a) 90 yaw

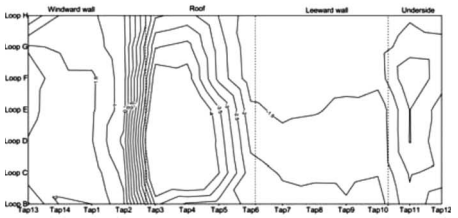

(b) 75 yaw

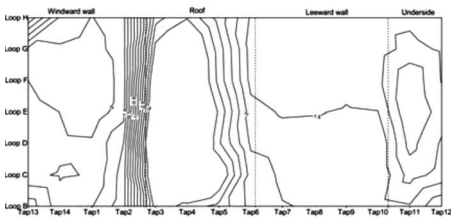

(c) 60 yaw

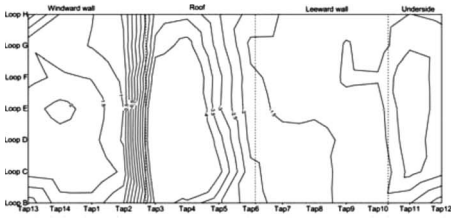

(d) 45 yaw

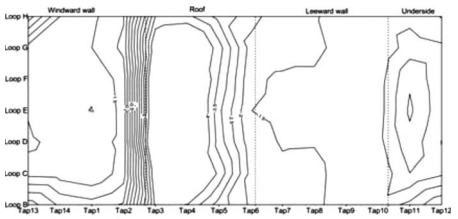

(e) 30 yaw

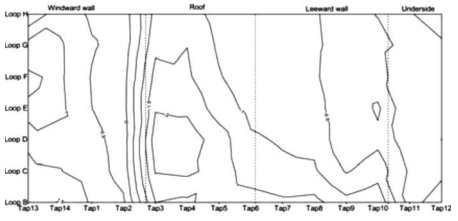

(f) 15 yaw

Fig. 25 Ensemble average pressure distribution corresponding to a lift force peak event

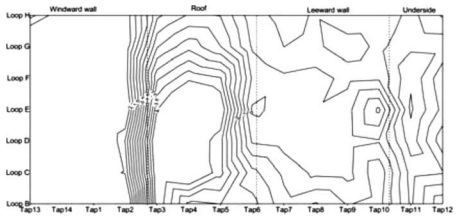

(a) 90 yaw

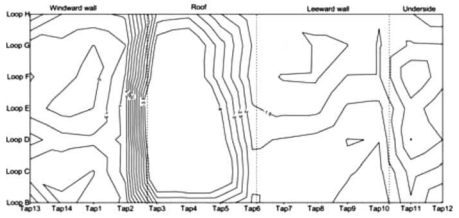

(b) 75 yaw

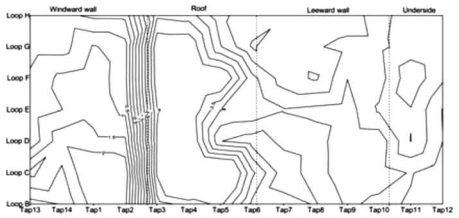

(c) 60 yaw

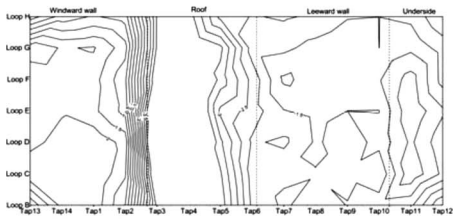

(d) 45 yaw

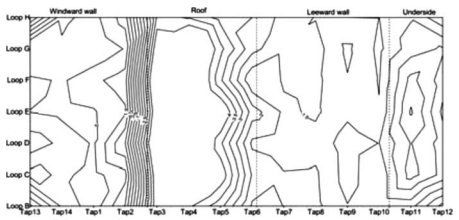

(e) 30 yaw

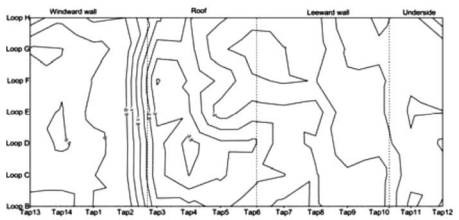

(f) 15 yaw

Fig. 26 Instantaneous pressure distributions resulting in a maximum value of the lift force coefficient occurring for a peak value of the side force coefficient

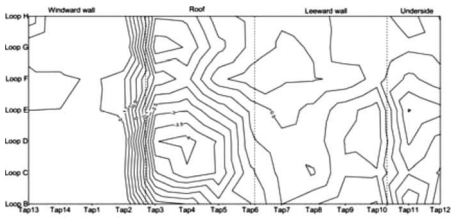

(a) 90 yaw

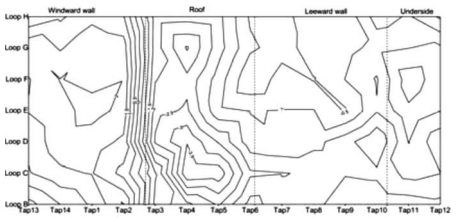

(b) 75 yaw

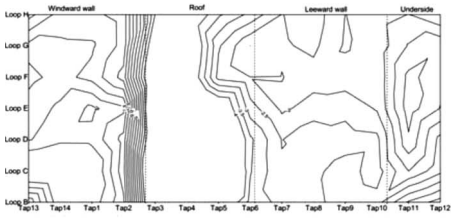

(c) 60 yaw

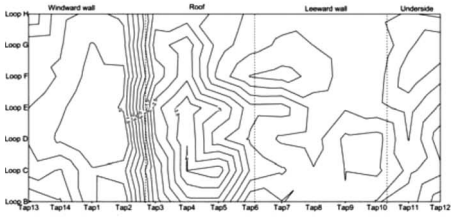

(d) 45 yaw

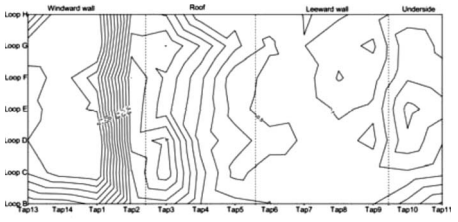

(e) 30 yaw

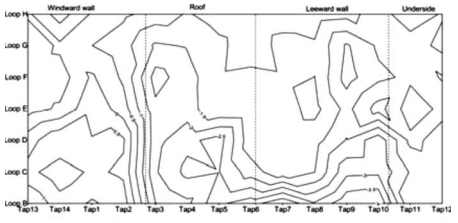

(f) 15 yaw

Fig. 27 Instantaneous pressure distributions resulting in a minimum value of the lift force coefficient occurring for a peak value of the side force coefficient

$I(z)$ = turbulence intensity of the streamwise velocity, $\sigma_u(z)/U(z)$
L = lift force (N)
${}^xL_U$ = turbulent length scale in the streamwise direction (m)
n = frequency (Hz)
p = surface pressure (N/m^2)
p_r = reference pressure (N/m^2)
S = side force (N)
$S_{CL}(n)$ = lift force coefficient spectrum
$S_{CS}(n)$ = side force coefficient spectrum
$S_p(n)$ = pressure spectrum ($s\ N^2/m^4$)
$S_u(n)$ = streamwise velocity spectrum (m^2/s)
$U(z)$ = mean velocity in the streamwise direction at a height of z (m/s)
z = full-scale equivalent height above the ground (m)
ρ = density of air (kg/m^3)
σ_{CL} = standard deviation of the lift force coefficient
σ_{CS} = standard deviation of the side force coefficient
σ_p = standard deviation of the surface pressure (N/m^2)
$\sigma_u(z)$ = standard deviation of the streamwise velocity (m/s)
ψ = yaw angle (the angle between the train axis and the streamwise tunnel velocity) (deg)

References

[1] Cooper, R. K., 1979, "The Probability of Trains Overturning in High Winds," Proceedings of the Fifth International Conference on Wind Engineering, Fort Collins, CO.

[2] Bradbury, W. M. S., Pottrill, P., and Murtagh, V., 2003, "Enhanced Permissible Speed on the West Coast Mainline: Investigations of Wind Overturning Effects," Proceedings of the Sixth World Congress on Railway Research, Edinburgh, UK, pp. 476–485.

[3] Gautier, P. E., Sacre, C., Delaunay, D., Parrot, M., Dersigny, C., and Bodere, S., 2001, "TGV Méditerranée High Speed Line Safety Against Cross-Winds: A Slow-Down System Based on Anemometric Measurements and Spatial Short-Term Meteorological Prediction," Proceedings of the Fifth World Congress on Railway Research, Köln, Germany.

[4] Imai, T., Fujii, T., Tanemoto, K., Shimamura, T., Maeda, T., Ishida, H., and Hibino, Y., 2002, "New Train Regulation Method Based on Wind Direction and Velocity of Natural Wind Against Strong Winds," J. Wind Eng. Ind. Aerodyn., **90**, pp. 1601–1610.

[5] Tielkes, T., Heine, C., Möller, M., and Driller, J., 2008, "A Probabilistic Approach to Safeguard Cross Wind Safety of Passenger Railway Operation in Germany: The New DB Guideline Ril 80704," Proceedings of the Eighth World Congress on Railway Research, Seoul, South Korea.

[6] Andersson, E., Häggström, J., Sima, M., and Stichel, S., 2004, "Assessment of Train-Overturning Risk Due to Strong Cross-Winds," Proc. Inst. Mech. Eng., F J. Rail Rapid Transit, **218**(3), pp. 213–223.

[7] Baker, C. J., Lopez-Calleja, F., Jones, J., and Munday, J., 2004, "Measurements of the Cross Wind Forces on Trains," J. Wind Eng. Ind. Aerodyn., **92**, pp. 547–563.

[8] Bocciolone, M., Cheli, F., Corradi, R., Muggiasca, S., and Tomasini, G., 2008, "Crosswind Action on Rail Vehicles: Wind Tunnel Experimental Analyses," J. Wind Eng. Ind. Aerodyn., **96**(5), pp. 584–610.

[9] Diedrichs, B., 2003, "On Computational Fluid Dynamics Modelling of Cross-wind Effects for High-Speed Rolling Stock," Proc. Inst. Mech. Eng., F J. Rail Rapid Transit, **217**, pp. 203–226.

[10] EC, 2006, "Technical Specification for Interoperability of the Trans-European High Speed Rail System," European Law, Official Journal of the European Communities.

[11] CEN, 2008, "Railway Applications Aerodynamics Part 6: Requirements and Test Procedures for Cross Wind Assessment," European Norm, CEN/TC 256, prEN 14067.

[12] Ferreira, A. D., and Vaz, P. A., 2003, "Wind Tunnel Study of Coal Dust Release From Train Wagons," 11th International Conference on Wind Engineering, Jun. 2–5.

[13] Bouferrouk, A., Baker, C. J., Sterling, M., O'Neil, H., and Wood, S., 2008, "Calculation of the Cross Wind Displacement of Pantographs," Proceedings of BBAA VI, Milano, Italy, Jul. 20–24.

[14] Baker, C. J., and Humphreys, N. D., 1996, "Assessment of the Adequacy of Various Wind Tunnel Techniques to Obtain Aerodynamic Data for Ground Vehicles in Cross Winds," J. Wind Eng. Ind. Aerodyn., **60**, pp. 49–68.

[15] Quinn, A. D., Sterling, M., Robertson, A. P., and Baker, C. J., 2007, "An Investigation of the Wind Induced Rolling Moment on a Commercial Vehicle in the Atmospheric Boundary Layer," Proc. Inst. Mech. Eng., Part D (J. Automob. Eng.), **221**(11), pp. 1367–1379.

[16] ESDU, 1985, "Characteristics of Atmospheric Turbulence Near the Ground: Part 2 Single Point Data for Strong Wind-Neutral Atmosphere," Engineering Sciences Data Unit, Data Item 85020.

[17] Sanquer, S. S., Barré, C., Dufresne de Virel, M., and Cléon, L. M., 2004, "Effect of Cross Winds on High-Speed Trains: Development of a New Experimental Methodology," J. Wind Eng. Ind. Aerodyn., **92**(7–8), pp. 535–545.

[18] Holmes, J. D., Sankaran, R., Kwok, K. C. S., and Syme, M. J., 1997, "Eigenvector Modes of Fluctuating Pressure on Low Rise Building Models," J. Wind Eng. Ind. Aerodyn., **69–71**, pp. 697–707.

[19] Baker, C. J., 2000, "Aspects of the Use of the Technique of Orthogonal Decomposition of Surface Pressure Fields," Wind Struct., **3**(2), pp. 97–115.

[20] Sterling, M., Baker, C. J., Bouferrouk, A., O'Neil, H., Wood, S., and Crosbie, E., 2008, "An Investigation of the Aerodynamic Admittances and Aerodynamic Weighting Functions of Trains," BBAA VI International Colloquium on Bluff Bodies Aerodynamics and Applications, Milan, July 20–24.

[21] Sterling, M., Baker, C. J., Richards, P. J., Hoxey, R. P., and Quinn, A. D., 2006, "An Investigation of the Wind Statistics and Extreme Gust Events at a Rural Site and Implications for Wind Tunnel Testing," Wind Struct., **9**(3), pp. 193–216.

[22] Cooper, R., 1979, "The Effect of Cross Winds in Trains," *Aerodynamics of Transportation I*, ASME, New York, pp. 127–136.

The Aerodynamic Interaction Between an Inverted Wing and a Rotating Wheel

M. A. van den Berg

X. Zhang

School of Engineering Sciences,
University of Southampton,
Southampton SO17 1BJ, UK

The fundamental aerodynamic influence of downstream wheels on a front wing flow field and vice versa has been investigated using generic wind tunnel models. The research has been conducted using a wing with a fixed configuration, whereas the wing ride height with respect to the ground has been varied as the primary variable. The overlap and gap between the wing and wheels have been kept constant within the context of the current paper. At higher ride heights the wheels reduce wing downforce and increase wing drag, whereas the drag of the wheels themselves also rises. At low ride heights, however, the opposite happens and the wing performance improves, while the wheels produce less drag. The ride height range has been subdivided into force regions with consistent characteristics throughout each of them. Force and pressure measurements, particle image velocimetry results, and oil flow images have been used to explain the differences between the force regions and to derive the governing flow mechanisms. The trajectories and interaction of vortices play a dominant role in the observed force behavior, both as force enhancing and reducing mechanisms. The effect of wheel circulation, flow separation, and flow channeling by the ground and by the wheels are among the other main contributors that have been discussed within this paper. [DOI: 10.1115/1.3215942]

1 Introduction

The aerodynamic research that is applicable to competitive car racing has developed along two distinct roads. On one hand, empirical research is driven by instant performance gains within a specific set of technical regulations, optimizing every component in relation to the surrounding parts. On the other hand, academic research has mainly focused on components in isolation and on trying to understand the governing flow physics, such as the ground effect, for unique problems. The latter approach has yielded several generic studies of simplified wing, wheel, and diffuser flow problems [1,2], but application of this knowledge to practical racecar problems has not always been straightforward due to the inherent complexity of the complete car compared with that of isolated components.

One major conclusion of such works is that the generation of downforce in racecar applications is much more reliant on vortex phenomena than on the use of efficient high aspect ratio wings, in contrast to those in aeronautical practices. Inevitably, this observation leads to the subsequent conclusion that the downstream management of vortex trajectories is essential to the optimization of aerodynamic performance, and thus that flow interaction between the various car components is an area of prime interest. This thus leaves scoop for further fundamental research, which is not only restricted to isolated components in ground effect (wings and diffusers) or ground contact (wheels), but which also examines the influence of surrounding components.

Fackrell and Harvey [3–5] played a dominant role in the field of wheel aerodynamics, introducing both commonly used experimental methods and providing benchmarks results. Fackrell and Harvey's tests were the first to incorporate a wheel in contact with a moving ground system—in contrast to previous studies that used a stationary ground [6] or a gap between a rotating wheel and moving ground [7,8]—and they showed that this is an essential condition for accurate simulation. They also discovered a large positive pressure peak in front of the contact patch and predicted a downstream negative peak, while further giving more insight into the general flow field, including the "jetting vortical structures" originating from the corners of the contact patch. Finally, Fackrell [3] also pioneered the use of the "indirect measurement method" to determine the wheel lift and drag via integration of on-surface pressure measurements. Until then the "direct method" had been preferred, using load cells to measure the aerodynamic forces directly. The indirect method requires sufficient spatial resolution of the measurements to be accurate, but at the same time has the advantage of providing insight into the on-surface flow features via the information contained in the pressure contour plots. Recent developments in wheel aerodynamic research include the return of direct force measurements [9] and the use of computational fluid dynamics (CFD) [10–13], which has revealed more about the governing flow structures, especially via unsteady simulations [14].

Inverted wings in ground effect produce an increasing amount of downforce with reducing ride height. The downforce reaches higher than freestream values at a characteristic ride height of approximately 30% of the chord length [15]. At even lower ride heights the downforce decreases sharply in a similar way as to the wing stall, which is experienced at high angles of attack in freestream [15]. A comprehensive series of studies into aerodynamics of single and double element wings in ground effect can be found in literature [16–22], which has led to the classification of force regions within the ride height domain. Additionally, on- and off-surface experiments have been performed using oil flow, pressure measurements, particle image velocimetry (PIV), and laser Doppler anemometry (LDA) techniques, which have resulted in a better understanding of the governing flow mechanisms and flow features, such as the trailing tip vortices. A variety of force enhancing and limiting mechanisms define the force behavior of a wing in ground effect and the previous mentioned tip vortices can, for example, increase the suction on the lower wing surfaces, or reduce the downforce due to vortex dilution or breakdown [23]. Close to the ground, the balance between these mechanisms can depend on the direction in which the ride height changes, leading to hysteresis effects in the force behavior [23].

Contributed by the Fluids Engineering Division of ASME for publication in the JOURNAL OF FLUIDS ENGINEERING. Manuscript received January 16, 2009; final manuscript received June 29, 2009; published online September 18, 2009. Review conducted by Joseph Katz.

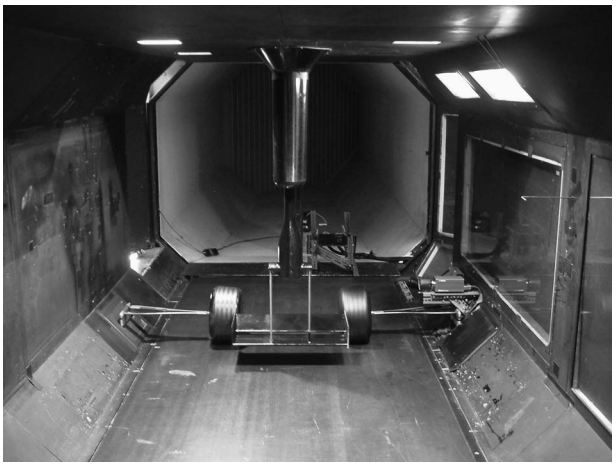

Fig. 1 Experimental setup in the Southampton wind tunnel test facility, viewed from upstream. The PIV test equipment is installed to analyze the flow over the crown of the port side wheel in a streamwise direction (the camera is located on top of the port side wheel arm and the laser off-center downstream).

Research into aerodynamic interaction of racecar components has been extremely limited and restricted to simplified problems, such as a two-dimensional (2D) study of wing-wheel interaction [24], which logically ignores the dominant three-dimensional (3D) effects. Related subjects, such as rear wing-car body interaction [25], a wing following in the wake of another simplified vehicle [26], and slip streaming effects [27], do however give an indication of the large influence that aerodynamic interaction can have on the overall performance.

The aim of this paper is to take a next step in fundamental aerodynamic research by studying the interaction between front wing and wheel flow fields. This multiple components problem will be tackled with the help of the simplified generic building blocks of previous research, while also incorporating the established knowledge on ground effect aerodynamics. This research studies how the performance of the front wing changes in the presence of the wheels and vice versa how the flow field around the wheels is modified by that of the wing in comparison to the solutions for these components in isolation. The wing ride height will be the primary variable that is used to derive the governing flow mechanisms, which cause these changes in the force behavior, and to explore the delicate balance between force enhancing and force limiting mechanisms.

2 Description of Experiments

The research that is described in this paper consisted of experimental and computational investigations, which were performed in parallel [28]. The results presented here concentrate however on the experimental side of the study.

2.1 Test Facility. Tests were conducted in the 2.1×1.7 m^2 wind tunnel of the University of Southampton. This tunnel features a closed test section and is of a conventional closed-jet, return channel type (see Fig. 1). A large moving belt system is fitted for correct ground simulation and a boundary layer suction system upstream of the belt is used for boundary layer reduction. The freestream turbulence level is less than 0.3% at 30 m/s and the velocity profile in vertical direction reaches freestream velocity $\pm 0.2\%$ within 2 mm above the moving belt. Tests were performed at a constant dynamic head of 56.19 mm of water, which is equivalent to 30 m/s at standard atmospheric conditions and matches the average velocity over a lap for typical racing circuits, when evaluated at the 50% model scale dimensions that have been used. The temperature of the tunnel is not actively controlled and varies during testing; the encountered experimental Reynolds numbers based on the total chord of the model wing ranged from 5.7×10^5 to 5.9×10^5, depending on the atmospheric conditions. The Reynolds number for the wind tunnel tests is approximately a quarter of that experienced on track for real racecar applications, due to the scaling of velocity and model dimensions. The test facilities allowed only straight-line testing and as a result the model setup is symmetric with respect to the vertical center plane in streamwise direction. Further details of the testing can be found in Ref. [28].

2.2 Models. The experiments were conducted using 50% scale models. The wing is a generic representation of a double element front wing with flat vertical endplates. The wing is supported from the roof of the tunnel with a strut connected by two vertical pillars (see Fig. 1 and Fig. 2). The pillars are connected to the strut by a three-component load cell and the strut allows automated vertical adjustment of the ride height. This wing ride height (h) is defined as the distance between the ground and the lowest point on the main element of the wing. The results for increasing and decreasing ride height are obtained separately to be able to determine any hysteresis effects, depending on the direction of ride height variation. The wing profiles are depicted in Fig. 3 and further geometrical aspects as well as test results for the wing in isolation are described in detail by Mahon [23]. The combined wing chord, c, is 284 mm (139 mm for the main element and 145 mm for the flap) and the wingspan is 580 mm. The endplates are $275 \times 5 \times 115$ mm^3 in size and extend 5 mm below the lowest point of the main element of the wing.

The wheels are accurate representations of 2005 F1 tires with four longitudinal grooves. They are manufactured from carbon-fiber and do therefore not deform, like rubber tires would do. The geometry is modeled with a conical tire tread surface to simulate a 2.4 deg camber angle (see Fig. 3). The maximum wheel diameter is 313.9 mm and the width is 172.8 mm (see Fig. 3). The wheels feature representative spoke design hubs, but these have been covered flush with flat nondeformable disks to simplify the geometry. The wheels are supported from the side of the tunnel with Y-shaped wheelarms, which are connected to pillars that are partly covered by the windtunnel corner fillets (see Fig. 1). These wheelarms can be adjusted in streamwise and spanwise direction to adjust the gap (G) and the overlap (O) between the wing and the wheels respectively. The overlap and gap dimensions have both been kept at 20 mm each for all the results presented in this paper, whereas the wing ride height has been varied from 15 mm to 180 mm.

2.3 Experimental Methods. The experimental tests during this research have been selected and organized in such a way that every subsequent step reveals more about the aerodynamic wing-wheel interaction. First, force measurements are used to obtain a global integral overview of the force behavior and to divide the ride height domain into force regions with unique characteristics, similar to previously employed procedures [18]. Hereto direct force measurements of the wheel drag have been conducted using a one-component strain-gauge load cell, which connects the wheel to the wheelarm. Downforce, drag, and pitching moment for the wing have been measured with a three-component load cell mounted between the vertical support pillars of the wing and the movable strut. The wheel drag has been corrected for rolling resistance with the use of trundle tests, whereas the wing forces have been modified with tare measurements for the influence of the support structure in isolation. The effect of (temperature) drift of the load cells was limited by linear interpolation between pre- and postrun zero measurements. Data acquisition took place at a sampling frequency of 1 kHz over 30 blocks of 1000 samples each. Within the context of this research all data has been averaged over the sampling period.

Next, on-surface measurements were performed for a typical ride height condition within each of the force regions in order to

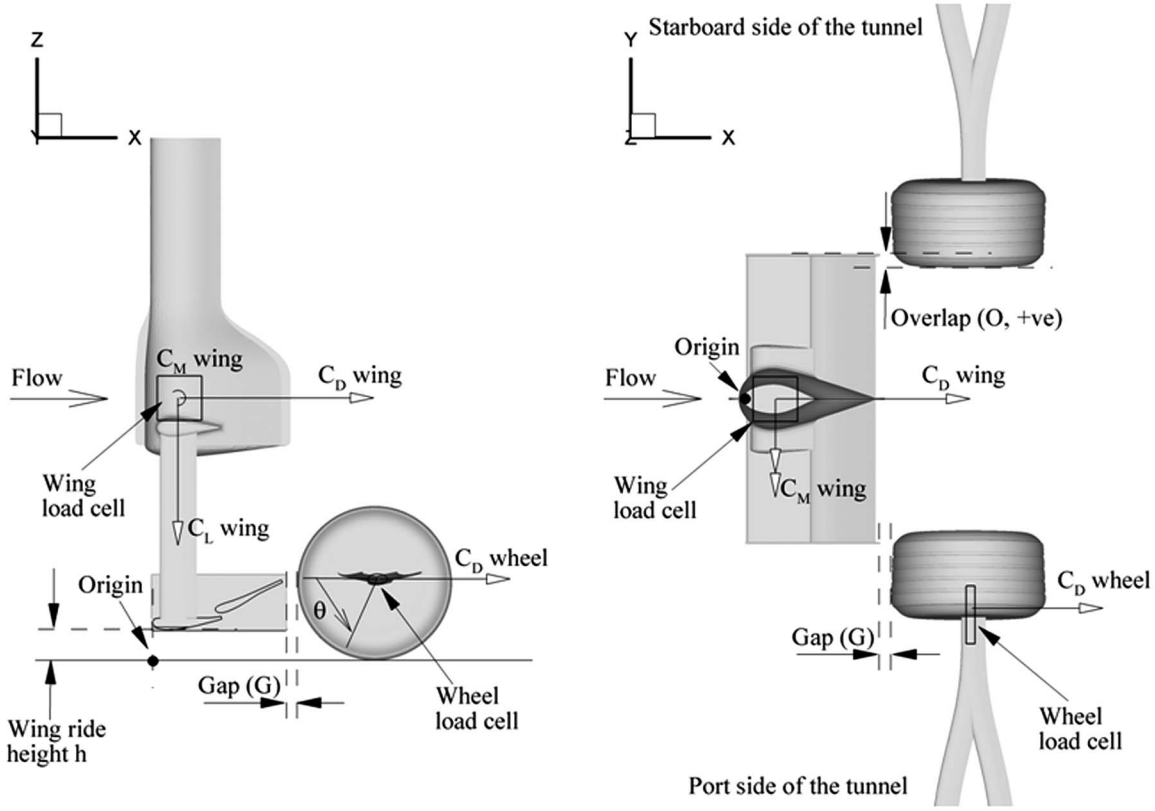

Fig. 2 Definitions of test setup and force measurement conventions

examine in more detail which flow features caused the observed force behavior. Flow visualization on the wing surfaces was conducted using a liquid suspension of titanium dioxide in paraffin. Also pressure measurements on the wing and on the starboard side wheel have been taken, but in both cases the spatial resolution of this pressure data was insufficient to derive the aerodynamic loading via integration with the help of the indirect method. Special duplicate models were used for the pressure measurements, because the pressure tubes through the wing strut would otherwise have bridged the load cell during force measurements and pres-

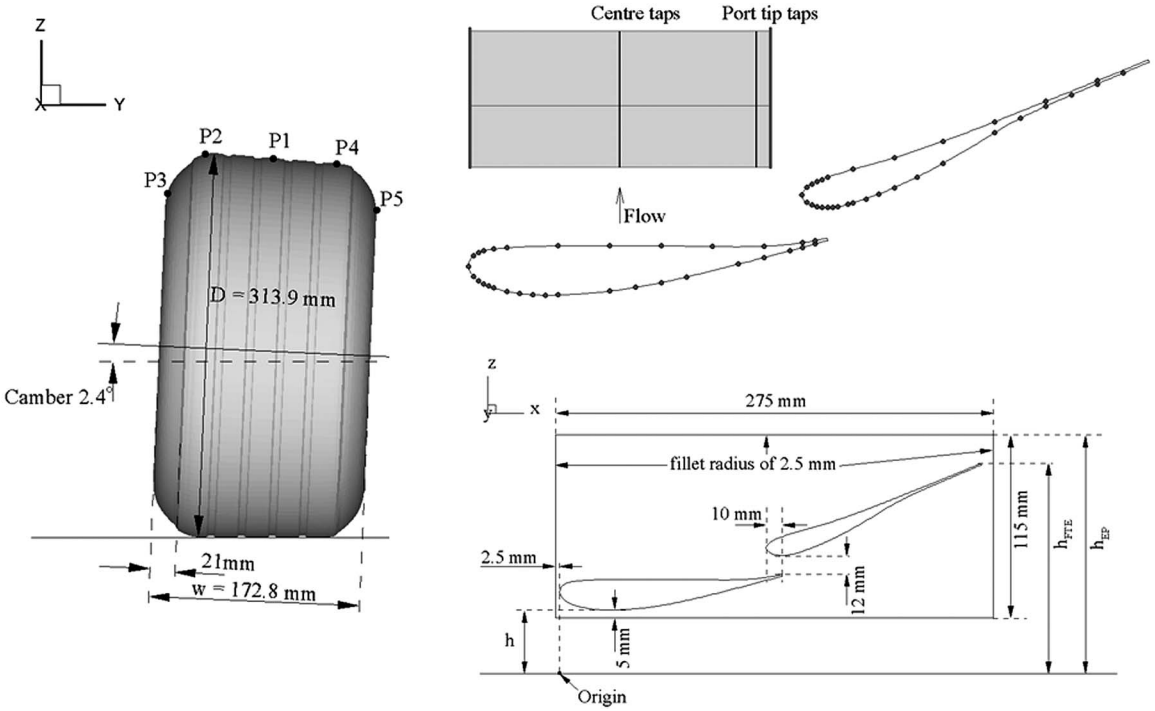

Fig. 3 Wheel and wing characteristics and pressure tap locations for the wheel (P1–P5) and wing (marked on the sections in the top right figure)

sure tubes could be clogged by oil flow application. The second wing had an identical geometry to the 'clean wing' that was used for the other measurements, but the pressure measurement wheel differed in a few aspects from the 'clean wheel'. The main difference was that a noncambered wheel was used, due to a lack of cambered spares. Furthermore the pressure measurement wheel could only be run at 20 m/s instead of the normal 30 m/s, because the extra internal weight of the system caused imbalance at higher velocities. The wheel pressure measurement results should therefore primarily be analyzed qualitatively in order to derive trends and flow features and not necessarily as absolute quantitative values for validation purposes.

The wheel pressures have been measured at five different locations (see Fig. 3) with an in-house developed system that uses one high quality pressure transducer, which is moved around the tire circumference by hand between tests to cover all five locations. Data is stored within the wheel and transferred to a PC via radio transmission. Approximately 360 samples per revolution were taken and the data was averaged over 250 cycles, omitting the cycles which did not feature the pressure peak in front of the contact patch due to wheel bounce (typically less than 25%). The results have been filtered for a natural vibration frequency of 750 Hz and corrections have been applied for centrifugal forces on the diaphragm and reference pressure, dependent on the pressure tap location and orientation. The wing pressures were measured at 128 streamwise positions, equally divided between the centerline and a location 25 mm inside of the port side endplate (see Fig. 3). The used Scanivalve zero-operate-calibrate (ZOC) pressure measurement system has a scanning rate of 20 kHz and sampled for a 5 s period per ride height. Once more only averaged results have been analyzed.

Finally, off-surface tests were conducted for a limited set of ride heights to evaluate how the governing mechanisms interact in the flow field. PIV measurements in vertical and horizontal streamwise planes were conducted for this purpose (see Fig. 1 for a typical setup). A Dantec (Skovlunde, Denmark) PowerFlow system was used in combination with a Gemini laser. The double laser sheet thickness was of the order of 2 mm to 3 mm and the time interval between the images was typically $20-50$ μs. During every test run 500 double image samples were taken and adaptive cross-correlation with interrogation areas of 32×32 pixels with a 75% overlap in both directions were used. Only range validation was applied to the correlated data. The resultant vector fields have been averaged over the amount of data samples.

3.4 Accuracy and Uncertainties. The uncertainty in the experimental results with a 95% confidence level has been estimated using Moffat's method [29]. The ride height has been set to ±0.05 mm with the use of metal slip gauges, whereas overlap and gap have been set to ±0.5 mm accuracy using rules. The wing incidence has been set with a digital inclinometer with an accuracy of ±0.005 deg and the tunnel velocity to a dynamic head of ±0.2 mm of water. The calibration of the load cells was checked and showed less than 0.25% difference between the applied and measured loads over the range of encountered forces. In total, the resulting uncertainty levels with 95% confidence are $\pm0.0092C_L$, $\pm0.0018C_D$, and $\pm0.0029C_M$ for the wing and $\pm0.0068C_D$ for the wheel force measurements. The maximum uncertainty in wheel pressures is $\pm0.0239C_P$ and $\pm0.0287C_P$ for the wing, although the average uncertainty for the latter is only $\pm0.0087C_P$ [23]. The long term repeatability of the force and pressure measurements over a period of more than a year were of the same order as the uncertainty limits. The blockage factor of the complete configuration with support structures in the windtunnel varies between 9.0% and 9.6%, depending on the wing ride height and wing-wheel overlap value. This is on the high side for quantitative purposes, but is deemed acceptable for the current qualitative investigations, which are aimed at exploring trends in the force behavior and look at relative differences. The values in this paper primarily give an indication of the scale of the experienced variations. However it needs to be kept in mind that further blockage corrections need to be applied in case the results are to be used as absolute values for the current configuration.

3 Force Behavior With Ride Height Variation

The aerodynamic loading on the wheels and wing varies as a function of the wing ride height. The results of the experimental force measurements are plotted in Fig. 4. The wing ride height range has been chosen to exceed the conditions experienced during practical applications in order to allow examination of the balance between the various flow mechanisms over a wider variety of situations. This generates more scope to derive the individual mechanisms from the combined integral result by covering more extreme variations of the flow mechanisms.

The wing ride height, h, has been nondimensionalized with the total wing chord, c, as can be seen on the x-axes of the plots in Fig. 4. The wing downforce is defined as a downwards pointing vertical force, see Fig. 2. The forces are presented as nondimensional coefficients based on the dynamic pressure and the projected top view area of the component to which they relate. The pitching moment has originally been nondimensionalized using the same parameters and the additional combined wing chord as moment arm, but in this paper has instead been presented as the nondimensionalized streamwise position of the center of pressure of the wing, x/c_{CoP}. Hereto the wing downforce, drag, and pitching moment have been combined to derive the center of pressure location relative to the leading edge of the main element of the wing, assuming its position is only varying in x-direction with aerodynamic loading changes. The force measurement results for the isolated wheel and isolated wing cases have also been included in Fig. 4.

3.1 Definition of Force Regions. When the wheel drag plot of Fig. 4(a) is analyzed, it can be seen that it features several (local) minima and maxima within the ride height range. Each of these extremes represents a condition at which the balance between the force enhancing and limiting mechanisms is in equilibrium, but this balance changes to either side of these ride heights. These extremes have been chosen as the force region boundaries, whereas the lowest region has been subdivided in a branch for decreasing (V) and one for increasing (VI) ride heights to reflect the influence of hysteresis effects. Although the wing loading curves do not show extremes at all of the region boundaries, it can still be noticed that the force behavior features a change in the derivative of the curve for most of them.

Starting at the highest ride height, the different force regions can be characterized as follows.

I. At high ride heights the wheel drag (Fig. 4(a)) is considerably higher than for the isolated wheel and increases with reducing ride height; the wing downforce (Fig. 4(b)) is down by a constant offset compared with the isolated case and wing drag (Fig. 4(c)) is a little lower as well, whereas the center of pressure of the wing (Fig. 4(d)) lies further downstream.
II. The wheel drag decreases, first gradually and then abruptly; the wing downforce and drag start growing at a higher rate toward the lower boundary.
III. The wheel drag slowly climbs from a minimum; the wing downforce almost reaches the level of the isolated wing case and drag is a little up.
IV. The wheel drag drops again; the wing downforce and drag start growing rapidly and reach higher levels than for the wing on its own.
V. The wheel drag stays fairly constant; but the wing downforce falls away, while the wing drag still increases.
VI. With increasing ride height, the wheel drag is at a constant and higher level than for the decreasing branch; the wing downforce also shows hysteresis signs and is at a much

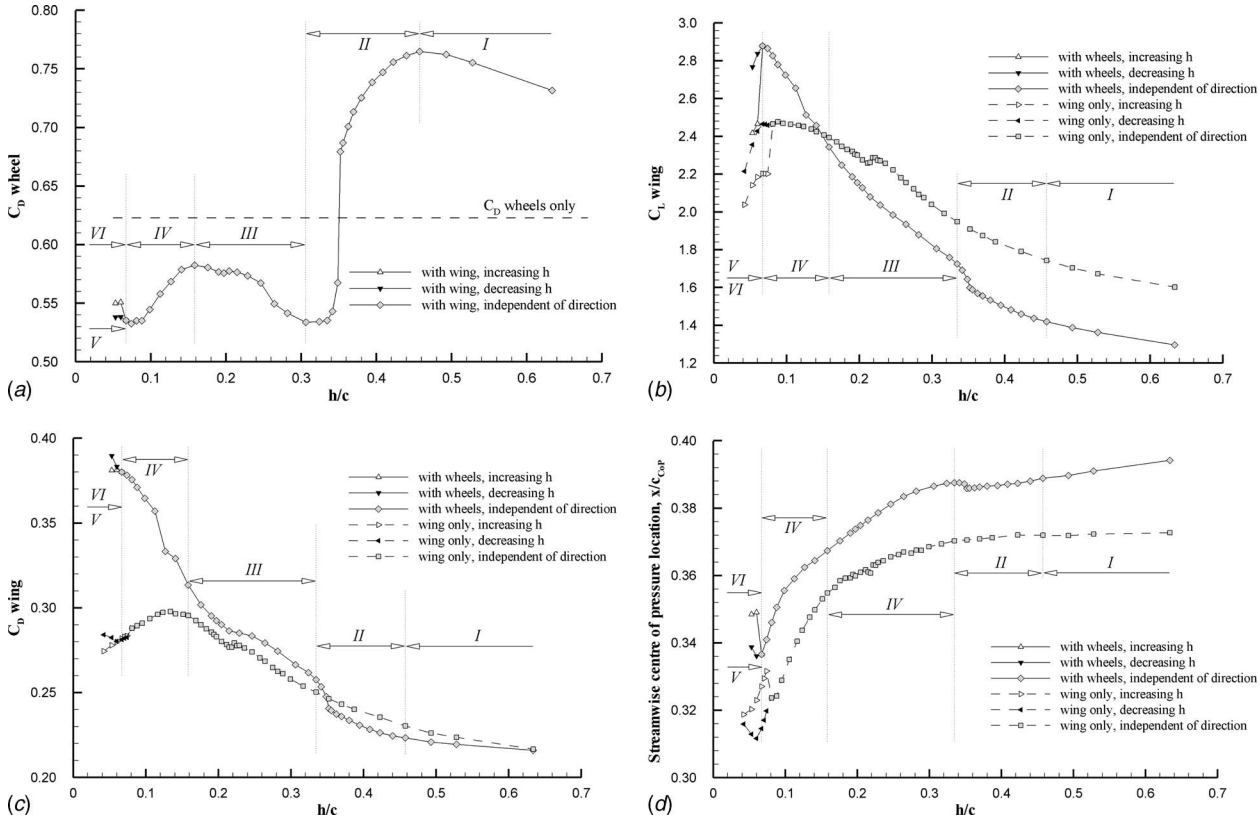

Fig. 4 Wheel and wing force coefficients as functions of the wing ride height and definitions of the derived force regions I–VI; (a) wheel drag, (b) wing downforce, (c) wing drag, (d) wing centre of pressure location

lower level, jumping up at the upper boundary, the wing drag reduces very slowly.

3.2 The Two Fundamental Wheel Drag Phases. From the above subdivision into force regions it becomes clear that the wheel drag shows a varied behavior over the conditions, but alternatively the ride height domain can also be separated in two, more fundamental, phases: the first with higher wheel drag than for the isolated case (regions I and the biggest part of II) and the second with lower drag (the remaining regions). The increase in wheel drag can be as much as 23% in the higher drag phase, whereas reductions of up to 15% are possible in the low drag phase.

The precise reasons for these variations will be explained in Secs. 4 and 5, but Fig. 5 is introduced here to give an idea of the fundamental differences in the flow field between the two phases. Figure 5 shows the vortex structures in the flow field by depicting isosurfaces of Q (an identification parameter for vortices and coherent structures derived from the second invariant of the velocity gradient tensor [30]), which have been obtained from steady-state computational simulations on a fully structured grid, using the

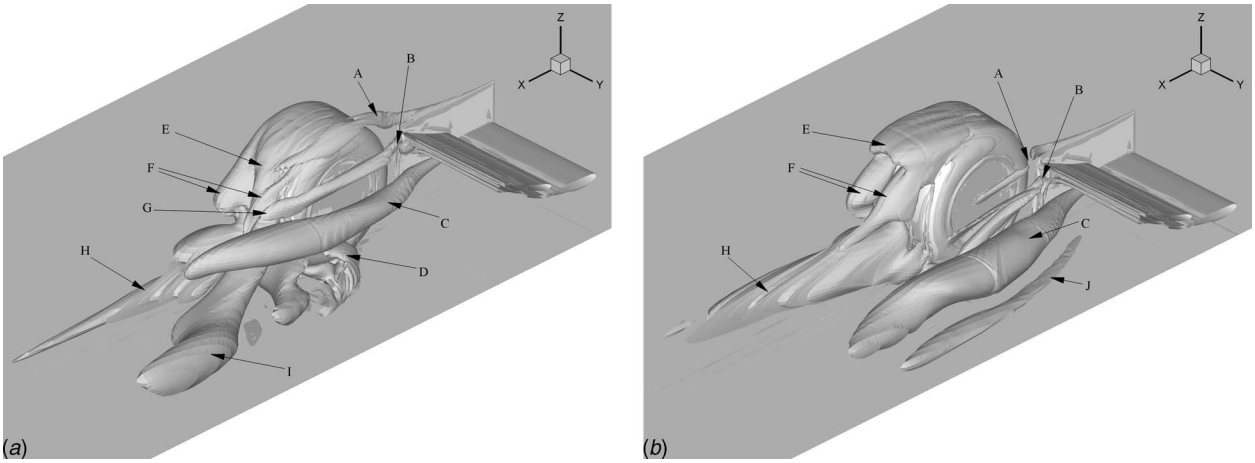

Fig. 5 Representations of the two fundamental wheel drag phases; (a) high drag phase, (b) low drag phase; figures show iso-surfaces of Q obtained from steady-state computational simulations [28]

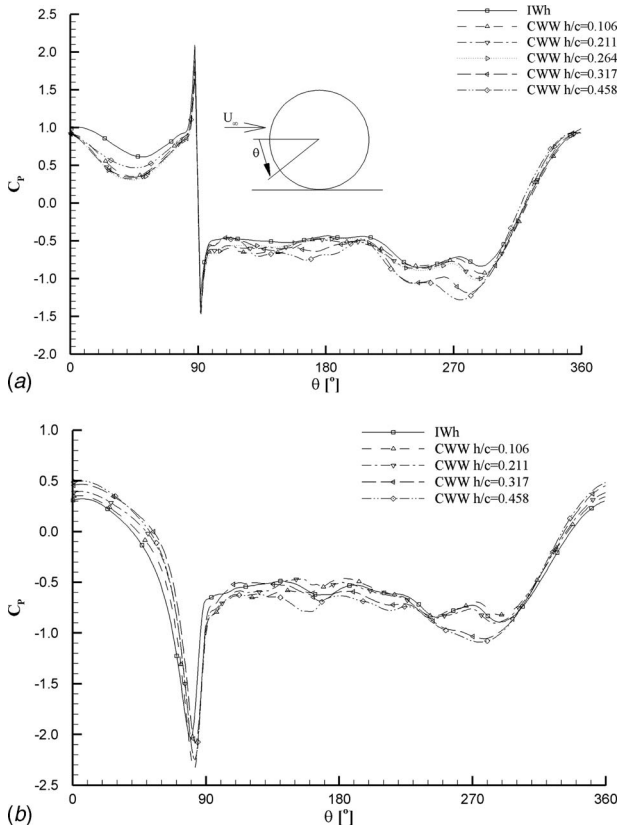

Fig. 6 Pressure distributions for two locations along the wheel circumference of the starboard side wheel; (a) center line P1, (b) outboard tire tread; for the isolated wheel (IWh) and for the wheel combined with the wing (CWW) at various ride heights

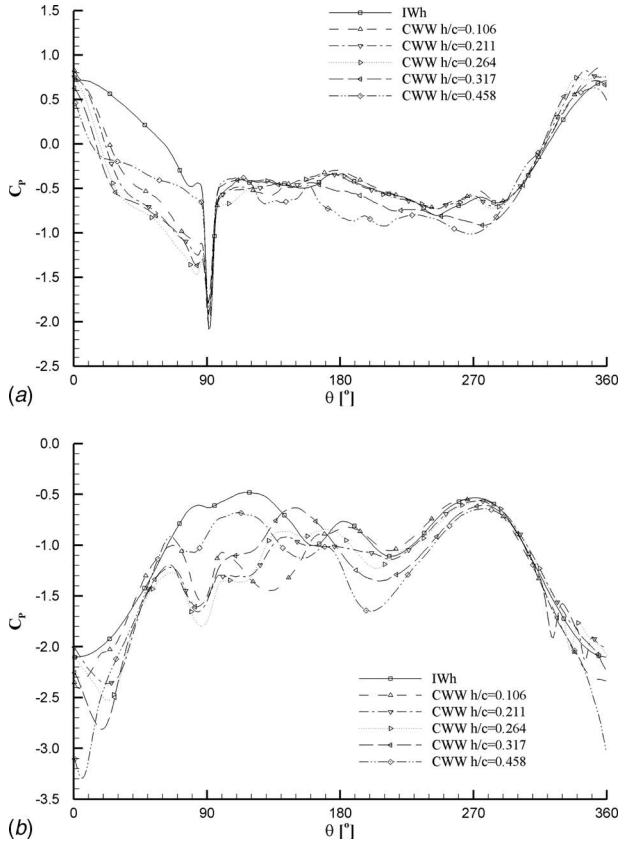

Fig. 7 Pressure distributions for further two locations along the wheel circumference of the starboard side wheel; (a) inboard tire tread P4, (b) inboard sidewall P5; for the isolated wheel (IWh) and for the wheel combined with the wing (CWW) at various ride heights

model dimensions of the experiments and at the same velocity of 30 m/s (the complete computational specifications have not been included in this experimental paper, for details see Ref. [28]). The vortex trajectories provide a revealing answer for the differences between the two phases; for the low wheel drag phase the top edge vortex originating from the top of the endplate (feature "A" in Fig. 5) travels on the inside of the wheel, whereas in the high drag phase it moves over the crown of the wheel and then interacts with the other vortices in the wheel wake. Incidentally the wing drag is low when the wheel drag is high and vice versa. This can partly be related to the variation in the downforce induced drag component, but does not explain this correlation in region III.

4 Effect of Wing on the Wheel Aerodynamics

The wheel drag behavior displayed in Fig. 4(*a*) is governed by a fine balance between the force enhancing and limiting mechanisms. The more subtle changes are the result of a shift in equilibrium between the mechanisms, but the large difference between the high and low drag phase can be related to clear differences in the flow field and governing flow mechanisms. Previously it was postulated that the contrast can be explained with the change in trajectory of the top edge vortex, as shown in Fig. 5 and this will now be supported with experimental results.

4.1 Governing Mechanisms for the High Wheel Drag Phase. The wheel wake is characterized by a strong recirculation area in the high wheel drag phase. This recirculation induces high velocities along the back face of the wheel, which causes the low pressures around $\theta=180$ deg in Figs. 6 and 7, for the high ride heights. The PIV results, of which a selection is presented in Fig. 8, show the recirculation in the form of a strong focal point in this horizontal plane, which is situated at the wheel axle height. This focal point is present for all ride heights from $h/c=0.342$ and upwards, but not for $h/c=0.317$, which is the highest sampled ride height in the low drag phase. The focal point lies closest to the wheel surface for $h/c=0.458$ and the PIV results show that the induced velocities along the wheel surface are largest with the focal point in this location. This coincides with the maximum drag ride height in Fig. 4(*a*) and therefore confirms that this wake characteristic is the dominant mechanism of the high wheel drag phase. The reduction in wheel drag, when moving to higher and lower ride heights, away from $h/c=0.458$ (in region I and the higher part of region II), can be further explained primarily by a movement of the focal point away from the wheel surface, which leads to increased base pressures.

Further analysis of the experimental results reveals that the recirculation in the wheel wake only occurs when the top edge vortex of the front wing endplate passes over the crown of the wheel. The pressure distribution in Fig. 7(*b*) on the inboard sidewall of the wheel presents the clearest evidence for this correlation. The imprint of the top edge vortex can clearly be seen as a local minimum around $\theta=350$ deg for $h/c=0.211$, which gradually rises to $\theta=320$ deg for $h/c=0.317$. This trend can be extrapolated in both directions; for $h/c=0.458$—the only sampled ride height in the high drag phase—this imprint is not present, whereas for the lowest ride height, $h/c=0.106$, an imprint below the most forward point of the wheel at $\theta=10$ deg can be distinguished. Similarly, in Fig. 7(*a*), the imprint can be seen to move upwards with increasing ride height on the inboard side of the tire tread as well. The local minimum at $\theta=350$ deg for $h/c=0.211$

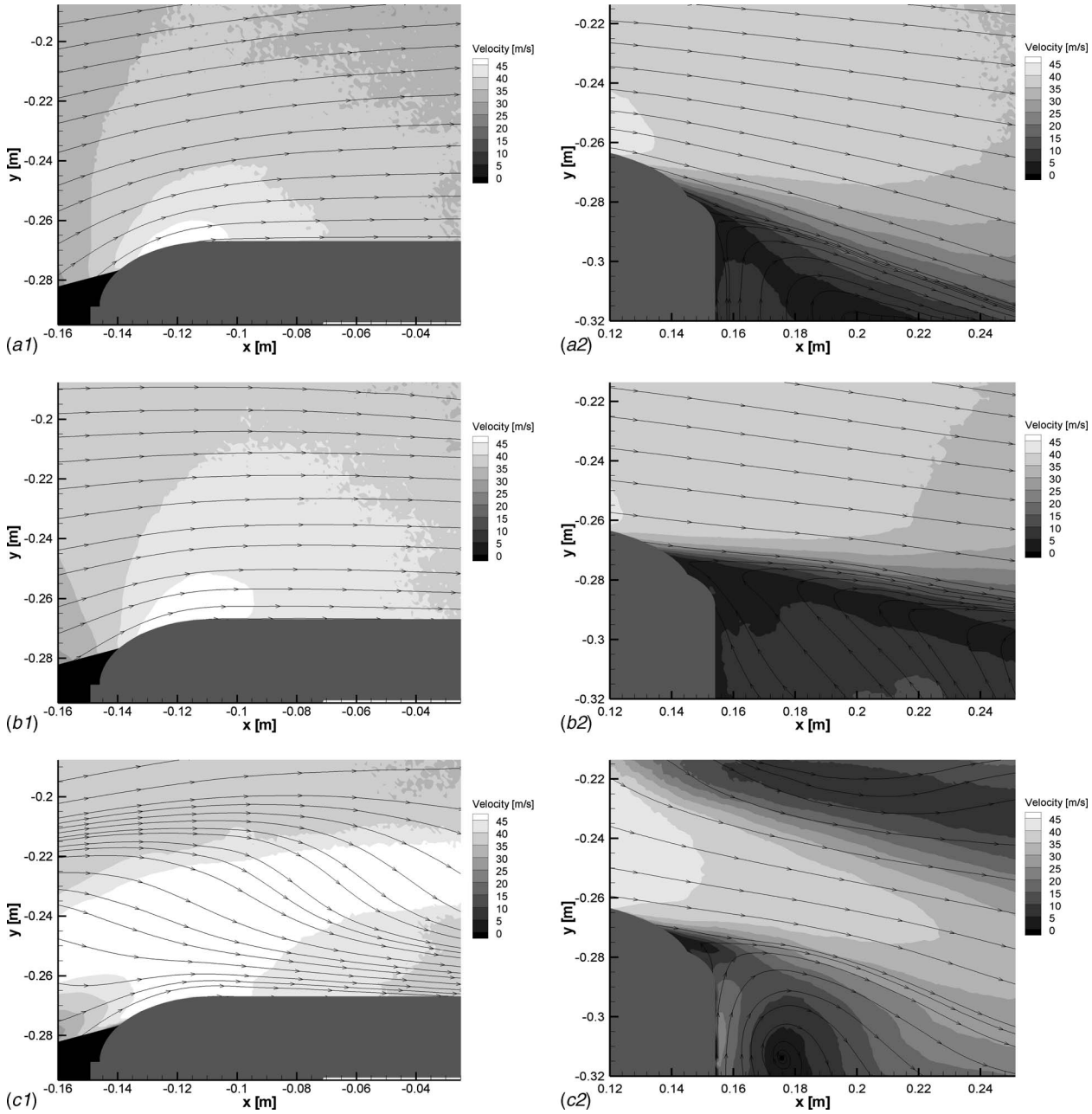

Fig. 8 Velocity contours derived from PIV results; (a) isolated wheel, (b) combined wing and wheels at $h/c=0.106$, (c) combined wing and wheels at $h/c=0.528$; inboard front corner (left figures; at $z=165$ mm) and inboard rear corner (right figures; at $z=174$ mm), and the wheel contour is visualized in dark gray and the shadow upstream is blacked out (left lower corner of left figures)

changes into a ripple around $\theta=310$ deg for $h/c=0.458$, when the vortex passes over the wheel.

This shows that the top edge vortex changes trajectory on the boundary of the high wheel drag phase and it is therefore proposed that the wake recirculation is a direct result of the top edge vortex position. When this vortex (feature "A" in Fig. 5) passes over the wheel it starts a strong interaction with the wheel vortex originating from the top of the wheel (feature "F"), the vortex originating from the flap trailing edge (TE) junction (feature "B") and the lower edge vortex (feature "C"), accumulating in a strong circulation represented as feature "G." The sudden change in wheel drag is thus directly coupled to the abrupt change in trajectory of the top edge vortex.

4.2 Governing Mechanisms for the Low Wheel Drag Phase. The above discussion has explained how the wheel drag can rise to above the level of the isolated wheel case, next it will be analyzed how for lower ride heights the wheel drag can fall below this level. The pressure distributions in Fig. 6 and Fig. 7 show that the main qualitative difference between the isolated wheel and the combined case at low ride heights is the low pressure on the lower front half of the wheel (from 0 deg to 90 deg) at the center line (Fig. 6(*a*)) and at the inboard side of the tire tread (Fig. 7(*a*)). In contrast, the pressures in this area on the outside of the wheel have increased once the wing is added, as can be seen in Fig. 6(*b*). The explanation for this is that the accelerated flow originating from the wing is directed into the converging channel

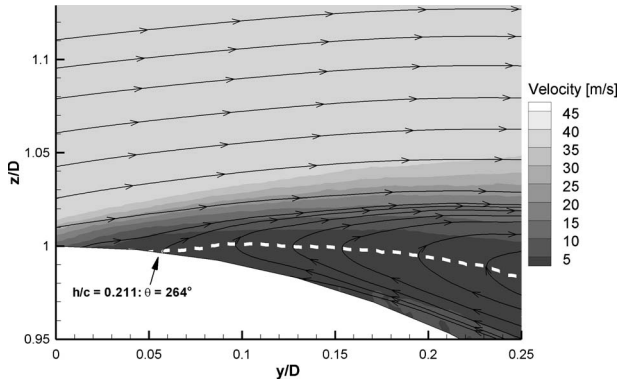

Fig. 9 Separation streamline (white dashed) from the top of the wheel in the center *xz*-plane for the *h*/*c*=0.211 combined case; results based on PIV measurements for the in-plane velocity components, which are obtained with the setup of Fig. 1. Angle definition is shown in Fig. 2 and angle variation with ride height is summarized in Table 1.

between the wheels and the ground. Hereto the flow is deflected around the inboard corner of the wheel, due to the overlap with the wing, which leads to an additional suction in this area. The blockage caused by the top edge vortex on the inside of the wheel for the lower wheel drag phase enhances the acceleration around the wheel corner even further.

It is this suction caused by the channeling effect that explains the reduction in wheel drag at low ride heights. However, logically, this channeling effect is still effective at high ride heights as well and it can thus be concluded that the wheel drag would also be lower in these force regions, if the wake effect and strong recirculation did not generate a much larger increase in drag. Furthermore, Sec. 5 will show that the channeling effect also has a dominant influence on the wing performance.

The beneficial influence of the channeling effect on the wheel drag reaches a maximum when the accelerated flow from the wing is diverged around the closest, most forward, point of the wheel. The areas with highest flow velocities in the wing wake are the top edge and lower edge vortices and the flow on the suction side of the flap, so it is expected that the largest part of the wheel is exposed to these when the top edge vortices and flap suction flow impact above the wheel center line and the lower edge vortices below. This is at a ride height when $h-\frac{1}{2}\,h_{\mathrm{EP}}\approx\frac{1}{2}\,\mathrm{D}$, which translates to $h/c\approx 0.35$. Indeed Fig. 4(*a*) shows that the minimum drag on the boundary between region II and III is reached close to this ride height.

The increase in wheel drag with decreasing wing ride height in region III can be explained with two mechanisms. First of all the beneficial influence of the channeling effect reduces as explained before, leading to less suction on the inboard corner of the wheel. Second, the wheel drag increases due to a reduction in suction just upstream of the crown of the wheel as a result of a movement of the separation position (see Figs. 6(*a*), 6(*b*), and 7(*a*) between $\theta=270$ deg and 300 deg). This mechanism is however of secondary importance to the channeling effect, as the pressure component in *x*-direction is small for this area of the wheel due to its orientation. Figure 9 and especially Table 1 reveal that the separation streamline at the centerline of the wheel moves upstream with decreasing wing ride height. The effect of the wing circulation on the wheel flow field is the primary cause of this, since the induced velocity from the suction side of the flap delays separation, when this impacts above the wheel center line. Another way to look at this is the analogy that the separation moves upstream when a stationary wheel starts rotating, the wing induces a circulation of opposite direction to the one caused by the wheel rotation and will thus delay separation, especially at higher ride heights.

Table 1 Angle at which the separation streamline at the centerline of the wheel (see Fig. 9) leaves the wheel surface for the isolated wheel and for various wing ride heights for the combined configuration

Case	Separation angle θ (deg)
Isolated wheel	265
$h/c=0.063$	269
$h/c=0.106$	269
$h/c=0.211$	264
$h/c=0.317$	262
$h/c=0.342$	259
$h/c=0.458$	251

With respect to the separation from the top of the wheel, it is interesting to notice that in the high wheel drag phase the separation is even further delayed due to the downwash that the top edge vortex generates over the top of the wheel in this situation. Figures 6 and 7 show that this leads to further suction downstream of the crown of the wheel and this increased suction is maintained throughout the top part of the wake until $\theta<180$ deg. At high ride heights the wheel drag actually thus increases, the more the separation from the top of the wheel is delayed. This counterintuitive observation, which contradicts conclusions from 2D cylinder flow, reveals that for a wheel with relative low aspect ratio the secondary flow around the wheel side edges dominates the primary 2D flow over the top [31].

Whereas the previously discussed variations in wheel drag could clearly be coupled to characteristics of the pressure distributions on the wheel surface and the governing mechanisms could be derived from the additional experimental results, it is more difficult to pinpoint the flow physics that cause the reduction in wheel drag in region IV for decreasing ride height. The separation from the top of the wheel on its own would in fact lead to a drag increase in this region. It is however expected that the topological changes in the lower part of the wheel wake, shown in Fig. 5, are partly responsible for this wheel drag reduction. From this figure it can be concluded that at low ride heights the lower edge vortex (feature "C") replaces the downstream part of the contact patch "bow wave" (feature "D"). At these low ride heights the lower edge vortex has retarded and grown in circumference and it is possibly close to breakdown or has even burst. This weaker vortex implies less interaction in the lower wheel wake and thus, in a similar way as for the interaction in the upper wake in the high wheel drag phase, less suction in this area, leading to a reduction in wheel drag.

Second, the channeling effect also potentially reduces the wheel drag further in this region. At low ride heights the wing flow has less possibility to expand in vertical direction due to the close proximity to the ground; this means that a larger part of the flow has to be diverged into the channel between the wheels or around them. This implies that a larger area of the front of the wheel will be exposed to increased suction, and thus that the wheel drag will be lower. The available experimental pressure data is insufficient to confirm this effect, but CFD analysis during the research [28] has revealed that the stagnation position on the wheel lays indeed further away form the overall symmetry plane for the lower ride heights, providing evidence for the increased flow deflection in horizontal direction.

Finally, the difference between the wheel drag level in the hysteresis regions V and VI can be explained with the help of the wing flow field that will be further discussed in Secs 5.1–5.6. The increasing ride height region, VI, is characterized by a lower wing downforce (see Fig. 4(*b*)) than the decreasing ride height branch, V. The loss in downforce is a result of large scale separation from the wing surfaces. The downstream effect of this retarded flow with lower total pressure on the wheel is a weakening of the

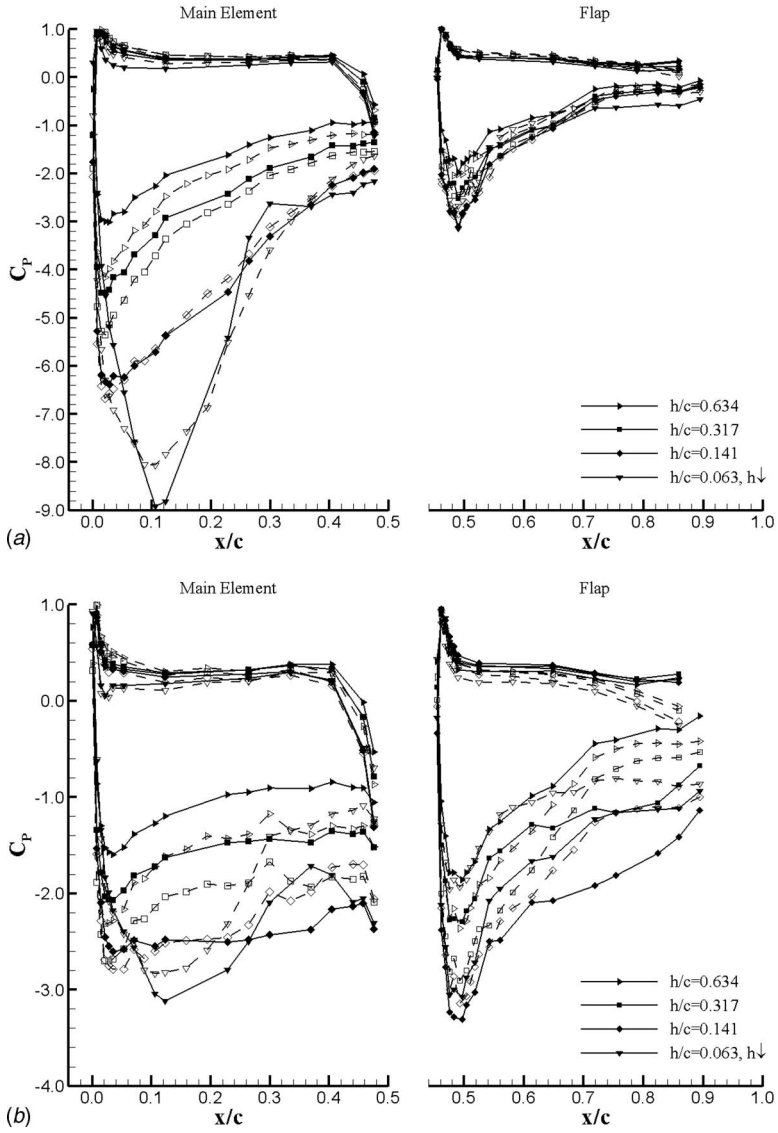

Fig. 10 Wing pressure distributions along the main element and flap for a range of ride heights; for the isolated wing (dotted lines, open symbols) and the wing-wheel configuration (solid lines, black symbols); (a) at the centre line, (b) at the tip 25 mm inboard of the port side endplate

channeling effect and thus less suction on the lower inboard upstream part of the wheel. For the decreasing ride height region the wing separation is much reduced and the stronger channeling effect therefore leads to a lower wheel drag than for the increasing ride height branch. Tests at a dynamic pressure equivalent to 20 m/s instead of 30 m/s showed that the hysteresis region boundary moves to higher ride heights when the test velocity is reduced. This is consistent with the above explanation, since the lower Re number will mean that the wing boundary layer is less resilient to the adverse pressure gradient and thus separates earlier from the surface, or at a higher ride height for a lower freestream velocity.

5 Effects of the Wheels on the Wing Aerodynamics

Not only does the wing influence the downstream located wheels, but the aerodynamic interaction also acts in the opposite direction. Figures 4(*b*)–4(*d*) show the effect that the wheels have on the wing performance in comparison to the isolated wing case. At higher ride heights the wing downforce is reduced due to the presence of the wheels, but below approximately $h/c=0.15$ it has increased disproportionally and reaches a 16.2% higher value at $h/c=0.067$. This section will once more use experimental results to derive the governing force enhancing and limiting mechanisms, but first the force behavior for the isolated wing will be discussed for reference.

5.1 Governing Mechanisms for Isolated Wing in Ground Effect. The force behavior of the isolated wing in ground effect is the result of a ride height dependent balance between two force enhancing and two force limiting mechanisms [23,28]. The downforce is primarily enhanced by the channeling effect. This influence increases with reducing ride height and is equivalent to how a diffuser produces downforce [32]. Evidence for this can be found in the location of the suction peak on the main element, which moves downstream below $h/c=0.141$, from the point of maximum curvature to the lowest point, as can be concluded from Fig. 10. The channeling effect is always active, but mainly affects the suction side of the main element (the suction on the main element increases 94% from $h/c=0.634$ to 0.063 in contrast to the 36% increase on the flap), leading to a forward movement of the center of pressure relative to a wing in freestream conditions.

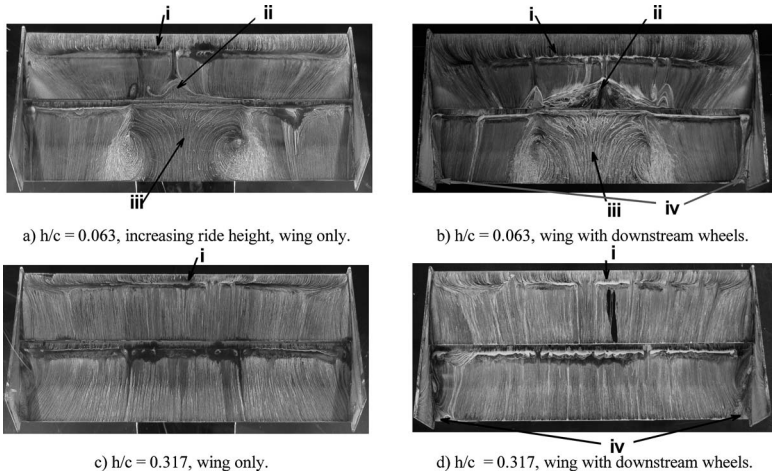

Fig. 11 On-surface flow visualization on the suction surfaces of the wing for the isolated wing and for the combined case with downstream wheels; flow direction from top to bottom; shown features are (i) LE separation bubble, (ii) main element TE separation, (iii) flap full chord separation, and (iv) tip separation

The exponential growth in downforce with reducing ride height in Fig. 4(*b*) up to approximately $h/c=0.25$ is the combined result of a second force enhancing mechanism that acts parallel to the channeling effect. This is the lower edge vortex effect, which refers to the additional suction on the underside of the main element and flap close to the tip that is caused by the higher velocities resulting from the imprint of the lower edge tip vortex. This vortex effect also becomes stronger with decreasing ride height, due to the increasing pressure difference between the suction side of the wing and the outside of the endplate. However the influence of this effect diminishes at the local maximum in the downforce, around $h/c=0.23$, as the increasing adverse pressure gradient downstream causes the vortex to dilute and breakdown, reducing the additional suction on the wing tips. From the small reduction in downforce up to the local minimum in downforce just below this ride height it can be concluded that the lower vortex loses its beneficial effect quicker than the channeling effect increases in strength.

Below this ride height the channeling effect is once more the only active force enhancing mechanism, which now in balance with the vortex dilution, causes a fairly linear growth in downforce with ride height reduction. The final decay in downforce growth is the result of full vortex bursting underneath the flap, which negatively influences the suction on the tips due to the velocity reduction and additional blockage. The vortex (dilution and) breakdown is still close to equilibrium with the channeling effect, but it is the second force limiting mechanism, flow separation, that causes the downforce to drop off at low ride heights. At such conditions the center part of the main element of the wing on the suction side experiences trailing edge separation (see Fig. 11, feature "ii"), which moves progressively upstream, resulting in the downforce reduction. This once more resembles diffuser behavior, leading to a much more gradual downforce reduction than what would be experienced in freestream due to wing stall as a result of leading edge separation. The reason for the lower downforce for the increasing ride height branch of the hysteresis zone compared with the decreasing branch is the full chord center span flap separation, which can be seen for $h/c=0.063$ in Fig. 11 as feature "iii." This only occurs for a startup at low ride heights and perseveres when the wing is moved upwards until the upper boundary of the hysteresis region is reached, at which the flow is able to stay attached from the flap leading edge onwards and thus leads to a sudden increase in downforce. For the decreasing branch however the boundary layer is resilient enough to stay attached; this difference in boundary layer behavior is at the heart of the hysteresis effects. In Secs. 5.2–5.5 it will be discussed how each of the mechanisms is affected by the presence of the wheels.

5.2 Modified Channeling Effect. The channeling effect, which causes an increase in acceleration on the underside of the wing, shows a modified behavior due to the presence of the wheels. Analysis of PIV results at center span below the wing main element, (see Fig. 12) reveals that at $h/c=0.106$ the velocity reaches a 3.3% higher value with the wheels added, whereas at $h/c=0.317$ this is 3.8% lower. Since these measurements have been taken at center span, where the 3D influences of the tip flow are minimal, it can be concluded that this is the result of modification of the channeling effect by the wheels, showing an increase at low and reduction at high ride heights.

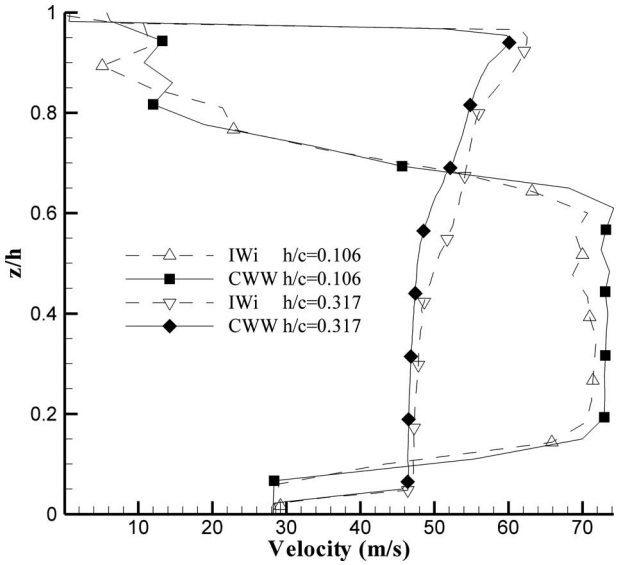

Fig. 12 In plane velocity for the symmetry plane underneath the main element of the wing at $x/c=0.112$, derived from PIV results for the isolated and combined wing case at two different ride heights. Parallax effects are responsible for the velocity deficit in the data close to the ground and close to the wing (especially for $h/c=0.106$), because of blockage of the laser sheet.

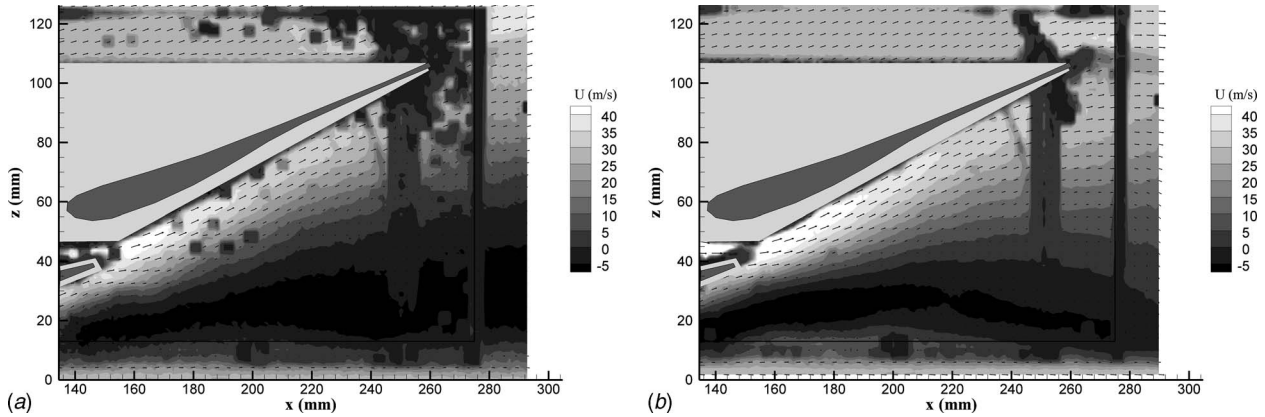

Fig. 13 PIV velocity contours in a plane 25 mm inboard of the port side endplate; (a) the isolated wing, (b) in combination with the wheels for $h/c=0.063$; the wing profiles are visualized in dark gray and the shadow areas in light gray

It is obvious that the wheels, in case of a positive overlap, create a further converging step with increased blockage to the channel between the wheels and wing, leading to additional acceleration around the upstream corner of the wheel. However the PIV results showed that relative to the isolated wing case the channeling effect is enhanced at low ride heights, but reduced at higher. The explanation for this can be found in the movement direction of the sidewalls of the wheels. Below the wheel axis the sidewalls move downstream and therefore help to extract the flow from the channel, enhancing the effect. In contrast above the wheel axis the wheel rotation leads to an upstream movement of the sidewalls, which hinders the channel flow and thus reduces the suction on the main element underside.

Just as for the isolated wing, it is to be expected that the channeling effect mainly affects the suction side of the main element due to the closest proximity to the ground. Figure 10 confirms this statement by showing that the suction peak increases 194% in value from the highest to the lowest ride height, reaching a 11.6% higher value than for the isolated wing and thus confirming the enhancement at low ride heights. Furthermore at the highest ride height the suction is 27% lower than for the isolated wing, showing the effect of the reduced channeling effect at these conditions. The influence of the channeling effect on the flap is however clouded by the effects of the other mechanisms, but the variation at high ride heights is much less whereas at low ride heights it is bigger than for the isolated wing. From the results it is difficult to determine at which ride height the channeling effect for the combined case switches between these two states. Nevertheless, Fig. 10 shows that at $h/c=0.141$ the center span suction on the main element is very similar for the isolated and combined case; based on this it is expected that the channeling effect is enhanced below $h/c=0.141$ and reduced above this height.

5.3 Separation Effects. The main force limiting effects due to separation for the combined configuration are similar to for the isolated wing case. At the lowest ride heights trailing edge separation from the suction side of the main element of the wing reduces the downforce. This separation can once more be seen in Fig. 11 (feature "ii"), which also shows the full chord center span separation from the flap suction side (feature "iii") that occurs for the increasing ride height branch. Both these separation effects start occurring at lower ride heights than for the isolated wing, because the enhanced channeling effect at these ride heights postpones separation due to a more gentle pressure recovery. For all conditions the flap also shows a separation bubble near the leading edge (feature "i"), due to off-surface transition. This feature has not changed noticeably due to the presence of the wheels and more information on this for the wing in isolation can be found in Ref. [23].

Additionally, the wheels induce a new form of separation at the flap tips (feature "iv"), resulting from the adverse pressure gradient caused by the increased blockage from the downstream wheels. This tip separation is present for all ride heights, as can be seen for two examples in Fig. 11, but is largest when the flap is located closest to the wheel, around $h/c=0.24$ (with the flap trailing edge at the same height as the wheel axis). The imprint of this separated zone on the wing tip flap pressures is difficult to recognize in Fig. 10, because the pressure taps are located too far inboard. However, this separated zone has a tempering influence on both the lower edge vortex effect and on the vortex dilution/breakdown effect as will be discussed next.

5.4 Vortex Effects. The lower edge vortices influence the downforce for the isolated wing in several ways; a local increase in suction at the tip enhances the downforce for medium and higher ride heights, whereas vortex dilution leads to the local drop in downforce, vortex breakdown at even lower ride heights is responsible for the start of the decay in downforce. For the combined configuration with the wheels present all these effects are reduced, because the separated zones at the flap tips shield the wing surface from the imprints of these effects. Figure 4(*b*) shows that the combined configuration has no local drop in downforce due to vortex dilution. This can on one hand be related to a reduced positive influence of the lower vortex effect at higher ride heights and therefore to a smaller drop off in downforce relative to the continuing growth resulting from the channeling effect, or on the other hand to less negative influence of the vortex dilution.

It is expected that vortex dilution and breakdown become prominent for the combined case from $h/c=0.113$ downwards, because from here the downforce growth reduces and becomes more linear. Additional, nonpresented PIV data, shows that the lower edge vortices are still strong and coherent at $h/c=0.211$, but are falling apart at $h/c=0.106$. Nevertheless, even when the vortices start breaking up, their negative influence is still less apparent than for the isolated wing case, because the vortex structures are diverted downwards, away from the wheel surface due to the wheel rotation. This can be seen in Fig. 13, where the areas with reversed flow are the remains of the burst lower edge vortex, which are weaker and appear lower when the wheels are present (Fig. 13(*b*)).

5.5 Wheel Circulation Effect. The modified channeling effect mainly influences the central part of the suction side of the main element of the wing, but finally an additional force enhancing mechanism needs to be discussed that affects the tips most and primarily the flap tips. The wheel circulation can be considered to locally act as a further wing element downstream of the flap, which has a beneficial effect when the flap is located below the

wheel axis height. Just as for multiple element wing configurations [33], the circulation from the wheel will induce favorable conditions for the upstream elements, resulting in a local increase in downforce. At high ride heights the wheel circulation will have a relative negative influence, similarly to when a flap would be positioned at the pressure side of an upstream element.

5.6 Summary of Wing Downforce Regions. Figure 4(*b*) shows that at higher ride heights the downforce for the combined case is considerably lower than for the isolated wing, which is a result of the reduced channeling effect, the negative wheel circulation effect, and the flap tip separation. In the first two force regions the center of pressure location, which lies further downstream than for the isolated wing, moves faster forward (see Fig. 4(*d*)). This is the result of a smaller growth in downforce from the flap tips relative to the isolated wing case, because the separated regions at the tips grow in size. Interestingly, the drag is only marginally lower for the combined case than for the isolated wing, which is a direct consequence of the difference in pressure distributions on the wing elements. With the wheels present the flap carries a larger part of the loading, which is reflected in the downstream center of pressure location, and due to the orientation of the flap this contains a larger drag component.

The end of force region II is characterized by a sudden increase in downforce that cannot be observed for the isolated wing. The switch in wheel circulation effect from having a negative to a positive influence plays a role in this. However, it is expected that the top edge vortex trajectories are more important, because this change in downforce coincides with the sudden change in wheel drag. The downstream blockage increases when the vortices move from the crown to the inside of the wheel, which will enhance the channeling effect and thus the downforce from the wing. This affects the flap tips most, due to the location of the added blockage, which is confirmed by the downstream movement of the center of pressure at the sudden increase in downforce.

For lower ride heights the wing downforce increases more with the wheels present and reaches a higher downforce level before the decay due to surface separation sets in. This is the combined result of the enhanced channeling effect, the positive wheel circulation effect and the reduced influence of vortex breakdown and delayed trailing edge separation. At the upper boundary of the hysteresis zone the downforce starts dropping off due to center span separation from the main element of the wing, but there is no plateau of constant downforce prior to this, because of the still dominant force enhancing mechanisms. The difference between the increasing and decreasing ride height branch is, for the combined case, also the result of full chord flap separation at center span, which exists when the flow is started with the wing at a low ride height.

6 Conclusions

The results presented in this paper show that the aerodynamic performance of a wing is affected by the presence of the wheels and that vice versa the wheel drag depends on the wing position. The variation in force coefficients confirms that data from studies of isolated components does not always lead to reliable conclusions for the combined configuration. It also gives an idea of the scope of the performance improvements that can be made by optimizing the wing in the presence of surrounding components. Furthermore, the influence of the wheels on the total vehicle drag is estimated to be as much as 40% [34], implying that the potential variation in wheel drag that was seen during this research will have a significant influence on the overall performance.

At low ride heights the wing downforce is increased and the wheel drag reduced relative to for the components on their own, but at higher ride heights the opposite happens. The trajectories of the top edge vortices are the dominant characteristics that affect the aerodynamic performance and it is crucial to prevent that these go over the crown of the wheels when maximum wing downforce and minimum wheel drag are required. For most practical racecar applications this should be achievable, as the critical ride height is approximately $h/c=0.35$ and front wings typically act closer to the ground to benefit from the ground effect.

This research has stressed the importance of modeling the flow problem, which heavily relies on vortex interaction, with all the relevant components included. A parametrical study, examining the influence of wing-wheel gap and overlap, has been conducted at the same time of this work and is to be presented in a separate paper. The mechanisms introduced in this paper can be used to consistently explain the force behavior for different gap and overlap settings. Finally, the influence of wheel steer and yaw of the configuration relative to the wind direction will have a large effect on the vortex interaction as well and are therefore potential subjects for future research.

Acknowledgment

The authors would like to thank the School of Engineering Sciences and Honda Racing F1 for sponsoring and supporting the research that is presented in this paper.

Nomenclature

c = total combined wing chord, 284 mm
C_D = drag coefficient
C_L = downforce coefficient
C_M = pitching moment coefficient
C_P = pressure coefficient
D = wheel diameter, 313.9 mm
G = gap
h = wing ride height
h_{EP} = height from ground to top of endplate, h +110 mm
h_{FTE} = height from ground to the trailing edge of the flap
$h\downarrow$ = decreasing ride height
O = overlap
Q = second invariant of the velocity gradient tensor, measurement of vorticity
x = horizontal coordinate in flow direction
x/c_{CoP} = nondimensionalized wing center of pressure location in x-direction
y = horizontal coordinate perpendicular to the flow direction
z = vertical coordinate

Greek symbols

θ = wheel rotation angle, anticlockwise from the upstream point when looking from the left (see Fig. 2)

Abbreviations

2D = two-dimensional
3D = three-dimensional
CFD = computational fluid dynamics
CWW = combined wing wheel configuration
IWh = isolated wheel configuration
LDA = laser Doppler anemometry
PIV = particle image velocimetry
TE = trailing edge
ZOC = Zero-Operate-Calibrate pressure measurement system

References

[1] Zhang, X., Toet, W., and Zerihan, J. D. C., 2006, "Ground Effect Aerodynamics of Race Cars," Appl. Mech. Rev., **59**, pp. 33–49.
[2] Katz, J., 2006, "Aerodynamics of Race Cars," Annu. Rev. Fluid Mech., **38**, pp. 27–63.
[3] Fackrell, J. E., 1974, "The Aerodynamics of an Isolated Wheel Rotating in Contact With the Ground," Ph.D. thesis, University of London, London, UK.
[4] Fackrell, J. E., and Harvey, J. K., 1975, "The Aerodynamics of an Isolated

Road Wheel," *Proceedings of the 2nd AIAA Symposium of Aerodynamics of Sports and Competition Automobiles*.
[5] Fackrell, J. E., and Harvey, J. K., 1973, "The Flow Field and Pressure Distribution of an Isolated Road Wheel," *Advances in Road Vehicle Aerodynamics*, BHRA Fluid Engineering.
[6] Morelli, A., 1969, "Aerodynamic Effects on an Automobile Wheel," MIRA Technical Report Translation, 47/69. (Translated in Italian), "Aerodynamic Effects on the Car Wheel," ATA Review, **22**(6), pp. 281–288.
[7] Stapleford, W. R., and Carr, G. W., 1970, "Aerodynamic Characteristics of Exposed Rotating Wheels," Report 1970/2, Moter Industry Research Association, Nuneaton, UK.
[8] Cogotti, A., 1983, "Aerodynamic Characteristics of Car Wheels," Int. J. Veh. Des., **33**, pp. 173–196.
[9] Wäschle, A., Cyr, S., Kuthada, T., and Wiedemann, J., 2004, "Flow Around an Isolated Wheel—Experimental and Numerical Comparison of Two CFD Codes," SAE Technical Paper No. 2004-01-0445.
[10] Axon, L., Garry, K., and Howell, J., 1998, "An Evaluation of CFD for Modelling the Flow Around Stationary and Rotating Wheels," SAE Publication No. 980032.
[11] Skea, A. F., Bullen, P. R., and Qiao, J., 2000, "CFD Simulations and Experimental Measurements of the Flow Over a Rotating Wheel in a Wheel Arch," SAE 2000 World Congress, Detroit, MI, Mar. 6–9, SAE Publication No. 2001-01-0487, reprinted from Vehicle Aerodynamics (SP-1524).
[12] Knowles, R., Saddington, A., and Knowles, K., 2002, "Simulation and Experiments on an Isolated Racecar Wheel Rotating in Ground Contact," Fourth MIRA International Vehicle Conference, Gaydon, UK.
[13] Basara, B., Beader, D., and Przulj, V., 2000, "Numerical Simulation of the Air Flow Around a Rotating Wheel," Third MIRA International Vehicle Aerodynamics Conference, Rugby, UK.
[14] McManus, J., and Zhang, X., 2006, "A Computational Study of the Flow Around an Isolated Wheel in Contact With the Ground," ASME Trans. J. Fluids Eng., **128**(3), pp. 520–530.
[15] Zerihan, J. D. C., 2001, "An Investigation into the Aerodynamics of Wings in Ground Effect," Ph.D. thesis, Aerodynamics and Flight Mechanics Department, University of Southampton, Southampton, UK.
[16] Zerihan, J. D. C., and Zhang, X., 2000, "Aerodynamics of a Single Element Wing in Ground Effect," J. Aircr., **37**(6), pp. 1058–1064.
[17] Zerihan, J. D. C. and Zhang, X., 2001, "A Single Element Wing in Ground Effect; Comparisons of Experiments and Computation," AIAA Technical Report No. AIAA 2001-0423.
[18] Zhang, X., and Zerihan, J. D. C., 2003, "Aerodynamics of a Double-Element Wing in Ground Effect," AIAA J., **41**(6), pp. 1007–1016.
[19] Jeffrey, D., Zhang, X., and Hurst, D. W., 2000, "Aerodynamics of Gurney Flaps on a Single-Element High-Lift Wing," J. Aircr., **37**(2), pp. 295–301.
[20] Jeffrey, D., Zhang, X., and Hurst, D. W., 2001, "Some Aspects of the Aerodynamics of Gurney Flaps on a Double Element Wing," ASME Trans. J. Fluids Eng., **123**, pp. 99–104.
[21] Zerihan, J. D. C., and Zhang, X., 2001, "Aerodynamics of Gurney Flaps on a Wing in Ground Effect," AIAA J., **39**(5), pp. 772–780.
[22] Zhang, X., Zerihan, J. D. C., Ruhrmann, A., and Deviese, M., 2002, "Tip Vortices Generated by a Wing in Ground Effect," 11th International Symposium: Applications of Laser Techniques to Fluid Mechanics.
[23] Mahon, S. A., 2005, "The Aerodynamics of Multi-Element Wings in Ground Effect," Ph.D. thesis, Aerodynamics and Flight Mechanics Department, University of Southampton, Southampton, UK.
[24] Diasinos, A., Barber, T. J., Leonardi, E., and Gatto, A., 2004, "The Interaction of a Rotating Cylinder and an Inverted Aerofoil in Ground Effect: Validation and Verification," 24th Applied Aerodynamics Conference, San Francisco, CA, AIAA Paper No. 2006-3325.
[25] Katz, J. and Dykstra, L., 1992, "Effect of Wing/Body Interaction on the Aerodynamics of Two Generic Racing Cars," SAE Technical Report No. SAE 92-0349.
[26] Soso, M. D., and Wilson, P. A., 2006, "Aerodynamics of a Wing in Ground Effect in Generic Racing Car Wake Flows," Proc. Inst. Mech. Eng., Part D (J. Automob. Eng.), **220**, pp. 1–13.
[27] Dominy, R. G., Ryan, A., and Sims-Williams, D. B., 2000, "The Influence of Slipstreaming on Sports Prototype Race Car Performance," Proc. Inst. Mech. Eng., Part D (J. Automob. Eng.), **214**(8), pp. 887–894.
[28] Van den Berg, M. A., 2007, "Aerodynamic Interaction of an Inverted Wing With a Rotating Wheel," Ph.D. thesis, Aerodynamics and Flight Mechanics Department, University of Southampton, Southampton, UK.
[29] Moffat, R. J., 1982, "Contributions to the Theory of Single-Sample Uncertainty Analysis," ASME Trans. J. Fluids Eng., **140**, pp. 250–260.
[30] Jeong, J., and Hussain, F., 1995, "On the Identification of a Vortex," ASME J. Fluid Mech., **285**, pp. 69–94.
[31] Zdravkovich, M. M., Flaherty, A. J., Pahle, M. G., and Skelhorne, I. A., 1998, "Some Aerodynamic Aspects of Coin-Like Cylinders," ASME J. Fluid Mech., **360**, pp. 73–84.
[32] Senior, A. E., and Zhang, X., 2001, "The Force and Pressure of a Diffuser-Equipped Bluff Body in Ground Effect," ASME J. Fluids Eng., **123**(1), pp. 105–111.
[33] Smith, A. M. O., 1975, "High-Lift Aerodynamics," J. Aircr., **12**(6), pp. 501–530.
[34] Agathangelou, B. and Gascoyne, M., 1998, "Aerodynamic Design Considerations of a Formula 1 Racing Car," SAE Publication No. 980399.

Numerical Investigation of Combined Effects of Rarefaction and Compressibility for Gas Flow in Microchannels and Microtubes

Xiaohong Yan

Qiuwang Wang[1]
e-mail: wangqw@mail.xjtu.edu.cn

State Key Laboratory of Multiphase Flow in Power Engineering,
Xi'an Jiaotong University,
Xi'an, Shaanxi 710049, China

In this paper, first, the Navier–Stokes equations for incompressible fully developed flow in microchannels and microtubes with the first-order and second-order slip boundary conditions are analytically solved. Then, the compressible Navier–Stokes equations are numerically solved with slip boundary conditions. The numerical methodology is based on the control volume scheme. Numerical results reveal that the compressibility effect increases the velocity gradient near the wall and the friction factor. On the other hand, the increment of velocity gradient near the wall leads to a much larger slip velocity than that for incompressible flow with the same value of Knudsen number and results in a corresponding decrement of friction factor. General correlations for the Poiseuille number (fRe), the Knudsen number (Kn), and the Mach number (Ma) containing the first-order and second-order slip coefficients are proposed. Correlations are validated with available experimental and numerical results. [DOI: 10.1115/1.3215941]

Keywords: friction factor, rarefaction effect, compressibility effect, general correlations

1 Introduction

Microchannels and microtubes are basic elements of microfluidic devices and the gas flow in these channels has been extensively studied in the past decade due to their simple geometric configuration, rich physics, and wide applications. A number of experimental, analytical, and numerical studies have revealed that the flow behavior for gas flow in microchannels and microtubes deviates from the classical theory in conventional-scale channels. Rarefaction and compressibility are two of the dominant effects that are responsible for the deviation.

The rarefaction effect is an important factor. Analytical solutions [1–3] derived from Navier–Stokes equations with the first-order slip boundary condition were presented for various geometries of the microchannels in the slip region ($Kn < 0.1$) and it agreed well with the numerical results [4,5]. The experimental results [6–8] were also in rough agreement with the analytical solutions. It is widely accepted in the past decade that the first-order slip boundary condition is accurate when the Knudsen number is less than 0.1. Hence, above studies were based on the first-order slip boundary condition. However, experimental studies [9] revealed that the first-order slip boundary condition was not so accurate when the Knudsen number is larger than 0.05. Many researchers devoted to develop more accurate slip boundary conditions. Sreekanth [10] experimentally investigated slip flow through long circular microtubes and proposed a second-order slip boundary condition according to the pressure distribution along the microtube. Ewart et al. [11] proposed a second-order slip boundary condition according to the experimentally measured mass flow rate. As yet, no consensus has been reached on the correct form of higher-order approach and the magnitude of the second-order slip coefficient exhibits large discrepancy. The review of slip boundary conditions developed by different researchers was done by Barber and Emerson [12].

The compressibility effect is another important factor for gas flow in microtubes even for very low velocity (low Mach number), which results in the nonlinear pressure distribution and the increment of friction factor. Guo and co-workers [13,14] numerically examined the compressibility effect on the friction factor of gas flow in smooth microtubes. They concluded that the pressure gradient and the flow acceleration increased the dimensionless velocity gradient at the wall surface and consequently increased the local friction factor compared with that for conventional-scale tubes. They also indicated that the neglect of the flow compressibility effect may be one of the reasons for the discrepancy of the experimental results of different authors. Li et al. [15] solved the coupled momentum and energy equations for microtubes with a perturbation method and a correlation between the Poiseuille number and the Mach number was proposed. Du et al. [16] experimentally studied the compressibility effect on the friction factor using a tube-cutting method. Asako and co-workers [17,18] numerically investigated the compressibility effect for gas flow in parallel plate microchannels and microtubes. Correlations for the Poiseuille number and the Mach number were obtained ($Ma < 0.5$). Turner et al. [8] investigated the effects of rarefaction, compressibility, and roughness for gas flow in rectangular microchannels systematically. The experimental data ($Ma < 0.4$) were curve fitted and a correlation for the Poiseuille number and the Mach number was proposed. Morini et al. [19] compared three different methods to calculate the friction factor for incompressible and compressible flows and analyzed the limitations and advantages of each method. Tang et al. [20] studied the gas flow in rectangular microchannels and microtubes experimentally. A correlation was proposed for the evaluation of the compressibility effect ($Ma < 0.4$).

The rarefaction and compressibility effects always act simultaneously in actual microsystems. Sun and Faghri [21] simulated the gas flow in microchannels with both rarefaction and compressibility effects using the direct simulation Monte Carlo (DSMC) method. They concluded that the compressibility effect dominated at large Reynolds number and the rarefaction effect dominated at small Reynolds number. Jain and Lin [22] simulated the gas flow in microchannels for a range of inlet conditions. The results showed that the friction factor might be larger than that for

[1]Corresponding author.

Manuscript received November 14, 2008; final manuscript received July 2, 2009; published online September 17, 2009. Assoc. Editor: Joseph Katz.

conventional-scale channels when the inlet Mach number and Reynolds number were large while the friction factor might be less than the conventional value for small inlet Mach number and Reynolds number. Because rarefaction and compressibility effects contrast each other, the scatter of the friction factor data for gaseous flows may be large and the study of the combined effects is important. To our best knowledge, the only relevant study on the friction factor correlation by considering the combined effects of rarefaction and compressibility is by Hong et al. [23] who proposed that the friction factor correlations for gas flow in slip flow regime as a function of Mach number and Knudsen number. First-order slip boundary condition was employed in their study. However, the range of Knudsen number was very small ($0.0035 < \mathrm{Kn} < 0.0175$) by considering the applicability of the first-order slip boundary condition and the tangential momentum accommodation coefficient was assumed to be unity in their study. Barber and Emerson [12] summarized different first-order and second-order slip boundary and used a generalized second-order slip formulation for analysis.

In this paper, generalized second-order slip formulation is used for the analysis of combined effects of rarefaction and compressibility for gas flow in microchannels and microtubes. There is no assumption of the tangential momentum accommodation coefficient. General correlations for Poiseuille number, Knudsen number, and Mach number are proposed. It is expected that these correlations could be easily extended to other slip boundary conditions with the development of more accurate slip model. The aim of this paper is to provide some fundamental insight into the friction factor for gas flow in microchannels and microtubes.

2 Governing Equations

The schematic microchannel or microtube is shown in Fig. 1. Inlet and outlet pressures p_{in} and p_e are given. The wall temperature is isothermal and which is equal to the fluid temperature at the inlet, which is fixed at 300 K. Nitrogen gas is employed with a specific heat ratio $\gamma=1.4$, a Prandtl number $\mathrm{Pr}=0.7$, a viscosity coefficient $\mu=1.77\times10^{-5}$ Pa s, a specific heat capacity $c_p=1040$ J/(kg K), and a gas constant $R=297$ J/(kg K). The governing equations [24] can be expressed as follows:

$$\mathrm{div}(\rho \boldsymbol{U}) = 0 \tag{1}$$

$$\mathrm{div}(\rho \boldsymbol{U} u) = -\frac{\partial p}{\partial x_1} + \mathrm{div}(\mu \mathbf{grad} u) + \frac{\mu}{3}\frac{\partial}{\partial x_1}(\mathrm{div}\boldsymbol{U}) \tag{2}$$

$$\mathrm{div}(\rho \boldsymbol{U} v) = -\frac{\partial p}{\partial x_2} + \mathrm{div}(\mu \mathbf{grad} v) + \frac{\mu}{3}\frac{\partial}{\partial x_2}(\mathrm{div}\boldsymbol{U}) \tag{3}$$

$$\mathrm{div}(\rho \boldsymbol{U} T) = \mathrm{div}\left(\frac{k}{c_p}\mathbf{grad} T\right) + \frac{1}{c_p}\left(u\frac{\partial p}{\partial x_1} + v\frac{\partial p}{\partial x_2}\right) + \phi \tag{4}$$

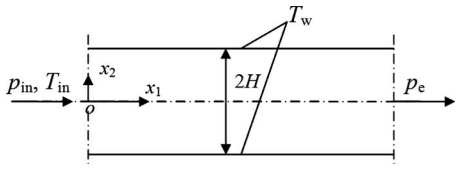

Fig. 1 Sketch of the microchannel and the microtube

For microchannels $x_1=x$ and $x_2=y$, u is the velocity along the x-direction, v is the velocity along the y-direction, and

$$\phi = \frac{\mu}{c_p}\left(2\left[\left(\frac{\partial u}{\partial x_1}\right)^2 + \left(\frac{\partial v}{\partial x_2}\right)^2\right] + \left(\frac{\partial u}{\partial x_2} + \frac{\partial v}{\partial x_1}\right)^2 - \frac{2}{3}\left(\frac{\partial u}{\partial x_1} + \frac{\partial v}{\partial x_2}\right)^2\right)$$

For microtubes $x_1=x$ and $x_2=r$, u is the velocity along the x-direction, v is the velocity along the r-direction, and

$$\phi = \frac{\mu}{c_p}\left(2\left[\left(\frac{\partial u}{\partial x_1}\right)^2 + \left(\frac{v}{x_2}\right)^2 + \left(\frac{\partial v}{\partial x_2}\right)^2\right] + \left(\frac{\partial u}{\partial x_2} + \frac{\partial v}{\partial x_1}\right)^2 - \frac{2}{3}\left(\frac{\partial u}{\partial x_1} + \frac{1}{x_2}\frac{\partial (x_2 v)}{\partial x_2}\right)^2\right)$$

The equation of state for the ideal gas can be expressed as

$$p = \rho R T \tag{5}$$

According to the Maxwell's slip flow theory, the gas velocity at the wall is not equal to the wall velocity. At the wall, the normal velocity is equal to zero and the tangential velocity is equal to the slip velocity [12], which was defined as

$$u_{\mathrm{slip}} = \frac{2-\sigma}{\sigma}\lambda\frac{\partial u}{\partial \boldsymbol{n}}\bigg|_{\mathrm{wall}} + \left(\frac{3+j}{4}\right)\left(\frac{\mu}{\rho T}\right)\frac{\partial T}{\partial x_1}\bigg|_{w} \tag{6}$$

where $\boldsymbol{n}$ is the inner normal direction of the wall and j is the rotational freedom. For nitrogen gas, the translational freedom is 3 and the rotational freedom is 2. The second item of Eq. (6) indicates the effect of thermal creep. The wall is isothermal for this study so the item is not considered in this study. A similar expression was derived to describe the temperature jump at the solid-gas interface [12]

$$T_{\mathrm{slip}} = \frac{2-\sigma_T}{\sigma_T}\left[\frac{2\gamma}{\gamma+1}\right]\frac{\lambda}{Pr}\frac{\partial T}{\partial \boldsymbol{n}}\bigg|_{\mathrm{wall}} \tag{7}$$

Equations (6) and (7) are the standard first-order velocity slip and temperature jump boundary conditions, respectively. During these years, many second-order velocity slip boundary conditions were proposed and the general expression for microchannels and microtubes [12] can be written as

$$u_{\mathrm{slip}} = A_1\lambda\frac{\partial u}{\partial \boldsymbol{n}}\bigg|_{\mathrm{wall}} - A_2\lambda^2\frac{\partial^2 u}{\partial \boldsymbol{n}^2}\bigg|_{\mathrm{wall}} \tag{8}$$

In some papers, such as Ewart et al. [11], the second-order velocity slip boundary condition for microtubes is written as

$$u_{\mathrm{slip}} = A_1'\lambda\frac{\partial u}{\partial \boldsymbol{n}}\bigg|_{\mathrm{wall}} - A_2'\lambda^2\frac{1}{n}\frac{\partial}{\partial \boldsymbol{n}}\left(n\frac{\partial u}{\partial \boldsymbol{n}}\right)\bigg|_{\mathrm{wall}} \tag{9}$$

where λ is the mean free path of the gas and σ is the tangential momentum accommodation coefficient. σ_T is the thermal accommodation coefficient and it is assumed to be the unity in this study. A_1 and A_2 are the first-order and second-order slip coefficients, respectively, and the effect of tangential momentum accommodation coefficient is combined into these slip coefficients. In this paper, Eq. (8) is used as the general expression of velocity slip boundary condition and coefficients of Eq. (9) is converted into that of Eq. (8).

The boundary conditions of this problem are summarized as follows: inlet is $p=p_{\mathrm{in}}$ and $T_{\mathrm{in}}=300$ K, outlet is $p=p_e$, symmetry plane is $\partial u/\partial x_2=0$, and wall is $u=u_{\mathrm{slip}}$, $T=T_{\mathrm{slip}}$, $v=0$, and $T_w=300$ K.

The velocity at the inlet is first assumed at the start of the numerical simulation and a pressure at the inlet can be obtained through a round of numerical calculation and the inlet velocity is then updated according to the actual inlet pressure p_{in}. Finally, the velocity field in the channel will be steady.

The average values over the cross section of the microchannel are defined as

$$\bar{u} = \frac{1}{2H}\int_{-H}^{H} u dx_2, \quad \bar{\rho} = \frac{\int_{-H}^{H}\rho u dx_2}{\int_{-H}^{H} u dx_2}, \quad \bar{T} = \frac{\int_{-H}^{H}\rho u T dx_2}{\int_{-H}^{H}\rho u dx_2} \tag{10}$$

while the average values over the cross section of the microtube are defined as

$$\bar{u} = \frac{1}{\pi H^2}\int_{0}^{H} u \cdot 2\pi x_2 dx_2, \quad \bar{\rho} = \frac{\int_0^H \rho u \cdot 2\pi x_2 dx_2}{\int_0^H u \cdot 2\pi x_2 dx_2},$$

$$\bar{T} = \frac{\int_0^H \rho u T \cdot 2\pi x_2 dx_2}{\int_0^H \rho u \cdot 2\pi x_2 dx_2} \tag{10a}$$

Some dimensionless parameters are defined as

$$\mathrm{Kn} = \frac{\lambda}{2H}, \quad \mathrm{Re} = \frac{\bar{\rho}\bar{u}D_h}{\mu}, \quad \mathrm{Ma} = \frac{\bar{u}}{\sqrt{\gamma R\bar{T}}}, \quad f = \frac{4\cdot\mu\cdot\partial u/\partial x_2|_{\mathrm{wall}}}{\bar{\rho}\bar{u}^2/2} \tag{11}$$

where D_h is the hydraulic diameter. $D_h=4H$ for microchannels and $D_h=2H$ for microtubes.

The control volume scheme is adopted to solve the compressible momentum and energy equations. The pressure and velocity are linked by the SIMPLE algorithm developed by Patankar [25]. The solution domain is confined to the upper half of the microchannel or microtube because of the symmetry.

The Poiseuille number (Po), defined as the product of friction factor (f) and Reynolds number (Re), is usually used to describe the characteristics of laminar flow. The Poiseuille number for compressible gas flow in a microtube with length to diameter ratio of 100 is examined to investigate the effect of mesh size. For the same value of Mach number (Ma=0.3), Poiseuille numbers for different mesh sizes are presented in Table 1. Several combinations of mesh numbers are tested. These meshes are distributed in a uniform manner. It can be seen from Table 1 that the difference in the Poiseuille number between very fine meshes (200×500) and fine meshes (150×300) is 0.52%. Considering the computing time, fine meshes (150×300) are used in the present work.

3 Results and Discussion

3.1 Rarefaction Effect. Previous researchers [1–3] solved the incompressible fully developed flows with the first-order slip boundary condition. Here, we solve the incompressible fully developed flows with the second-order slip boundary condition. The momentum equation is shown as follows:

$$\mathrm{div}(\mu\mathbf{grad}u) = \frac{\partial p}{\partial x_1} \tag{12}$$

Combining with the slip boundary conditions (Eq. (8)), the velocity distribution can be obtained as

Table 1 Effect of mesh size on Poiseuille number (Ma=0.3)

Mesh size	Po	Deviation (%)
50×300	69.634	1.31
100×300	69.887	0.95
150×200	70.108	0.64
150×300	70.193	0.52
150×500	70.265	0.42
200×300	70.478	0.11
200×500	70.559	0

$$u = \frac{D_h^2}{32\mu}\frac{dp}{dx_1}\left[\left(\frac{x_2}{H}\right)^2 - 1 - 4A_1\cdot\mathrm{Kn} - 8A_2\cdot\mathrm{Kn}^2\right] \tag{13}$$

for microchannels and

$$u = \frac{D_h^2}{16\mu}\frac{dp}{dx_1}\left[\left(\frac{x_2}{H}\right)^2 - 1 - 4A_1\cdot\mathrm{Kn} - 8A_2\cdot\mathrm{Kn}^2\right] \tag{13a}$$

for microtubes.

The average velocity is

$$\bar{u} = \frac{D_h^2}{48\mu}\frac{dp}{dx_1}[-1 - 6A_1\cdot\mathrm{Kn} - 12A_2\cdot\mathrm{Kn}^2] \tag{14}$$

for microchannels and

$$\bar{u} = \frac{D_h^2}{32\mu}\frac{dp}{dx_1}[-1 - 8A_1\cdot\mathrm{Kn} - 16A_2\cdot\mathrm{Kn}^2] \tag{14a}$$

for microtubes.

Hence, the local Poiseuille number is

$$\mathrm{Po} = \frac{-\frac{dp}{dx_1}\cdot D_h}{\bar{\rho}\bar{u}^2/2}\cdot\frac{\bar{\rho}\bar{u}D_h}{\mu} = \frac{-\frac{dp}{dx_1}\cdot D_h^2}{\mu\cdot\bar{u}/2} = \frac{96}{1 + 6A_1\cdot\mathrm{Kn} + 12A_2\cdot\mathrm{Kn}^2} \tag{15}$$

for microchannels and

$$\mathrm{Po} = \frac{-\frac{dp}{dx_1}\cdot D_h}{\bar{\rho}\bar{u}^2/2}\cdot\frac{\bar{\rho}\bar{u}D_h}{\mu} = \frac{-\frac{dp}{dx_1}\cdot D_h^2}{\mu\cdot\bar{u}/2} = \frac{64}{1 + 8A_1\cdot\mathrm{Kn} + 16A_2\cdot\mathrm{Kn}^2} \tag{15a}$$

for microtubes.

The effect of rarefaction on the Poiseuille number can be measured by the ratio of Poiseuille number for microchannels and microtubes to that for conventional-scale channels and tubes, which is

$$C_{\mathrm{slip}} = \frac{\mathrm{Po}_{\mathrm{incomp,slip}}}{\mathrm{Po}_{\mathrm{incomp,noslip}}} = \frac{1}{1 + 6A_1\cdot\mathrm{Kn} + 12A_2\cdot\mathrm{Kn}^2} \tag{16}$$

for microchannels and

$$C_{\mathrm{slip}} = \frac{\mathrm{Po}_{\mathrm{incomp,slip}}}{\mathrm{Po}_{\mathrm{incomp,noslip}}} = \frac{1}{1 + 8A_1\cdot\mathrm{Kn} + 16A_2\cdot\mathrm{Kn}^2} \tag{16a}$$

for microtubes. It is called the rarefaction factor in this paper.

Figure 2 shows the rarefaction factor for different slip models based on Eqs. (16) and (16a). As seen from the figure, the value of the rarefaction factor is equal to unity when the Knudsen number is zero and this means that the Poiseuille number equals that for incompressible no-slip flow. The value of the rarefaction factor

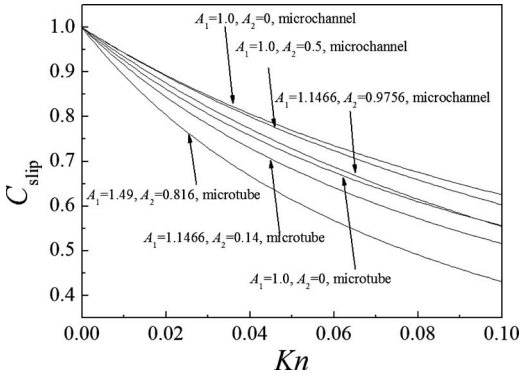

Fig. 2 Effect of rarefaction for various slip models ($C_{\mathrm{slip}}=\mathrm{Po}_{\mathrm{incomp,slip}}/\mathrm{Po}_{\mathrm{incomp,noslip}}$)

decreases with the increment of the Knudsen number and it varies significantly for different slip models, which indicates the discrepancy of rarefaction effect for different slip models. We can see from the figure that the value of C_{slip} for the first-order slip boundary condition ($A_2=0$) is larger than those for second-order slip boundary conditions. A large value of C_{slip} means a small slip velocity. The result indicates that the slip velocity predicted by the first-order velocity slip boundary condition ($A_2=0$) is less than that predicted by other second-order velocity slip boundary conditions in the figure. There is no consensus on the slip coefficients due to lack of accurate experimental data. Hence, correlations in present study are based on the general form of slip boundary condition (Eq. (8)).

3.2 Compressibility Effect. The compressibility effect must be taken into account for gas flow in microchannels and microtubes. For gas flow in conventional-scale channels, the Mach number is typically used to characterize the flow. Therefore, the relationship between the Poiseuille number and the Mach number is first investigated in this work to evaluate the compressibility effect for no-slip flow. Because gas flow in microchannel is often subsonic (the Mach number in open literature is usually less than 0.5), the Mach number in present study is less than 0.5. Here, we define a so called compressibility factor $C_{comp}=Po_{comp,noslip}/Po_{incomp,noslip}$ to measure the compressibility effect. The larger the value of the compressibility factor, the greater the influence of compressibility. Figure 3 shows the effect of the Mach number on the compressibility factor. As seen from the figure, the compressibility factor increases with the Mach number. This is because the compressibility effect makes the velocity profile much flatter than that for incompressible flow and the velocity gradient near the wall increases (as shown in Fig. 4). So, for the same value of Reynolds number, the friction factor for compressible flow is larger than that for incompressible flow according to the definition of friction factor (Eq. (11)). Correlations and experimental data in open literature [8,14–18,20,26] are compared with present numerical results in Fig. 3 and the agreement is well. Present numerical results are curve fitted and exponential correlations are obtained as

$$C_{comp}=0.009e^{(Ma/0.167)}+0.991 \tag{17}$$

for microchannels and

$$C_{comp}=0.016e^{(Ma/0.169)}+0.984 \tag{17a}$$

for microtubes.

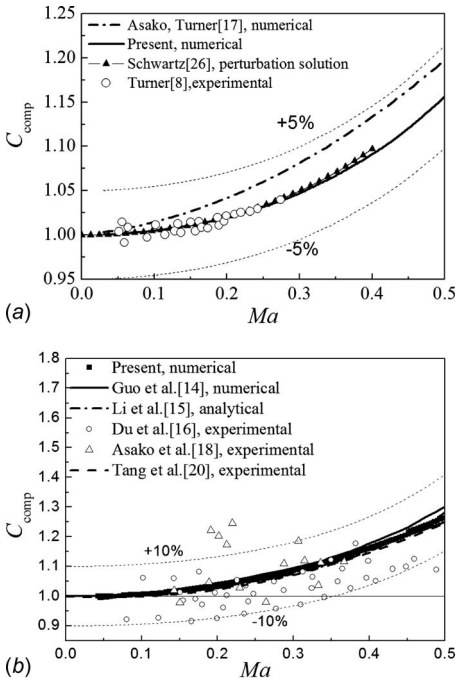

Fig. 3 Comparison of reduced Poiseuille number ($C_{comp}=Po_{comp,noslip}/Po_{incomp,noslip}$) with available results (effect of compressibility, (*a*) microchannel, and (*b*) microtube)

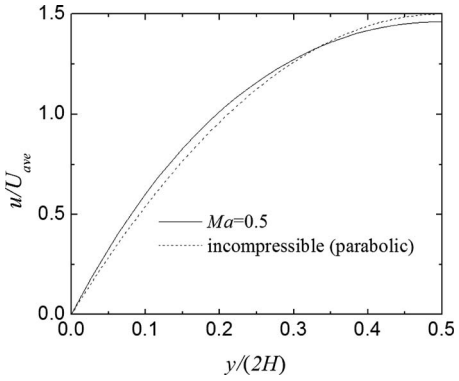

Fig. 4 Comparison of dimensionless velocity profile of compressible and incompressible flow

For flows under the second-order slip boundary condition, the second-order velocity derivative near the wall will influence the slip velocity. As analyzed above, the velocity profile becomes flatter for compressible flow than that for incompressible flow and which implies the increment of the second-order velocity derivative. A dimensionless second-order velocity derivative is defined as

$$C_{deri}=\left(\left.\frac{\partial^2 u}{\partial x_2^2}\right|_{wall}\right)_{comp}\Big/\left(\left.\frac{\partial^2 u}{\partial x_2^2}\right|_{wall}\right)_{incomp} \tag{18}$$

Figure 5 depicts the distribution of the dimensionless second-order velocity derivative C_{deri}. As can be observed, C_{deri} increases dramatically with the increasing Mach number. The numerical results are curve fitted and exponential correlations are obtained as

$$\text{Microchannel: } C_{deri}=0.032e^{(Ma/0.151)}+0.968 \tag{19}$$

$$\text{Microtube: } C_{deri}=0.068e^{(Ma/0.149)}+0.932 \tag{19a}$$

3.3 Combined Effects of Rarefaction and Compressibility. For the gas flow in an actual microchannel or microtube, the Knudsen number and the Mach number vary along the channel, it is difficult to obtain the relationship between the Poiseuille num-

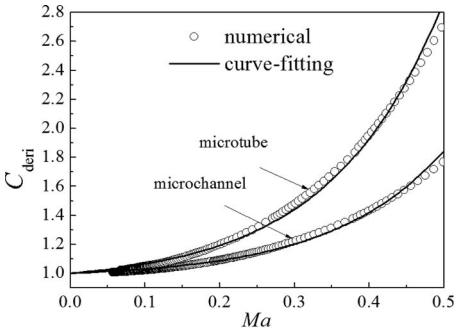

Fig. 5 Second-order velocity derivative for compressible flow ($C_{deri}=(\partial^2 u/\partial x_2^2)_{wall,comp}/(\partial^2 u/\partial x_2^2)_{wall,incomp}$, which indicates the enhancement of the second-order velocity derivative due to compressibility)

ber and the Mach number for a given Knudsen number. Numerical simulation of Navier–Stokes equations can easily control the slip velocity for a given Knudsen number. Therefore, the combined effects of rarefaction and compressibility can be obtained for several specified Knudsen numbers.

Figure 6 shows the reduced Poiseuille number $C_{comp,slip} = Po_{comp,slip}/Po_{incomp,noslip}$ for three Knudsen numbers (Kn=0.01, 0.05, and 0.1). $C_{comp,slip}$ reflects the combined effects of rarefaction and compressibility. It can be seen that $C_{comp,slip}$ increases with the increasing Mach number for all the three Knudsen numbers and $C_{comp,slip}$ decreases with the increasing Knudsen number.

Many researchers proposed several higher-order slip boundary conditions to extend the applicability of Navier–Stokes equations. Four second-order slip boundary conditions proposed by Sreekanth [10], Ewart et al. [11], Cercignani and Daneri [27], and Hsia and Domoto [28] are employed here. As shown in Fig. 6, $C_{comp,slip}$ for different slip boundary conditions are apparently different from each other. For example, for gas flow in microtubes, when the Mach number is 0.5 and the Knudsen number is 0.1, the value of $C_{comp,slip}$ is 0.434 for the slip model proposed by Ewart et al. [11] while it is 0.547 for the slip model proposed by Sreekanth [10] and 0.6 for the first-order slip boundary condition. The results indicate that developing an accurate slip boundary condition is of great importance.

As demonstrated above, the compressibility effect increases the dimensionless velocity gradient near the wall and increases the Poiseuille number. On the other hand, the rarefaction effect leads to a velocity slip at the wall and decreases the velocity gradient near the wall and thus decreases the friction factor. As seen from the expression of the slip velocity (Eq. (8)), the slip velocity depends on the first-order and second-order velocity derivative near the wall. As analyzed above, the compressibility effect changes the velocity derivative near the wall and thus will change the slip velocity. This means that the rarefaction and compressibility effect interact and the rarefaction effect for compressible flow will be different from that of incompressible flow.

For the combined effects of rarefaction and compressibility, there are two extreme cases.

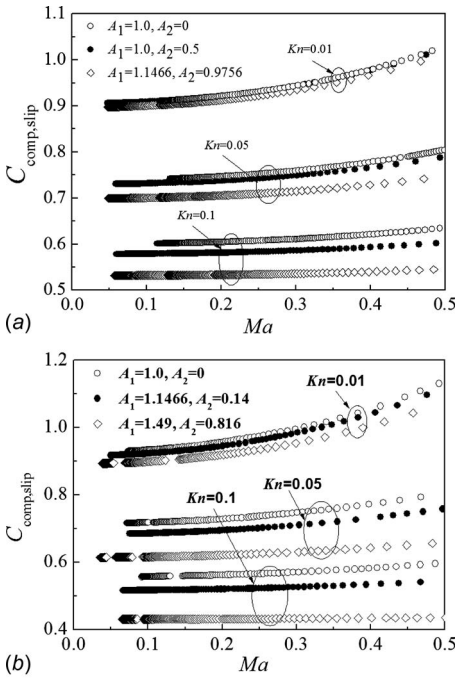

Fig. 6 Combined effects of rarefaction and compressibility under various slip boundary conditions ($C_{comp,slip} = Po_{comp,slip}/Po_{incomp,noslip}$, (*a*) microchannel, and (*b*) microtube)

(1) The rarefaction is negligible, Kn=0, so the Poiseuille number should be $Po = Po_0 \cdot C_{comp}$.
(2) The compressibility is negligible, Ma=0, $C_{comp}=1.0$, and $C_{deri}=1.0$, so the Poiseuille number should be $Po = Po_0 \cdot C_{slip}$.

Po_0 denotes the Poiseuille number for channels and tubes with conventional scale. The value of Po_0 is equal to 96 for channels and which is equal to 64 for tubes.

According to the analysis above, we propose a correlation to predict the combined effects of rarefaction and compressibility as follows:

$$Po = Po_0 \cdot C_{slip} \cdot C_{comp} \cdot \frac{1 + C_1 \cdot A_1 Kn + C_2 \cdot A_2 Kn^2}{1 + C_1 \cdot A_1 C_{comp} Kn + C_2 \cdot A_2 C_{deri} Kn^2} \tag{20}$$

where C_1 and C_2 are constants and they can be obtained according to the numerical results. C_{comp} and C_{deri} indicate the variation in the first-order and second-order velocity derivative due to the compressibility and the effect of this variation in the Poiseuille number is measured by the form of Eq. (20) in this paper. According to numerical results as shown in Fig. 6, constants in Eq. (20) can be obtained as $C_1=14.28$, $C_2=13.99$ for microchannels and $C_1=21.7$, $C_2=19.36$ for microtubes. The average and maximum square deviation between the correlation and the numerical results is 0.42% and 4.19%. In fact, the expression as shown in Eq. (20) with factors obtained here ($C_1=14.28$, $C_2=13.99$ for microchannels and $C_1=21.7$, $C_2=19.36$ for microtubes) is applicable for many other second-order slip boundary conditions because the general form of second-order slip boundary condition (Eq. (8)) is used for analysis in this study. The form of Eq. (20) is expected to be suitable for many other geometric configuration and the only correction needed is the value of C_1 and C_2.

The fourth item at the right hand side of Eq. (20) indicates the effect of compressibility on the slip velocity. $C_{comp}Kn$ denotes the equivalent Knudsen number caused by the change in first-order velocity derivative and $C_{deri}Kn^2$ denotes the change in second-order slip velocity caused by the change in second-order velocity derivative. The general effect of compressibility on the slip velocity can be measured by $C_{comp,slip}/(C_{slip} \cdot C_{comp})$ and it is shown in Fig. 7. As shown in the figure, the value of $C_{comp,slip}/(C_{slip} \cdot C_{comp})$ is less than 1.0 and this indicates that the compressibility causes an additional slip velocity and decreases the friction factor.

In Sec. 3.4, we simulate a special case and compare the prediction of correlations.

3.4 Prediction of Special Cases. In Sec. 3.3, we proposed correlations of friction factor (Eq. (20)) according to the numerical data as shown in Fig. 6. The data are obtained by numerical simulation for several specific Knudsen numbers (Kn=0.01, 0.05, 0.1). Here, we simulate actual gas flows in a microchannel and a microtube. The Knudsen number and the Mach number vary along the channel and so does the friction factor. Correlations in previous sections are used to predict the distribution of the friction factor. Gas flows in a microchannel and a microtube in the slip regime are simulated and the distributions of Poiseuille number are presented in Fig. 8. The second-order slip boundary condition proposed by Cercignani and Daneri [27] ($A_1=1.1466$, $A_2=0.9756$) is used for flow in the microchannel and that proposed by Ewart et al. [11] ($A_1=1.49$, $A_2=0.816$) is used for flow in the microtube. For the flow in the microchannel, the Knudsen number increases from 0.0038 at the inlet to 0.017 at the outlet and the Mach number increases from 0.089 to 0.41. For the flow in the microtube, the Knudsen number increases from 0.0023 at the inlet to 0.013 at the outlet and the Mach number increases from 0.058 to 0.31. Three correlations considering only the rarefaction effect, only the compressibility effect and combined effects of rarefaction, and the compressibility are presented in the figure for com-

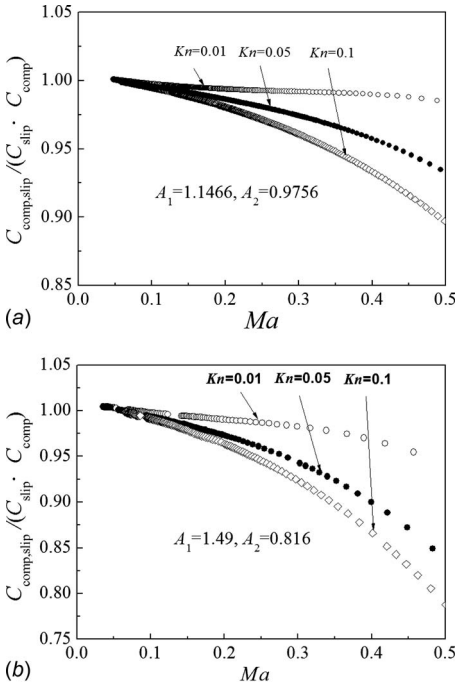

Fig. 7 Combined effects of rarefaction and compressibility ($C_{comp,slip}/(C_{slip} \cdot C_{comp})$ indicates the effect of velocity derivative on the slip velocity, (*a*) microchannel, and (*b*) microtube)

parison. As seen from the figure, predictions of Poiseuille number considering rarefaction or compressibility effect separately deviate from the numerical results obviously, while the prediction considering combined effects of rarefaction and compressibility agrees well with the numerical results except the entrance region. The effect of the microchannel length-height ratio is also tested in the relative large outlet Kn number (Kn≈0.1). Four length-height ratios are tested (5, 10, 50, and 100). Results are shown in Fig. 9. We can see that the prediction of Eq. (20) is very well for all the four cases. Although constants C_1 and C_2 in Eq. (20) are obtained from numerical results in Fig. 6, the expression (Eq. (20)) is also suitable for any other second-order slip models in the form of Eq. (8). In order to validate the expression, Poiseuille number along the microchannel calculated for three second-order slip boundary conditions by Schamberg [29], Hadjiconstantinou [30], and Maurer et al. [31] are predicted by Eq. (20). As shown in Fig. 10, symbols denote numerical results and lines denote predictions of Eq. (20), expression (Eq. (20)) predicts the distribution of Poiseuille number along the microchannel very well with the maximum deviation of 0.32% near the entrance of the microchannel. Hence, for microchannels and microtubes, expression as shown in Eq. (20) can predict the distribution of friction factor under second-order slip boundary condition in the form of Eq. (8).

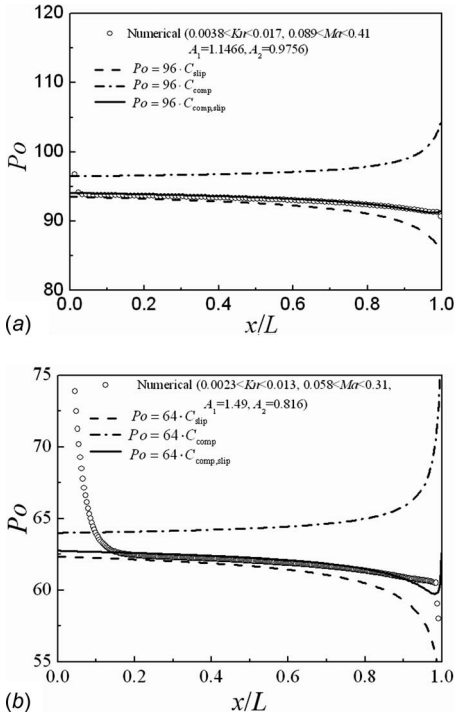

Fig. 8 Prediction of Poiseuille number for a special case (C_{comp} indicates the effect of compressibility, C_{slip} indicates the effect of rarefaction, and $C_{comp,slip}$ indicates the combined effects of rarefaction and compressibility, (*a*) microchannel, and (*b*) microtube)

4 Concluding Remarks

Numerical simulations of gas flow in microchannels and microtubes are conducted to study the combined effects of rarefaction and compressibility on the friction factor. The rarefaction effect is measured by the Knudsen number and the compressibility effect is measured by the Mach number. The first-order and second-order velocity derivative increases due to the compressibility effect and

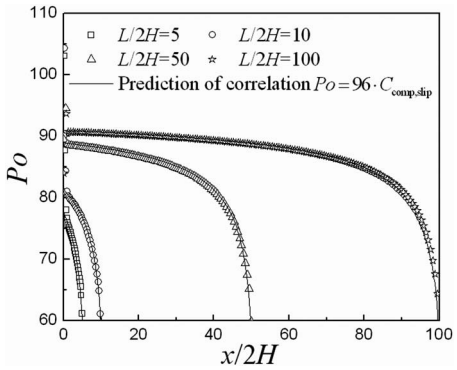

Fig. 9 Prediction of Poiseuille number along microchannels with different length-height ratios. (second-order slip boundary condition is used for A_1=1.1466 and A_2=0.9756—the symbols denote the numerical results and the lines denote the predictions of Eq. (20))

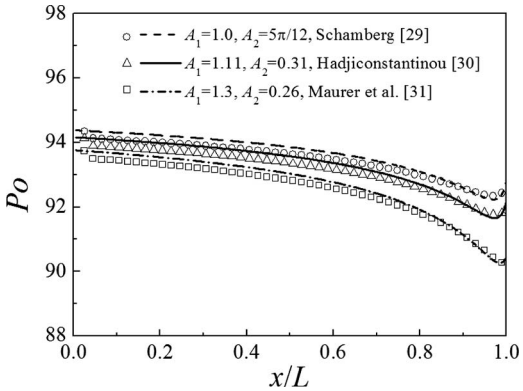

Fig. 10 Prediction of Poiseuille number along a microchannel under three second-order slip boundary conditions (the symbols denote the numerical results and the lines denote the predictions of Eq. (20))

this increasing velocity derivative leads to the change in slip velocity. Results indicate that the combined effects of rarefaction and compressibility on the friction factor for slip flow are weaker than the product of rarefaction factor for incompressible flow and compressibility factor for no-slip flow and the combined effects of rarefaction and compressibility for different slip boundary conditions are different from each other. General correlations are proposed to measure the combined effects of rarefaction and compressibility for gas flow in microchannels and microtubes. Correlations are applicable for various first-order and second-order slip boundary conditions. With the development of the second-order slip boundary condition, the correlation may be extended to transition flow regime and be suitable for various geometric configurations.

Acknowledgment

This work was supported by the National Natural Science Foundation of China (Grant No. 50376050).

Nomenclature

A_1 = first-order slip coefficient
A_2 = second-order slip coefficient
c_p = specific heat capacity, J/(kg K)
C_{deri} = dimensionless second-order velocity derivative is $(\partial^2 u/\partial x_2^2)_{\text{wall,comp}}/(\partial^2 u/\partial x_2^2)_{\text{wall,incomp}}$
C_{slip} = reduced Poiseuille number is $\text{Po}_{\text{incomp,slip}}/\text{Po}_{\text{incomp,noslip}}$
C_{comp} = reduced Poiseuille number is $\text{Po}_{\text{comp,noslip}}/\text{Po}_{\text{incomp,noslip}}$
$C_{\text{comp,slip}}$ = reduced Poiseuille number is $\text{Po}_{\text{comp,slip}}/\text{Po}_{\text{incomp,noslip}}$
D_h = hydraulic diameter, m
f = friction factor
H = half of height of microchannels or radius of microtubes
j = number of freedom inside gas molecules
Kn = Knudsen number
L = length of microchannel or microtube, m
Ma = Mach number
p = gas pressure, Pa
Po = Poiseuille number
Pr = Prandtl number
R = gas constant
Re = Reynolds number
T = temperature, K
u = streamwise velocity, m/s
v = velocity in normal direction of wall, m/s
x_1 = streamwise coordinate, m
x_2 = coordinate in normal direction of wall, m

Greek Symbols

ϕ = source of energy equation
γ = specific heat ratio
κ = thermal conductivity, W/(m K)
λ = gas mean free path, m
μ = viscosity coefficient, Pa s
ρ = gas density, kg/m^3
σ = tangential momentum accommodation coefficient
σ_T = thermal accommodation coefficient

Subscripts

comp = value for compressible flow
incomp = value for incompressible flow
noslip = value for no-slip flow
slip = value for slip flow
wall = value near wall

References

[1] Ebert, W. A., and Sparrow, E. M., 1965, "Slip Flow in Rectangular and Annular Ducts," ASME J. Basic Eng., **87**, pp. 1018–1024.
[2] Zhu, X., Liao, Q., and Xin, M. D., 2006, "Gas Flow in Microchannel of Arbitrary Shape in Slip Flow Regime," Nanoscale Microscale Thermophys. Eng., **10**, pp. 41–54.
[3] Duan, Z. P., and Muzychka, Y. S., 2007, "Slip Flow in Non-Circular Microchannels," Microfluid. Nanofluid., **3**, pp. 473–484.
[4] Kavehpour, H. P., Faghri, M., and Asako, Y., 1997, "Effects of Compressibility and Rarefaction on Gaseous Flows in Microchannels," Numer. Heat Transfer, **32**, pp. 677–696.
[5] Morini, G. L., Spiga, M., and Tartarini, P., 2004, "The Rarefaction Effect on the Friction Factor of Gas Flow in Microchannels," Superlattices Microstruct., **35**, pp. 587–599.
[6] Harley, J. C., Huang, Y., Bau, H. H., and Zemel, J. N., 1995, "Gas Flow in Micro-Channels," J. Fluid Mech., **284**, pp. 257–274.
[7] Araki, T., Kim, M. S., Iwai, H., and Suzuki, K., 2002, "An Experimental Investigation of Gaseous Flow Characteristics in Microchannels," Nanoscale Microscale Thermophy. Eng., **6**, pp. 117–130.
[8] Turner, S. E., Lam, L. C., Faghri, M., and Gregory, O. J., 2004, "Experimental Investigation of Gas Flow in Microchannels," ASME J. Heat Transfer, **126**, pp. 753–763.
[9] Colin, S., Lalonde, P., and Caen, R., 2004, "Validation of a Second-Order Slip Flow Model in Rectangular Microchannels," Heat Transfer Eng., **25**, pp. 23–30.
[10] Sreekanth, A. K., 1969, "Slip Flow Through Long Circular Tubes," *Proceedings of the Sixth International Symposium on Rarefied Gas Dynamics*, L. Trilling and H. Y. Wachman, eds., Academic, New York.
[11] Ewart, T., Perrier, P., Graur, I., and Meolans, J. G., 2006, "Mass Flow Rate Measurements in Gas Micro Flows," Exp. Fluids, **41**, pp. 487–498.
[12] Barber, R. W., and Emerson, D. R., 2006, "Challenges in Modeling Gas-Phase Flow in Microchannels: From Slip to Transition," Heat Transfer Eng., **27**, pp. 3–12.
[13] Guo, Z. Y., and Wu, X. B., 1997, "Compressibility Effect on the Gas Flow and Heat Transfer in a Microtube," Int. J. Heat Mass Transfer, **40**, pp. 3251–3254.
[14] Guo, Z. Y., and Wu, X. B., 1998, "Further Study on Compressibility Effects on the Gas Flow and Heat Transfer in a Microtube," Nanoscale Microscale Thermophys. Eng., **2**, pp. 111–120.
[15] Li, Z. X., Xia, Z. Z., and Du, D. X., 1999, "Analytical and Experimental Investigation on Gas Flow in a Microtube," Kyoto University-Tsinghua University Joint Conference on Energy and Environment, Kyoto, Japan.
[16] Du, D. X., Li, Z. X., and Guo, Z. Y., 2000, "Friction Resistance for Gas Flow in Smooth Microtubes," Sci. China, Ser. E: Technol. Sci., **43**, pp. 171–178.
[17] Asako, Y., Pi, T., Turner, S. E., and Faghri, M., 2003, "Effect of Compressibility on Gaseous Flows in Micro-Channels," Int. J. Heat Mass Transfer, **46**, pp. 3041–3050.
[18] Asako, Y., Nakayama, K., and Shinozuka, T., 2005, "Effect of Compressibility on Gaseous Flows in a Micro-Tube," Int. J. Heat Mass Transfer, **48**, pp. 4985–4994.
[19] Morini, G., Lorenzini, M., Colin, S., and Geoffroy, S., 2007, "Experimental Analysis of Pressure Drop and Laminar to Turbulent Transition for Gas Flows in Smooth Microtubes," Heat Transfer Eng., **28**, pp. 670–679.
[20] Tang, G. H., Li, Z., He, Y. L., and Tao, W. Q., 2007, "Experimental Study of Compressibility, Roughness and Rarefaction Influences on Microchannel Flow," Int. J. Heat Mass Transfer, **50**, pp. 2282–2295.
[21] Sun, H. W., and Faghri, M., 2000, "Effect of Rarefaction and Compressibility of Gaseous Flow in Microchannel Using DSMC," Numer. Heat Transfer, **38**, pp. 153–168.
[22] Jain, V., and Lin, C. X., 2006, "Numerical Modeling of Three-Dimensional Compressible Gas Flow in Microchannels," J. Micromech. Microeng., **16**, pp. 292–302.
[23] Hong, C., Asako, Y., Turner, S. E., and Faghri, M., 2007, "Friction Factor Correlations for Gas Flow in Slip Flow Regime," ASME J. Fluids Eng., **129**, pp. 1268–1276.
[24] Currie, I. G., 2003, *Fundamental Mechanics of Fluids*, 3rd ed., Marcel Dekker, New York.
[25] Patankar, S. V., 1981, "A Calculation Procedure for Two-Dimensional Elliptic Situations," Numer. Heat Transfer, **4**, pp. 409–425.
[26] Schwartz, L. W., 1987, "A Perturbation Solution for Compressible Viscous Channel Flows," J. Eng. Math., **21**, pp. 69–86.
[27] Cercignani, C., and Daneri, A., 1963, "Flow of a Rarefied Gas Between Two Parallel Plates," J. Appl. Phys., **34**, pp. 3509–3513.
[28] Hsia, Y. T., and Domoto, G. A., 1983, "Experimental Investigation of Molecular Rarefaction Effects in Gas Lubricated Bearings at Ultra-Low Clearances," ASME J. Lubr. Technol., **105**, pp. 120–130.
[29] Schamberg, R., 1947, "The Fundamental Differential Equations and The Boundary Conditions for High Speed Slip-Flow, and Their Application to Several Specific Problems," Ph.D. thesis, California Institute of Technology.
[30] Hadjiconstantinou, N. G., 2003, "Comment on Cercignani's Second-Order Slip Coefficient," Phys. Fluids, **15**, pp. 2352–2354.
[31] Maurer, J., Tabeling, P., Joseph, P., and Willaime, H., 2003, "Second-Order Slip Laws in Microchannels for Helium and Nitrogen," Phys. Fluids, **15**, pp. 2613–2621.

Experimental Investigation of Vortex-Induced Vibration in One and Two Dimensions With Variable Mass, Damping, and Reynolds Number

Robert D. Blevins
Goodrich,
850 Lagoon Drive,
Chula Vista, CA 91910

Charles S. Coughran
Scripps Institution of Oceanography,
9500 Gilman Drive,
La Jolla, CA 92093

Measurements are made of vortex-induced vibration of an elastically supported circular cylinder in water with reduced velocity (U/f_nD) from 2 to 12, damping factors (ζ) from 0.2% to 40% of critical damping, mass ratios ($m/\rho D^2$) from $\pi/2$ to $\pi/17$, and transverse, inline, and combined inline and transverse motions at Reynolds numbers up to 150,000. Effects of mass, damping, Reynolds number, and strakes on vortex-induced vibration amplitude, frequency, entrainment, and drag are reported.
[DOI: 10.1115/1.3222904]

1 Introduction

It is well known that vortex shedding induces vibration of elastic cylinders in cross flow and that feedback from cylinder motion affects the shedding process [1–11]. Studies visualized the vortex street wake at low Reynolds numbers [12–16]. This paper, however, is devoted to the measurement of elastic cylinder response to vortex shedding. Recent experimental studies of vortex-induced vibration include Laneville [17], Sanchis et al. [18], Carberry and Sheridan [19], Govardhan and Williamson [20], Klamo et al. [21], and Jauvtis and Williamson [22]. The present experiment covers a larger Reynolds number range of 170–150,000 and develops a larger systematic database for one-dimensional and two-dimensional cylinder response amplitude, frequency, and drag. Damping factor was varied from 0.2% to 40% and mass ratio was varied by a factor of 10. The lowest mass cylinder is neutrally buoyant. The effectiveness of six strake configurations is reported.

2 Description of the Experiment

The experiments were made with water flow in the stratified flow channel at the Scripps Institution of Oceanography in La Jolla, CA. The flow channel is 1.12 m wide and 1.13 m deep. The working test section is 16 m long and has a maximum velocity of 1.25 m/s. At 1 m/s at the midsection where the experiments were performed, the root-mean-square turbulence of axial velocity was 1% above 0.2 Hz and 2% at lower frequencies where the unsteadiness is associated with surface waves. The vertical profile of axial velocity was flat to within 4%. Tests in Figs. 2, 4, 7, and 8 were made with a 6.35 cm (2.5 in.) outside diameter aluminum tube whose surface was sanded with 220 grit sand paper to give an average roughness divided by cylinder diameter of 10^{-5}, which is smooth to touch but not polished, and a mass ratio within 2% of $m/\rho D^2 = 5.02$ except as noted. The cylinder pierces the water surface. Its long 17.8 diameter span in the water flow minimizes the influence of surface effects on the results. Its Reynolds number (UD/ν) is 30,000 at the response peaks in Fig. 2. Additional tests were made with cylinders diameters from 0.305 cm to 12.7 cm (Table 1, Figs. 3, 5, 6, 9, and 10) at Reynolds numbers between 170 and 150,000.

The objective of the experimental design was to replicate, as far as practical, an ideal two-dimensional spring-supported rigid cylinder that displaces perpendicular to its axis. As shown in Fig. 1, the cylinder is rigidly mounted to a square frame that is suspended by four parallel bars from an overhead platform. Flexures at the ends of the bars allow four diameters of elastic inline (x) and transverse (y) motion while maintaining the cylinder vertical and perpendicular to the water surface. Lateral (x and y) stiffness is controlled by coil springs at the corners of the frame. As the cylinder displaces laterally (x or y) 6.35 cm (1 diameter), the suspended frame moves vertically (z) 1.2 mm, 1.9% of cylinder diameter, and 0.1% of the submerged span. The small vertical (z) motion is felt to have negligible effect. By adding or subtracting mass to the frame, the cylinder mass is changed.

Damping proportional to cylinder velocity is achieved with a magnet on the frame that reacts with a fixed contoured copper plate through an air gap. By changing the air gap, damping of the suspended cylinder can be adjusted from 0.2% to 40%.

The structural bending and torsional natural frequencies are above the shedding frequency, minimizing their participation in the suspensions' fundamental lateral natural frequency f_n near 1 Hz (1.203 Hz in Fig. 2 and 1.18 Hz in Fig. 7). A 3.4 m steel tether restrains the frame from moving down stream under drag loads for tests with one-dimensional transverse motion. One diameter of transverse (y) motion is 1.06 deg of arc and it produces 0.59 mm inline (x) motion, which is 0.9% of cylinder diameter. Halving the tether length did not perceptibly change cylinder motions. To allow both transverse and inline motions, the steel tether was replaced with a rubber tether whose stiffness was less than 1/100 of a frame coil spring. The upstream end of the tether was wound on a drum to maintain mean cylinder position and suspension spring geometry as flow velocity increased. Drag was measured by a load cell between the tether and the frame and corrected for suspension stiffness and cylinder buoyancy. See Fig. 1.

Inline and transverse positions of the cylinder were measured optically with an accuracy of 0.1 mm by Acquity™ laser displacement sensors and digitally recorded every 1/100 s for 100 s. Time histories were analyzed statistically.

Contributed by Fluids Engineering Division of ASME for publication in the JOURNAL OF FLUIDS ENGINEERING. Manuscript received May 20, 2008; final manuscript received July 26, 2009; published online September 30, 2009. Review conducted by Joseph Katz.

Table 1 Measured maximum transverse amplitude as a function of Reynolds number, surface roughness, and damping $m/\rho D^2 = 5.02$

D (cm)	k/D	ζ	UD/ν	A_y/D
0.305	0.0001	0.006	204	0.48
0.794	0.00001	0.002	418	0.60
1.59	0.00001	0.002	1170	0.68
3.49	0.00001	0.002	4020	0.82
3.49	0.00001	0.002	10,300	1.03
6.35	0.00001	0.002	29,300	1.17
12.7	0.00001	0.002	67,400	1.29
12.7	0.00001	0.002	139,100	1.75
12.7	0.005	0.002	132,500	1.09
0.305	0.0001	0.02	204	0.37
0.794	0.00001	0.02	418	0.45
1.59	0.00001	0.02	1300	0.62
3.49	0.00001	0.02	4020	0.70
3.49	0.00001	0.02	10,600	0.83
6.35	0.00001	0.02	28,300	1.02
12.7	0.00001	0.02	63,400	1.13
12.7	0.00001	0.02	127,000	1.49
12.7	0.005	0.02	136,700	0.76

3 Test Results

Steady-state response of the elastically supported cylinder was measured at flow velocities in approximately 1 cm/s steps at six values of damping, (0.2%, 2%, 5%, 10%, 20%, and 40%) for transverse-only (y), inline only (x), and both transverse and inline (x and y) motions. Structural (i.e., magnetic) damping ζ was measured in decay tests with a dry cylinder weighted to simulate the cylinder added mass in still water, which was consistent with Vandiver [23], Skop [24], and Khalak and Williamson [6]. The characteristic transverse amplitude A_y was chosen statistically to be the third largest amplitude (one-half peak-to-peak displacement) in a sample of 100 transverse oscillation to be suitable for fatigue damage calculations; there is a 90% confidence that the third largest event will be exceeded by 95% [25]. Reduced velocity U/f_nD is freestream channel velocity U divided by cylinder diameter D multiplied by still water natural frequency f_n. The cylinder mass per unit length m is the sum of the cylinder (dry) mass, still water added mass, and suspended frame mass divided by the wetted length of the cylinder.

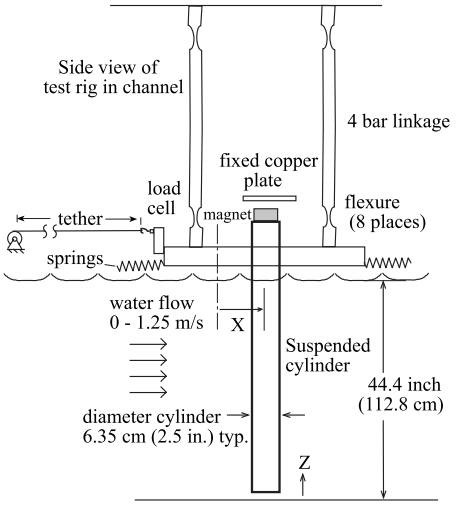

Fig. 1 Test cylinder and experimental apparatus. *Y* is out of plane.

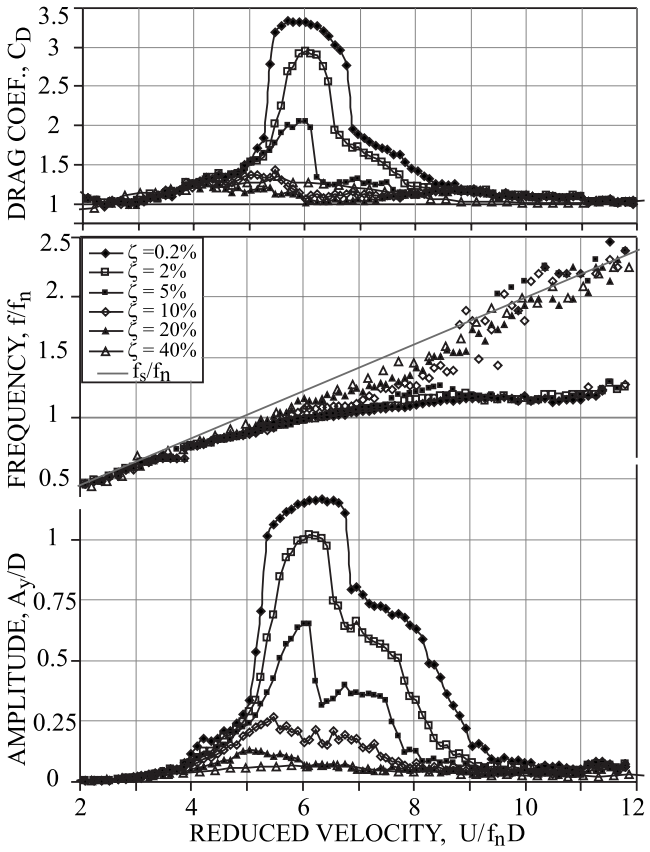

Fig. 2 One-dimensional transverse-only motion amplitude, frequency, and drag for six levels of damping, $m/\rho D^2 = 5.02$ and $D = 6.35$ cm

3.1 Transverse Response and Entrainment. The 6.35 cm diameter cylinder with $m/\rho D^2 = 5.02$ was mechanically restrained to move transverse (y) to the freestream channel flow. Its amplitude, frequency, and drag coefficients are given in Fig. 2 as function of reduced velocity U/f_nD where $f_n = 1.203$ Hz and damping. Large amplitude sinusoidal responses begin near $U/f_nD = 1/\mathrm{St}$, that is, $f_n \approx f_s$. Figure 2, shows that a factor of 10 increase in damping from $\zeta = 0.002$ to 0.02, produces only about 15% decrease in maximum amplitude from about 1.15 D to 1 D, suggesting high amplitudes are self limiting. But a further factor of 10 increase in damping from $\zeta = 0.02$ to 0.20 proportionately, reduces the maximum amplitude from one to one-tenth diameter, which suggests a linear forced vibration model is appropriate at low amplitudes [26]. Figure 2 is consistent with plots by Feng [27] in air and with Klamo et al. [21] and Govardhan and Williamson [20] but it includes drag coefficient, frequency, and larger ranges of amplitude and damping. Figure 2 shows the drag on an excited cylinder with 1 diameter amplitude is three times that of the stationary cylinder, which is in agreement with Sarpkaya [4,5].

Tests in Fig. 3 were made with four cylinder mass ratios with the same reduced damping.

Reduced damping $2m(2\pi\zeta)/\rho D^2$	1.24	1.24	1.24	1.24
Diameter, cm	6.35	6.35	6.35	10.16
Mass ratio $m/\rho D^2$	2.80	5.01	17.1	1.57
Damping factor ζ	0.035	0.02	0.0058	0.063
Maximum amplitude, diameter	1.048	1.017	1.049	1.028
Entrainment $(U/f_nD)_2/(Uf_nD)_1$	1.9	1.47	1.3	3.6

The maximum amplitudes are nearly identical and they occur at nearly the same reduced velocity despite the fact that damping and

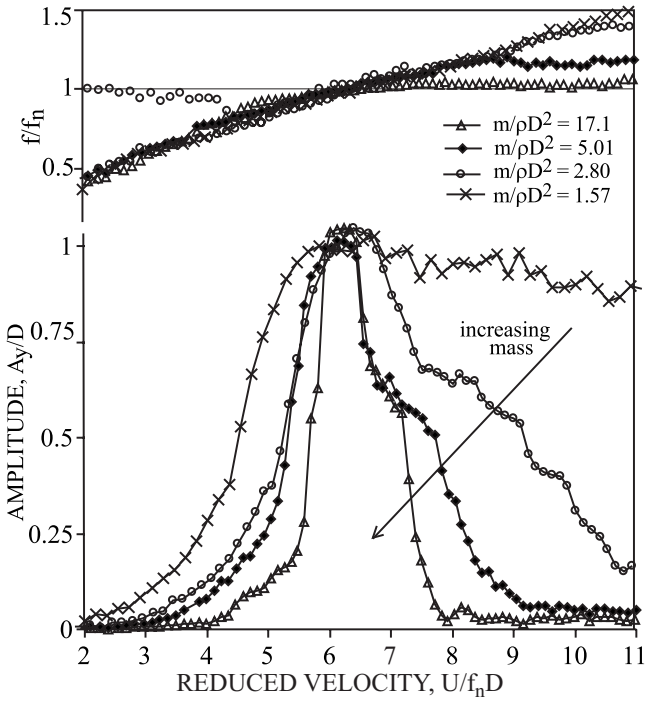

Fig. 3 Transverse cylinder response for four cylinder masses at constant reduced damping, $2m(2\pi\zeta)/\rho D^2=1.24$

mass change by a factor of 10. This suggests that transverse-only maximum amplitude is a function of reduced damping [8,20–24,26,28] at constant Re.

Figure 4 has time histories of cylinder displacement. For small amplitude, less than about 0.1–0.2 diameters, the cylinder displacement time histories are irregular, amplitude and frequency vary, and both the cylinder shedding frequency and the cylinder

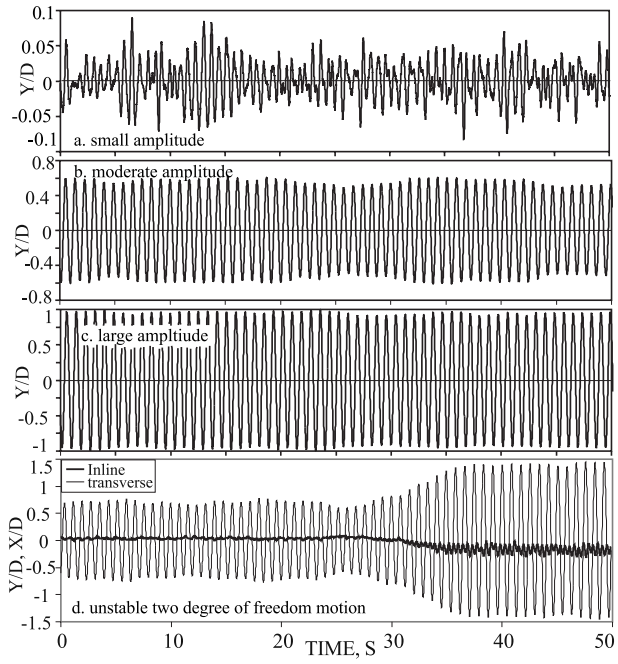

Fig. 4 Time histories of vortex-induced cylinder motion. One degree-of-freedom transverse motion: (*a*) $U/f_nD=11.52$, $\zeta=0.002$, (*b*) $U/f_nD=6.15$, $\zeta=0.05$, (*c*) $U/f_nD=6.15$, $\zeta=0.02$, and (*d*) two degrees-of-freedom $U/f_nD=8.25$, $\zeta=0.02$.

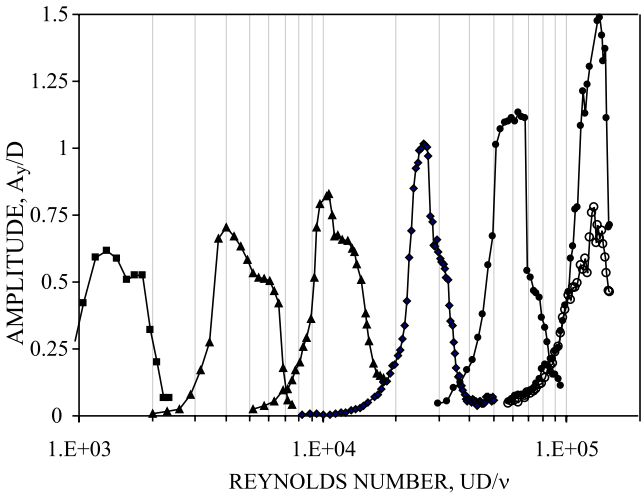

Fig. 5 Amplitude of transverse cylinder response as a function of Reynolds number. $m/\rho D^2=5.02$, $\zeta=0.02$ m, and $2m(2\pi\zeta)/\rho D^2=1.24$. Surface roughness/cylinder diameter =0.00001 solid symbols and 0.005 open symbols.

natural frequency appear in the response. For example, the higher amplitude cycles in Fig. 4(*a*) have lower frequencies (larger distance between peaks) than the lower cycles. At one diameter amplitude, the cylinder displacement is nearly sinusoidal indicating that shedding and cylinder are locked-in (entrained or synchronized) to the same frequency.

The entrainment band's range of large sinusoidal motions of lightly damped cylinders increases as cylinder mass decreases and the start of entrainment moves slightly to the left.

$$\frac{U/f_nD|_2}{U/f_nD|_1}=0.25+\sqrt{\frac{m/\rho D^2}{m/\rho D^2-1.4}} \tag{1}$$

$(U/f_nD)_2$ and $(U/f_nD)_1\approx 1/\mathrm{St}$ are the upper and lower intercepts of the data in Fig. 3 at $A_y/D=0.4$. Infinite entrainment is predicted at $m/\rho D^2\leq 1.4$, similar to the predictions of Williamson and coworkers [29,30], which yields $m/\rho D^2=1.29$. Figure 3 shows that the frequency of the high mass cylinder $m/\rho D^2=17.5$ entrains to the cylinder natural frequency $f\approx f_n$, but the vibration frequency f of light, $m/\rho D^2=2.8, 1.57$, cylinders continually increases across the entrainment band $f\geq 0.6$ $\mathrm{St}U/D$ with increasing velocity. Figure 3 is consistent with plots in [6] but Fig. 3 includes the practically important neutrally buoyant $m/\rho D^2=1.57$ case and higher Reynolds numbers.

3.2 Reynolds Number. Tests were made with cylinder diameters between 0.305 mm and 12.7 cm (0.12 in. and 5 in.) with $m/\rho D^2=5.02$ at flow velocities between 6 cm/s and 125 cm/s corresponding to Reynolds numbers (UD/ν) between 170 and 150,000, respectively. Figure 5, with $\zeta=0.02$, and Table 1 show transverse motion maximum amplitude increases with an increasing Reynolds number between 200 and 100,000, which is in agreement with Ref. [20]. The maximum measured amplitude was 1.75 diameters at a Reynolds number of 139,000. However, at Reynolds number 1.2×10^5 the amplitude of a rough surface cylinder (roughness/diameter=0.005) drops by a factor of 2 from that of a smooth cylinder, probably owing to boundary layer transition [31].

3.3 Inline Response. Tests were made with the cylinder mechanically restricted to one degree-of freedom inline (x) motion only, that is, motion only parallel to the freestream channel flow $m/\rho D^2=3.27$, $D=6.35$ cm, and $f_n=2.53$ Hz. There was no transverse cylinder motion. Figure 6 shows that the cylinder oscillates inline at or near its still water natural frequency in two inline

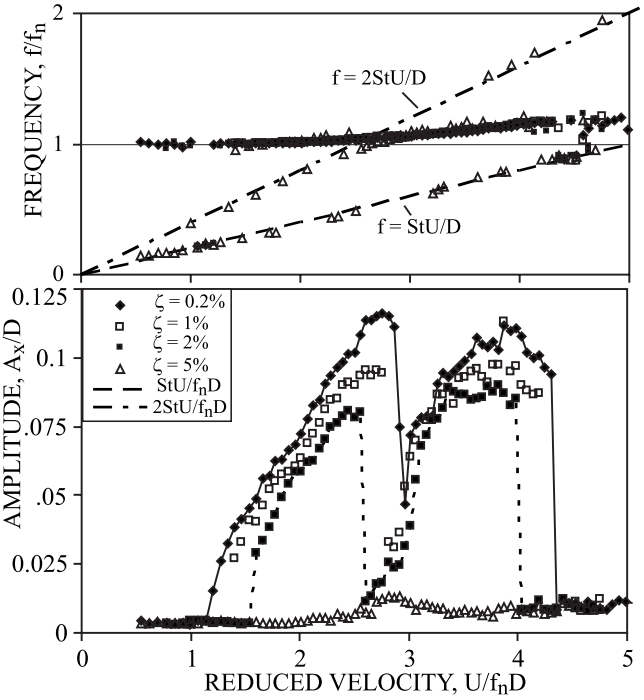

Fig. 6 One degree-of-freedom inline only motion parallel to the freestream flow. Amplitude and frequency as a function of damping, $m/\rho D^2=3.27$.

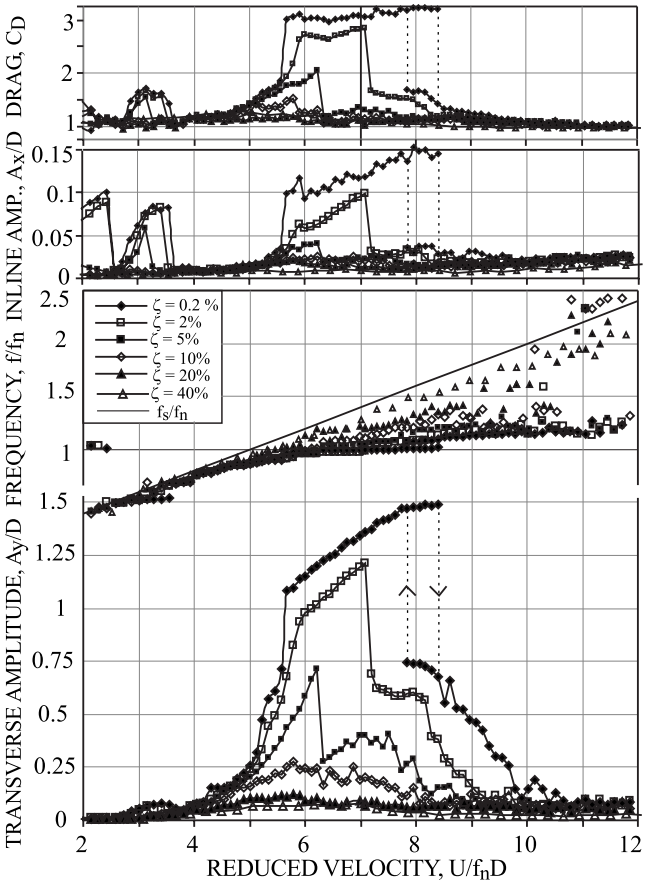

Fig. 7 Two degrees-of-freedom inline (A_x) and transverse (A_y) amplitudes, frequency and drag coefficient (C_D) for six levels of damping. $m/\rho D^2=5.02$. Dashed lines are jump in Fig. 4(*d*).

response bands. In the first band, $1.2 \leq U/f_n D \leq 3$, twice the stationary cylinder shedding frequency ($f_s = \mathrm{St}U/D$) is just below the cylinder natural frequency (f_n), $2f_s \leq f_n$. In this band, King [10] found that two nearly symmetrical vortices are shed per cycle and they coalesce downstream to form the usual staggered vortex street pattern. In the second band, $3 \leq U/f_n D \leq 4.4$, twice the shedding frequency is just above the natural frequency $2f_s \geq f_n$. Looking ahead to Figs. 7–9 and 11, we see that these inline response bands reappear with two degrees-of-freedom motion but the second inline band is a two degrees-of-freedom, as seen in the figure 8 orbit.

The maximum inline amplitude of 0.12 diameter in Fig. 6 is about one-tenth of the transverse motion amplitudes in Fig. 5 for the same damping, which is in agreement with King [10]. Five percent damping $\zeta=0.05$ ($2m2\pi\zeta/\rho D^2=2$) reduces inline oscillations to less than 0.02 diameters whereas more than 40% damping ($2m2\pi\zeta/\rho D^2=30$) is required to reduce resonant transverse oscillations to 0.05 diameter amplitude (Fig. 2).

3.4 Two Degrees-of-Freedom, Transverse and Inline Response. Tests shown in Figs. 7–11 have free cylinder movement both inline and transverse to the freestream flow. $m/\rho D^2=5.02$ except as noted in Figs. 8 and 9. Inline and transverse stiffness of the cylinder suspension were within 1% of each other. Unlike the transverse-only response tests in Fig. 2, the two degrees-of-freedom tests in Figs. 4(*d*), 7–9, and 11 have separate distinct regions of inline motion, transverse motion, and figure 8 orbital motion.

Above 0.7 diameters amplitude the motion is sinusoidal in time, locked-in to a single frequency, and the two degrees-of-freedom cylinder orbits in the $x-y$ plane in a wind-blown Fig. 8 with its tips pointing downstream. The inline frequency is within 10% of twice the transverse frequency $f_x \approx 2f_y$. This figure 8 motion was observed by Alexander [32], Staubli [33], Vandiver and coworkers [34,35], Laneville [17], and Jauvtis and Williamson [22].

Figure 4(*d*) is a time history where the cylinder spontaneously switches between transverse motion with $A_y/D=0.7$ and figure 8 motion with $A_y/D=1.4$. The jump velocity depends on whether velocity is increased or decreased in Fig. 7. Figures 2 and 7 show that the two degrees-of-freedom figure eight amplitudes are larger

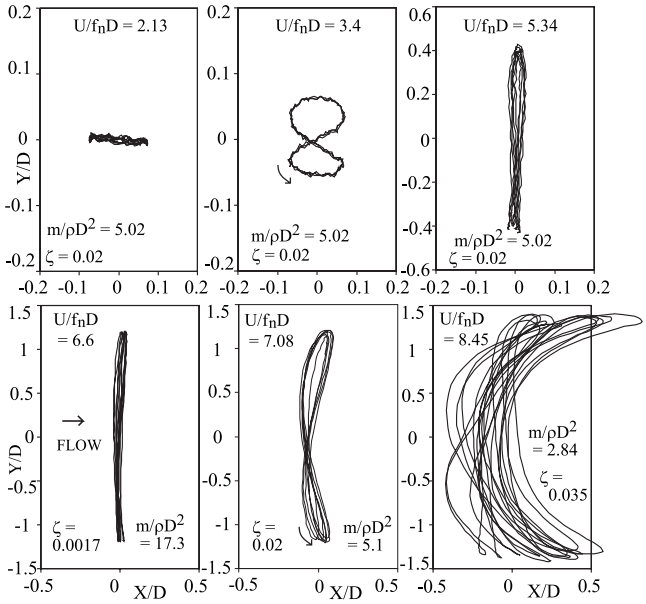

Fig. 8 Two degree-of-freedom $X-Y$ orbits of transverse and inline motion. Velocity increases from left to right, $2m(2\pi\zeta)/\rho D^2=1.24$

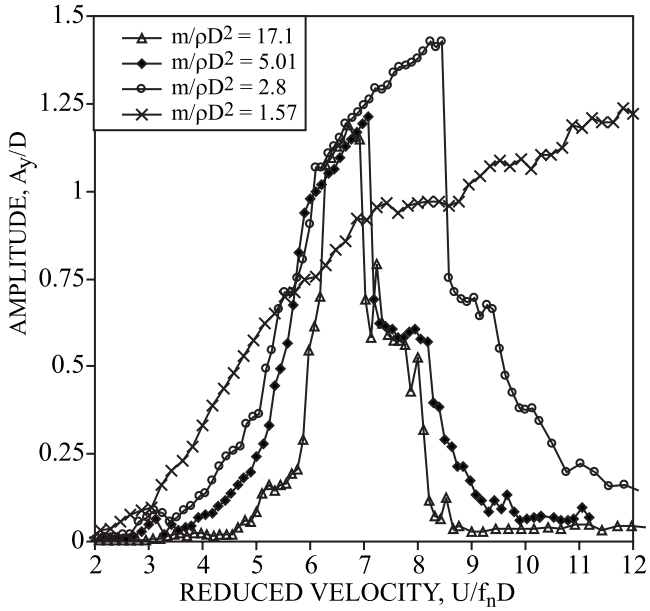

Fig. 9 Transverse cylinder response with two degree-of-freedom motion for four cylinder masses at constant reduced damping, $2m(2\pi\zeta)/\rho D^2=1.24$. Compare with Fig. 3.

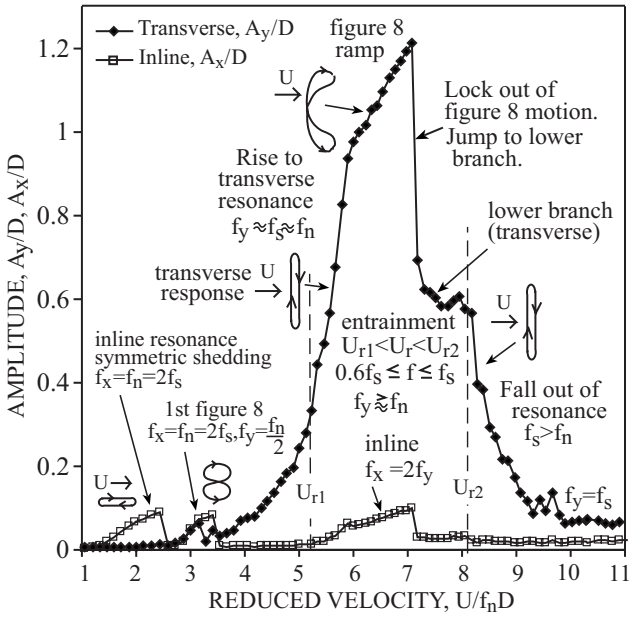

Fig. 11 Annotated two-dimensional motion showing regimes of inline, transverse, and figure 8 motion. $\zeta=0.02$, $m/\rho D^2=5.02$. See orbits in Fig. 8. f_s is stationary cylinder shedding frequency and f_n is cylinder natural frequency in still water.

than transverse-only amplitudes at the same mass and damping. Figures 8 and 9 show the inline to transverse ratio A_x/A_y and the amplitude A_y of Fig. 8 motion are functions of both damping and mass ratio: In Fig. 9, the maximum two degrees-of-freedom response increases and moves to higher velocities with decreasing cylinder mass at constant reduced damping. The frequency and amplitude of the curve labeled $\zeta=0.002$ in Fig. 7 is nearly identical to Fig. 5 [21] for their higher damping of $0.013/3.6=0.004$, mass ratio of $m/\rho D^2=2.04$, and Reynolds numbers presumably of 2000–11,000.

3.5 Strakes. Tests were made with 5%, 7%, and 13% of diameter high helical strakes. They were two complete spiral turns of three strakes over the 10 diameter (35 in. or 88.9 cm) wetted length of a 3.5 in. (8.89 cm) diameter cylinder with 0.2% damping and $m/\rho D^2=4.43$. The results in Fig. 10 show 5%, 7%, and 13% of diameter high Strakes, successfully suppresses large amplitude vortex-induced vibration; the remaining oscillations were small and irregular. However, when one diameter length of 7% high strakes was removed (that is, 90% of the cylinder span has strakes and 10% is bare cylinder) to simulate a local strake defect, then oscillation amplitude increased by a factor of 4 at the worst orientation. Removing one diameter length of the 10% and 13% high strakes did not significantly change the cylinder response. This suggests that the local strake irregularities such as at pipe joints, strake clamps, access holes, and marine growth impair the effectiveness of low strakes.

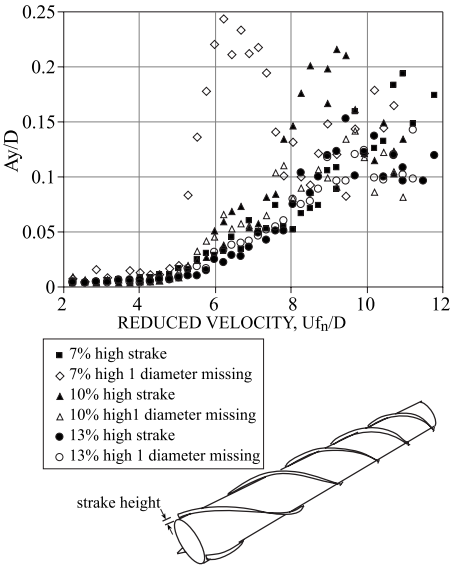

Fig. 10 Response of straked cylinders, $m/\rho D^2=4.4$, $\zeta=0.002$

4 Guide Lines for Avoidance of Vortex-Induced Vibration

Often, one wishes to avoid large amplitude vortex-induced vibration by stiffening to avoid the high amplitude entrainment bands that clearly appear in Figs. 2, 3, 5–7, 9, and 11. The transverse entrainment band lie between reduced velocities U_{r1} and U_{r2}, Eq. (1). Entrainment band can be expressed in terms of the reduced velocity, $U_r=U/f_nD=(f_s/f_n)/\mathrm{St}$, stationary cylinder shedding frequency $f_s=\mathrm{St}U/D$ or natural frequency f_n.

The entertainment band is between reduced velocities U_{r1} and U_{r2}.

$$U_{r1} < U/(f_nD) < U_{r2} \tag{2a}$$

or equivalently, in terms of shedding frequency

$$\mathrm{St}U_{r1}f_n < f_s < \mathrm{St}U_{r2}f_n \tag{2b}$$

or equivalently, in terms of natural frequency

$$f_s/\mathrm{St}U_{r2} < f_n < f_s/\mathrm{St}U_{r1} \tag{2c}$$

Figures 2, 3, 5, 7, 9, and 11 suggest the following entrained response band limits.

Inline motion is $U_{r1}=1/4\mathrm{St}$ $U_{r2}=4.5$

$$\text{Transverse motion is} \quad U_{r1} = 0.9/\text{St}, \quad U_{r2} = U_{r1}(U_{r2}/U_{r1}|_{\text{Eq.1}}) \tag{3}$$

For St=0.2 [26] and $m/\rho D^2 \geq 2.8$, this results in entrainment bands as a function of the stationary cylinder shedding frequency, as seen in Eq. (2*c*) and Figs. 3 and 11.

$$\text{inline is} \quad 0.25f_n < f_s < 0.9f_n$$

$$\text{transverse is} \quad 0.9f_n < f_s < 2f_n \tag{4}$$

Often, the flow velocity U can vary from zero to a maximum value $U_{\max}$ where $f_{s\,\max}=\text{St}U_{\max}/D$. To avoid all entrainment bands from zero to $U_{\max}$ the natural frequency must exceed the shedding frequency at the band lower limit (U_{r1}).

$$f_n > f_{s\,\max}/\text{St}U_{r1} = \begin{cases} 4f_{s\,\max} & \text{inline} \\ 1.1f_{s\,\max} & \text{transverse} \end{cases} \tag{5}$$

The inline criterion is governing; however, many designs maybe able to tolerate the 0.12 D amplitudes (Figs. 6–8 and 11) produced by inline resonance of lightly damped cylinders.

Figures 2, 3, 6, 7, and 11 show that damping can suppress cylinder response in the entrainment bands. The required reduced damping for $A_x/D < 0.02$ is

$$\text{Inline response suppression:} \quad 2m(2\pi\zeta)/\rho D^2 \geq 2 \tag{6a}$$

and for $A_y/D \leq 0.05$

$$\text{Transverse response suppression:} \quad 2m(2\pi\zeta)/\rho D^2 > 30 \tag{6b}$$

If the structure is within the entrainment band and has less damping than indicated by Eqs. (6*a*) and (6*b*) then a more detailed analysis can be applied to determine its amplitude, Eq. 29 of Ref. [26], or strakes (Fig. 10) can be applied.

5 Conclusions

Tests have been made of the vortex-induced vibration of an elastically supported cylinder in water as a function of flow velocity, damping, mass ratio, inline and transverse degrees-of-freedom, Reynolds number, and strake configuration.

1. At small amplitude below 0.1–0.2 diameters amplitude, the cylinder displacement time history trace is irregular and unsteady. The unsteadiness at lower amplitudes seems to be associated lack of spanwise coherence and unstable shedding at the stationary cylinder shedding frequency and the cylinder natural frequency; both frequencies appear in the cylinder response. Above 0.7 diameters amplitude the time histories are more or less sinusoidal, indicating lock-in (synchronization and/or entrainment) at a single frequency has occurred between shedding and cylinder motion
2. The entrainment or lock-in band of reduced velocities where lightly damped cylinders oscillate sinusoidally transverse to the flow begins near the stationary cylinder shedding resonance (f_s=0.9 to 1.0 f_n). Within the band, heavy cylinders ($m/\rho D^2 > 5$) oscillate at or very nearly at the cylinder natural frequency but light cylinders' ($m/\rho D^2 < 2.8$) frequency increases with velocity $f \geq 0.6$ StU/D and 0.9 f_n across the band reaching 50% above the cylinder natural frequency. Entrainment band width increases as mass ratio decreases (Eq. (1)).
3. The two degrees-of-freedom cylinder orbits in the $x-y$ plane in a wind-blown figure 8 with its tips pointing downstream above about 0.7 diameter amplitude. The inline frequency is approximately twice the transverse frequency. The inline-to-transverse amplitude ratio A_x/A_y of the figure 8 and the amplitude A_y are a function of both damping and mass ratio where as transverse-only motion maximum amplitude is a function of reduced damping alone. Two degrees-of-freedom motion has a larger velocity entrainment band than transverse-only motion. There is a hysteresis associated with the transition from transverse motion to larger amplitude two degrees-of-freedom figure 8 motion.
4. Maximum resonant amplitude of lightly damped smooth cylinders increased with increasing Reynolds number between 200 and 120,000. At Reynolds number of 120,000, the amplitude dropped by a factor of two when the surfaced was significantly roughened. The measured maximum amplitude was 1.75 diameters for a smooth two degrees-of-freedom cylinder at Reynolds number of 139,000.
5. Reduced damping above $2m(2\ \zeta)/\rho D^2 = 30$ reduces maximum transverse resonant cylinder amplitude to 5% of cylinder diameter. Reduced damping above $2m(2\pi\zeta)/\rho D^2 = 2$ reduces one degree-of-freedom inline resonant vibration to less than 2% of cylinder diameter.
6. The inline cylinder motion occurs twice the shedding frequency in two adjacent inline bands: $3 \geq U/f_n D > 1.2$ and $4.5 \geq U/f_n D > 3$. In the first band, twice the stationary cylinder shedding frequency (Eq. (1)) is just below the cylinder still water natural frequency $2f_s \leq f_n$. In the second band, twice the shedding frequency is just above the natural frequency $2f_s \geq f_n$ and the cylinder describes a figure 8 when permitted to have both inline and transverse motion. Maximum inline amplitudes are one-tenth of transverse motion amplitudes for 0.002 damping.
7. Continuous 7%, 10%, and 13% high strakes running the full length of the cylinder are effective suppressors of vortex-induced vibration but the performance of low strakes is sensitive to local strake defects. Removing strakes from 10% of the length of a cylinder with 7% high strakes produced about a factor of four increase in the cylinder amplitude at the worst orientation. Removing strakes from 10% of the length of a cylinder of the 10% and 13% high strakes did not significantly change the cylinder response.

Acknowledgment

This work was supported in part by the Pressure Vessel Research Council. The authors acknowledge the craftsmanship of John Lyons and Dave Aglietti of Scripps and Roland Dexter in building the experimental apparatus.

Nomenclature

- A_y = amplitude of vibration, transverse to tube axis and flow
- A_x = amplitude of vibration in line with flow
- C_D = drag coefficient, drag force/$(1/2)\rho U^2 DL$, dimensionless
- D = cylinder outside diameter
- L = span of cylinder in water, 112.5 cm (44.3 in.) typical
- $\text{Re}=UD/\nu$ = Reynolds number
- St = Strouhal number for stationary cylinder, dimensionless
- U = freestream flow velocity
- $U_r=U/f_n D$ = reduced velocity, dimensionless
- f = cylinder oscillation frequency, Hz
- f_o = natural frequency in still air, Hz
- f_n = natural frequency in still water, 1.2 Hz typical
- f_s = StU/D stationary cylinder vortex shedding frequency, Hz
- f_x, f_y = frequencies of inline and transverse motions, respectively
- m = mass of cylinder per unit length of cylinder; still water added mass and live suspension components divided wetted length L of cylinder
- $m/\rho D^2$ = mass ratio, dimensionless (identical to $(\pi/4)(m^*+C_a)$ of Ref. [6])

t = time
x = direction of freestream flow, inline direction
y = direction perpendicular to freestream flow, transverse
z = direction along cylinder axis
ρ = fluid mass density; 998.6 kg/m^3 (62.343 lb/ft^3) typical
ζ = damping factor in still air with fluid added mass, $\zeta\% = 100\zeta$, dimensionless
ν = kinematic viscosity. 0.01054 cm^2/s (1.14×10^{-5} ft^2/s) typical
δ_r = $2m(2\pi\zeta)/\rho D^2$ reduced damping based on in-air damping factor and in-water mass

References

[1] Gabbai, R. D., and Benaroya, H., 2005, "An Over View of Modeling and Experiments of Vortex-Induced Vibration," J. Sound Vib., **282**, pp. 575–616.
[2] Williamson, C. H. K., and Govardhan, R., 2004, "Vortex-Induced Vibrations," Annu. Rev. Fluid Mech., **36**, pp. 413–455.
[3] Norberg, C., 2003, "Fluctuating Lift on a Circular Cylinder: Review and New Measurements," J. Fluids Struct., **17**, pp. 57–96.
[4] Sarpkaya, T., 1979, "Vortex-Induced Oscillations," ASME J. Appl. Mech., **46**, pp. 241–258.
[5] Sarpkaya, T., 2004, "A Critical Review of the Intrinsic Nature of Vortex Induced Vibrations," J. Fluids Struct., **19**, pp. 389–447.
[6] Khalak, A., and Williamson, C. H. K., 1999, "Motions, Forces and Mode Transitions in Vortex-Induced Vibrations at Low Mass-Damping," J. Fluids Struct., **13**, pp. 813–851.
[7] Griffin, O. M., and Hall, M. S., 1991, "Review-Vortex Shedding Lock-on and Flow Control in Bluff Body Wakes," ASME J. Fluids Eng., **113**, pp. 526–537.
[8] Blevins, R. D., 1990, *Flow-Induced Vibration*, 2nd ed., Krieger, Malabar, FL.
[9] Bearman, P. W., 1984, "Vortex Shedding From Oscillating Bluff Bodies," Annu. Rev. Fluid Mech., **16**, pp. 195–222.
[10] King, R., 1977, "A Review of Vortex Shedding Research and Its Applications," Ocean Eng., **4**, pp. 141–171.
[11] Leinhard, J. H., 1966, "Synopsis of Lift, Drag, and Vortex Frequency Data for Rigid Circular Cylinders," Washington State University College of Engineering, Research Division Bulletin 300.
[12] Griffin, O. M., and Ramberg, S. E., 1974, "The Vortex Street Wakes of Vibrating Cylinders," J. Fluid Mech., **66**, pp. 553–576.
[13] Williamson, C. H. K., and Roshko, A., 1988, "Vortex Formation in the Wake of an Oscillating Cylinder," J. Fluids Struct., **2**, pp. 355–381.
[14] Jeon, D., and Gharib, M., 2004, "On the Relationship Between the Vortex Formation Process and Cylinder Wake Vortex Patterns," J. Fluid Mech., **519**, pp. 161–181.
[15] Prasanth, T. K., and Mittal, S., 2008, "Vortex-Induced Vibrations of a Circular Cylinder at Low Reynolds Numbers," J. Fluid Mech., **594**, pp. 463–491.
[16] Williamson, C. H. K., and Jauvtis, N., 2004, "A High Amplitude 2Y Mode of Vortex-Induced Vibration for a Light Body in XY Motion," Eur. J. Mech. B/Fluids, **23**, pp. 107–114.
[17] Laneville, A., 2006, "On Vortex-Induced Vibrations of Cylinders Describing X-Y Trajectories," J. Fluids Struct., **22**, pp. 773–782.
[18] Sanchis, A., Saelevik, G., and Grue, J., 2008, "Two Degrees-of-Freedom Vortex-Induced Vibrations of a Spring Mounted Rigid Cylinder With Low Mass Ratio," J. Fluids Struct., **24**, pp. 907–919.
[19] Carberry, J., and Sheridan, J., 2007, "Wake States of a Tethered Cylinder," J. Fluid Mech., **592**, pp. 1–21.
[20] Govardhan, R. N., and Williamson, C. H. K., 2006, "Defining the Modified Griffin Plot in Vortex Induced Vibration," J. Fluid Mech., **561**, pp. 147–180.
[21] Klamo, J. T., Leonard, A., and Roshko, A., 2006, "The Effects of Damping on the Amplitude and Frequency Response of a Freely Vibrating Cylinder in Cross Flow," J. Fluids Struct., **22**, pp. 845–856.
[22] Jauvtis, N., and Williamson, C. H. K., 2004, "The Effect of Two Degrees of Freedom on Vortex-Induced Vibration and at Low Mass and Damping," J. Fluid Mech., **509**, pp. 23–62.
[23] Vandiver, J. K., 1993, "Dimensionless Parameters Important to the Prediction of Vortex-Induced Vibration of Long Flexible Cylinders in Ocean Currents," J. Fluids Struct., **7**, pp. 423–455.
[24] Skop, R. A., and Balasubramanian, S., 1997, "A New Twist on an Old Model for Vortex-Excited Vibrations," J. Fluids Struct., **11**, pp. 395–412.
[25] Battelle Memorial Institute, 2008, "Metallic Material Properties Development and Standardization," MMPDS-04, Chap. 9.
[26] Blevins, R. D., 2009, "Models for Vortex-Induced Vibration of Cylinders Based on Measured Forces," J. Fluids Eng., **131**, p. 101203.
[27] Feng, C. C., 1968, "The Measurement of Vortex-Induced Effects in Flow Past Stationary and Oscillating Circular and D-Section Cylinders," MS thesis, University of British Columbia.
[28] Blevins, R. D., and Burton, T. E., 1976, "Fluid Forces Induced by Vortex Shedding," ASME J. Fluids Eng., **95**, pp. 19–24.
[29] Govardhan, R., and Williamson, C. H. K., 2004, "Critical Mass in Vortex-Induced Vibration of a Cylinder," Eur. J. Mech. B/Fluids, **23**, pp. 17–27.
[30] Khalak, A., and Williamson, C. H. K., 1997, "Investigation of Relative Effects of Mass and Damping in Vortex-Induced Vibration," J. Wind. Eng. Ind. Aerodyn., **69**, pp. 341–350.
[31] Allen, D., and Henning, D. L., 2001, "Surface Roughness Effects on Vortex-Induced Vibration at Critical and Supercritical Reynolds Numbers," Offshore Technology Conference, Paper No. OCT 13302.
[32] Alexander, C. M., 1981, "The Complex Vibrations and Implied Drag of a Long Oceanographic Wire in Cross-Flow," Ocean Eng., **8**, pp. 379–406.
[33] Staubli, T., 1983, "Calculation of the Vibration of an Elastically Mounted Cylinder Using Experimental Data From Forced Oscillation," ASME J. Fluids Eng., **105**, pp. 225–229.
[34] Vandiver, J. K., and Jong, J.-K., 1987, "The Relationship Between In-Line and Cross Vortex-Induced Vibration of Cylinders," J. Fluids Struct., **1**, pp. 381–399.
[35] Vandiver, J. K., Jaiswal, V., and Jhingran, V., 2009, "Insight on Vortex-Induced, Traveling Waves on Long Risers," J. Fluids Struct., **25**, pp. 641–651.

Models for Vortex-Induced Vibration of Cylinders Based on Measured Forces

Robert D. Blevins
Goodrich,
850 Lagoon Drive,
Chula Vista, CA 91910

This paper develops experimentally based nonlinear models for the vortex shedding forces on oscillating cylinders. The lift in-phase and out-of-phase with cylinder motion and mean drag are determined from experiments with cylinder amplitudes from 0.05 cm to 1.5 cm, and reduced velocities between 2 and 12. The results are reduced to a uniform grid, tabulated, and applied to prediction of resonant, nonresonant, and time history vortex-induced vibration. The results are reduced to a uniform grid, tabulated, and applied to prediction of resonant, nonresonant and time history vortex-induced vibration.
[DOI: 10.1115/1.3222906]

1 Introduction

It is well known that cylinders in steady cross flow shed vortices that create the periodic vortex street, as shown in Fig. 1 [1], and induce vibration of elastic cylinders such as pipelines, thermowells, and stacks [2–5]. However, accurate prediction of vortex-induced vibration has proved difficult, owing to nonlinear fluid forces and feedback between the cylinder and the fluid flow [5–11]. This paper develops experimentally based models for the forces imposed by the periodic vortex shedding on oscillating cylinders. These are applied to prediction of vortex-induced vibration of elastic structures in fluid flow.

Figure 2 presents existing measurements for maximum amplitude of lightly damped elastic cylinders (top), Strouhal number (middle), and drag coefficient of stationary cylinders (bottom) as functions of Reynolds number $\mathrm{Re}=UD/\nu$, where ν is the fluid kinematic viscosity [6,12–22]. The Strouhal number (St) is the dimensionless proportionality constant between the vortex shedding frequency (f_s) from a stationary cylinder in Hz and the freestream velocity (U) divided by the cylinder diameter (D) in the same unit system.

$$f_s = \mathrm{St}U/D \tag{1}$$

It is also the frequency of oscillating lift forces on a stationary cylinder. The mean drag coefficient is defined as

$$C_{Do} = F_D/[(1/2)\rho U^2 DL] \tag{2}$$

where F_D is the mean drag force, which is the force in the direction of freestream flow on a cylinder length L in a cross flow averaged over many vortex shedding cycles, and ρ is the fluid density.

Below about $\mathrm{Re}=5\times10^5$, the Strouhal number and drag coefficient for a stationary cylinder are functions of the Reynolds number. Above about $\mathrm{Re}=10^5$ they are also functions of the cylinder surface roughness k. Above 5×10^5, they are nearly independent of Reynolds number for rough surface cylinders [14,21]. Empirical fits have been made to the Strouhal number data for rough surface stationary cylinders in Fig. 2.

$$\mathrm{St} = \begin{cases} 0.22(1-22/\mathrm{Re}), & 45 \le \mathrm{Re} < 1300 \\ 0.213 - 0.0248(\log_{10}\mathrm{Re}/1300)^2 + 0.0095(\log_{10}\mathrm{Re}/1300)^3 & \\ \qquad\qquad 1300 \le \mathrm{Re} < 5\times10^5 & \\ 0.22, \quad 5\times10^5 < \mathrm{Re} < 10^7 & \end{cases} \tag{3}$$

The first and last expression are based on Refs. [14,21,22]. The middle expression is a fit to the data of Norberg [13] between $1300<\mathrm{Re}<5\times10^5$. Also see Refs. [7,23].

2 Models for Vortex-Induced Forces on Cylinders

Vortex-induced fluid forces on oscillating cylinders are functions of the cylinder motion. Cylinder vibration, at or near the shedding frequency with amplitude above about a few percent of cylinder diameter, increases the strength of the shed vortices and the spanwise correlation of the wake, and shifts the vortex shedding frequency from the stationary cylinder shedding frequency (Eq. (1)) toward the cylinder vibration frequency [8–11,24–27], which is called lock-in, entrainment, or synchronization. As a result lift measured on a stationary cylinder is not generally a reliable predictor of vortex-induced cylinder motion.

Three models for the time dependent fluid dynamic forces per unit span on a cylinder in the direction of displacement $y(t)$ are (a) the oscillating drag model for oscillations in still fluid, (b) lift coefficient model with forcing at the stationary shedding frequency f_s (Eq. (1)), and (c) the two parameter self-excitation model of Hartlen and Currie [28] and Sarpkaya [29] with in-phase and out-of-phase forces at cylinder oscillation frequency f.

$$F_y = -(1/2)\rho|\dot{y}|\dot{y}DC_D - \rho(\pi/4)D^2C_a\ddot{y}, \quad (U=0) \tag{4a}$$

$$F_y = (1/2)\rho U^2 DC_L \sin(2\pi f_s t + \varphi) \tag{4b}$$

$$F_y = (1/2)\rho U^2 DC_{mv}\sin(2\pi ft) - (1/2)\rho U^2 DC_{dv}\cos(2\pi ft) \tag{4c}$$

The over dot ($\bullet$) denotes differentiation with respect to time. If the cylinder motion is harmonic in time with amplitude A_y and frequency f in Hz, that is

Contributed by the Fluids Engineering Division of ASME for publication in the JOURNAL OF FLUIDS ENGINEERING. Manuscript received May 20, 2008; final manuscript received July 26, 2009; published online September 30, 2009. Assoc. Editor: Joseph Katz.

Fig. 1 Vortex street behind a stationary cylinder [1]

$$y(t) = A_y \sin(2\pi ft), \quad \frac{dy}{dt} = A_y(2\pi f)\cos(2\pi ft), \quad \frac{d^2y}{dt^2} = -A_y(2\pi f)^2\sin(2\pi ft) \tag{5}$$

then there are relationships between the dimensionless force coefficients in Eqs. (4*a*)–(4*c*). These are

$$C_{mv} = 2\pi^3\left(\frac{fD}{U}\right)^2\frac{A_y}{D}C_a \tag{6a}$$

$$C_{dv} = \frac{32\pi}{3}\left(\frac{A_y}{D}\frac{fD}{U}\right)^2 C_D \tag{6b}$$

and if the stationary cylinder shedding frequency equals the oscillation frequency $f_s = f$ then

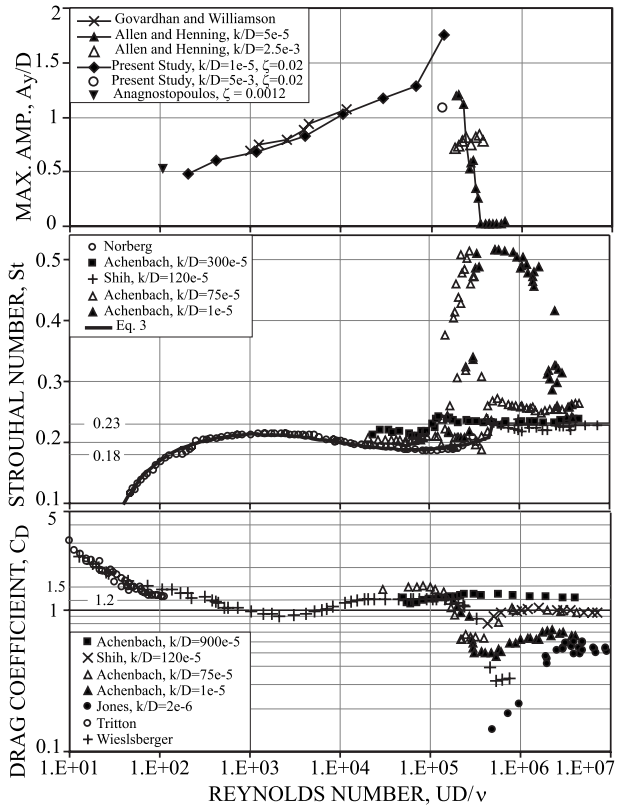

Fig. 2 Maximum transverse amplitude of lightly damped elastically supported cylinders, Strouhal number, and drag coefficient of stationary cylinders as functions of Reynolds number [6,12,18–22]. Equations (1)–(3). At top, $2^{1/2}$ was used to convert rms to peak in Ref. [18].

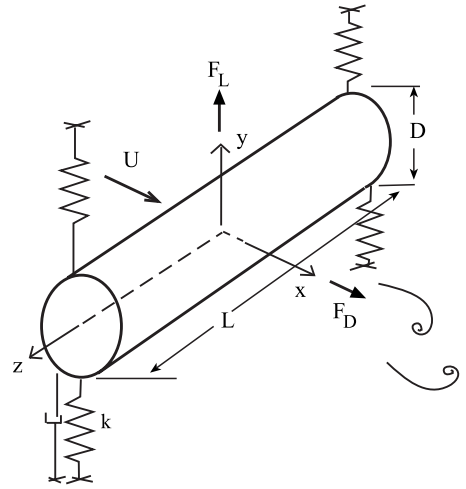

Fig. 3 Idealized spring supported damped cylinder

$$C_L\cos\varphi = C_{mv}, \quad C_L\sin\varphi = -C_{dv}, \quad C_L^2 = C_{mv}^2 + C_{dv}^2$$

$$C_{mv} = (1-(\mathrm{St}U/f_nD)^2)C_L/\sqrt{[(1-(\mathrm{St}U/f_nD)^2\ ]^2 + (2\zeta_n\mathrm{St}U/f_nD)^2} \tag{7}$$

$$C_{dv} = -2\zeta_n(\mathrm{St}U/f_nD)C_L/\sqrt{[(1-(\mathrm{St}U/f_nD)^2\ ]^2 + (2\zeta_n\mathrm{St}U/f_nD)^2}$$

The C_{dv} relationship in Eq. (6*b*) applies to the first Fourier series term for oscillating drag $|\cos\omega t|\cos\omega t \approx (8/3\pi)\cos\omega t$. The phase φ in Eq. (7) comes from Eq. (19*a*). Measured values of C_{mv} in the paper are normalized to zero for still water added mass $C_a = 1$.

Flow visualization experiments [2,25,26] and force and response measurements [6,29] show that the vortex wake and the dimensionless coefficients C_a, C_D, C_{mv}, and C_{dv} are functions of A_y/D and $\mathrm{St}U/fD$. Experiments [4,29–37] have measured the fluid force on cylinders undergoing forced motion in a flow. An alternate approach is taken here. C_a, C_D, C_{mv}, and C_{dv} are computed from a test program of natural vortex-induced vibration [19,38].

3 Added Mass and Fluid Damping From Free Decay Measurements

Consider the free decay of a damped elastically supported cylinder (Fig. 3) in a fluid modeled with Eq. (4*a*). The equation of motion of cylinder displacement $y(t)$ is

$$m_o\ddot{y} + 2m_o\zeta_o(2\pi f_o)\dot{y} + m_o(2\pi f_o)^2 y = F_y = -(1/2)\rho|\dot{y}|\dot{y}DC_D - \rho(\pi/4)D^2C_a\ddot{y} \tag{8}$$

where structural quantities are on the left, while fluid forces are on the right, and m_o is the dry mass of cylinder per unit length. Linearization of the nonlinear drag term, as performed earlier, allows an exact solution for the decaying oscillations with $\zeta < 1$ [39].

$$y(t) = A_y e^{-\zeta(2\pi f)t}\cos 2\pi f(1-\zeta^2)^{1/2}t \tag{9a}$$

$$\zeta = \zeta_o\frac{m_o}{m}\frac{f_o}{f} + \frac{2}{3\pi}\frac{\rho D^2}{m}\frac{A_y}{D}C_D, \quad f = f_o\sqrt{\frac{m_o}{m_o + \rho(\pi/4)D^2C_a}} \tag{9b}$$

An elastically suspended cylinder with a diameter of 6.35 cm [19] was off set and released in an otherwise still water. Measured amplitudes A_{yi} $(i=1,2,3\ldots N)$ of successive cycles during free decay were used to determine damping $\zeta = [1/(2\pi N)]\ln(A_i/A_{i+N})$. The corresponding frequencies f_i $(i=1,2,3\ldots N)$ are the inverse

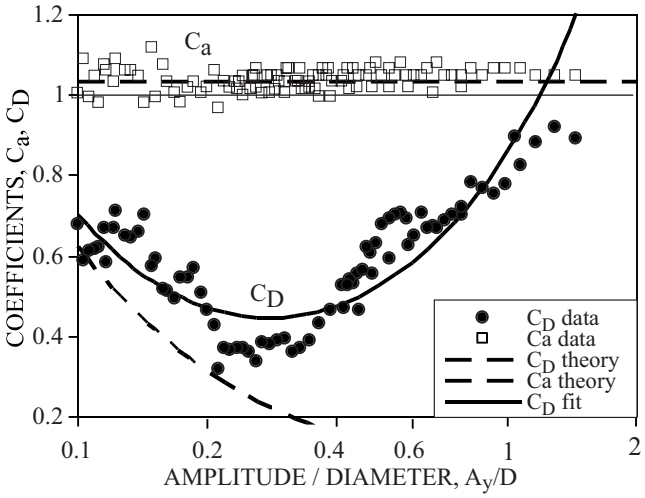

Fig. 4 Added mass and drag coefficients measured in still water in comparison with theory (Eq. (11))

of the time between successive peaks. These were used with Eq. (9*b*) to compute the added mass and drag coefficients of the oscillating cylinder as a function of its amplitude.

$$C_a = \frac{4}{\pi}\frac{m_o}{\rho D^2}\left[\left(\frac{f_o}{f}\right)^2 - 1\right], \quad C_D = \frac{3\pi}{2}\frac{m}{\rho D^2}\frac{D}{A_y}\left(\zeta - \zeta_o\frac{f_o}{f}\frac{m_o}{m}\right) \tag{10}$$

In air $f_o \approx 1.3$ Hz and $\zeta_o \approx 0.002$. There is also a stiffness correction for cylinder buoyancy.

Values of C_D and C_a measured in still water ($fD^2/\nu = 4550$, $\nu = 1.08\times10^{-6}$ m^2/s, $f \sim 1.2$ Hz, $D = 6.35$ cm) are plotted in Fig. 4 in comparison with theoretical viscous fluid solutions [40,41]

$$C_a = 1 + 4(\nu/\pi D^2 f)^{1/2} + (\nu/\pi D^2 f)^{3/2}, \tag{11a}$$

$$C_D = (3\pi^2/4)(D/A_y)(\nu/\pi D^2 f)^{1/2} \tag{11b}$$

The average measured added mass coefficient (1.038) is within 1% of the theoretical value (1.032). Measured drag coefficients exceed the theory, consistent with Refs. [42–44]. The drag coefficient has a minimum amplitude diameter near 0.3 cm [44,45]. C_D increases beyond diameter of 0.3, owing to separation and shed vortices [42–48]. The following expression correlates drag on oscillating cylinders in still water as the sum of viscous (Eq. (11*b*)) and amplitude-dependent components:

$$C_D = \frac{3\pi^{3/2}}{4}\frac{D}{A_y}\left(\frac{\nu}{fD^2}\right)^{1/2} + 0.8\frac{A_y}{D} \quad 0 < \frac{A_y}{D} < 1.5 \tag{12}$$

Next, the cylinder was off set transversely and released in water flowing at velocities from 15 cm/s to 92 cm/s. Measured cylinder damping and frequency in the initial decay are converted to fluid force coefficients C_{dv} and C_{mv} by the same process used for still water but starting with Eq. (15) instead of Eq. (8) to invoke the two parameter model. The following expressions correlate the measured C_{mv}, C_{dv}, and mean drag $C_D = 2F_D/\rho U^2 L$ for $1.5 > A_y/D > 0$ and $2.1 \geq \mathrm{St}U/fD \geq 0.4$ as functions of the cylinder amplitude and reduced velocity based on vibration frequency f.

$$C_{dv} = 0.4\pi(A_y/D)(fD/U) + (32\pi/3)(A_y/D)^2(fD/U)^2 C_{Do}$$

$$C_{mv} = F(\mathrm{St}U/fD)A_y/D \tag{13}$$

$$C_D = C_{Do} + 2(A_y/D)(1 - 0.45\mathrm{St}U/fD)$$

where C_{dv} is positive for the decaying oscillations. C_{mv} changes sign across resonance $\mathrm{St}U/fD \sim 1$. The function $F(\mathrm{St}U/fD)$ is approximated by line segments through points $(\mathrm{St}U/fD, F) = (0.3,0)$, $(0.6,1.25)$, $(1,1.25)$, $(1.05,-1.8)$ $(1.7,-1.8)$, $(3.5,0)$.

Hydrodynamic cylinder damping is obtained by substituting C_D (Eq. (12)) into Eq. (9*b*) for still water and C_{dv} (Eq. (13)) into Eq. (15) for water with freestream velocity U

$$\zeta_f = \begin{cases} \dfrac{\pi^{1/2}}{2}\dfrac{\rho D^2}{m}\left(\dfrac{\nu}{fD^2}\right)^{1/2} + \dfrac{1.6}{3\pi}\dfrac{\rho D^2}{m}\left(\dfrac{A_y}{D}\right)^2 & \text{for still fluid} \\ \dfrac{0.1}{4\pi}\dfrac{\rho D^2}{m}\dfrac{U}{fD} + \dfrac{2}{3\pi}\dfrac{\rho D^2}{m}\dfrac{A_y}{D}C_{Do} & \text{for moving fluid} \end{cases} \tag{14}$$

The first term in the moving fluid damping is similar in magnitude to that of Vandiver [49], but he does not include the second, amplitude-dependent, term. The still fluid damping expression is similar to that of Skop [44] but with a quadratic fit.

4 Fluid Force From Steady-State Response Measurements in Flowing Water

Measured cylinder amplitude and frequency during steady-state vortex-induced cylinder vibration are used to determine the vortex-induced fluid forces. The equation for steady self-excited vortex induced vibrations of an elastically supported cylinder (Fig. 3) in cross flow with the two parameter lift force model (Eq. (4*c*))

$$m\ddot{y} + 2m\zeta_n\omega_n\dot{y} + ky = F_y = \frac{1}{2}\rho U^2 D C_{mv}\sin(2\pi ft) - \frac{1}{2}\rho U^2 D C_{dv}\cos(2\pi ft) \tag{15}$$

is solved with Eq. (5) by separating in-phase and out-of-phase components to give C_{mv} and C_{dv} as functions of oscillation frequency f and cylinder amplitude A_y

$$C_{mv} = 8\pi^2\mathrm{St}^2\frac{m}{\rho D^2}\frac{A_y}{D}\left(1 - \frac{f^2}{f_n^2}\right)\left(\frac{\mathrm{St}U}{f_n D}\right)^{-2} \tag{16a}$$

$$C_{dv} = -4\pi\mathrm{St}^2\frac{2m(2\pi\zeta_n)}{\rho D^2}\frac{A_y}{D}\frac{f}{f_n}\left(\frac{\mathrm{St}U}{f_n D}\right)^{-2} \tag{16b}$$

where ζ_n is the structural damping factor measured in still air with the cylinder weighted to simulate the still water added mass.

Tests. Steady-state cylinder amplitude A_y and frequency f were measured during a series of tests with water velocities between 15 cm/s and 92 cm/s in steps of 1 cm/s, corresponding to $2 < U/f_n D < 12$ with a 6.35 cm (2.5 inch) diameter cylinder [19]. Reynolds number range from 10,000 to 80,000. At each velocity, the structural (magnetic) damping factor varied between 0.002 and 0.4 to achieve the target amplitudes A_y/D between 0.05 and 1.45 in steps of 0.1. Measured amplitude, frequency, and drag were converted to C_{mv}, C_{dv}, and C_D with Eqs. (2), (16*a*), and (16*b*).

Measured Coefficients. Triplets of $C_{mv}[A_y/D, \mathrm{St}U/fD]$, $C_{dv}[A_y/D, \mathrm{St}U/fD]$, and $C_D[A_y/D, \mathrm{St}U/fD]$ from approximately 1000 tests were reduced to a uniform grid by sorting them into $15\times18 = 270$ cells with A_y/D ranging from 0 to 1.5 in steps of 0.1 and $\mathrm{St}U/(fD)$ from 0.4 to 2.4 in steps of 0.1. Decay tests (described above as $C_{dv} > 0$) were used to fill cells for nonexcited cases.

A typical table cell has about four measured points. Every cell has at least one measured data point with the exception of the two cells centered at $A_y/D = 0.05$ and $1.4 < \mathrm{St}U/fD < 1.6$, where no response was observed; their values are interpolated. Tests on cell boundaries were removed and the cell average was taken. The results are shown in Tables 1–3 for transverse-only motion.

Trends can be seen in the tables. C_{mv} is positive for $f/f_n > 1$ and negative for $f/f_n < 1$. C_{dv} is negative for all cases with steady-

Table 1 C_{mv} for transverse motion

StU/fD Ay/D	0.5 to 0.6	0.6 to 0.7	0.7 to 0.8	0.8 to 0.9	0.9 to 1.0	1.0 to 1.1	1.1 to 1.2	1.2 to 1.3	1.3 to 1.4	1.4 to 1.5	1.5 to 1.6	1.6 to 1.7	1.7 to 1.8	1.8 to 1.9	1.9 to 2.0	2.0 to 2.1	2.1 to 2.2	2.2 to 2.3
0 to 0.1	0.032	0.082	0.106	0.086	0.100	-0.126	**-0.087**	-0.231	**-0.090**	**-0.090**	**-0.090**	**-0.090**	**-0.088**	**-0.083**	**-0.158**	**-0.134**	**-0.090**	**-0.094**
0.1 to 0.2	0.063	0.164	0.201	0.158	0.184	0.852	0.125	-0.337	**-0.463**	**-0.367**	**-0.292**	**-0.238**	**-0.376**	**-0.291**	**-0.255**	**-0.204**	**-0.194**	**-0.193**
0.2 to 0.3	0.119	0.278	0.350	0.273	0.312	0.852	1.237	0.162	**-0.433**	**-0.547**	**-0.471**	**-0.410**	**-0.486**	**-0.414**	**-0.398**	**-0.387**	**-0.320**	**-0.292**
0.3 to 0.4	0.145	0.408	0.501	0.394	0.465	**-0.101**	1.121	0.564	**-0.336**	**-0.626**	**-0.660**	**-0.581**	**-0.669**	**-0.587**	**-0.547**	**-0.527**	**-0.412**	**-0.438**
0.4 to 0.5	0.208	0.522	0.644	0.448	0.575	0.036	1.147	0.533	**-0.371**	**-0.675**	**-0.733**	**-0.672**	**-0.844**	**-0.757**	**-0.750**	**-0.658**	**-0.547**	**-0.616**
0.5 to 0.6	0.266	0.635	0.800	0.606	0.686	**-0.181**	1.279	0.535	**-0.421**	**-0.736**	**-0.870**	**-1.044**	**-1.069**	**-0.941**	**-0.916**	**-0.798**	**-0.708**	**-0.735**
0.6 to 0.7	0.323	0.781	0.953	0.573	0.815	**-0.366**	1.552	0.544	**-0.547**	**-0.801**	**-0.878**	**-1.250**	**-1.284**	**-1.111**	**-1.085**	**-0.996**	**-0.815**	**-0.838**
0.7 to 0.8	0.423	0.855	1.085	0.789	0.945	**-0.190**	**-1.475**	0.504	**-0.540**	**-0.710**	**-1.140**	**-1.459**	**-1.457**	**-1.270**	**-1.226**	**-1.138**	**-0.941**	**-0.970**
0.8 to 0.9	0.506	0.964	1.252	0.929	1.116	**-0.194**	**-1.597**	0.466	**-0.569**	**-1.362**	**-1.291**	**-1.614**	**-1.656**	**-1.452**	**-1.390**	**-1.289**	**-1.093**	**-1.096**
0.9 to 1.0	0.609	1.100	1.359	0.998	1.220	**-0.316**	1.500	0.483	**-0.181**	**-1.580**	**-1.440**	**-1.793**	**-1.845**	**-1.623**	**-1.553**	**-1.441**	**-1.217**	**-1.225**
1.0 to 1.1	0.514	1.233	1.574	1.182	1.338	**-0.455**	0.909	0.357	**-0.345**	**-1.748**	**-1.583**	**-1.998**	**-2.040**	**-1.807**	**-1.706**	**-1.588**	**-1.347**	**-1.374**
1.1 to 1.2	0.755	1.331	1.670	1.267	1.407	**-0.284**	0.446	-0.010	**-0.401**	**-1.898**	**-1.747**	**-2.158**	**-2.280**	**-1.945**	**-1.880**	**-1.726**	**-1.462**	**-1.485**
1.2 to 1.3	0.818	1.447	1.815	1.253	1.604	**-0.126**	**-2.374**	**-2.351**	**-1.634**	**-2.077**	**-1.879**	**-2.379**	**-2.468**	**-2.163**	**-2.044**	**-1.896**	**-1.611**	**-1.594**
1.3 to 1.4	0.888	1.563	1.961	1.571	1.733	**-0.333**	**-2.564**	**-2.539**	**-1.759**	**-2.239**	**-2.061**	**-2.551**	**-2.603**	**-2.297**	**-2.207**	**-2.048**	**-1.729**	**-1.741**
1.4 to 1.5	0.370	1.696	2.117	1.528	1.855	**-0.668**	**-2.934**	**-2.774**	**-1.897**	**-2.382**	**-2.233**	**-2.758**	**-2.817**	**-2.477**	**-2.371**	**-2.200**	**-1.866**	**-1.870**

Table 2 C_{dv} for transverse motion

StU/fD Ay/D	0.5 to 0.6	0.6 to 0.7	0.7 to 0.8	0.8 to 0.9	0.9 to 1.0	1.0 to 1.1	1.1 to 1.2	1.2 to 1.3	1.3 to 1.4	1.4 to 1.5	1.5 to 1.6	1.6 to 1.7	1.7 to 1.8	1.8 to 1.9	1.9 to 2.0	2.0 to 2.1	2.1 to 2.2	2.2 to 2.3
0 to 0.1	0.062	0.051	0.034	0.022	0.054	**-0.661**	**-0.423**	**-0.176**	0.010	0.009	0.009	0.008	0.008	0.007	0.005	0.005	0.011	0.018
0.1 to 0.2	0.163	0.158	0.086	0.057	0.108	**-0.021**	**-0.563**	**-0.365**	**-0.238**	**-0.075**	**-0.033**	**-0.015**	0.014	0.011	0.009	0.016	0.053	0.034
0.2 to 0.3	0.388	0.347	0.232	0.137	0.272	**-0.021**	**-0.014**	**-0.461**	**-0.300**	**-0.112**	**-0.042**	**-0.006**	0.019	0.024	0.018	0.062	0.098	0.064
0.3 to 0.4	0.578	0.537	0.390	0.236	0.383	0.200	**-0.017**	**-0.666**	**-0.342**	**-0.222**	**-0.047**	**-0.026**	0.032	0.035	0.089	0.088	0.122	0.139
0.4 to 0.5	0.894	0.687	0.502	0.513	0.398	0.199	**-0.230**	**-0.636**	**-0.336**	**-0.209**	**-0.040**	**-0.010**	0.104	0.153	0.226	0.162	0.209	0.269
0.5 to 0.6	1.282	0.984	0.754	0.580	0.494	0.240	**-0.197**	**-0.641**	**-0.354**	**-0.177**	**-0.034**	0.166	0.472	0.405	0.402	0.419	0.351	0.329
0.6 to 0.7	2.207	1.522	1.001	0.823	0.614	0.624	**-0.044**	**-0.595**	**-0.316**	**-0.094**	**-0.025**	0.151	0.399	0.337	0.390	0.420	0.350	0.284
0.7 to 0.8	3.148	1.710	1.224	0.901	0.704	0.958	0.287	**-0.597**	**-0.212**	**-0.027**	0.446	0.574	0.501	0.790	0.677	0.615	0.467	0.426
0.8 to 0.9	3.610	2.538	1.951	1.397	0.772	0.992	0.873	**-0.546**	**-0.134**	0.531	0.475	0.649	0.644	0.742	0.852	0.775	0.615	0.438
0.9 to 1.0	5.130	3.618	2.314	1.608	1.514	1.564	**-0.090**	**-0.441**	**-0.399**	0.483	0.676	0.647	0.833	0.981	0.953	0.866	0.777	0.539
1.0 to 1.1	6.387	4.465	3.588	2.317	1.971	1.767	**-0.066**	**-0.303**	**-0.220**	0.801	0.622	0.737	0.955	0.998	1.478	1.072	0.818	0.744
1.1 to 1.2	6.210	4.380	3.257	2.840	2.095	1.874	**-0.052**	**-0.053**	**-0.064**	0.544	0.918	0.864	1.168	1.196	1.470	1.270	1.160	0.830
1.2 to 1.3	6.750	4.761	3.542	3.197	2.508	2.150	1.910	1.685	1.491	1.060	0.810	0.827	1.299	1.187	1.597	1.595	1.193	0.876
1.3 to 1.4	8.747	6.170	4.099	3.728	2.786	2.309	2.062	1.820	1.571	1.299	1.231	1.024	1.405	1.471	1.928	1.845	1.379	1.008
1.4 to 1.5	9.700	6.577	4.161	4.687	3.583	2.765	2.243	1.908	2.009	1.551	1.381	1.123	1.759	1.729	2.181	1.982	1.552	1.082

Table 3 C_D for transverse motion

StU/fD Ay/D	0.5 to 0.6	0.6 to 0.7	0.7 to 0.8	0.8 to 0.9	0.9 to 1.0	1.0 to 1.1	1.1 to 1.2	1.2 to 1.3	1.3 to 1.4	1.4 to 1.5	1.5 to 1.6	1.6 to 1.7	1.7 to 1.8	1.8 to 1.9	1.9 to 2.0	2.0 to 2.1	2.1 to 2.2	2.2 to 2.3
0 to 0.1	1.16	0.96	0.93	0.96	1.13	1.07	1.11	1.09	1.11	1.11	1.10	1.11	1.10	1.09	1.13	1.06	1.08	1.01
0.1 to 0.2	1.23	0.98	0.94	1.03	0.93	1.13	1.16	1.09	1.13	1.15	1.15	1.15	1.00	1.00	1.12	1.10	1.11	1.03
0.2 to 0.3	1.31	1.02	0.98	1.09	1.07	1.36	1.36	1.25	1.18	1.19	1.19	1.19	1.06	1.03	1.14	1.16	1.16	1.07
0.3 to 0.4	1.42	1.09	1.04	1.18	1.14	1.56	1.51	1.44	1.27	1.24	1.23	1.20	1.12	1.06	1.19	1.21	1.18	1.13
0.4 to 0.5	1.52	1.17	1.11	1.34	1.32	1.60	1.69	1.63	1.41	1.33	1.24	1.20	1.19	1.12	1.24	1.23	1.24	1.23
0.5 to 0.6	1.68	1.26	1.22	1.44	1.47	1.76	1.73	1.78	1.57	1.51	1.32	1.26	1.29	1.19	1.32	1.29	1.31	1.19
0.6 to 0.7	1.87	1.07	1.34	1.64	1.57	1.93	1.81	1.93	1.74	1.64	1.44	1.39	1.39	1.25	1.35	1.36	1.35	1.25
0.7 to 0.8	2.00	1.49	1.46	1.77	1.71	1.99	2.41	2.09	1.92	1.80	1.64	1.50	1.47	1.30	1.41	1.40	1.41	1.30
0.8 to 0.9	2.01	1.62	1.63	1.97	1.89	2.12	2.54	2.32	2.08	1.93	1.77	1.59	1.56	1.36	1.46	1.45	1.47	1.34
0.9 to 1.0	2.24	1.81	1.76	2.16	2.00	2.27	2.65	2.84	2.47	2.08	1.90	1.69	1.64	1.42	1.51	1.51	1.51	1.38
1.0 to 1.1	2.53	2.02	2.05	2.29	2.13	2.39	3.03	3.06	2.65	2.23	2.03	1.81	1.73	1.49	1.56	1.55	1.56	1.43
1.1 to 1.2	2.69	2.18	2.19	2.73	2.33	2.48	3.33	3.32	2.91	2.37	2.18	1.92	1.79	1.54	1.62	1.60	1.62	1.47
1.2 to 1.3	2.94	2.39	2.42	2.67	2.41	2.60	3.17	3.06	2.90	2.52	2.29	2.02	1.89	1.62	1.67	1.66	1.67	1.51
1.3 to 1.4	3.21	2.62	2.67	2.93	2.55	2.73	3.32	3.22	3.02	2.67	2.46	2.12	1.98	1.66	1.73	1.71	1.70	1.56
1.4 to 1.5	3.47	2.90	2.96	2.93	2.68	2.95	3.51	3.41	3.15	2.80	2.61	2.24	2.08	1.72	1.78	1.76	1.77	1.60

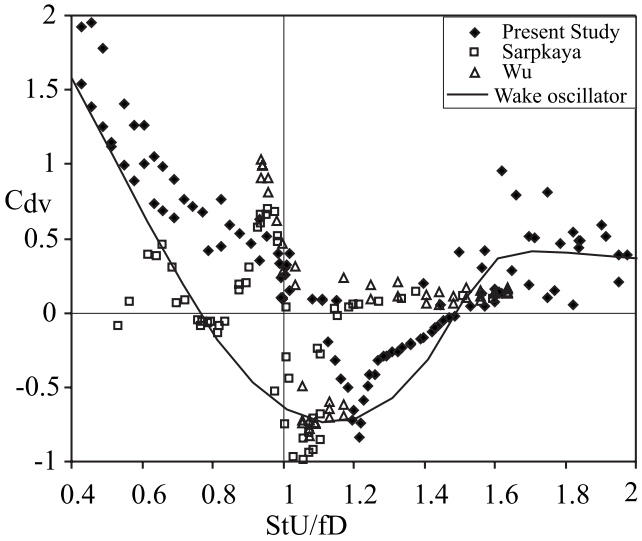

Fig. 5 Measured C_{dv} with StU/fD compared with forced vibration test data [29,50] for $0.5<A_y/D<.6$ and wake oscillator model (Eq. (24))

state cylinder response; it becomes positive at large amplitude, creating damping and limiting the maximum amplitude of vortex-induced vibrations. Negative values of C_{dv} occur between $1 \leq \mathrm{St}U/fD < 1.6$ so large amplitude oscillations have frequencies between the 70% and 100% of the stationary shedding frequency (Fig. 3 (top) [19]). This implies that large extensive entrainment is only possible if the oscillation frequency follows the shedding frequency upward as velocity increases [19]. Measured C_{dv} in Fig. 5 compare well with forced oscillations experiments [29,50] and measured steady drag at maximum resonant response compares well with the correlation of Sparkaya [29] in Fig. 6.

Intermediate values of C_{mv} and C_{dv} are biharmonically interpolated from the tabulated values. For example, C_{mv} at A_y/D and StU/fD is interpolated from the four surrounding C_{mv} values V_1, V_2, V_3, and V_4 counting clockwise from the upper left in Table 1, $a=(V_1+V_2+V_3+V_4)/4$, $b=(-V_1-V_2+V_3+V_4)/2$, $c=(-V_1+V_2+V_3-V_4)/2$, and $d=(V_1-V_2+V_3-V_4)/2$, that is

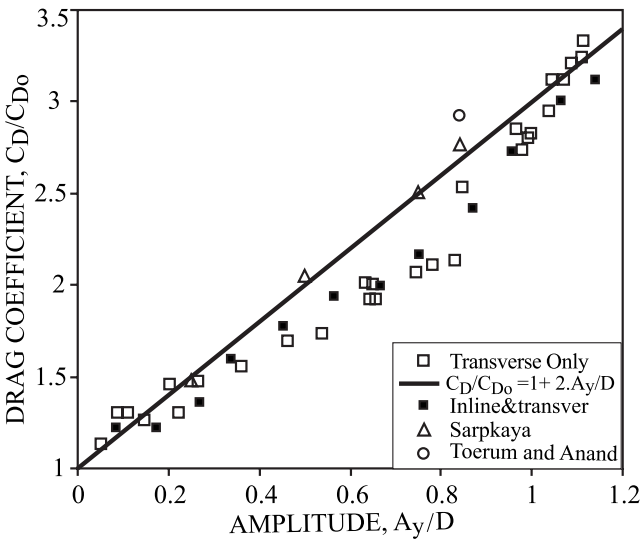

Fig. 6 Drag coefficient at maximum response amplitude: present data, Ref. [19], and Refs. [29,51].

$$C_{mv}(A_y/D, \mathrm{St}U/fD) = a + br + cs + drs, \quad -0.5 \leq r,s < 0.5 \tag{17}$$

where r and s are values of A_y/D and StU/fD relative to their values at the center of the surrounding four table cells, divided by the table grid spacing of 0.1. Below the diameter of 0.05, a table row corresponding to $A_y/D=-0.05$ is created by repeating the row at $A_y/D=+0.05$ or alternately with the lift coefficient model (Eq. (7)) or wake oscillator model (Eqs. (22*a*), (22*b*), and (24)) can be applied. Figures 8 and 9 were created using the first approach.

5 Prediction of Vortex-Induced Vibration Using the Measured Forces

The fluid forces measured in Sec. 4 are applied to the prediction of transverse vortex-induced vibration of circular cylinders using the (1) lift coefficient, (2) two parameter, and (3) wake oscillator models.

5.1 Constant C_L Model. The equation of transverse motion of a spring supported cylinder responding (Fig. 2) to the constant lift coefficient force (Eq. (4*b*)) at the stationary cylinder shedding frequency $f=f_s|_{\mathrm{Eq.\ 1}}$ has an exact steady-state harmonic solution (Eq. (5)) [39] as follows:

$$m\ddot{y} + 2m\zeta_n\omega_n\dot{y} + ky = F_y = (1/2)\rho U^2 D C_L \sin(2\pi f_s t + \varphi) \tag{18}$$

$$f_s = \mathrm{St}U/D, \quad f_n = (1/2\pi)(k/m)^{1/2}, \quad f_s/f_n = \mathrm{St}U/f_n D$$

$$\frac{A_y}{D} = \frac{C_L}{8\pi^2}\frac{\rho D^2}{m}\left(\frac{U}{f_n D}\right)^2\left[\left(1-\frac{f_s^2}{f_n^2}\right)^2 + \left(\frac{2\zeta_n f_s}{f_n}\right)^2\right]^{-1/2} \tag{19a}$$

$$= \frac{C_L}{4\pi \mathrm{St}^2 \delta_r} \text{ at } f_n = f_s \text{ where } \varphi = \frac{\pi}{2} \tag{19b}$$

$$\tan\varphi = \frac{2\zeta_n f_s/f_n}{1-f_s^2/f_n^2}, \quad \delta_r = \frac{2m(2\pi\zeta_n)}{\rho D^2} \tag{19c}$$

The cylinder response amplitude A_y is proportional to the lift coefficient C_L divided by the mass ratio $m/\rho D^2$. $C_L=1$ with St $=0.2$ bounds transverse response data in Fig. 9 but $C_L=0.7$ is a better fit to low amplitude data in Figs. 7 and 8. At small amplitudes the finite spanwise correlation length l_c of vortex shedding, often between diameters of 3 and 7 for a stationary cylinder, reduces the root mean square lift by the factor $(l_c/L)^{1/2}$ [7,9,10,25,38,51–53].

The constant C_L model accurately predicts experimental data below 0.05 diameter amplitude, but it lacks the rightward shift of maximum response, entrainment, and self-limiting response at larger amplitudes. These shortcomings are addressed by the amplitude and frequency dependent coefficients C_{mv} $(A_y/D, \mathrm{St}U/fD)$ and C_{dv} $(A_y/D, \mathrm{St}U/fD)$ of Tables 1 and 2, as used in the two parameter model (Sec. 5.2).

In 1956, Scruton introduced dimensionless reduced mass damping $\delta_r=2m(2\pi\zeta)/\rho D^2$ (Eq. (19*c*)) to correlate the maximum amplitude of cylinders in the wind [54,55] and this predates the 1973 application of the monogram $S_G=(2\pi\mathrm{St})^2\delta_r$ by Skop and Balasubramanian [56] and Griffin et al. [57] to offshore piping. References [6,10,53,57,58] have correlations for $A_{y\,\max}$ with δ_r and S_G. Figure 7 uses a log scale to show both high and low amplitude behaviors of data and two correlations—Eq. (29) and $A_y/D=[1-1.124\delta_r/\pi^2+0.296(\delta_r/\pi^2)^2)]\log_{10}(0.41\,\mathrm{Re}^{0.36})$ [6]—for maximum amplitude as function of δ_r. The latter expression fits in the upper range and addresses the Reynolds number effects but it crosses zero twice for $\delta_r>10$.

5.2 Two Parameter Force Model at Steady-State. Steady-state solutions to the two parameter model are sought by inverting

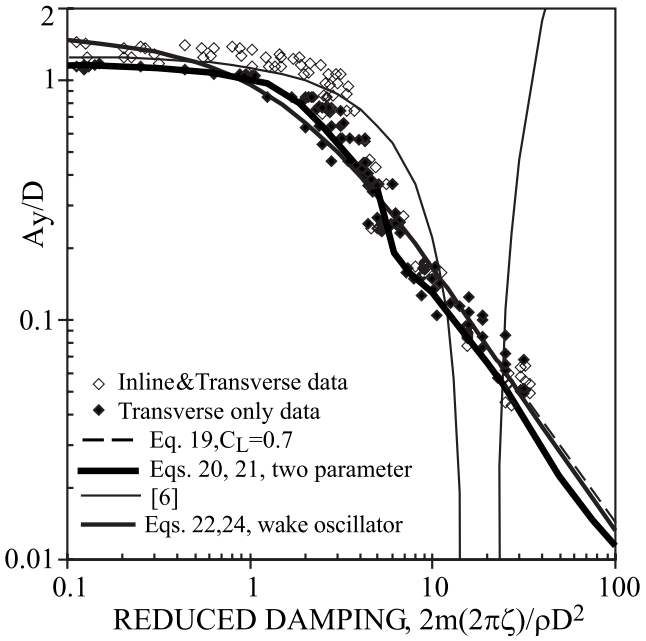

Fig. 7 Scruton plot of resonant transverse amplitude versus reduced damping. Dark solid line is two parameter (Eqs. (20) and (21)) solution with Tables 1 and 2 and St=0.21.

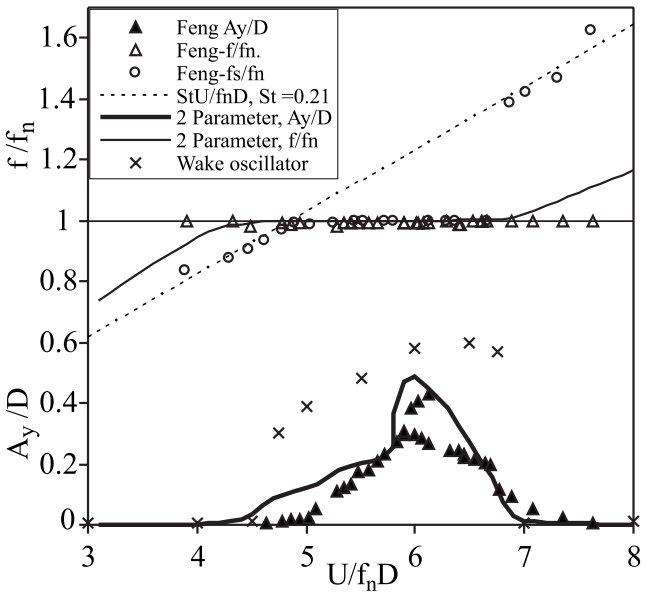

Fig. 9 Comparison of predicted response amplitude (—) (Eqs. (20) and (21)) using data from Tables 1 and 2 as a function of velocity with data from spring supported rigid cylinder tests in air [59]

the measurement equations (Eq. (16)), and solving the two coupled nonlinear equations for cylinder amplitude A_y and frequency f

$$\mathrm{St}^2\frac{A_y}{D}\left[1-\frac{f^2}{f_n^2}\right]=\frac{1}{4\pi^2}\frac{\rho D^2}{2m}\left(\frac{\mathrm{St}U}{f_nD}\right)^2 C_{mv}\left[\frac{A_y}{D},\frac{\mathrm{St}U}{fD}\right] \quad (20)$$

$$4\pi\mathrm{St}^2\frac{2m(2\pi\zeta_n)}{\rho D^2}\frac{A_y}{D}\frac{f}{f_n}=-\left(\frac{\mathrm{St}U}{f_nD}\right)^2 C_{dv}\left[\frac{A_y}{D},\frac{\mathrm{St}U}{fD}\right] \quad (21)$$

Substituting the biharmonic interpolation (Eq. (17)) for C_{mv} into Eq. (20) produces a cubic equation in terms of f/f_n with exact solutions for f given A_y/D that are substituted into Eq. (21), which is then numerically searched for amplitudes A_y/D in the interpolation range of each cell. Multiple solutions, some unstable, can exist. Once A_y and f are known, the mean drag coefficient is read from Table 3. Figure 8 shows the two parameter model solution reproduces entrainment and self-limiting effects for lightly damped cylinders responding at large amplitude. At zero structural damping Eq. (21) becomes $C_{dv}[A_y/D,\mathrm{St}U/fD]=0$, which is outlined in Table 2.

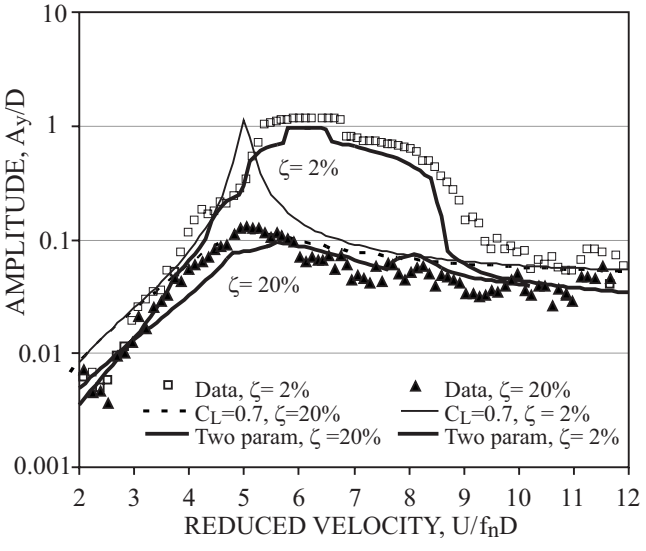

Fig. 8 Vortex-induced cylinder response predicted by lift coefficient model (Eq. (19)) with $C_L=0.7$, and two parameter coupled model (Eqs. (20) and (21)) using Tables 1 and 2 data in comparison with experimental data; $\rho D^2/(2m)=0.1$ and St =0.21

Figure 8 shows that the two parameter model (Eqs. (20) and (21) with Tables 1 and 2) predictions agree with the measured data. Figure 9 compares the two parameter numerical solution with the data of Feng [59] for transverse motion of a spring supported two dimensional cylinder (Fig. 3) for $\rho D^2/2m=0.00257$, $\zeta_n=0.00145$, $\delta_r=3.54$, and St=0.21. Note that his experiment in air is at $\frac{1}{38}$ of the mass ratio of the present experiments.

5.3 Wake Oscillator Model. Wake oscillator model for vortex-induced vibration is a self-excited, single degree of freedom van der Pol oscillator model of near wake fluid coupled to transverse cylinder vibrations [10,56,60,62–64]

$$a_0\rho D^2\ddot{z}+a_0\rho D^2\omega_{s1}^2 z=(a_1-a_{41})\rho UD\dot{z}-a_2\rho D\dot{z}^3/U+a_{42}\rho UD\dot{y} \quad (22a)$$

$$\omega_{s1}^2=a_0\rho D^2\omega_s^2 a_6/(1+a_5(z^2+\dot{z}^2/\omega_s^2)^{1/2}/D) \quad (22b)$$

$$m\ddot{y}+2\zeta m\omega_y\dot{y}+ky=F_y=a_{43}\rho UD\dot{z}-a_{44}\rho UD\dot{y} \quad (22c)$$

where z represents the fluid degree of freedom. This formulation is same as in Refs. [10,61] but with coefficients $a_0=0.48$, $a_1=0.44$, $a_2=0.2$, $a_3=0$, and a_4 expanded to four coefficients, namely, $a_{41}=0.35$, $a_{42}=1$, $a_{43}=0.4$, and $a_{44}=0.5$, to increase the entrainment and fit data in Figs. 5 and 7. A softening spring $a_5=0.3$ and $a_6=1+a_5A_{z0}/D$ shifts the resonance to the right at higher amplitude.

Harmonic solutions ($z=A_z\sin\omega t$) are sought by expanding the cubic $\cos^3\omega t=(3/4)\cos\omega t-(1/4)\cos 3\omega t$ and retaining only the first term. For a stationary cylinder ($y=0$), this gives

$$z = A_{zo} \cos \omega_s t, \quad A_{zo} = ((4(a_1 - a_{41})/3a_2)^{1/2}/2\pi S \tag{23}$$

$$F_y = a_{43}\rho UDz = (1/2)\rho U^2(4\pi \mathrm{St} a_{43} A_{zo}), \text{ hence } C_L = 4\pi \mathrm{St} a_{43} A_{zo}$$

With St=0.2 and the above parameters $A_{zo}/D=0.616$ and $C_L=0.62$, the wake oscillator and lift coefficient model are nearly identical for predictions of the lift force and response (Fig. 7) at small amplitudes. The wake oscillator has entrainment and self-limiting response at higher amplitude.

For forced cylinder motion $y(t)=A_y \sin \omega t$ (Eq. (5)) at circular frequency ω (Eq. (23)) becomes a classical forced van der Pol oscillator. The solution (see Appendix) is

$$z = b_1 \cos \omega t + b_2 \sin \omega t$$

$$C_{mv} = -4\pi \mathrm{St} a_{43}(\omega/\omega_s)(b_1/D), \tag{24}$$

$$C_{dv} = 4\pi \mathrm{St}(\omega/\omega_s)(a_{43}b_2/D - a_{44}A_y/D)$$

The result for C_{dv} is shown in comparison with the data in Fig. 5.

5.4 Application to Continuous Structures. Galerkin modal analysis [61,65] is applied to the partial differential equation of motion of a slender elastic structure responding to the transverse forces of Eq. (4*c*) to reduce it to a single degree of freedom that is solved using the previous procedure.

$$L[Y(z,t)] + m(z)\frac{\partial^2 Y(z,t)}{\partial t^2} = \frac{1}{2}\rho U^2 D C_{mv} \sin(2\pi f t) - \frac{1}{2}\rho U^2 D C_{dv} \cos(2\pi f t) \tag{25}$$

The displacement $Y(z,t)$ is a function of time t and longitudinal span z, and $L[Y(z,t)]$ is the differential stiffness operator. Harmonic response in a single mode, which is the ith mode, is expressed as a one term series

$$Y(z,t) = A_{yi} y_i(z) \sin(2\pi f t) \tag{26}$$

that is substituted into Eq. (25), which is then multiplied through by $y_i(x)$, and integrated over the span. For a uniform diameter and flow, modal force coefficients C_{mvi} and C_{dvi} can be defined.

$$C_{mvi} = \frac{\int_0^L C_{mv}[\mathrm{St}U/fD, A_y/D]|y_i(z)|dz}{\int_0^L y_i^2(z)dz},$$

$$C_{dvi} = \frac{\int_0^L C_{dv}[\mathrm{St}U/fD, A_y/D]|y_i(z)|dz}{\int_0^L y_i^2(z)dz} \tag{27}$$

Modal analysis reduces Eq. (25) to Eqs. (20) and (21) with redefinitions of Eq. (27) of the fluid force coefficients, so the previous solution method applies. Still fluid drag-damping can be incorporated by replacing Eq. (4*c*) with Eq. (4*a*) for portions of the cylinder in still water.

When applied to the wake oscillator model (Eq. (22)), with $a_5=0$ and $a_6=0$, this modal procedure results in the following expression for maximum resonant response:

$$\frac{A_y}{D} = \frac{a_{43}(4/3)^{1/2}\gamma}{2\pi \mathrm{St}^2(\delta_r + a_{44}/\mathrm{St})}\sqrt{\frac{a_1 - a_{41}}{a_2} + \frac{a_{42}a_{43}}{a_2 \mathrm{St}(\delta_r + a_{44}/\mathrm{St})}} = \frac{0.0735\gamma}{\mathrm{St}^2(\delta_r + 0.5/\mathrm{St})}\sqrt{0.45 + \frac{2}{\mathrm{St}(\delta_r + 0.5/\mathrm{St})}} \tag{28}$$

The dimensionless modal parameter $\gamma=1$ for a rigid two dimensional motion (Fig. 3, $\gamma=1.155$ for a sinusoidal mode shape, and $\gamma=1.291$ for a pivoted cantilever, where A_y now refers to the maximum amplitude along the mode shape [10,62].

5.5 Time History Solutions. The equation of motion can be numerically integrated step-by-step in time. The two parameter mode (Eq. (15)) is put in suitable form [66] using Eq. (5).

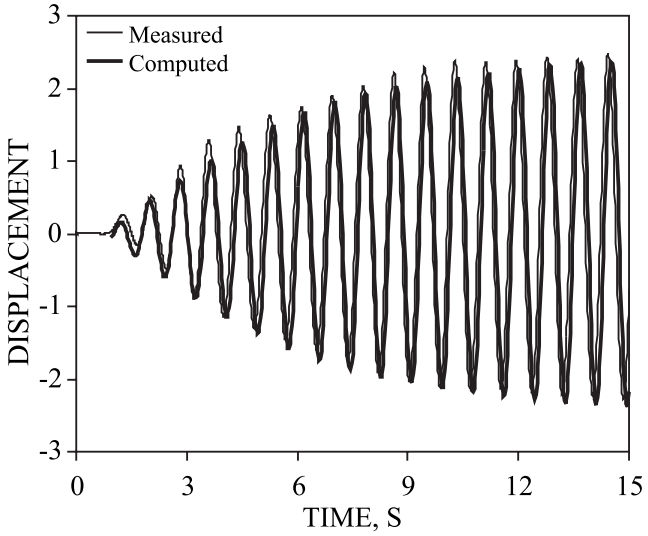

Fig. 10 Transient prediction with two parameter model (Eqs. (30), (31), and (17)) (Tables 1 and 2) and measured transient response; $\rho D^2/m=0.2$, $\varsigma=0.02$. St=0.205, $U/f_nD=6.21$

$$\left(m + \frac{1}{2}\rho U^2 D C_{mv}/\omega^2 A_y\right)\ddot{y} + \left(2m\zeta_n\omega_n + \frac{1}{2}\rho U^2 D C_{dv}/\omega A_y\right)\dot{y} + ky = 0 \tag{29}$$

where C_{mv} and C_{dv} at the current step are evaluated with Tables 1 and 2 and Eq. (17) using the amplitude and frequency estimated from the previous time, that is

$$f_n^2/f^2 = 1 + (1/(8\pi^2))(\rho D^2/m)(U/fD)^2(D/A_y)C_{mv}[A_y/D, \mathrm{St}U/fD] \tag{30a}$$

$$A_y^2 = y(t)^2 + y(t)^2/(2\pi f)^2 \tag{30b}$$

Figure 10 is a computed startup of a cylinder released in a steady flow in comparison with the data. Time history analysis can be extended to continuous structure, multiple mode responses, or direct integration, using the autocorrelation of previous time history

$$R_{yy}(\tau) = \frac{1}{t_1 - t_2}\int_{t1}^{t2} y(t)y(t+\tau)dt, \quad 0 < \tau < (t_1 - t_2) \tag{31}$$

to determine frequency f and amplitude of the dominant amplitude A_y in the entrainment range of frequencies, based on negative $C_{dv}<0$ (Table 1) and experiments [19]

$$f_s/1.6 < f < f_s \tag{32}$$

The corresponding phase is found from the Fourier series expansion of the previous time history at this frequency. An initial offset can be applied to start the solution, or alternately, the wake oscillator or lift coefficient model, could be applied.

6 Conclusions

Oscillating vortex-induced lift coefficients in-phase (C_{mv}) and out-of-phase (C_{dv}) with cylinder motion and mean drag (C_D) have been determined for cylinder amplitudes from 0.05 to 1.5 diameters and reduced velocities between 2 cm/s and 12 cm/s, by post-processing a large number of experiments for response of elastically supported cylinders in water flow. These force coefficients have been reduced to a uniform tabular grid as functions of non-dimensional frequency and amplitude of cylinder motion and employed in predictive models for vortex-induced vibration.

1. The oscillating lift forced model (Eqs. (18) and (19)) with $C_L=0.7$ is a good fit to data for small amplitude vortex-induced vibration, $Ay/D<0.5$.
2. Moderate and large amplitude vortex-induced vibrations are well represented by the two parameter model (Eqs. (4*c*), (15), (20), and (21)). It has good agreement for steady-state and transient cylinder response in both water and air, including frequency entrainment, large amplitude response, and self-limiting amplitudes greater than one diameter. However, for transient analysis it requires tracking of the dominant amplitude and frequency of the response.
3. The wake oscillator model (Eq. (22*a*)–(22*c*)) with tuned coefficients reproduces entrainment, self-limiting amplitude, and frequency shift. It envelopes the data from small to large amplitudes, but it does not reproduce the finer details of cylinder response.
4. The negative values of C_{dv} fall in the range $1 \leq \mathrm{St}U/fD < 1.6$. This implies that extensive entrainment is only possible if the oscillation frequency f follows the shedding frequency upward from the cylinder natural frequency, $f > 0.9f_n$, as velocity increases.

Nomenclature

- A_y = amplitude of vibration transverse to tube axis and flow
- C_a = added mass coefficient, dimensionless (Eqs. (4*a*) and (11))
- C_L = lift coefficient, dimensionless (Eq. (4*b*))
- C_{Do} = drag coefficient for stationary cylinder in steady flow, dimensionless (Eq. (2))
- C_{dv} = oscillating negative damping coefficient, dimensionless (Eq. (4*c*))
- C_{mv} = oscillating inertia coefficient, normalized to zero for still water added mass, dimensionless (Eq. (4*c*))
- D = cylinder outside diameter
- F_D = mean drag on the cylinder
- F_y = transverse force, transverse to flow, per unit length of cylinder
- L = wetted span of cylinder
- $\mathrm{Re}=UD/\nu$ = Reynolds number, dimensionless
- St = Strouhal number for stationary cylinder, dimensionless (Eq. (1))
- U = freestream flow velocity
- f = cylinder oscillation frequency, generally differs from f_o, f_s, or f_n (Hz)
- f_o = natural frequency in still air (Hz)
- f_n = natural frequency in still water, $(\mathrm{k/m})^{1/2}/2\pi$ (Hz)
- f_s = vortex shedding frequency from stationary cylinder (Hz) (Eq. (1))
- k = surface roughness of cylinder (Fig. 2) or spring constant per unit length
- m_o = dry mass of cylinder and moving suspension in air per unit length
- m = mass per unit length of cylinder with still water added mass, $m_o+\rho(\pi D^2/4)C_a$
- $m/\rho D^2$ = mass ratio, dimensionless
- t = time
- y = direction perpendicular to freestream flow, transverse
- $y(t)$ = displacement perpendicular to freestream flow
- z = direction along cylinder axis, or fluid degree of freedom
- ρ = fluid mass density
- ζ_f = cylinder fluid damping factor, dimensionless
- ζ_n = cylinder damping factor, fraction of critical damping, dimensionless, in air with additional mass equal to fluid added mass in water
- ζ_o = cylinder damping factor, fraction of critical damping, dimensionless, in air, without magnetic damping or additional mass
- φ = phase angle between force and displacement (Eq. (4*b*))
- ω = circular frequency, $2\pi f$ (rad/s)
- ω_s = circular shedding frequency from stationary cylinder, $2\pi f$ (rad/s)
- ν = kinematic viscosity, 1.14×10^{-5} $\mathrm{ft^2/s}$ (0.01054 $\mathrm{cm^2/s}$) typical for experiment
- δ_r = reduced damping based on in-air damping factor; also, known as Scruton number, dimensionless, $2m(2\pi\zeta_n)/\rho D^2$

Appendix: Further Results

The equation of transverse motion of a uniform elastic cylinder responding to the two parameter lift force model (Eq. (15)) has a steady-state exact solution (Eq. (5)), if C_{mv} and C_{dv} are known.

$$\frac{A_y}{D}=\frac{1}{4\pi}\frac{\rho D^2}{2m(2\pi\zeta_n)}\left(\frac{U}{f_nD}\right)^2\{\zeta_nC_{mv}+\sqrt{\zeta_n^2C_{mv}^2+C_{dv}^2}\}$$

$$\frac{f}{f_n}=\frac{1}{C_{dv}}\{\zeta_nC_{mv}-\sqrt{C_{dv}^2+\zeta_n^2C_{mv}^2}\} \tag{A1}$$

The solution to Eq. (22*a*) for a given cylinder oscillation $y=A_y \sin \omega t$ is obtained by substituting $z=b_1 \cos \omega t+b_2 \cos \omega t$ into the equation, separating sine and cosine terms into two equations, setting $x=b_1\omega/A_{zo}\omega_s t$ and $y=b_1\omega/A_{zo}\omega_s$, $x^2+y^2=r^2$, and $\sigma=2\pi S(\omega_s^2-\omega^2)a_0/\omega\omega_s(a_1-a_{41})$ to produce a cubic in r^2 with an exact solution [67].

References

[1] Bearman, P. W., 1987, Private Communication.
[2] Jeon, D., and Gharib, M., 2004, "On the Relationship Between the Vortex Formation Process and Cylinder Wake Vortex Patterns," J. Fluid Mech., **519**, pp. 161–181.
[3] Khalak, A., and Williamson, C. H. K., 1999, "Motions, Forces and Mode Transitions in Vortex-Induced Vibrations at Low Mass-Damping," J. Fluids Struct., **13**, pp. 813–851.
[4] Dahl, J. M., Hover, F. S., and Triantafyllou, M. S., 2006, "Two Degree-of-Freedom Vortex-Induced Vibrations Using a Force Assisted Apparatus," J. Fluids Struct., **22**, pp. 807–818.
[5] Gabbai, R. D., and Benaroya, H., 2005, "An Overview of Modeling and Experiments of Vortex-Induced Vibration," J. Sound Vib., **282**, pp. 575–616.
[6] Govardhan, R. N., and Williamson, C. H. K., 2006, "Defining the Modified Griffin Plot in Vortex Induced Vibration," J. Fluid Mech., **561**, pp. 147–180.
[7] Norberg, C., 2003, "Fluctuating Lift on a Circular Cylinder: Review and New Measurements," J. Fluids Struct., **17**, pp. 57–96.
[8] Sarpkaya, T., 1995, "Hydrodynamic Damping, Flow-Induced Oscillations, and Biharmonic Response," ASME J. Offshore Mech. Arct. Eng., **117**, pp. 232–238.
[9] Pantazopoulos, M., 1994, "Vortex-Induced Vibration Parameters: Critical Review," ASME 13th International Conference on Offshore Mechanics and Arctic Engineering, Vol. 1, pp. 199–255.
[10] Blevins, R. D., 1990, *Flow-Induced Vibration*, 2nd ed., Krieger, Malabar, FL.
[11] Bearman, P. W., 1984, "Vortex Shedding From Oscillating Bluff Bodies," Annu. Rev. Fluid Mech., **16**, pp. 195–222.
[12] Achenbach, E., and Heinecke, E., 1981, "On Vortex Shedding From Smooth and Rough Cylinders in the Range of Reynolds Numbers 6×10^3 to 5×10^6," J. Fluid Mech., **109**, pp. 239–251.
[13] Norberg, C., 1987, "Reynolds Number and Freestream Turbulence Effect on the Flow and Fluid Forces of a Circular Cylinder in Cross Flow," Ph.D. thesis, Chalmers University of Technology, Goteborg, Sweden.
[14] Shih, W. C. L., Wang, C., Coles, D., and Roshko, A., 1993, "Experiments on Flow Past Rough Circular Cylinders at Large Reynolds Numbers," J. Wind Eng. Ind. Aerodyn., **49**, pp. 351–368.
[15] Tritton, D. J., 1959, "Experiments on the Flow Past a Circular Cylinder at Low Reynolds Numbers," J. Fluid Mech., **6**, pp. 547–567.
[16] Wieselsberger, V. C., 1921, "Neuere Feststellungen uber die Gesetze des Flussigkeits- und Luftwiderstandes," Phys. Z., **22**(11), pp. 321–328.
[17] Jones, G. W., Cincotta, J. J., and Walker, R. W., 1969, "Aerodynamic Forces on a Stationary and Oscillating Circular Cylinder at High Reynolds Numbers," National Aeronautics and Space Administration, Report No. NASA TR R-300.
[18] Allen, D., and Henning, D. L., 2001, "Surface Roughness Effects on Vortex-

Induced Vibration at Critical and Supercritical Reynolds Numbers," Offshore Technology Conference, Paper No. OTC 13302.
[19] Blevins, R. D., and Coughran, C. S., 2009, "Experimental Investigation of Vortex-Induced Vibration in One and Two Dimensions With Variable Mass, Damping, and Reynolds Number," ASME J. Fluids Eng., **131**, p. 101202.
[20] Anagnostoulos, P., and Bearman, P. W., 1992, "Response Characteristics of a Vortex Excited Cylinder at Low Reynolds Numbers," J. Fluids Struct., **6**, pp. 39–50.
[21] Zan, S. J., and Matsuda, K., 2002, "Steady and Unsteady Loading on a Roughened Circular Cylinder at Reynolds Numbers up to 900,000," J. Wind. Eng. Ind. Aerodyn., **90**, pp. 567–581.
[22] Roshko, A., 1954, "On the Drag and Shedding Frequency of Two-Dimensional Bluff Bodies," National Advisory Committee for Aeronautics, NACA Technical Note 3169.
[23] Fey, U., Kong, M., and Eckelmann, H., 1998, "A New Strouhal-Reynolds Number Relationship," Phys. Fluids, **10**(7), pp. 1547–1549.
[24] Toebes, G. H., 1969, "The Unsteady Flow and Wake Near an Oscillating Cylinder," ASME J. Basic Eng., **91**, pp. 493–502.
[25] Griffin, O. M., and Ramberg, S. E., 1974, "The Vortex Street Wakes of Vibrating Cylinders," J. Fluid Mech., **66**, pp. 553–576.
[26] Williamson, C. H. K., and Roshko, A., 1988, "Vortex Formation in the Wake of an Oscillating Cylinder," J. Fluids Struct., **2**, pp. 355–381.
[27] Zdravkovich, M. M., 1996, "Different Modes of Vortex Shedding: An Overview," J. Fluids Struct., **10**, pp. 427–437.
[28] Hartlen, R. T., and Currie, I. G., 1970, "Lift Oscillator Model of Vortex-Induced Vibration," J. Eng. Mech. Div., **96**, pp. 577–591.
[29] Sarpkaya, T., 1978, "Fluid Forces on Oscillating Cylinders," J. Wtrwy., Port, Coast., and Oc. Div., **104**, pp. 270–290.
[30] Mercier, J. A., 1973, "Large Amplitude Oscillations of a Circular Cylinder in a Low-Speed Stream," Ph.D. thesis, Stevens Institute of Technology.
[31] Staubli, T., 1983, "Calculation of the Vibration of an Elastically Mounted Cylinder Using Experimental Data From Forced Oscillation," ASME J. Fluids Eng., **105**, pp. 225–229.
[32] Moe, G., and Wu, Z.-J., 1990, "The Lift Force on a Circular Cylinder Vibrating in a Current," ASME J. Offshore Mech. Arct. Eng., **112**, pp. 297–303.
[33] Gopalkrishnan, R., 1993, "Vortex-Induced Forces on Oscillating Bluff Cylinders," Ph.D. thesis, Department of Ocean Engineering, MIT.
[34] de Wilde, J., et al., 2004, "Cross Section VIV Model Test for Novel Riser Geometries," DOT Conference, New Orleans, LA, Paper No. 12-3.
[35] Blackburn, H. M., and Melbourne, W. H., 1997, "Section Lift Force for an Oscillating Circular Cylinder," J. Fluids Struct., **11**, pp. 413–431.
[36] Morse, T. L., and Williamson, C. H. K., 2006, "Employing Controlled Vibrations to Predict Fluid Forces," J. Fluids Struct., **22**, pp. 877–884.
[37] Dahl, J. M., Hover, F. S., and Triantafyllou, M. S., 2008, "Higher Harmonic Forces and Predicted Vibrations From Forced Cylinder Motions," Proceeding of the 18th Offshore and Polar Engineering Conference, Vancouver, Canada.
[38] Blevins, R. D., and Burton, T. E., 1976, "Fluid Forces Induced by Vortex Shedding," ASME J. Fluids Eng., **95**, pp. 19–24.
[39] Thomson, W. T., 1988, *Theory of Vibration With Applications*, 3rd ed., Prentice-Hall, Englewood Cliffs, NJ.
[40] Bearman, P. W., Downie, M. J., Graham, J. M. R., and Obasju, E. D., 1985, "Forces on Cylinders in Viscous Oscillatory Flow at Low Keulegan–Carpenter Numbers," J. Fluid Mech., **154**, pp. 337–356.
[41] Sarpkaya, T., 1986, "Force on a Circular Cylinder in Viscous Oscillatory Flow at Low Keulegan–Carpenter Numbers," J. Fluid Mech., **165**, pp. 61–71.
[42] Chaplin, J. R., and Subbiah, K., 1998, "Hydrodynamic Damping of a Cylinder in Still Water and in Transverse Current," Appl. Ocean Res., **20**, pp. 251–259.
[43] Chaplin, J. R., 2000, "Hydrodynamic Damping of at Cylinder at $\beta \approx 10^6$," J. Fluids Struct., **14**, pp. 1101–1172.
[44] Skop, R. A., Ramberg, S. E., and Ferer, K. M., 1976, "Added Mass and Damping Forces on Circular Cylinders," Naval Research Laboratory, Report No. 7970.
[45] Otter, A., 1990, "Damping Forces on a Cylinder Oscillating in a Viscous Fluid," Appl. Ocean Res., **12**, pp. 153–155.
[46] Anaturk, A. R., Tromans, P. S., van Haxzendonk, H. C., Sluis, C. M., and Otter, A., 1992, "Drag Force on Cylinders Oscillating at Small Amplitude: A New Model," ASME J. Offshore Mech. Arct. Eng., **114**, pp. 91–104.
[47] Brouwers, J. J. H., and Meijssen, T. E. M., 1985, "Viscous Damping Forces on Oscillating Cylinders," Appl. Ocean Res., **7**, pp. 118–123.
[48] Honji, H., 1981, "Streaked Flow Around an Oscillating Circular Cylinder," J. Fluid Mech., **107**, pp. 509–520.
[49] Vandiver, J. K., 1993, "Dimensionless Parameters Important to the Prediction of Vortex-Induced Vibration of Long Flexible Cylinders in Ocean Currents," J. Fluids Struct., **7**, pp. 423–455.
[50] Wu, Z.-J., 1989, "Current Induced Vibrations of a Flexible Cylinder," Ph.D. thesis, Norwegian Institute of Technology, Trondheim.
[51] Toerum, A., and Anand, N. M., 1985, "Free Span Vibrations of Submarine Pipelines in Steady Flows—Effect of Free-Stream Turbulence on Mean Drag Coefficients," ASME J. Energy Resour. Technol., **107**, pp. 415–420.
[52] Szepessy, S., 1994, "On the Spanwise Correlation of Vortex Shedding From a Circular Cylinder," Phys. Fluids, **6**, pp. 2406–2416.
[53] West, G. S., and Apelt, C. J., 1997, "Fluctuating Lift and Drag Forces on Finite Lengths of a Circular Cylinder in the Subcritical Reynolds Number Range," J. Fluids Struct., **11**, pp. 135–158.
[54] Zdravkovich, M. M., 1982, "Scruton Number: A Proposal," J. Wind Eng. Ind. Aerodyn., **10**(3), pp. 263–265.
[55] Scruton, C., 1963, "On the Wind Excited Oscillation of Stacks, Towers, and Masts," Proceedings of the Conference on Wind Effects on Buildings and Structures, National Physical Laboratory, Teddington, England.
[56] Skop, R. A., and Balasubramanian, S., 1997, "A New Twist on an Old Model for Vortex-Excited Vibrations," J. Fluids Struct., **11**, pp. 395–412.
[57] Griffin, O. M., Skop, R. A., and Koopman, G. H., 1973, "The Vortex-Excited Resonant Vibrations of Circular Cylinders," J. Sound Vib., **31**, pp. 235–249.
[58] Sarpkaya, T., 2004, "A Critical Review of the Intrinsic Nature of Vortex Induced Vibrations," J. Fluids Struct., **19**, pp. 389–447.
[59] Feng, C. C., 1968, "The Measurement of Vortex-Induced Effects in Flow Past Stationary and Oscillating Circular and D-Section Cylinders," M.A.Sc. thesis, University of British Columbia.
[60] Facchinetti, M. L., de Langre, E., and Biolley, F., 2004, "Coupling of Structure and Wake Oscillators in Vortex-Induced Vibrations," J. Fluids Struct., **19**, pp. 123–140.
[61] Iwan, W. D., 1975, "The Vortex Induced Oscillation of Elastic Structural Elements," ASME J. Eng. Ind., **97**, pp. 1378–1382.
[62] Violette, R., de Langre, E., and Szydlowski, J., 2007, "Computation of Vortex-Induced Vibration of Long Structures Using a Wake Oscillator Model," Comput. Struct., **85**, pp. 1134–1144.
[63] Poore, A. B., Doedel, E. J., and Cermak, J. E., 1986, "Dynamics of the Iwan–Blevins Wake Oscillator Model," Int. J. Non-Linear Mech., **21**, pp. 291–302.
[64] Hall, S. A., and Iwan, W. D., 1984, "Oscillations of a Self-Excited Nonlinear System," ASME J. Appl. Mech., **97**, pp. 1378–1382.
[65] Hamid, E., 2009 "Semi-Empirical Time Doman VIV—Analysis Modle Based on Force Decomposition," M.S. thesis, Newcastle University, Newcastle.
[66] Meirovitch, L., 1967, *Analytical Methods in Vibrations*, Macmillan, NY, p. 235.
[67] Retorys, K., 1969, *Survey of Applicable Mathematics*, MIT, Cambridge, pp. 77–79.

Application of a Volume Averaged k-ε Model to Particle-Laden Turbulent Channel Flow

J. D. Schwarzkopf

C. T. Crowe

P. Dutta
e-mail: dutta@mme.wsu.edu

School of Mechanical and Materials Engineering,
Washington State University,
Pullman, WA 99164-2920

A closed set of volume averaged equations for modeling turbulence in the carrier phase of particle-laden flows is presented. The equations incorporate a recently developed dissipation transport equation that contains an additional production of dissipation term due to particle surfaces. In the development, it was assumed that each coefficient was the sum of the coefficient for single phase flow and a coefficient quantifying the contribution of the particulate phase. To assess the effects of this additional production term, a numerical model was developed and applied to particles falling in a channel of downward turbulent air flow. Boundary conditions were developed to ensure that the production of turbulent kinetic energy due to mean velocity gradients and particle surfaces balanced with the turbulent dissipation near the wall. The coefficients associated with the production of dissipation due to mean velocity gradients and particle surfaces were varied to assess the effects of the dispersed phase on the carrier phase turbulent kinetic energy across the channel. The results show that the model predicts a decrease in turbulent kinetic energy near the wall with increased particle loading, and that the dissipation coefficients play a critical role in predicting the turbulent kinetic energy in particle-laden turbulent flows. [DOI: 10.1115/1.3203204]

Keywords: turbulence, modeling, particles, dissipation, volume average

1 Introduction

Particle-laden turbulent flows are common in industrial applications. Large industries such as the chemical, pharmaceutical, agricultural, and mining industries can benefit from an understanding of particle-laden turbulent flows [1]. Two-phase gas-solid suspension flows are prevalent in chemical engineering applications such as spray drying, cyclone separation, pneumatic conveying, pulverized coal gasification, and combustion [2]. Turbulence is also responsible for enhancing heat transfer, mixing of chemical species, and altering the wall shear stress [3].

The addition of particles to a turbulent flow has been experimentally shown to alter the carrier phase turbulence [4–8]. Particle-laden turbulent flows are complicated to model, and understanding the physics well enough to develop a general model to predict the interactions between the continuous and dispersed phases becomes even more of a challenge. The ideal approach to modeling these interactions would require boundary conditions at the surface of each particle in the flow. However, the mesh associated with this type of analysis would require enormous computational efforts. In order to circumvent the computational difficulties associated with considering every particle, many researchers [2,9–14] have assumed that the effect of the particles could be incorporated by including a force to the instantaneous form (i.e., a point in space and an instance in time) of the momentum equation, such as

$$\frac{\partial}{\partial t}(\rho u_i) + \frac{\partial}{\partial x_j}(\rho u_j u_i) = -\frac{\partial P}{\partial x_i} + \frac{\partial}{\partial x_j}\left(\mu \frac{\partial u_i}{\partial x_j}\right) + \rho g_i + F_i \qquad (1)$$

where F_i is a force per unit volume due to the presence of particles. In order for the above equation to be valid at a point (e.g., the limiting volume of the fluid [15]), the force due to the particles must be continuous and definable. However, the term F_i is not definable at any point in the continuous phase. To better understand this claim, consider an arbitrary particle and an arbitrary point near the particle, as shown in Fig. 1(*a*). The effect of the particle on the fluid within some arbitrary control volume cannot be represented by a force per unit volume, F_i.

The force on the fluid due to the particles can only be defined if the control volume contains enough particles, as shown in Fig. 1(*b*). In order for F_i to be valid at a point, it must be continuous; thus the limiting volume would have to contain sufficient particles to have stationary average properties. For cases which typify fluid-particle flows this limiting volume would be many orders of magnitude larger than a point in the conveying phase. In addition, a pointwise approach to modeling turbulence in particle-laden flows by decomposing the force, F_i, into mean and fluctuating components, in time, is also meaningless based on the above argument. Several turbulence models [2,9–14,16] have been developed for particle-laden flows, most of which are based on temporal averaging approaches. A fundamental approach to capture the effects of the particles in the momentum, turbulent kinetic energy (TKE), and dissipation equations is through volume averaging (a further discussion is presented in Sec. 2).

To assess the validity of volume averaging, Zhang and Reese [17] studied the additional source and sink terms due to the presence of particles in the TKE equations proposed by Crowe and Gillant [18] and Chen and Wood [2] and compared them to the data of Tsuji et al. [4]. They concluded that the temporal averaged model did not predict the altered turbulent intensity due to particle mass loading, but they showed that the volume averaged model did produce changes in turbulent kinetic energy with respect to particle loading. Overall, they conclude that the generation terms proposed by Crowe and Gillant [18] more accurately match the experimental data.

In a recent review of the status of modeling particle-laden turbulence, Eaton [19] stated that many models have been developed to understand the turbulence modulation associated with dilute particle-laden flows, yet there still remains a general model that can account for subjective factors such as particle size, relative Reynolds number, volume fraction, number density, mass density,

Contributed by the Fluids Engineering Division of ASME for publication in the JOURNAL OF FLUIDS ENGINEERING. Manuscript received December 8, 2008; final manuscript received April 20, 2009; published online August 26, 2009. Assoc. Editor: Ian Eames.

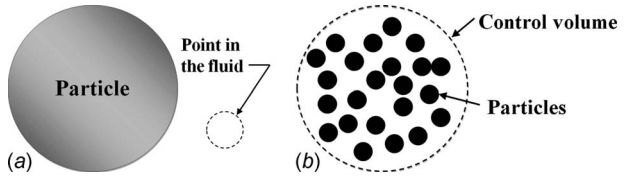

Fig. 1 Illustration of (*a*) a "point" in the flow relative to a particle and (*b*) many particles within the control volume of the continuous phase

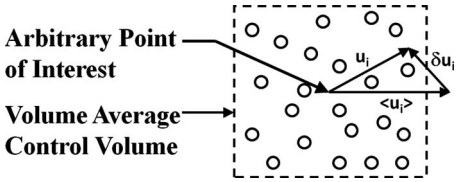

Fig. 3 A vector representation of the volume deviation velocity at a point within the control volume

surface roughness, etc. The present study reviews a fundamental approach to obtaining a system of equations that include the surface effects of particles and many of the subjective factors identified by Eaton [19] and Curtis and van Wachem [1]. In addition, the modeling procedure is further developed and applied to the experimental data of Kulick et al. [6] and Paris and Eaton [8]. Furthermore, the production coefficients within the dissipation equation are varied to assess their effect on the turbulent kinetic energy.

2 A Review of the Volume Averaged Equation Set for the Continuous Phase Turbulence in Particle-Laden Flows

The volume average momentum equations can be obtained from Newton's second law [20] or by volume averaging the Navier–Stokes equations [21]. When particle rotation and mass transfer are neglected, both methods show that the volume averaged momentum equations for incompressible, particle-laden flows are of the form

$$\frac{\partial}{\partial t}\alpha_c\langle \rho u_i\rangle + \frac{\partial}{\partial x_j}\alpha_c\langle \rho u_j u_i\rangle = -\alpha_c\frac{\partial\langle P\rangle}{\partial x_i} + \alpha_c\frac{\partial\langle \tau_{ij}\rangle}{\partial x_j} + \alpha_c\langle \rho g_i\rangle - \frac{3\pi\mu}{V}\sum_n f\ D(u_i - v_i) \tag{2}$$

where α_c is the volume fraction of the continuous phase, ρ is the density of the continuous phase, μ is the dynamic viscosity of the continuous phase, V is the mixture volume, f is the drag factor, D is the particle diameter, n is the particle number, and $\langle\ \rangle$ is the volume average [21]. For the above equation to be valid, a control volume, larger than the limiting volume of the fluid that contains N number of particles, must be used to obtain a statistical average, illustrated in Fig. 2. Some researchers [9] have used Reynolds averaging procedures on the volume averaged equations. However, the average velocities in the volume averaged equations do not represent the local (pointwise) instantaneous velocity of a given flow and thereby are not amenable to the Reynolds averaging procedures used in single phase flows. In other words, the temporal fluctuations of the averaged velocities do not reflect the flow turbulence of the carrier phase.

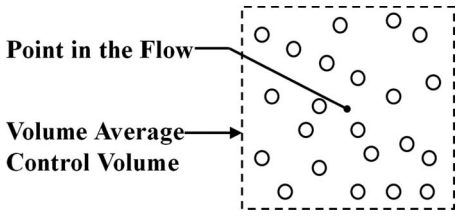

Fig. 2 A control volume containing *N* number of particles such that a statistical average can be discerned. This volume must be larger than the limiting volume of the fluid yet small enough to use differential operators.

Aside from temporal decomposition, another way of identifying turbulence within the carrier phase is by the velocity deviation from the volume averaged velocity, such as [18]

$$u_i = \langle u_i\rangle + \delta u_i \tag{3}$$

where u_i is the instantaneous velocity (i.e., the velocity at an instance in time and at an arbitrary location within the continuous phase region of the volume of interest), $\langle u_i\rangle$ is the volume averaged velocity, and δu_i is the volume deviation velocity, as illustrated in Fig. 3. Here the instantaneous velocity is used to describe the velocity at a point within the continuous phase of the control volume, which allows one to capture the local effects cause by turbulence.

The volume averaged momentum equations for particle-laden turbulent flows are obtained by substituting Eq. (3) into Eq. (2) and applying volume averaging techniques. This decomposition presents a volume deviation stress, which is analogous to the Reynolds stress found by Reynolds averaging procedures. Assuming that the material properties of the continuous phase are constant over the volume of interest, Eq. (2) becomes

$$\alpha_c\frac{\partial\langle u_i\rangle}{\partial t} + \alpha_c\langle u_j\rangle\frac{\partial\langle u_i\rangle}{\partial x_j} = -\frac{\alpha_c}{\rho}\frac{\partial\langle P\rangle}{\partial x_i} - \frac{\partial}{\partial x_j}(\alpha_c\langle \delta u_i\delta u_j\rangle) + \alpha_c\langle g_i\rangle + \alpha_c\frac{1}{\rho}\frac{\partial\langle \tau_{ij}\rangle}{\partial x_j} - \frac{3\pi v}{V}\sum_n f\ D(\langle u_i\rangle - \delta u_i - v_i) \tag{4}$$

The above equation describes the momentum of the continuous phase in particle-laden turbulent flows, but it requires a closure model to evaluate the volume deviation stress.

To close the equation set, the turbulent-viscosity hypothesis is assumed to apply. The volume deviation stress is then modeled as

$$\langle \delta u_i\delta u_j\rangle = \frac{2}{3}\delta_{ij}k - \nu_T\left(\frac{\partial\langle u_i\rangle}{\partial x_j} + \frac{\partial\langle u_j\rangle}{\partial x_i}\right) \tag{5}$$

where v_T is the turbulence viscosity defined as

$$\nu_T = C_\mu\frac{k^2}{\varepsilon} \tag{6}$$

where k is the volume average turbulent kinetic energy defined as [18]

$$k = \frac{1}{V_c}\int_{V_c}\frac{\delta u_i\delta u_i}{2}dV = \left\langle\frac{\delta u_i\delta u_i}{2}\right\rangle \tag{7}$$

and ε is the volume average dissipation defined as [18]

$$\varepsilon = \frac{1}{V_c}\int_{V_c}\nu\frac{\partial\delta u_i}{\partial x_j}\frac{\partial\delta u_i}{\partial x_j}dV = \nu\left\langle\frac{\partial\delta u_i}{\partial x_j}\frac{\partial\delta u_i}{\partial x_j}\right\rangle \tag{8}$$

and C_μ is a constant (0.09). Thus a transport equation for the volume average turbulent kinetic energy and dissipation is needed.

A volume average turbulent kinetic energy transport equation was derived by Crowe and Gillandt [18]. The transport equation for turbulent kinetic energy within the carrier phase of a particle-laden flow is shown to be [18]

$$\alpha_c \frac{Dk}{Dt} = -\alpha_c \langle \delta u_i \delta u_j \rangle \frac{\partial \langle u_i \rangle}{\partial x_j} - \frac{\beta_V}{\rho_c}[\langle \delta u_i \delta v_i \rangle - \langle \delta v_i \delta v_i \rangle] + \frac{\beta_V}{\rho_c}[\langle u_i \rangle - \langle v_i \rangle]^2 + \left\langle \frac{\partial}{\partial x_j}\left(\alpha_c\left(\nu + \frac{\nu_T}{\sigma_k}\right)\frac{\partial k}{\partial x_j}\right)\right\rangle - \alpha_c \varepsilon \tag{9}$$

where β_V is the hydraulic drag coefficient defined as [21]

$$\beta_V = \frac{\alpha_d \rho_d f}{\tau_p} \tag{10}$$

and α_d is the volume fraction of the dispersed phase, ρ_d is the material density of the dispersed phase particles, and τ_p is the particle response time.

A volume average turbulent dissipation transport equation was derived by Schwarzkopf et al. [22]. The form of the transport equation for turbulent dissipation is found to be

$$\begin{aligned}\alpha_c \frac{D\varepsilon}{Dt} = & -2\nu\alpha_c \frac{\partial \langle u_k \rangle}{\partial x_j}\left\langle \frac{\partial \delta u_i}{\partial x_j}\frac{\partial \delta u_i}{\partial x_k}\right\rangle - \alpha_c \varepsilon_{ik}\frac{\partial \langle u_i \rangle}{\partial x_k} \\ & - 2\nu\alpha_c\left\langle \delta u_k \frac{\partial \delta u_i}{\partial x_j}\right\rangle \frac{\partial^2 \langle u_i \rangle}{\partial x_j \partial x_k} - 2\nu\alpha_c\left\langle \frac{\partial \delta u_i}{\partial x_j}\frac{\partial \delta u_k}{\partial x_j}\frac{\partial \delta u_i}{\partial x_k}\right\rangle \\ & - \nu\frac{\partial}{\partial x_k}\left[\alpha_c\left\langle \delta u_k \frac{\partial \delta u_i}{\partial x_j}\frac{\partial \delta u_i}{\partial x_j}\right\rangle\right] - 2\frac{\nu}{\rho}\frac{\partial}{\partial x_i}\left[\alpha_c\left\langle \frac{\partial \delta u_i}{\partial x_j}\frac{\partial \delta P}{\partial x_j}\right\rangle\right] \\ & + \nu\frac{\partial^2}{\partial x_k^2}[\alpha_c \varepsilon] - 2\nu^2\alpha_c\left\langle \left(\frac{\partial^2 \delta u_i}{\partial x_j \partial x_k}\right)^2\right\rangle \\ & - \frac{\nu^2}{V}\frac{\partial}{\partial x_k}\int_{S_d}\frac{\partial \delta u_i}{\partial x_j}\frac{\partial \delta u_i}{\partial x_j}n_k dS + \frac{2\nu}{\rho V}\int_{S_d}\frac{\partial \delta u_i}{\partial x_j}\frac{\partial \delta P}{\partial x_j}n_i dS \\ & - \frac{\nu^2}{V}\int_{S_d}\frac{\partial}{\partial x_k}\left[\frac{\partial \delta u_i}{\partial x_j}\frac{\partial \delta u_i}{\partial x_j}\right]n_k dS \end{aligned} \tag{11}$$

with the assumptions of incompressible flow, irrotational particles, and no mass transfer. The above equation contains three integrals that represent the effects of particles on the turbulence within the carrier phase. The terms representing the effects of the particles were evaluated by assuming that the particles were smaller than the equivalent Kolmogorov length scale, such that the Stokes drag law would apply [22]. Based on this assumption, the development revealed a production term due to the presence of particles. The form of this term was then modified to extend beyond Stokes drag. In keeping with the modeling procedures used with single phase flows, the dissipation Eq. (11) becomes [22]

$$\alpha_c \frac{D\varepsilon}{Dt} = -\alpha_c C'_{\varepsilon 1}\langle \delta u_i \delta u_j \rangle \frac{\partial \langle u_i \rangle}{\partial x_j}\frac{\varepsilon}{k} - C'_{\varepsilon 2}\alpha_c \frac{\varepsilon^2}{k} + C_{\varepsilon 3}\frac{\nu^2}{V}\sum_n f_n \frac{|u_i - v_i|_n^2}{D_n} + \frac{\partial}{\partial x_i}\left[\alpha_c\left(\nu + \frac{\nu_T}{\sigma_\varepsilon}\right)\frac{\partial \varepsilon}{\partial x_i}\right] \tag{12}$$

where $C'_{\varepsilon 1}$ is the coefficient associated with the production of dissipation due to mean velocity gradients, $C'_{\varepsilon 2}$ is the coefficient associated with dissipation of dissipation, and $C_{\varepsilon 3}$ is the coefficient associated with the production of dissipation due to particle surfaces. The coefficients $C'_{\varepsilon 1}$ and $C'_{\varepsilon 2}$, shown in the above equation, are assumed to be a linear sum of the single phase coefficient and a coefficient that captures the effect of the particles. The ratio of the $C_{\varepsilon 3}/C'_{\varepsilon 2}$ was found by reducing data from experiments involving turbulence generation by particles in homogeneous flows [22] and can be represented by

$$\frac{C_{\varepsilon 3}}{C'_{\varepsilon 2}} = C_{\varepsilon p} \cdot \mathrm{Re}_p^m \tag{13}$$

where $C_{\varepsilon p}$ is the fit coefficient equal to 0.058, m is equal to 1.416, and Re_p is the Reynolds number based on the relative velocity between the particles and the fluid. The values of $C_{\varepsilon p}$ and m represent data for $\mathrm{Re}_p > 100$, and it is hypothesized that the particle loading has an additional effect at lower Re_p. The coefficient for the dissipation of dissipation ($C'_{\varepsilon 2}$) was found from a direct numerical simulation (DNS) study of isotropic turbulent decay with stationary particles [23] and can be represented by

$$C'_{\varepsilon 2} = C_{\varepsilon 2} + 0.355 \cdot \psi_p^{0.89} \tag{14}$$

where $C_{\varepsilon 2}$ is the standard coefficient for single phase flow (1.92) and ψ_p ($=3\pi\tilde{n}\tilde{D}\tilde{v}$) is the dimensionless momentum coupling factor [23]. It is noteworthy to mention that the dimensionless momentum coupling factor is related to the ratio of the dispersed phase mass concentration to the Stokes number [$\psi_p = \alpha_c \cdot C/\mathrm{St}$]. The production of dissipation coefficient due to mean velocity gradients ($C'_{\varepsilon 1}$) is unknown but assumed to have the following functional form [20]:

$$C'_{\varepsilon 1} = C_{\varepsilon 1} + \mathrm{func}(C, \mathrm{St}, \mathrm{Re}_p, \mathrm{Re}) \tag{15}$$

where Re_p is the particle Reynolds number, Re is the fluid Reynolds number, and $C_{\varepsilon 1}$ is the standard coefficient for single phase flow (1.44). The coefficient $C'_{\varepsilon 1}$ can be solved for analytically [20], however, data needed to evaluate the above coefficient are lacking. The effect of this coefficient is studied in Sec. 4.

3 Modeling the Continuous Phase Turbulence in Particle-Laden Channel Flow

To validate the volume average equation set presented above, we consider the data of Kulick et al. [6] and Paris and Eaton [8]. Graham [24] claimed that these data sets are challenging to predict with simple models and a more sophisticated model is needed. Eaton [10] claimed that a new model for the dissipation rate is needed to represent the additional dissipation generated by particles. The above dissipation rate Eq. (12) includes a production of dissipation due to particles.

Kulick et al. [6] and Paris and Eaton [8] used the same experimental setup, which was a high aspect ratio (11.4:1) vertical channel with a development section of 5.2 m. The particles fell down the channel in the same direction that the air was traveling. The particle response time for the 70 μm copper particles is approximately 130 ms [6]. Therefore these particles should have reached a terminal velocity well before the measurement section, and the particle velocity should have exceeded the air velocity throughout the channel. However, the data sets show that the air velocity exceeds the particle velocity at the center of the channel, yet the particle velocity exceeds the air velocity near the wall. The volume fractions of the particles are on the order of 10^{-5}, which implies the importance of two-way coupling and allows one to neglect particle-particle interaction [25]. However, the work of Nasr and Ahmadi [13] showed that when particle-particle and particle-wall collisions are included, a nearly flat particle velocity profile is obtained.

The data presented by Kulick et al. [6] and Paris and Eaton [8] are for steady fully developed particle-laden turbulent channel flow. For such a flow, a simple 1D modeling approach can be taken. Additional assumptions are uniform particle diameter, no mass transfer between the dispersed and continuous phase, particle rotational effects are neglected, and the particle velocity deviations are negligible compared with the mean slip velocity. The volume averaged conservation equations (4), (9), and (12) for the continuous phase are applied to a steady incompressible fully developed flow and are shown as follows.

For continuous phase momentum,

$$0 = -\alpha_c \frac{d\langle P \rangle}{dx} + \alpha_c \rho_c g + \alpha_c \frac{d}{dy}\left((\mu + \mu_T)\frac{d\langle u \rangle}{dy}\right) - \beta_V(\langle u \rangle - \langle v \rangle) \tag{16}$$

For continuous phase turbulent kinetic energy,

Table 1 Model coefficients

Parameter	Time averaged equation set	Volume averaged equation set
$C'_{\varepsilon 1}$	1.44	$1.44+C_{\varepsilon 1p}$
$C'_{\varepsilon 2}$	1.92	$1.92+0.355\cdot(\psi_p)^{0.89}$
$C_{\varepsilon 3}$	-	$0.058\cdot C'_{\varepsilon 2}\cdot \mathrm{Re}_p^{1.416}$
κ	0.41	0.41
C_μ	0.09	0.09
σ_k	1.0	1.0
σ_ε	1.3	1.3

$$0=\alpha_c\nu_T\left(\frac{d\langle u\rangle}{dy}\right)^2+\frac{\beta_V}{\rho_c}[\langle u\rangle-\langle v\rangle]^2+\alpha_c\frac{d}{dy}\left[\left(\nu+\frac{\nu_T}{\sigma_k}\right)\frac{dk}{dy}\right]-\alpha_c\varepsilon \tag{17}$$

For continuous phase turbulent dissipation,

$$0=C'_{\varepsilon 1}\alpha_c\nu_T\left(\frac{d\langle u\rangle}{dy}\right)^2\frac{\varepsilon}{k}-C'_{\varepsilon 2}\alpha_c\frac{\varepsilon^2}{k}+\alpha_d C_{\varepsilon 3}\frac{6v^2}{\pi D^4}f[(\langle u\rangle-\langle v\rangle)^2+2k]+\alpha_c\frac{d}{dy}\left[\left(\nu+\frac{\nu_T}{\sigma_\varepsilon}\right)\frac{d\varepsilon}{dy}\right] \tag{18}$$

where the turbulence kinematic viscosity (ν_T) is modeled by Eq. (6) and the coefficients, shown in the above equations, are given in Table 1. At the wall, the velocity of the continuous phase is zero and the shear at the wall is modeled by

$$\tau_w=\frac{\rho C_\mu^{1/4}k^{1/2}}{u^+}u \tag{19}$$

Near the wall, the production of turbulent kinetic energy is balanced by the dissipation and the diffusion is assumed negligible. Applying these assumptions to Eq. (17) shows

$$\varepsilon=\nu_T\left(\frac{d\langle u\rangle}{dy}\right)^2+\frac{\beta_V}{\alpha_c\rho_c}[\langle u\rangle-\langle v\rangle]^2 \tag{20}$$

The above equation assures that the net production of turbulent kinetic energy due to particles and mean velocity gradients is balanced by dissipation near the wall. Based on the data of Kulick et al. [6] and Paris and Eaton [8], it was assumed that the law of the wall can be applied to particle-laden flows; therefore, the dissipation near the wall is shown to be of the form

$$\varepsilon=\frac{u_\tau^3}{\kappa y}+\frac{\beta_V}{\alpha_c\rho_c}[\langle u\rangle-\langle v\rangle]^2 \tag{21}$$

The turbulent kinetic energy near the wall is found by assuming that the shear stress is constant near the wall, and the shear at the wall is related to the friction velocity by

$$u_\tau^2=C_\mu\frac{k^2}{\varepsilon}\frac{d\langle u\rangle}{dy} \tag{22}$$

Again, assuming the law of the wall is valid and eliminating dissipation from Eqs. (21) and (22) yields the following relation for the particle-laden turbulent kinetic energy near the wall:

$$k=\frac{u_\tau^2}{\sqrt{C_\mu}}\sqrt{\left(1+\frac{\beta_V\kappa y}{\alpha_c\rho_c u_\tau^3}[\langle u\rangle-\langle v\rangle]^2\right)} \tag{23}$$

A finite volume approach [26] was used to model Eqs. (16)–(18), and the boundary conditions applied near the wall were Eqs. (19), (21), and (23). The particle velocity profile was determined from the experimental data [6,8]. The turbulent kinetic energy could not be directly found from the data. For purposes of analysis, it was assumed that the turbulence was homogeneous in the transverse directions. The turbulent kinetic energy for laden and unladen cases was obtained from

Table 2 Data parameters

Parameter	Kulick et al. (1993)	Paris et al. (2001)
Particle material	Copper	Glass
Particle diameter (D) (μm)	70	150
Particle density (ρ_d) (kg/m^3)	8800	2500
Particle loading	10%, 20%	20%
Continuous phase	air	air
Centerline gas velocity (U_{cl}) (m/s)	10.5	10.5
Unladen piezometric pressure gradient (dP_z/dx) (Pa/m)	−14.28	−27.56

$$2k=\overline{u_1'^2}+2\cdot\overline{u_2'^2} \tag{24}$$

For the unladen case, the standard coefficients were used in the k-ε model; for the laden cases, the coefficients were the sum of the single phase coefficients and coefficients to account for the effects of the dispersed phase (see Table 1). The unladen piezometric pressure gradient was determined from the data of Kulick et al. [6] and found to be −14.28 Pa/m. Kulick et al. [6] could not measure the laden pressure gradient; Paris and Eaton [8] measured the laden pressure gradient but could not justify why it was so high. In the experiments of Kulick et al. [6] and Paris and Eaton [8], the continuous phase mass flow rate was adjusted for the different particle loadings in order to maintain a constant centerline velocity, shown in Table 2. In the model, for the laden cases, the piezometric pressure gradient was iterated until the centerline velocity matched that of the experimental data.

4 Results and Discussion

The unladen velocity profile and turbulent kinetic energy predicted by the model was compared with the data of Kulick et al. [6] and Paris and Eaton [8]. For this case, the standard k-ε model was used with the standard coefficients (shown in Table 1). The velocity was normalized by the centerline velocity and plotted in terms of y^+. The normalized unladen velocity profile predicted by the model agrees well with the measurements, shown in Fig. 4. Kulick et al. [6] used laser Doppler anemometry (LDA), and Paris and Eaton [8] used particle image velocimetry (PIV) to measure the mean and fluctuating velocities. The turbulent kinetic energy was determined from the data using Eq. (24); the data agree well with the model and are shown in Fig. 5.

Kulick et al. [6] obtained air velocity measurements for various particle sizes (50–90 μm) and loadings (0–0.8). The data col-

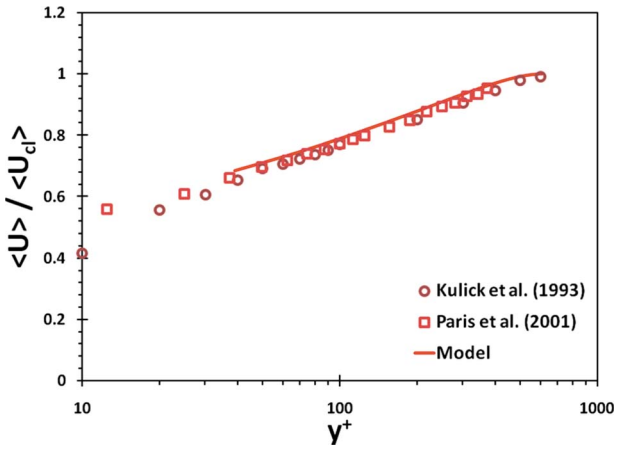

Fig. 4 Comparison of the unladen velocity profiles predicted by the model to the experimental data of Kulick et al. [6] and Paris and Eaton [8]

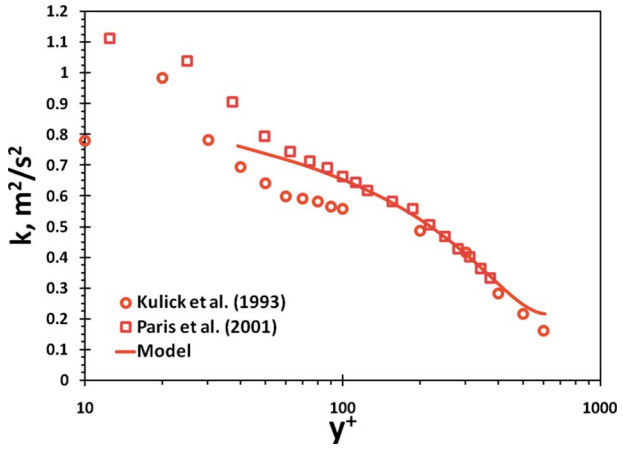

Fig. 5 Comparison of the unladen turbulent kinetic energy profiles predicted by the model to the experimental data of Kulick et al. [6] and Paris and Eaton [8]

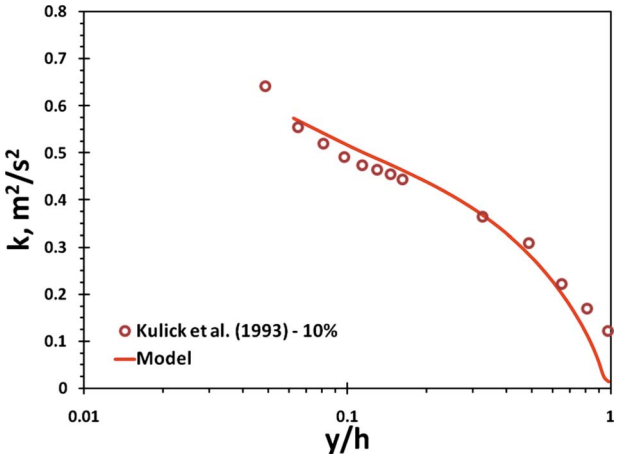

Fig. 7 Comparison of the particle-laden turbulent kinetic energy profiles predicted by the model to the experimental data of Kulick et al. [6]—copper particles, 70 μm dia., and 10% mass loading

lected by Kulick et al. [6] demonstrate that 50 μm and 90 μm glass particles produce little attenuation, however, 70 μm copper particles at mass loadings greater than 0.1 produce significant turbulence attenuation. For the case of 70 μm copper particles at mass loadings of 10% and 20%, the experimental data of Kulick et al. [6] are compared with the model predictions. For the particle-laden case, the coefficients used in the volume averaged k-ε equations are shown in Table 1. The velocity is normalized by the centerline velocity and shown in Fig. 6. For the 10% and 20% mass loading cases, the model shows to underpredict the velocity magnitude near the wall. It is also noticed that the velocity profiles predicted by the model are quite different than those found from the experimental data. The velocity profile predicted by the model for a mass loading of 10% shows a slight increase in the carrier velocity near the center of the channel, while the increase in velocity for a mass loading of 20% is more pronounced for $y/h > 0.6$. The turbulent kinetic energy predicted by the model is compared with experimental data for 10% mass loading (Fig. 7) and 20% mass loading (Fig. 8). The model compares well with the experimental data near the wall, but deviates toward the center of the channel. For the 20% mass loading case, a flat profile is noticed near the center of the channel. Although not seen in the data set of Kulick et al. [6], a similar flat profile for the turbulent kinetic energy near the centerline of a pipe is found in the data of Tsuji et al. [4] and Sheen et al. [5] for small particles. To illustrate the capability of the model predicting a decrease in TKE with increased mass loading, a comparison of the two mass loadings is shown in Fig. 9. Near the wall, the model predicts turbulence attenuation for increased mass loading, in agreement with the experimental data. Near the centerline of the channel, the predictions deviate from the experimental data.

Paris and Eaton [8] used the same experimental set up by Kulick et al. [6] and were able to reproduce the unladen flow characteristics. The data of Paris and Eaton [8] stops short of the centerline of the channel; a reason is not given. The particle size and loading is given in Table 2. A comparison of the velocity profile normalized by the centerline velocity for the laden case of 20% mass loading is shown in Fig. 10. The magnitude of the velocity profile is slightly lower than the experimental values but the predicted velocity trend agrees with the data. It is noteworthy to mention that the normalized velocity profile reported by Paris and Eaton [8] for the continuous phase matches very well to the unladen velocity profile of Kulick et al. [6], yet the model predicts two different velocity profiles. In light of the model, the only difference between these two data sets is the particle properties and the particle velocity profile, the last of which was determined

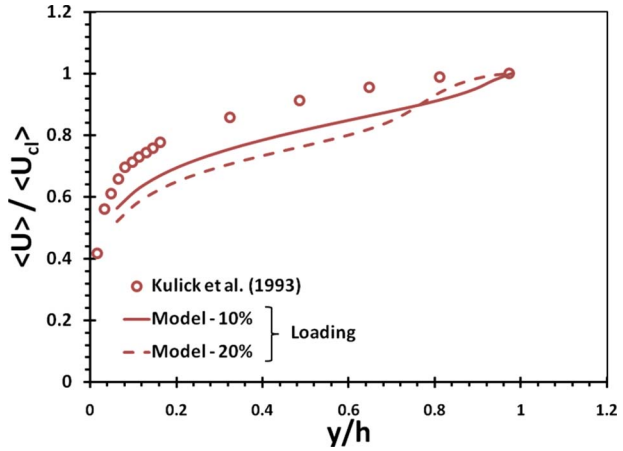

Fig. 6 Comparison of the velocity profiles predicted by the model to the experimental data of Kulick et al. [6]—copper particles, 70 μm dia., and mass loading indicated in the legend

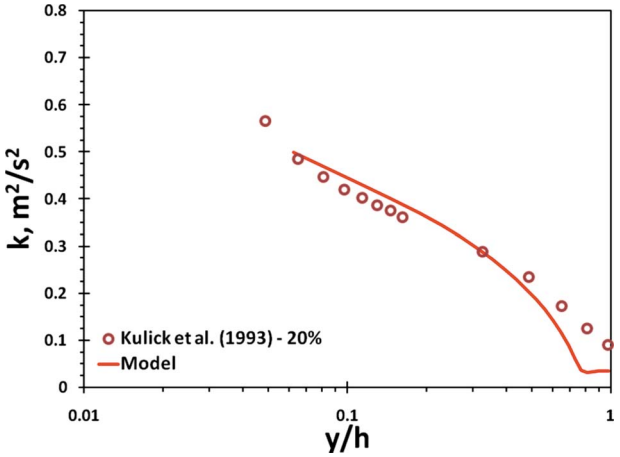

Fig. 8 Comparison of the particle-laden turbulent kinetic energy profiles predicted by the model to the experimental data of Kulick et al. [6]—copper particles, 70 μm dia., and 20% mass loading

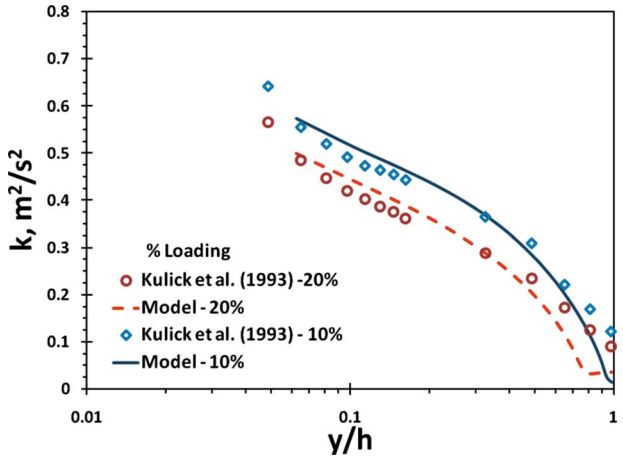

Fig. 9 Comparison of the particle-laden turbulent kinetic energy profiles predicted by the model to the experimental data of Kulick et al. [6]—copper particles, 70 μm dia., and mass loading indicated in the legend

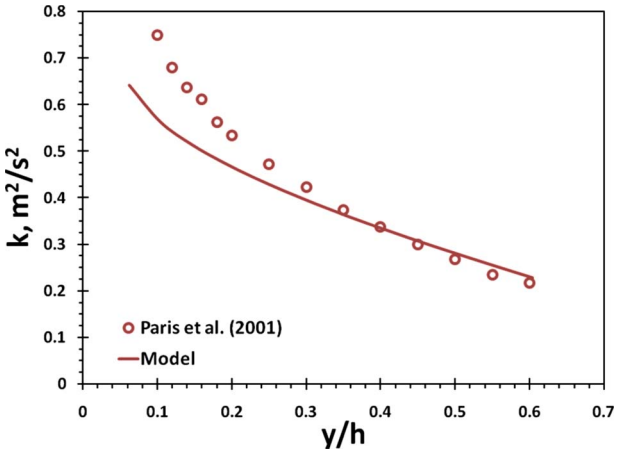

Fig. 11 Comparison of the turbulent kinetic energy profile predicted by the model to the experimental data of Paris and Eaton [8]—glass particles, 150 μm dia., and 20% loading

by different measurement techniques. The predicted turbulent kinetic energy is compared with the measurements and shown in Fig. 11.

Part of the reason for these deviations may be explained by the noninclusion of the redistribution terms in the turbulence energy equation, Eq. (9). For most cases involving particle-laden flows, $[\langle u\rangle-\langle v\rangle]^2 \gg \langle \delta v_i \delta v_i\rangle - \langle \delta u_i \delta v_i\rangle$ so the redistribution terms may be neglected for such cases. However, for cases when $[\langle u\rangle-\langle v\rangle]^2 \approx 0$, the redistribution terms may play a significant role in modeling turbulent kinetic energy near the wall. In the data of Kulick et al. [6] and Paris and Eaton [8], there is a point in the flow where the continuous phase and dispersed phase velocities are equal, but the data set does not give correlations for $\langle \delta u_i \delta v_i\rangle$. A method to model these terms has been proposed by Zhang and Reese [16] and may need to be considered.

Another reason for the deviation of turbulent kinetic energy near the center of the channel is the fact that the coefficient $C_{\varepsilon 3}$ was calibrated with minimal data at low relative Reynolds numbers [22]. The data at low relative Reynolds numbers suggested that particle loading affects the coefficient. To evaluate the effectiveness of the additional production term in the dissipation model, the production coefficient ($C_{\varepsilon 3}$) is varied. Within this coefficient, $C_{\varepsilon p}$ is varied from zero to 0.060 (to simulate an effect of particle concentration), while the exponent m remained at 1.416 (the effect of particle Reynolds number). When $C_{\varepsilon p}$ is set to zero, the additional production of dissipation due to particle surfaces is suppressed, yet the effects of the particles are still included in the turbulent kinetic energy equation. For such a case the dissipation is essentially modeled as the single phase dissipation with the standard coefficients (the effect of particles on $C'_{\varepsilon 2}$ is negligible). This formulation shows a nearly constant TKE across the channel (see Fig. 12). Increasing $C_{\varepsilon p}$ to 0.015 shows a drastic reduction in TKE. For this case, the TKE profile is nearly matched, but the predicted magnitude is higher than the experimental data. As $C_{\varepsilon p}$ is increased to 0.060, the TKE near the wall matches well; near the center of the channel, the model underpredicts the measurements and shows a constant TKE. The normalized velocity profiles show that as the production coefficient is reduced from 0.060 to 0.015, the trend and magnitude of the velocity profiles better match the data (shown in Fig. 13). It can be seen that if the production coefficient was zero, the velocity profile would be overpredicted; this substantiates that a production of dissipation term due to particles is necessary but a better calibration of the coefficient is needed at lower particle Reynolds numbers.

The other unknown is the production coefficient ($C'_{\varepsilon 1}$) due to mean velocity gradients. In the derivation of the dissipation equation, the production coefficient was assumed to vary with one or

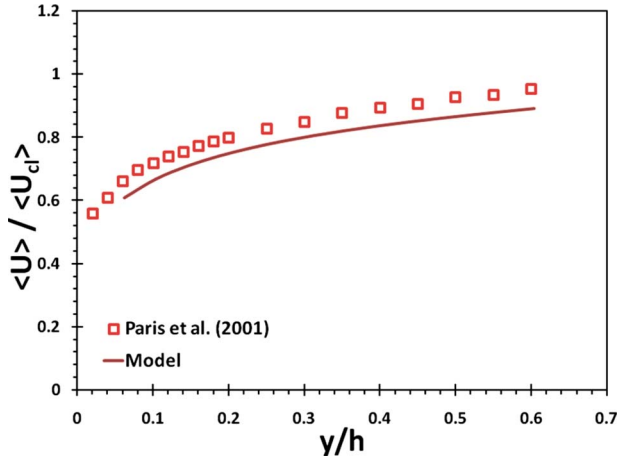

Fig. 10 Comparison of the velocity profile predicted by the model to the experimental data of Paris and Eaton [8]—glass particles, 150 μm dia., and 20% loading

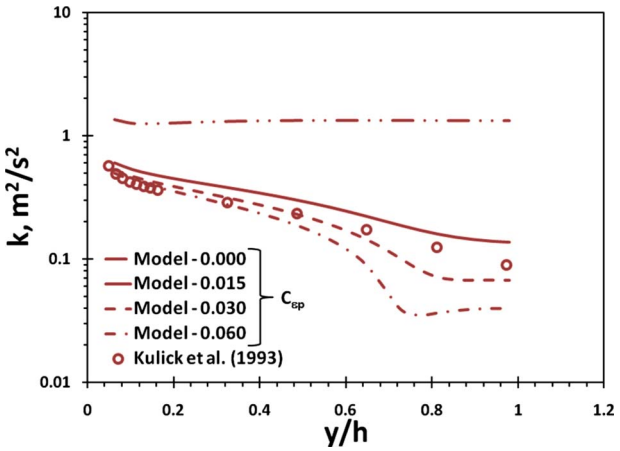

Fig. 12 Evaluation of the production of dissipation coefficient due to the particles—Kulick et al. [6], 20% loading, and $C_{\varepsilon p}$ indicated in the legend

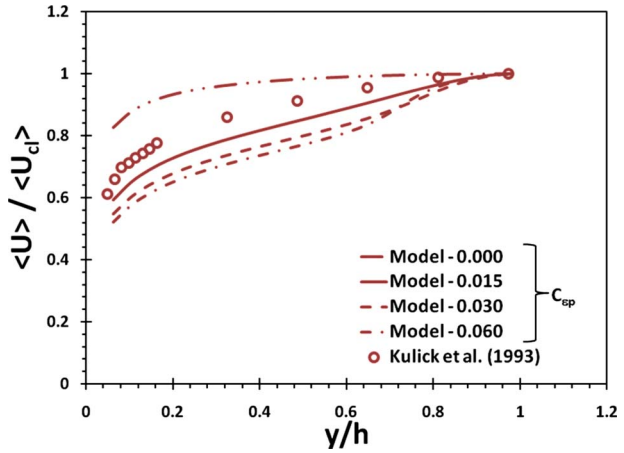

Fig. 13 Effect of the production of dissipation on the velocity profile—Kulick et al. [6], 20% loading, and $C_{\varepsilon p}$ indicated in the legend

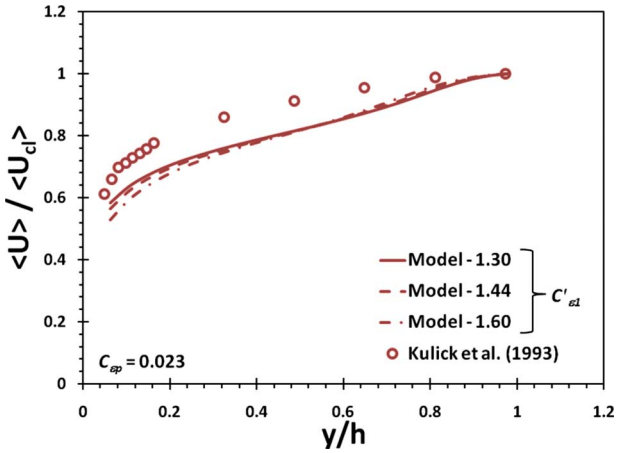

Fig. 15 Effect of the production of dissipation coefficient due to the mean velocity gradient on the normalized velocity profile—Kulick et al. [6], 20% loading, and $C'_{\varepsilon 1}$ indicated in the legend

more of the fundamental nondimensional parameters found in particle-laden flows, namely, particle loading, Stokes number, particle Reynolds number, or the Reynolds number of the flow [20]. The calibration of this coefficient is complex [20] and depends on the shear velocity and von Karman constant, both of which are unknown in the data presented in the literature. To simplify, $C'_{\varepsilon 1}$ was assumed constant between the wall and the center of the channel yet altered from its standard value (1.44) to understand its effect (see Fig. 14). In this figure, the coefficient $C_{\varepsilon p}$ is set to 0.023, which matches the magnitude of TKE at the center of the channel, and the production of dissipation ($C'_{\varepsilon 1}$) due to mean velocity gradients was varied to assess its influence on the predictions. If $C'_{\varepsilon 1}$ is set to 1.6 ($C_{\varepsilon p}$=0.023), the TKE is matched near the wall and at the center of the channel. However, the results show that there is still a constant TKE near the center of the channel, and the TKE predicted by the model deviates slightly from the data between $0.4 < y/h < 0.9$. The normalized velocity profile is shown in Fig. 15.

The predictions of the turbulent dissipation model with an additional production term due to the presence of particles are shown to improve the prediction of TKE and to also predict the turbulence modulation due to particle loading. Comparing Figs. 12 and 14 shows that the production of dissipation due to the particle surfaces mildly affects the TKE near the wall, and obviously the production of dissipation due to mean velocity gradients has no affect at the center of the channel. These results also highlight that $C'_{\varepsilon 1}$ and $C_{\varepsilon 3}$ may be slightly coupled in regions where the velocity gradient is nonzero. Overall, the additional production term shows to be an improvement over the standard single phase turbulent dissipation model. For flows with low particle Reynolds numbers, the prescribed coefficients are invalid, and additional studies are needed to validate these conditions. More results with supporting data, such as the laden pressure gradient, wall shear, particle concentration, and velocity distributions, are needed to further validate the model.

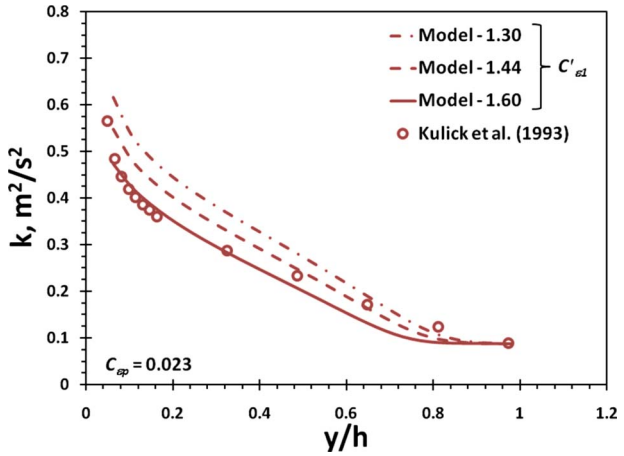

Fig. 14 Evaluation of the production of dissipation coefficient due to the mean velocity gradient on TKE—Kulick et al. [6], 20% loading, and $C'_{\varepsilon 1}$ indicated in the legend

5 Conclusion

A volume averaged equation set for particle-laden turbulent flow is presented. This includes momentum, TKE, and dissipation transport equations, coefficients, and boundary conditions for k and ε. A numerical model was developed and compared with the continuous phase TKE and velocity data of Kulick et al. [8] and Paris and Eaton [6]. The model shows good agreement with the TKE and continuous phase velocity data. The model also predicts the attenuation of TKE for increased particle loading and compares reasonably well with the experimental data.

In this study, the coefficients associated with the production of dissipation were varied to appreciate their effect on model predictions. It was found that the coefficient for production of dissipation due to mean velocity ($C'_{\varepsilon 1}$) gradients needs to be calibrated to balance the production of dissipation coefficient due to particle surfaces ($C_{\varepsilon 3}$). This study also showed that $C_{\varepsilon 3}$ is not calibrated correctly for low particle Reynolds number flows, and additional data are needed to understand the effect of particle loading at low particle Reynolds numbers. Such data would provide better calibration of these coefficients.

References

[1] Curtis, J. S., and van Wachem, B., 2004, "Modeling Particle-Laden Flows: A Research Outlook," AIChE J., **50**, pp. 2638–2645.
[2] Chen, C. P., and Wood, P. E., 1985, "A Turbulence Closure Model for Dilute Gas-Particle Flows," Can. J. Chem. Eng., **63**, pp. 349–360.
[3] Crowe, C. T., 2000, "On Models for Turbulence Modulation in Fluid-Particle Flows," Int. J. Multiphase Flow, **26**, pp. 719–727.
[4] Tsuji, Y., Morikawa, Y., and Shiomi, H., 1984, "LDV Measurements of an Air-Solid Two-Phase Flow in a Vertical Pipe," J. Fluid Mech., **139**, pp. 417–434.
[5] Sheen, H., Chang, Y., and Chiang, Y., 1993, "Two Dimensional Measurements of Flow Structure in a Two-Phase Vertical Pipe Flow," Proc. Natl. Sci. Counc., Repub. China, Part A: Phys. Sci. Eng., **17**, pp. 200–213.
[6] Kulick, J. D., Fessler, J. R., and Eaton, J. K., 1993, "On the Interactions

Between Particles and Turbulence in a Fully-Developed Channel Flow in Air," Stanford University, Report No. MD-66.
[7] Varaksin, A. Y., Kurosaki, Y., Satch, I., Polezhaev, Y. V., and Polyahov, A. F., 1998, "Experimental Study of the Direct Influence of Small Particles on Carrier Air Turbulence Intensity for Pipe Flow," Third International Conference on Multiphase Flow, Lyon, France, Jun. 8–12.
[8] Paris, A. D., and Eaton, J. K., 2001, "Turbulence Attenuation in a Particle-Laden Channel Flow," Stanford University, Report No. TSD-137.
[9] Elghobashi, S. E., and Abou-Arab, T. W., 1983, "A Two-Equation Turbulence Model for Two-Phase Flows," Phys. Fluids, **26**, pp. 931–938.
[10] Eaton, J. K., 1995, "Turbulence Modification by Particles in Shear Flows," FED (Am. Soc. Mech. Eng.), **228**, pp. 273–278.
[11] Vermorel, O., Bedat, B., Simonin, O., and Poinsot, T., 2003, "Numerical Study and Modelling of Turbulence Modulation in a Particle Laden Slab Flow," J. Turbul., **4**, pp. 1–39.
[12] Yan, F., Lightstone, M. F., and Wood, P. E., 2007, "Numerical Study on Turbulence Modulation in Gas-Particle Flows," Heat Mass Transfer, **43**, pp. 243–253.
[13] Nasr, H., and Ahmadi, G., 2007, "The Effect of Two-Way Coupling and Inter-Particle Collisions on Turbulence Modulation in a Vertical Channel Flow," Int. J. Heat Fluid Flow, **28**, pp. 1507–1517.
[14] Mohanarangam, K., and Tu, J. Y., 2007, "Two-Fluid Model for Particle-Turbulence Interaction in a Backward-Facing Step," AIChE J., **53**, pp. 2254–2264.
[15] White, F. M., 2003, *Fluid Mechanics*, 5th ed., McGraw-Hill, New York.
[16] Zhang, Y., and Reese, J. M., 2003, "Gas Turbulence Modulation in a Two-Fluid Model for Gas-Solid Flows," AIChE J., **49**, pp. 3048–3065.
[17] Zhang, Y., and Reese, J. M., 2001, "Particle-Gas Turbulence Interactions in a Kinetic Theory Approach to Granular Flows," Int. J. Multiphase Flow, **27**, pp. 1945–1964.
[18] Crowe, C. T., and Gillant, I., 1998, "Turbulence Modulation of Fluid-Particle Flows—a Basic Approach," Third International Conference on Multiphase Flows, Lyon, France, Jun. 8–12.
[19] Eaton, J. K., 2006, "Turbulence Modulation by Particles," *Multiphase Flow Handbook*, C. T. Crowe, ed., CRC, Boca Raton, FL.
[20] Schwarzkopf, J. D., 2008, "Turbulence Modulation in Particle Laden Flows: The Derivation and Validation of a Dissipation Transport Equation," Ph.D. thesis, Washington State University, Pullman, WA.
[21] Crowe, C. T., Sommerfeld, M., and Tsuji, Y., 1998, *Multiphase Flows With Droplets and Particles*, CRC, Boca Raton, FL.
[22] Schwarzkopf, J. D., Crowe, C. T., and Dutta, P., 2009, "A Turbulence Dissipation Model for Particle Laden Flow," AIChE J., **55**, pp. 1416–1425.
[23] Schwarzkopf, J. D., Crowe, C. T., Riley, J. J., Wetchagarun, S., and Dutta, P., 2009, "Direct Numerical Simulation of Stationary Particles in Homogenous Turbulence Decay: Application of the k-ε Model," Int. J. Multiphase Flow, **35**, pp. 411–416.
[24] Graham, D. I., 2000, "Turbulence Attenuation by Small Particles in Simple Shear Flows," ASME J. Fluids Eng., **122**, pp. 134–137.
[25] Elghobashi, S., 1994, "On Predicting Particle-Laden Turbulent Flows," Appl. Sci. Res., **52**, pp. 309–329.
[26] Patankar, S. V., 1980, *Numerical Heat Transfer and Fluid Flow*, Hemisphere, New York.

Transient Thin-Film Flow on a Moving Boundary of Arbitrary Topography

Roger E. Khayat
e-mail: rkhayat@uwo.ca

Tauqeer Muhammad

Department of Mechanical and Materials Engineering,
University of Western Ontario,
London, ON, N6A 5B9, Canada

The transient two-dimensional flow of a thin Newtonian fluid film over a moving substrate of arbitrary shape is examined in this theoretical study. The interplay among inertia, initial conditions, substrate speed, and shape is examined for a fluid emerging from a channel, wherein Couette–Poiseuille conditions are assumed to prevail. The flow is dictated by the thin-film equations of the "boundary layer" type, which are solved by expanding the flow field in terms of orthonormal modes depthwise and using the Galerkin projection method. Both transient and steady-state flows are investigated. Substrate movement is found to have a significant effect on the flow behavior. Initial conditions, decreasing with distance downstream, give rise to the formation of a wave that propagates with time and results in a shocklike structure (formation of a gradient catastrophe) in the flow. In this study, the substrate movement is found to delay shock formation. It is also found that there exists a critical substrate velocity at which the shock is permanently obliterated. Two substrate geometries are considered. For a continuous sinusoidal substrate, the disturbances induced by its movement prohibit the steady-state conditions from being achieved. However, for the case of a flat substrate with a bump, a steady state exists. [DOI: 10.1115/1.3222903]

1 Introduction

This study is a theoretical treatment of the pressure-driven high-speed transient two-dimensional coating flow over a moving substrate of arbitrary shape. The fluid is assumed to emerge from a channel, wherein Couette–Poiseuille conditions are assumed to prevail. The effect of substrate topography has been examined extensively for the case of stationary substrate [1–7]. The flow over a moving substrate has also been examined [8–10]. Contrary to the present paper, these studies, however, were limited to the case of a flat substrate only. Existing studies [3–10] have also been limited to steady-state coating flow since it is the long-term behavior that is typically of practical interest. However, steady-state conditions are not always possible to achieve in reality. In this case, although the steady state theoretically exists, it is simply unstable. The coating process can also be inherently transient as a result of geometrical variations or constant changes in processing conditions. Initial conditions will also be investigated extensively given their drastic influence in thin-film flow.

In this work, the flow is assumed to be induced by both pressure gradient and substrate movement. The study focuses on high-speed coating flow. In this case, flow inertia is important. Most existing studies do indeed neglect inertia since the fluids involved in coating are typically highly viscous. Similar to earlier studies on Newtonian and non-Newtonian flows [2,11–13], a spectral approach is proposed to model the problem. The flow is dictated by the thin-film equations of the "boundary layer" type, which are solved by expanding the flow field in terms of orthonormal modes in the depthwise direction and using the Galerkin projection, combined with a time-stepping implicit scheme, and integration along the flow direction. Assessment of convergence and accuracy is carried out by adopting different truncation levels, varying the time increment and mesh size. The influence of inertia, substrate movement and topography, as well as initial conditions is closely examined.

Manuscript received September 21, 2007; final manuscript received August 7, 2009; published online September 14, 2009. Editor: Joseph Katz.

2 Problem Formulation and Solution Procedure

The general two-dimensional thin-film formulation is implemented for the transient flow of a Newtonian fluid over a moving surface of arbitrary shape. The equations and boundary conditions are deduced for a flow that is driven by both an imposed pressure gradient in the channel and the movement of the substrate. The solution procedure is also outlined.

2.1 Thin-Film Equations and Boundary Conditions. Consider the flow of an incompressible Newtonian fluid of density ρ, viscosity μ, and surface tension coefficient σ, emerging from a channel, of width H, and moving on a substrate. The flow is induced in part by a pressure gradient inside the channel and in part by the translation of the substrate and lower channel plate. In this case, the film length, L, and H are taken as typical reference length and thickness in the streamwise and depthwise directions, respectively, with x and z being the corresponding dimensionless coordinates. Following the usual scaling process for a thin film, the dimensionless streamwise and depthwise velocity components, $u(x,z,t)$ and $w(x,z,t)$, are scaled by V and HV/L, respectively, where V is a reference velocity. In this work, L may be taken to correspond to the length of the initial fluid domain, and V is taken equal to the mean velocity part of the flow induced by the pressure gradient inside the channel. Time, t, is scaled by L/V, and, for a thin film, the pressure, $p(x,z,t)$, is scaled by $\mu VL/H^2$ (see below). The scaling for pressure is chosen to ensure the balance between pressure and viscous forces [14]. Figure 1 illustrates schematically the problem in the (x,z) plane using dimensionless notations. The shape of the free surface is given by $z=\eta(x,t)$, and that of the substrate by $z=h(x,t)$. Both $\eta(x,t)$ and $h(x,t)$ are scaled by H. There are four dimensionless groups that emerge, namely, the (modified) Reynolds number Re, the aspect ratio ε, the capillary number Ca, and the Froude number Fr. More explicitly,

$$\mathrm{Re}=\varepsilon\frac{\rho VH}{\mu},\quad \varepsilon=\frac{H}{L}\quad \mathrm{Ca}=\frac{\mu V}{\sigma},\quad \mathrm{Fr}=\frac{V^2}{gH} \tag{1}$$

The conservation equations are obtained in dimensionless form, with terms of $O(\varepsilon^2)$ and higher being excluded. It is important to

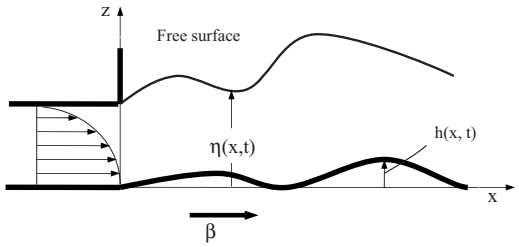

Fig. 1 Schematic illustration of the two-dimensional coating flow emerging from a channel. $\eta(x,t)$ and β, respectively, represent the free-surface height and the speed of the substrate. $h(x,t)$ represents the height/depth of the substrate.

observe that, similar to lubrication flow, the pressure scale for thin-film flow is taken as $\varepsilon^{-2}\mu V/L$. This scaling is necessary to avoid singularity in the limit $\varepsilon \to 0$. It is assumed that no external (wind) pressure acts on the free surface [15]. In this case, the continuity equation retains its original form to read

$$u_x + w_z = 0 \tag{2}$$

and the conservation of linear momentum in the x and z directions reduce to 2:

$$\mathrm{Re}(u_t + uu_x + wu_z) = -p_x + u_{zz} \tag{3a}$$

$$p_z = -\frac{\mathrm{Re}}{\mathrm{Fr}} \tag{3b}$$

respectively. Here a subscript with respect to x or z denotes partial differentiation. Re is sometimes referred to as the modified Reynolds number in lubrication theory [1,16]. In this case, $\mathrm{Re} = \varepsilon^2\ \mathrm{Re}_L$, where Re_L is the Reynolds number based on L. Although Re_L may be small for most process flows, it may be large for low-viscosity liquids. In this work, inertial effects will be included to cover the widest range possible of flows. In this case, it is assumed that Re is at least $O(1)$. Note that the aspect ratio ε, does not appear explicitly in the equations or boundary conditions.

The evolution of the free surface is dictated by the kinematic condition:

$$w(x, z = \eta, t) = \eta_t(x,t) + u(x, z = \eta, t)\,\eta_x(x,t) \tag{4}$$

The dynamic condition reduces to the balance between pressure and surface tension, and the vanishing of the shear stress at the free surface. Thus,

$$p(x, z = \eta, t) = -\frac{\varepsilon^3}{\mathrm{Ca}}\eta_{xx} \tag{5a}$$

$$u_z(x, z = \eta, t) = 0 \tag{5b}$$

The present study is focused on thin-film flow in the visco-inertial range. It is argued here that the effects of surface tension and gravity are negligible. These effects enter the conservation of momentum equation through the streamwise pressure gradient p_x. In fact, if Eq. (3*b*) is integrated and condition (5*a*) is used, then one finds, expectedly for a thin film, that the pressure gradient does not depend on z and is given by $p_x(x,t) = -(\mathrm{Re}/\mathrm{Fr})\,\eta_x - (\varepsilon^3/\mathrm{Ca})\,\eta_{xxx}$. Now, recalling that one of the major assumptions for thin film, and for the current boundary-layer approach to hold, is that the local curvature of the film surface must be sufficiently small, which is reflected here by the presence of ε^3 (note that $\eta_{xxx} \sim 1$). In addition, the surface tension coefficient of typical coating fluids is small. Lee and Mei [17] examined the formation of solitary waves on inclined thin-film flow, and determined the dependence of the Weber number of different liquids on the Reynolds number for both small and large angles of inclination. They found that surface tension effect decreases strongly with inertia. Lee and Mei's results show that, for a film of viscosity μ, surface tension σ, and thickness H, flowing at a mean velocity V, the capillary number behaves roughly like $\mathrm{Ca} \sim \mathrm{Re}_H^2/\varepsilon$, where $\mathrm{Re}_H = \rho VH/\mu$ is the Reynolds number based on the film thickness. Although the current film flow is not gravity driven, it is thin, and one may therefore reasonably assume that a similar (admittedly not identical) dependence on the Reynolds number exists for Ca when the thin film is pressure driven (excluding the substrate translation for this argument). Here ε is again the ratio of film thickness and length. This suggests, that the capillary number for the present problem can be estimated as being $\mathrm{Ca} = O(\mathrm{Re}^2/\varepsilon^3) = O(\varepsilon^{-3})$, considering $\mathrm{Re} = O(1)$. Now, recall that surface tension effect for thin-film flow is shown, as condition (5*a*) suggests, to be $O(\varepsilon^3/\mathrm{Ca})$ [13,14]. This shows, in turn, based on Lee and Mei's result, that surface tension effect is negligibly small for a thin film at moderate Reynolds number, and is $O(\varepsilon^6)$. Omodei [18] carried out a two-dimensional finite-element simulation of steady Newtonian jet flow. He found that the height of the free surface changes by 8% when the capillary number changes from 0.83 to infinity at a Reynolds number (based on channel exit half height) equal to 1, compared with a change in jet thickness of less than 1% when the Reynolds number is greater than 10. A further drop in capillary number is thus required to observe any palpable change in jet height at moderately large Reynolds number. However, further decrease in Ca is not realistic according to experiment. See, for instance, the early study by Goren and Wronski [19] on capillary jet flow. The capillary number can be large even for some (essentially) Newtonian fluids with high viscosity such as polybutene oils. As an illustration, consider polybutene oil with mean viscosity, $\mu = 80$ mPa s, density $\rho = 1200$ kg/m^3, and surface tension coefficient $\sigma = 50$ mN/m. The film is assumed to move at 12 m/s out of a channel of 2 mm gap, on a substrate of 20 mm length. In this case, $\varepsilon = 0.1$, $\mathrm{Re} = 36$ and $\mathrm{Ca} = 19.2$, making surface tension effect of $O(10^{-5})$. In this case, the effect of gravity also appears to be negligible, with $\mathrm{Re}/\mathrm{Fr} = 4.9 \times 10^{-3}$. Consequently, given the negligible effects of surface tension and gravity, condition (5*a*) and Eq. (3*b*) suggest that the pressure vanishes everywhere. The pressure will therefore be dropped from Eq. (3*a*).

The no-slip and no-penetration conditions at the substrate are, respectively,

$$u(x, z = h, t) = \beta \tag{6a}$$

$$w(x, z = h, t) = 0 \tag{6b}$$

where β is the dimensionless substrate velocity. Additional boundary conditions are also needed at the channel exit. In this study, the free-surface height and velocity are imposed at the origin $x = 0$, and are assumed to be independent of time. Thus,

$$\eta(x = 0, t) = 1 \tag{7a}$$

$$u(x = 0, z, t) = -6z(z - 1) + \beta(1 - z) \tag{7b}$$

Condition (7*b*) corresponds to fully developed Poiseuille–Couette flow at the channel exit. This assumption is not entirely unreasonable for thin-film flow. Tillett [20] examined the pressure-driven flow of a jet near the channel exit, and showed that the deviation from Poiseuille is of $O(\mathrm{Re}_H^{-1})$, where Re_H is the Reynolds number based on the channel width, H. Thus, the error resulting from assuming fully developed conditions at the channel exit in the present problem is, from Eq. (1), estimated to be $O(\varepsilon/\mathrm{Re})$. Since Re is assumed to be of $O(1)$, the error is at most of $O(\varepsilon)$. Finally, the initially conditions may be written as

$$\eta(x, t = 0) = \eta_0(x), \quad u(x, z, t = 0) = u_0(x, z) \tag{8}$$

where $\eta_0(x)$ and $u_0(x,z)$ will be specified later. Given the hyperbolic nature of the governing equation, the influence of the initial conditions on the ensuing flow is crucial (see below).

2.2 Modal Expansion and Time-Marching Scheme. Problems (2), (3*a*), (3*b*), (4), (5*a*), (5*b*), (6*a*), (6*b*), (7*a*), (7*b*), and (8)

are now reduced to a transient one-dimensional problem by expanding the flow field in terms of appropriately chosen orthonormal modes in the z direction, and applying the Galerkin projection method to generate the equations that govern the expansion coefficients. The procedure is closely related to that of Zienkiewicz and Heinrich in shallow-water theory [21], which includes the depth-averaging technique as a limit case. In particular, it is assumed that u can be represented by a contribution of polynomial shape functions $\phi_i(\xi)$, such that

$$u(x,z,t) = \beta + \sum_{i=1}^{M} U_i(x,t)\varphi_i(\xi) \tag{9}$$

where M is the number of modes, $U_i(x,t)$ are the unknown expansion coefficients, and $\xi = 1/\Delta[z-h]$ is the mapping coordinate from $z \in [h,\eta]$ to $\xi \in [0,\ 1]$, where $\Delta = \eta - h$. The functions ϕ_i are taken to satisfy the condition of orthonormality or

$$\langle \varphi_i \varphi_j \rangle = \delta_{ij}, \quad (\delta_{ij} = 0 \text{ if } i \neq j \text{ and } \delta_{ij} = 1 \text{ if } i = j) \tag{10}$$

where $\langle\ \rangle$ denotes the integral over $\xi \in [0,\ 1]$ and δ_{ij} is the Kronecker delta. In addition to the conditions of orthonormality, conditions (5) and (6) impose the following restrictions on the shape functions:

$$\varphi_i(\xi = 0) = 0, \quad \phi_i'(\xi = 1) = 0, \quad \forall\ i \in [1,M] \tag{11}$$

where a prime denotes differentiation with respect to ξ. The first five shape functions are given explicitly in the Appendix. Other shape functions have been used in the past, including trigonometric functions [12]. Polynomial functions are convenient to use for general boundary conditions, and seem to work very well. In any case, the choice of the shape functions is not that crucial given the not so significant variation of the flow across the thin film.

The vertical component of velocity is obtained by integrating Eq. (2) over the interval $[h,z]$, to give

$$w(x,z,t) = \sum_{i=1}^{M} \{[(\xi\phi_i - F_i)\Delta_x + h_x\phi_i]U_i - \Delta F_i U_{ix}\} \tag{12}$$

where $F_i(\xi) = \int_0^{\xi} \phi_i d\xi$. The evolution of the free surface is dictated by an equation that can be obtained by integrating the continuity Eq. (2) over the interval $z \in [h,\eta]$. Upon applying Leibnitz's rule and using expression (9), Eq. (4) becomes

$$\eta_t = -\Delta \sum_{i=1}^{M} \langle \varphi_i \rangle U_{ix} - \Delta_x \left(\beta + \sum_{i=1}^{M} \langle \varphi_i \rangle U_i \right) - h_x \beta \tag{13}$$

A hierarchy of equations is obtained for the coefficients $U_i(x,t)$, when expression (9) is substituted into the momentum Eq. (3), which is then multiplied by $\phi_i \geq 1$ and integrated over $\xi \in [0,\ 1]$. If w is eliminated by using Eq. (12), then one has

$$\sum_{j=1}^{M} [\Delta\langle\phi_i\phi_j\rangle(U_{jt} + U_{jx}\beta) - \{\langle\phi_i\phi_j'\rangle(h_t + h_x\beta) + \langle\phi_i\phi_j'\xi\rangle(\Delta_t + \Delta_x\beta)\}U_j] + \sum_{j=1}^{M}\sum_{k=1}^{M} [\Delta\langle\phi_i(\phi_j\phi_k - \phi_j'F_k)\rangle U_j U_{kx} - \Delta_x\langle\phi_i F_j \phi_k'\rangle U_j U_k] = \frac{1}{\Delta\ \mathrm{Re}} \sum_{j=1}^{M} \langle\phi_i\phi_j''\rangle U_j \tag{14}$$

Systems (13) and (14) are solved subject to conditions (7) and (8). Note that Eqs. (7*b*) and (8) give, respectively, $U_i(x=0,t) = \langle\phi_i u(x=0,\xi,t)\rangle - \beta\langle\phi_i\rangle$. $U_i(x,t=0) = \langle u_0(x,z)\rangle$. The solution of systems (13) and (14) is obtained by using an implicit finite-difference scheme in t, combined with a sixth-order Runge–Kutta integration in x.

3 Results and Numerical Assessment

The formulation and numerical implementation above are now applied to the transient flow emerging from a channel as schematically illustrated in Fig. 1. The domain of the fluid covers the range $x \in [0,\infty]$, but the domain of computation will be restricted to $x \in [0,10]$. The interplay between substrate translation and its topography is emphasized throughout the discussion. Numerical accuracy of the solution procedure is simultaneously assessed. Substrate topography has a significant effect on the evolution of the flow. Two substrate geometries will be considered to emphasize the interplay between substrate movement and its topography. Finally, the flow will be conveniently described in terms of the film height, $\eta(x,t)$, and the mean streamwise velocity, $U(x,t)$, namely,

$$U(x,t) = \beta + \sum_{i=1}^{M} \langle\phi_i\rangle U_i(x,t) \tag{15}$$

which is determined once the velocity coefficients are obtained.

3.1 Steady-Film Flow Over a Straight Moving Substrate. The steady-state solution represents the long-term behavior, after transient effects have died out, which is usually the behavior of practical interest in coating flow. For steady-state flow over a straight substrate, $h(x,t)=0$, and Eq. (13) is readily integrated to give a relation between the mean steady-state velocity $U_s(x) = U(x,t\to\infty)$, and steady free-surface height $\eta_s(x) = \eta(x,t\to\infty)$, namely,

$$\eta_s(x) = \frac{U_c}{U_s(x)} \tag{16}$$

where boundary conditions (7) are implied. Here $U_c = 1 + \beta/2$ is the mean velocity (or flow rate) at the channel exit, which is determined from Eq. (7*b*).

The steady-state flow is now assessed using four modes. It will be shown below that this level of truncation leads to acceptable accuracy. Although the effect of inertia on the flow for a *stationary* substrate has already been examined extensively by Khayat and Welke [2], some of the earlier results will be revisited here given the higher accuracy of the present formulation, which leads to a qualitatively different solution, especially near the channel exit. The $\beta=0$ results will also serve as reference. Figure 2 shows the steady-state film profiles at moderately high (Re=100) and low (Re=5) Reynolds number for different values of β. When $\beta=0$, the flow with dominant inertia exhibits a sharp depression or strong minimum in film height as it exits the channel, which is followed by an almost linear increase with distance downstream. The earlier calculation of Khayat and Welke [2] led to an essentially linear increase with distance everywhere. The current result may then be viewed as an improvement for small x. This behavior, which is typical of high-inertia flow, is similar to the one predicted by Watson's [22] similarity solution for radial and two-dimensional flow of a jet impinging on the disk. The reader is also referred to Fig. 5-2.1 in the book by Middleman [23], where a similar film height is shown for inviscid flow. This minimum in film height is located very closely to the channel exit in the absence of substrate movement. Some significant observations can be made in the presence of substrate movement ($\beta>0$). There is a widening of the depression, accompanied by a weakening of the minimum in surface height, as β increases. Simultaneously, the film height diminishes everywhere proportionately to β, while the mean flow gains strength with β. For any β, the film height is found to increase almost linearly downstream of the depression. At relatively large value of $\beta(\beta=2)$, the film height decreases as the flow emerges from the channel, but tends to level off at large x.

A different response is predicted for a flow at low Reynolds number, which is also typically illustrated in Fig. 2 for a flow at Re=5. In this case, the film height tends to expand strongly with

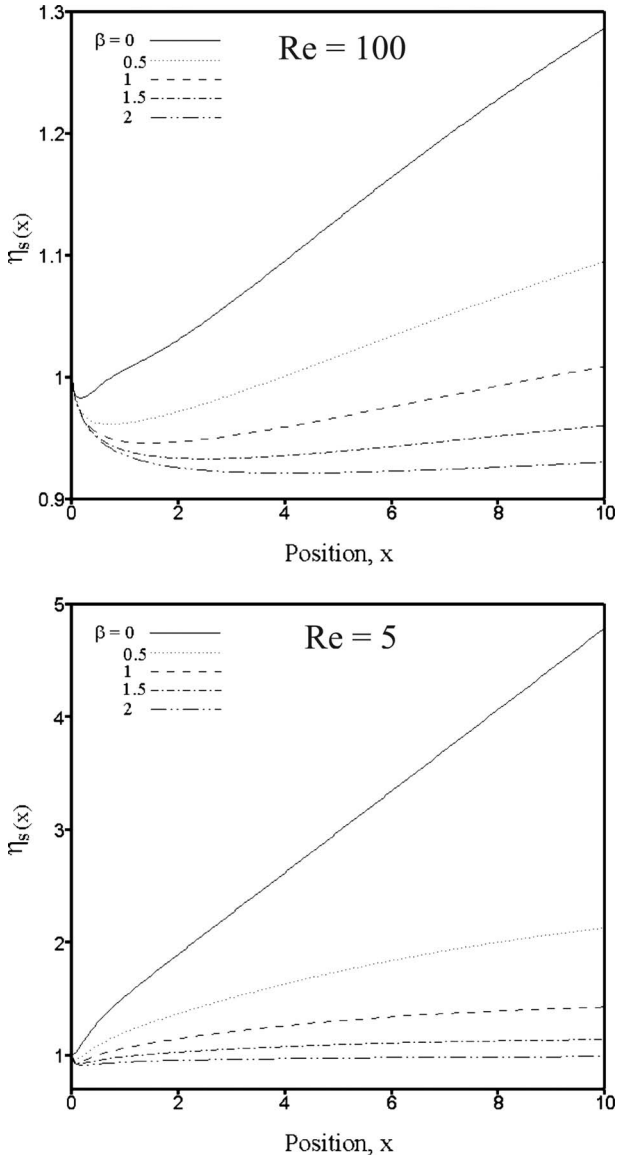

Fig. 2 Influence of substrate movement on steady-state film height for a fluid with moderately high inertia, Re=100, and low inertia, Re=5.

x, accompanied by a sharp fall in velocity. There is still, however, for $\beta>0$, a minimum in film height near the exit, but is located much closer to $x=0$. Note that the response is strictly monotonic with x when $\beta=0$. The strong expansion near the channel exit is typical of low-inertia thin-film flows [1]. The results for Re=5 clearly hint to potential difficulties that may be encountered in the coating of highly viscous fluids. They also indicate that substrate movement tends to attenuate the strength of the expansion, eventually leaving the film essentially flat when $\beta>2$. Far downstream, only the case $\beta=0$ exhibits an essentially linear growth with x. For $\beta>0$, the growth is much weaker with distance. In fact, the film height tends to level off at large x. The corresponding flow field shows a semiparabolic appearance compared with the parabolic response predicted at Re=100.

3.2 Assessment of Accuracy for Steady State and Limit Flows. It will be shown below that only a few modes ($M\leq 4$) are needed to secure convergence and accuracy of the numerical solution. However, an analytical solution is possible when only one mode is retained, which allows a preliminary exploration of the qualitative interplay between substrate movement and driving pressure. In order to simplify the (analytical) solution further, some limit flows will also be considered. For an arbitrary number of modes, the expansion coefficients for the velocity are obtained by solving Eq. (14), with the time derivative terms set equal to zero, as a set of ordinary differential equations in x. For a one-mode solution, $U_{i>1}(x,t)$ are set equal to zero, and the equation for $U_{1s}(x)\equiv U_1(x,t\to\infty)$ reads

$$(\beta+C_1U_{1s})U_{1sx}-(\beta C_5+C_2U_{1s})U_{1s}\frac{\eta_{sx}}{\eta_s}=C_4\frac{U_{1s}}{\eta_s^2\ \mathrm{Re}} \quad (17)$$

where $C_1=\langle\varphi_1(\varphi_1^2-\varphi_1'F_1)\rangle$, $C_2=\langle\varphi_1F_1\varphi_1'\rangle$, $C_3=\langle\varphi_1\rangle$, $C_4=\langle\phi_1\phi_1''\rangle$ and $C_5=\langle\varphi_1\varphi_1'\xi\rangle$. The equation that governs $U_s(x)$ is readily obtained upon integrating Eq. (17) and using Eq. (16), namely

$$\frac{1}{\beta}\ln\left[\frac{(U_s-\beta)U_c}{(U_c-\beta)U_s}\right]+C_A\left[\frac{1}{U_s}-\frac{1}{U_c}\right]+C_B\frac{\beta}{2}\left[\frac{1}{U_s^2}-\frac{1}{U_c^2}\right]=C_4\frac{x}{\mathrm{Re}\ U_c^2} \quad (18)$$

where $C_A=1-(C_1/C_3)-(C_2/C_3)$ and $C_B=(C_2/C_3)-C_5$. If $\beta=0$, the mean steady-state velocity and the corresponding film height are easily obtained.

$$U_s(x)=\frac{\mathrm{Re}}{\mathrm{Re}+cx},\quad \eta_s(x)=1+c\frac{x}{\mathrm{Re}} \quad (19)$$

where $c=2.22$. These expressions are comparable to those obtained by Watson [22] for two-dimensional flows using a similarity solution. In Watson's case, $c=\pi/\sqrt{3}=1.813$, which is smaller than the current value (based on one mode only). Note that the first mode steady-state solution leads to closer agreement with Watson's similarity solution than that based on the depth-averaging method. It is recalled that the depth-averaging formulation assumes a semiparabolic velocity profile in the transverse direction and gives $c=2.5$. The method can be regarded as corresponding to the leading-order formulation in ε. For further discussion on the physical significance of solution (19), the reader is referred to the paper by Khayat and Welke [2].

In general, Eq. (18) is a nonlinear algebraic equation, which can be solved numerically or symbolically. However, its form is algebraically complicated with little insight. Further insight is gained by considering the flow when the substrate velocity β is large ($\beta\gg 1$). In this case, one obtains the following asymptotic behavior for the solution of Eq. (18):

$$U_s=\frac{\beta}{2\left(\sqrt{\frac{2C_4x}{C_B\ \mathrm{Re}\ \beta}+4}-1\right)}+O\left(\frac{1}{\beta}\right) \quad (20a)$$

$$\eta_s=\sqrt{\frac{2C_4x}{C_B\ \mathrm{Re}\ \beta}+4}-1+O\left(\frac{1}{\beta}\right) \quad (20b)$$

Note that it is assumed that the product Re $\beta=O(1)$. Clearly, expressions (20) indicate that, at large β, the surface height (mean velocity) decreases (increases) monotonically with x. Also, in the absolute limit $\beta\to\infty$, the flow reaches plug-flow conditions ($\eta_s=1$, $U_s=\beta/2$). In this limit, and as expected, the motion is induced solely by the translation of the substrate, with the channel driving pressure having essentially no influence on the flow. It is, however, recalled that solutions (20) are based on the one-mode formulation, and may exhibit a significant discrepancy when higher-order modes are included.

The accuracy of the full formulation and numerical implementation can be further assessed against the similarity solution of Watson [22]. The (two-dimensional) similarity solution is assumed to be valid far from the channel exit. Comparison of the free-surface slopes based on the similarity and other (including

Table 1 Error assessment of various formulations against Watson's similarity solution

Formulation	$d\eta_s/dx$	Relative error (%)
Watson [22]	1.813	0
Depth averaging [24]	2.500	+38
Khayat and Welke [2]	1.950	+7
Current formulation $M=1$	2.220	+22
Current formulation $M=2$	1.770	−2
Current formulation $M=3$	1.826	+0.7
Current formulation $M=4$	1.809	−0.2

current) formulations is reported in Table 1. The calculated slopes are in fact the asymptotic values reached far downstream. Table 1 summarizes the influence of higher-order modes on the accuracy of the solution. When only the first mode is retained in the current formulation, the free-surface slope is overestimated by 22%, but the steady-state analytical solution can still give an overall qualitatively accurate prediction. The solution is under- or overestimated depending on the number of modes included, but the absolute value of the relative error decreases continuously with M. Convergence is essentially attained for $M \leq 4$.

Another useful criterion to assess the accuracy of the steady-state results is the conservation of mass. In this case, the values of the exact flow rate are compared with the one numerically calculated. Table 2 shows the relative error resulting from the lack of mass conservation, at different substrate velocities, β. It is clear from the table that the inclusion of only four modes is needed to reduce the error to less than 0.2%. It is also observed that the overall error depends weakly on β. Indeed, the error tends to decrease slightly as β increases. This is somewhat expected since the flow tends to align itself with the moving substrate as the velocity of substrate increases. In this case, shearing becomes less dominant, eventually resulting in plug-flow situation (as $\beta \to \infty$).

3.3 Transient Flow and Influence of Initial Conditions. The transient response is now considered in some detail. Although it is the long-term behavior that is of primary interest in coating operations, the transient behavior can be important because of its relevance to the beginning or the end of the coating process. More importantly, the examination of transient flow will help decipher some of the potential difficulties, encountered under processing conditions, which may prohibit the steady (long-term) process from being at all achieved. The transient response will of course depend on the initial conditions, which are expected to have a significant influence on the ensuing flow. In this case, the flow stability can depend on the type of conditions used. The sensitive dependence of the flow on initial conditions originates from the hyperbolic nature of the thin-film flow with non-negligible inertia. The flow response will be investigated for different initial conditions in order to establish the parameter range for shock formation.

Table 2 Error assessment based on conservation of mass

β	Exact flow rate	Mode	Calculated flow rate	Relative error (%)
0.0	1.0	1	0.875	−12.5
		2	1.023	+2.3
		3	0.993	−0.7
		4	1.002	+0.2
1.0	1.5	1	1.354	−9.7
		2	1.526	+1.7
		3	1.492	−0.5
		4	1.503	+0.2
2.0	2.0	1	1.833	−8.3
		2	2.030	+1.5
		3	1.990	−0.5
		4	2.003	+0.15

Consider the practical situation where the initial state of the fluid corresponds to an infinite fluid layer with a thickness that decreases with x. Thus, the thickness may, for instance, be taken to decrease from one at $x=0$, reaching 0.2 at $x=10$, and remaining 0.2 for $x>10$. The velocity is also assumed to decrease with x, but follows a parabolic dependence on z similar to the velocity distribution inside the channel, and reaches plug-flow conditions far downstream from the channel exit. The initial conditions may then be written as

$$\eta(x,t=0) = 1 - 0.8 \sin\frac{\pi x}{20}$$

$$u(x,\xi,t=0) = [-6\xi^2 - (\beta-6)\xi + \beta]\left(1 - \sin\frac{\pi x}{20}\right) + \beta \sin\frac{\pi x}{20} \tag{21}$$

Consider the flow with moderately high inertia, Re=100. The influence of substrate movement on transient flow is reflected in Fig. 3, where the film profiles are shown for different values of β. For $\beta=0$, the film experiences an increase in thickness with both x and t. The film surface exhibits a wave that propagates downstream and steepens with time. After some time, $t \approx 4$, the trailing edge of the wave ($x<3.5$) already attains the steady state. There is an accumulation of fluid in the depthwise direction, corresponding to a considerable steepening of the wave front, which eventually results in the emergence of a discontinuity or a shock wave. It is interesting to observe that the film height is practically unchanged for $x>10$.

For a moving substrate ($\beta>0$), Fig. 3 indicates that the growth rate of the wave is slower than for a stationary substrate ($\beta=0$), which eventually results in delaying the formation of shock. It is important to note that for relatively small substrate speed (see the case $\beta=1$) a shock indeed occurs but at a location further downstream ($x>10$). In contrast to the case $\beta=0$, the film surface tends to rise with time at $x=10$. It is evident that the trailing edge of the wave, which has advanced downstream, has already attained the steady state over more than half of the computational domain ($x \approx 7$ compared with $x \approx 3.5$ for $\beta=0$). Note that the steady state may be reached over the entire computational domain if the simulation is carried out for longer time (for $t>8$). Although the total simulation time is still 8 time units, the adherence to the steady state covers a longer distance than for $\beta=0$, and this behavior becomes even more evident as β increases further (refer to the case $\beta=2$). Hence, the flow tends to stabilize with increase in β regardless of the total simulation time.

Several distinct and significant changes in flow response occur when β is further increased. First, shock formation appears to be prohibited by substrate movement. This is simultaneously reflected in the relatively small deviation of film height from steady state, as well as in the lengthening (diffusion) of the wave tail, which embraces the steady state over the whole computational domain. Second, the steady-state film profile exhibits a significant departure from the linear growth predicted for small β, especially near the channel exit. There is a contraction that develops, which is typical of high Reynolds number flow. Third, the velocity loses its monotonic behavior with x as it exhibits a strong maximum near the channel exit, which is followed by a minimum and another maximum of approximately the same strength. Further downstream, however, the velocity tends to decrease essentially monotonically with x. Fourth, although the initial film height remains independent of β, the initial velocity distribution tends to become flat (independent of x) for large β. This flattening plays a

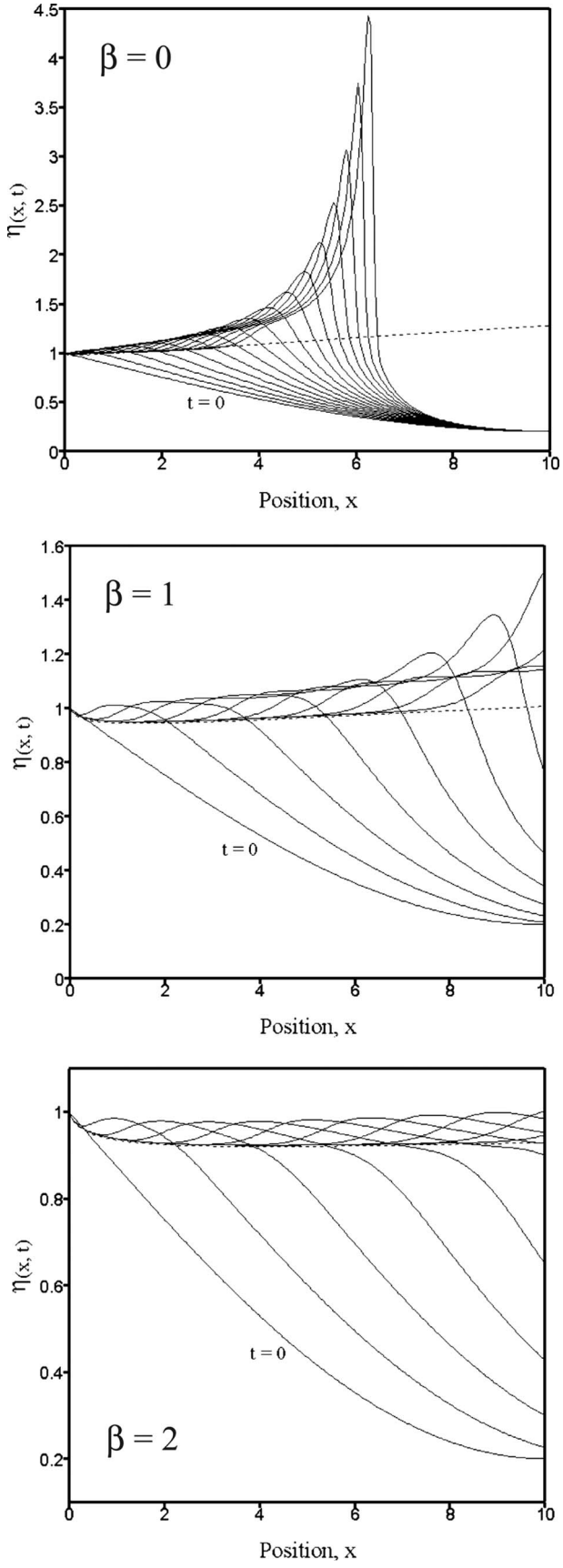

Fig. 3 Evolution of free surface at equal intervals of time, including the initial ($t=0$) and the steady state (dashed curve) profiles, at Re=100, for a flat substrate moving at different speeds

determining role in shock formation as will be seen below. Moreover, whether shock formation becomes completely prohibited once a critical β value is reached remains to be confirmed, and will be discussed next.

The observations above regarding the origin of wave growth and its decay, and the role of initial conditions are best understood for a system that is similar but is much simpler than the full M-mode system of equations. Since the wave growth depicted in Fig. 3 occurs for moderately high Reynolds number (Re=100), the discussion can and will be restricted to inviscid flow. In addition, only the solution based on the first mode will be examined, since the qualitative (and to a good extent the quantitative) response is captured by the first mode. The variation in the flow across the film, as well as the depthwise flow component, $w(x,z,t)$, in the momentum equation, will also turn out to be negligible (see below). In this case, the relevant equations are the continuity and the x-momentum equations, which reduce to

$$\eta_t + \eta U_x + U\eta_x = 0 \tag{22a}$$

$$U_t + (C_D U - C_C\beta)U_x = 0 \tag{22b}$$

where $C_C=\langle\varphi_1^3\rangle/\langle\varphi_1\rangle-1$ and $C_D=\langle\varphi_1^3\rangle/\langle\varphi_1\rangle$ are positive constants. Despite its simplicity, system (22) comprises the essence of nonlinear thin-film flow, and thus can explain the dependence of flow evolution on initial conditions and β. Note that Eqs. (22) must be solved subject to the following boundary conditions:

$$\eta(x=0,t)=1, \quad U(x=0,t)=\beta+\langle\phi_1\rangle(\langle u(x=0,\xi,t)\phi_1\rangle-\beta\langle\phi_1\rangle) \tag{23}$$

where $u(x=0,\xi,t)$ is given by Eq. (7b). It is not difficult to show that system (22) is indeed hyperbolic since it admits two real eigenvalues, corresponding to the two characteristic directions U and C_DU-$C_C\beta$. In this case, it is anticipated that the solution will be sensitive to the type of initial conditions used.

Consider first the case $\beta=0$. If U_x is negative at $t=0^+$ (with U and η being positive) such as for the sinusoidal conditions (21), system (22) indicates that both U and η grow initially. The growth rate is higher near the channel exit ($x=0$) owing to larger velocity gradient and free-surface slope. This explains why steady-state conditions are first reached upstream (of the wave). The continuous growth with time eventually results in a sharp discontinuity in both the velocity and the free surface as observed earlier. This is accentuated by the symmetry breaking ($x\rightarrow -x$) character of the convective terms. Unlike the free surface, the velocity cannot reach a maximum. In fact, Eq. (22b) indicates that, for $\beta=0$, the steady-state solution $U=1$ is the only maximum allowed. Equation (22a) indicates in turn that the maximum in the surface elevation grows at a rate $\sim-\eta U_x$, which reflects the direct relation between the steepness of the wave and elongational effect. When $\beta>0$ (with $U_x<0$ and $U>0$) U does grow, but at a slower rate according to Eq. (22a), and thus causes U to become discontinuous at a later time, at a location further downstream along the substrate. The free surface follows the same behavior, for it is coupled to the mean velocity through Eq. (22a). The delay in time and shift in location of the shock increase with β, as long as $\beta < C_DU/C_C$, at different rates that depend on the value of β. However, the shock is permanently obliterated at and after this value.

The arguments and observations above can be generalized by noting the close relation that exists between the nature of the initial conditions and the solution of hyperbolic systems. Indeed, system (22) is hyperbolic, and will now be analyzed using the method of characteristics. Since the velocity is decoupled from the surface height, discussion will be limited to the solution of Eq. (22b). The problem is here restated conveniently as

$$U_t + (C_D U - C_C\beta)U_x = 0 \tag{24}$$

subject to the following initial and boundary conditions:

$$U(x,t=0) \equiv U_0(x) = \beta + \langle \phi_1 \rangle (\langle u(x,\xi,t=0) \rangle - \beta \langle \phi_1 \rangle)$$

$$U(x=0,t) = \beta + \langle \varphi_1 \rangle (\langle u(x=0,\xi,t) \rangle - \beta \langle \varphi_1 \rangle) \tag{25}$$

over the interval $x \in [0,\infty)$. It is observed that Eq. (24) reduces to $dU/dt=0$ along the family of characteristics defined by $dx/dt = C_D U - C_C \beta$, forming a system of ordinary differential equations in U and x subject to initial conditions $U=U_0(\chi)$ and $x=\chi$, where χ is a parameter. Thus, $C_D U - C_C \beta$ is constant on $dx/dt = C_D U - C_C \beta$, and the characteristics are straight lines with speed $C_D U - C_C \beta$. It is well established that if U_0 is a nondecreasing function on the x interval, a smooth solution exists for all $t>0$, which is given by $U(x,t)=U_0(\chi)$ [25], where χ in this case is given implicitly by $\chi = x - [C_D U_0(\chi) - C_C \beta]t$. Therefore, for a singularity (which corresponds to the formation of a shock) to occur, U_0 must decrease in some open interval of x.

In order to demonstrate the occurrence of singularities, consider the case $U_0(x)>0$ and $U_0'(x)<0$ for $x \in [0,\infty)$. Therefore, the speeds of the characteristics satisfy $U_0(\chi_1) > U_0(\chi_2)$, where χ_1 and χ_2 are two points on the x-axis, with $\chi_1 < \chi_2$ from which the characteristics emanate. Thus, the characteristic emanating from χ_1 is faster than the one emanating from χ_2; the two characteristics eventually cross, thus giving rise to a double-valued solution. The situation is illustrated in Fig. 4, where the characteristics for different values of β are shown. For $\beta=0$, a smooth solution of problems (24) and (25) cannot exist for all $t>0$. Indeed, a time, called breaking time $t=t_b$, is reached when a gradient catastrophe occurs, at $x=x_b$, and the smooth solution breaks down giving rise to a shock, which manifests itself in the steepening of $U(x,t)$. In this case, $t_b=5.6$ and $x_b=6.3$. These values are in close agreement with the estimated breaking time 5.4 and location 6.4 based on the full solution in Fig. 3. For a moving substrate, the initial condition U_0 depends on β, the velocity of the substrate, and thus is not always decreasing with x (see Table 3). In order to determine t_b one first observes that, along the characteristic given by $\chi = x - [C_D U_0(\chi) - C_C \beta]t$, Eq. (24) admits the following implicit solution for U, namely, $U = U_0[x - (C_D U - C_C \beta)]t$. Consequently, the velocity gradient along the characteristic is given by $U_x = U_0'(\chi)/(1 + U_0'(\chi) C_D t)$. A gradient catastrophe occurs whenever the denominator vanishes. In general, once $U_0(\chi)$ is prescribed, the breaking time is given by $t_b = -1/U_0'(\chi_b) C_D$, with χ_b being the value of χ that corresponds to maximum $|U_0'(\chi)|$. It is important to observe that t_b is positive only if $U_0(\chi)$ is decreasing. Table 3 shows the breaking time t_b and the location of the singularity (blowup) point x_b at different values of β for an initial condition $U_0(x)$ corresponding to Eq. (21). It is important to note that as β increases the singularity occurs at a later time and further downstream. As is evident from the table, the absolute value of the slope $U_0'(\chi)$ decreases with β; this means that the difference between the speeds of the characteristics emanating from two arbitrary points χ_1 and χ_2 on the x-axis (with $\chi_1 < \chi_2$) decreases and thus these two straight lines cross after a longer time and distance.

Thus, a smooth solution exists for a long time. This explains why shock is delayed with increase in substrate velocity. The characteristics for $\beta=1$ in Fig. 4 are typical for all values of $\beta < 1.68$. As shown in the table at $\beta=1.68$ the breaking time and the location of the blowup are infinite, which means that the shock has been abated everywhere. This can be explained based on the fact that $U_0(\chi)$ is now nondecreasing. Since $U_0'(\chi)=0$ for $\beta = 1.68$, all the characteristics move at the same speed and never cross. Therefore, the solution is smooth for all $t>0$, for $\beta \geq 1.68$ as is confirmed in Fig. 4, by the characteristics for $\beta=2$. In this case, an expansion wave occurs as reflected by the fanning of the characteristics.

The observations based on the analysis above are now used to examine the flow with no possibility of shock formation. Thus, consider the problem with uniform initial conditions, which cor-

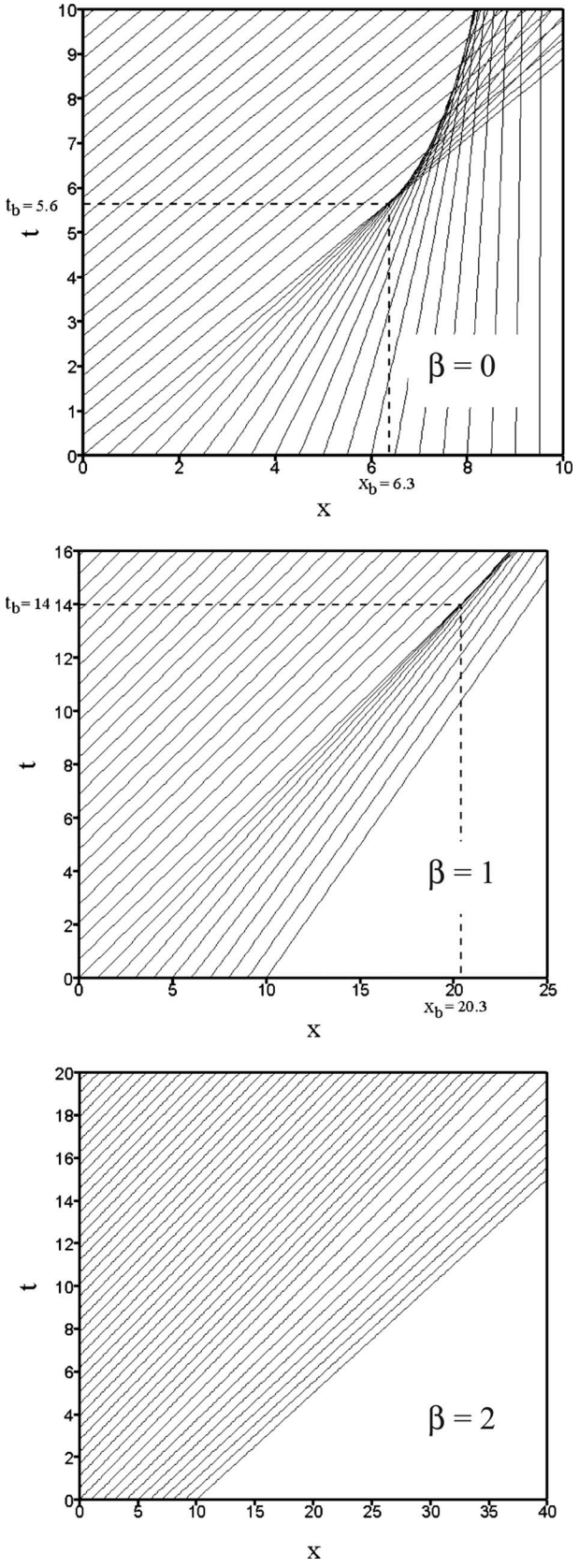

Fig. 4 Characteristic diagrams showing the characteristic curves $\xi = x - [C_D U_0(\xi) - C_C \beta]t$, for decreasing initial conditions (23) at different substrate speeds. The characteristics are parameterized by their intersection ξ with the x-axis ($x>0$)

Table 3 Time and location of the shock for sinusoidal initial conditions

β	$U_0'(\chi)$	$U_0'(\chi_b)$	t_b	x_b
0.0	<0	−0.134	5.6	6.3
0.5	<0	−0.096	8.1	10.4
1.0	<0	−0.055	14.0	20.3
1.68	=0	0.0	∞	∞
2.0	>0	0.03	−30.0	−53.0

respond to a fluid initially with the same conditions everywhere as at the channel exit. In other words, $\eta(x,t=0)=1$ and $U(x,t=0)=1+\beta/2$. The resulting flow is shown in Fig. 5 for $\beta=0$, 1, and 2, and Re=100. It is clear from the figure that there is no shock that forms with time for any substrate speed. Although the film height increases with t and x, there is no singularity experienced by the free surface. Indeed, the slope of the free surface remains essentially unchanged with time, after the initial stages. This is particularly evident from the evolution of the velocity profiles. The characteristics in this case, corresponding to problems (24) and (25) are straight parallel lines. Clearly t_b and x_b are infinite.

3.4 Flow Over a Moving Undulated Substrate. Consider the transient flow over an undulated (sinusoidal) substrate. The substrate geometry is defined as

$$h(x,t) = A \sin\left[\frac{2\pi\omega}{10}(x-\beta t)\right] \tag{26}$$

where A is the amplitude of modulation and ω is the wave number. It is important to note that for this substrate topography there is no steady state because of the presence of continuous disturbance induced by the movement of the modulated substrate. Nevertheless, the steady-state solution will be considered for $\beta=0$. Initial conditions (21) are used. The accuracy of the transient will also be assessed.

Consider the flow at a relatively high Reynolds number Re=100. The evolution of free-surface component is shown in Fig. 6 over a period of 4 time units, for $\beta=0$, 1, and 2. The results are shown for the sinusoidal substrate with high amplitude of modulation $A=0.5$ and wave number $\omega=1$. The figure for $\beta=0$ shows free-surface profiles at equal intervals of 0.4 time units, including the initial conditions and the substrate topography (thick curve at the bottom). There is a tendency of the fluid to propagate downstream, but more importantly, it tends to move upward, leading to the formation of a primary solitary wave, which is similar to that corresponding to a flat substrate. The presence of modulation, however, causes the formation of a secondary wave of growing amplitude with time, and traveling ahead of the primary wave, at a constant velocity. The two waves appear to propagate at almost the same speed, similarly to wave trains encountered in gravity driven flow [1]. There is also a tertiary wave of smaller amplitude that emerges, but in contrast to the primary and the secondary waves, it remains stationary; only its height changes with time. There is a significant qualitative difference between the primary and the secondary waves. The secondary wave is narrower, and exceeds the steady-state level. The primary wave increases in amplitude with time, exhibiting a parabolic shape that reflects the shape of the substrate crest, and eventually embraces the steady-state profile. It is evident that the steady-state film height exhibits a shape that is essentially similar to and in phase with the substrate topography. This behavior is reminiscent of the flow over mounds and trenches that are relatively large compared with the film thickness [4].

For relatively small β, a primary wave still forms, but its growth rate is slower than for a stationary substrate ($\beta=0$). In contrast to the case of stationary substrate, the primary wave moves downstream with time, with smaller amplitude. The secondary wave also exhibits a decrease in its growth rate, and moves downstream with time. It is important to note that there is still a sharp discontinuity (shocklike structure) in the film height, but it occurs with smaller amplitude at a distance further downstream,

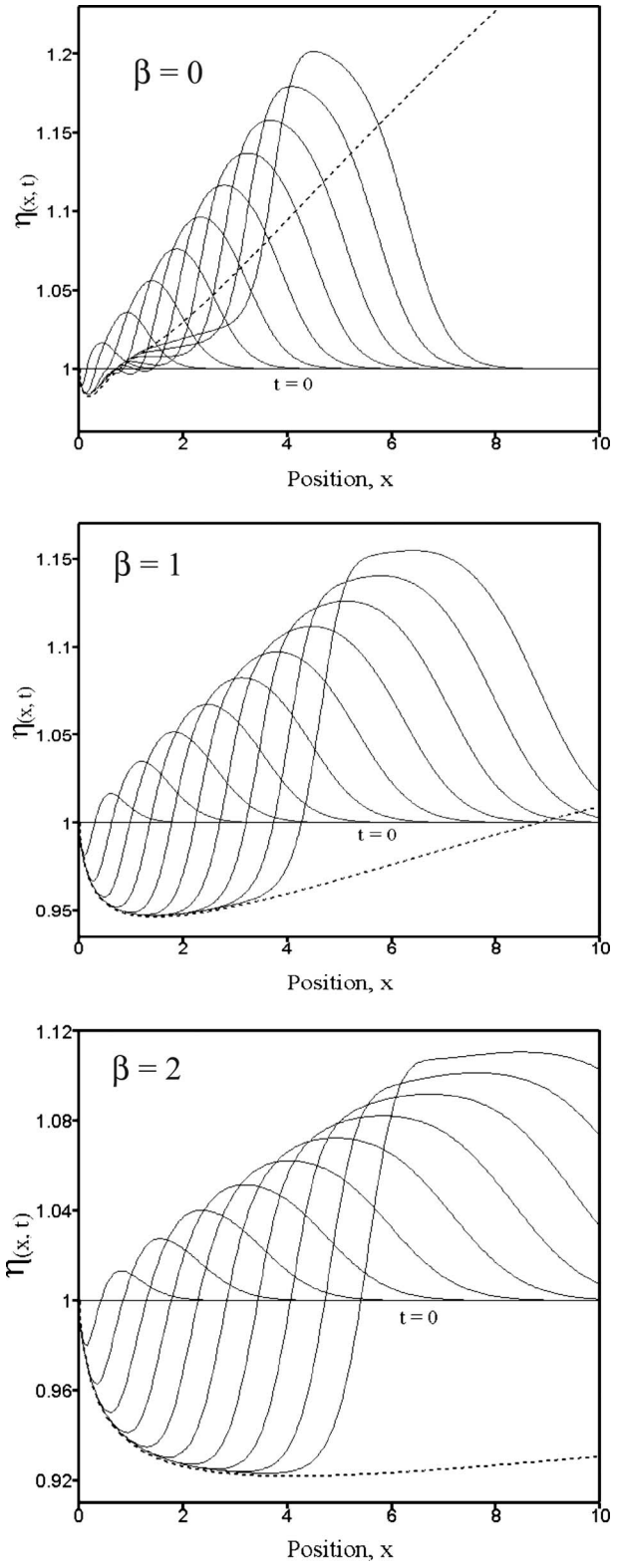

Fig. 5 Evolution of free surface at equal intervals of time, including the initial ($t=0$) and the steady state (dashed curve) profiles, for a stationary and a moving substrate. Flat initial conditions are used and Re=100.

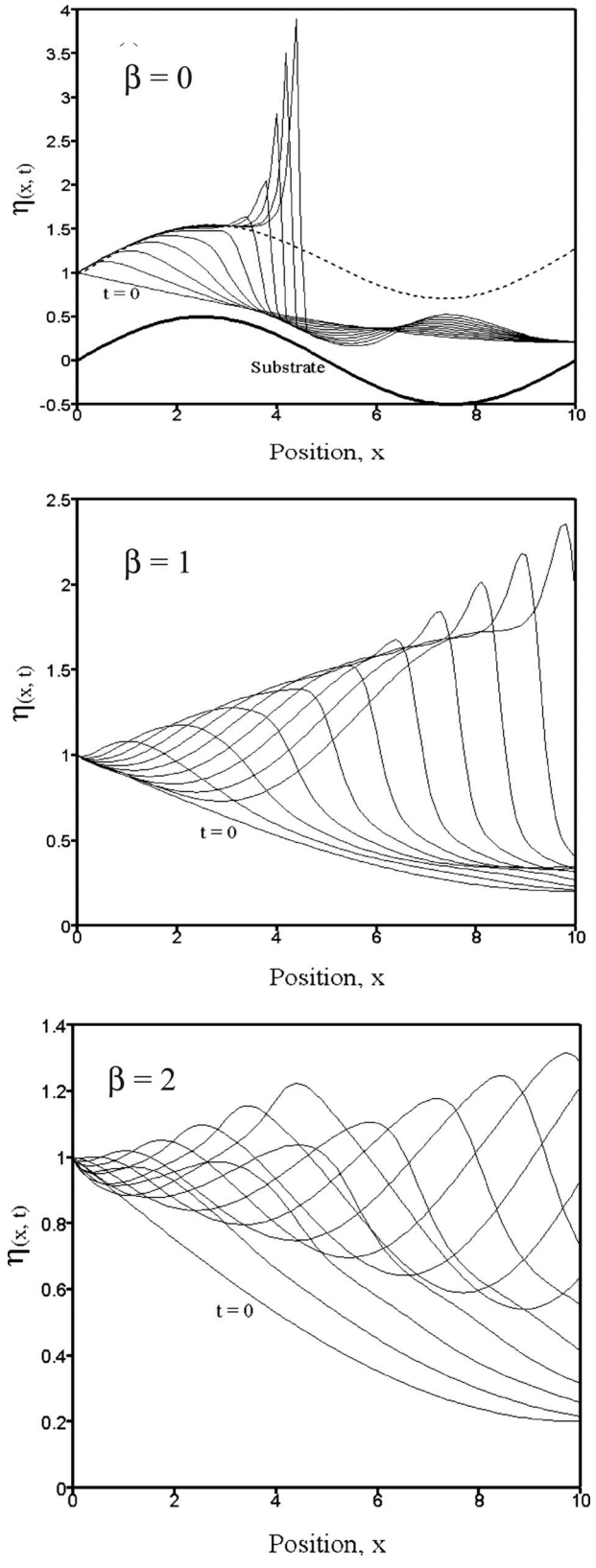

Fig. 6 Evolution of free surface at moderately high inertia (Re=100) at equal intervals of 0.4 time units over a period of 5.2 time units, including initial (t=0) profiles, for mildly undulated substrate at different speed (β=0,1,2). Here A=0.1 and ω=1. Also shown are the steady state (dashed) and substrate topography (thick solid) lines for the case β=0.

$x \approx 8$ for $\beta=1$ compare with $x \approx 4$ for $\beta=0$, and at a later time. The tertiary wave, however, is not stationary like the case $\beta=0$, but moves downstream with time. It is evident that the film height at $x>10$ is not constant as in the case of stationary substrate, but varies with time. It is evident that the demarcation between the primary and the secondary waves becomes less prominent when $\beta>0$. The secondary wave advances further downstream with a noticeable decrease in the amplitude; the amplitude has, in fact, decreased by 29% between $\beta=0.5$ (not shown) and $\beta=1$. The wave moves at a constant speed. Thus, the effect of substrate movement is to shift the shock spatiotemporally. This effect is much more pronounced if value of β is further increased.

The flow evolution for $\beta=2$ exhibits even further departure. The primary and secondary waves appear to have coalesced. In the early stages, the free-surface height experiences a minimum as the flow exits the channel and then following a maximum, decreases monotonically. With time, however, it exhibits alternate minima and maxima. It is evident that there is no steepening of the waves. In fact the waves translate downstream, thereby confirming the absence of any shocklike structure (gradient catastrophe). The flow details in the case of moderately high substrate speed ($\beta=2$) are further appreciated from Fig. 7, which shows the flow field and contours of velocity magnitude at different time units over a period of 6 time units. The initial flow field and the substrate geometry are also shown.

In order to assess the overall influence of substrate topography in the case of a continuous substrate, the flow over a substrate with smaller amplitude but higher wave number is examined, with $A=0.2$ and $\omega=2$. Figure 8 shows the flow evolution for Re=100. It is interesting to observe that the wave amplitude has actually decreased only for a moving substrate as a result of decrease in modulation amplitude of the substrate. For a stationary substrate, the secondary wave is of significant strength. The tertiary wave, however, is indeed there, but with almost negligible amplitude. The steady-state film profile embraces closely that of the substrate, showing a free-surface elevation essentially commensurate with that of the substrate.

For a moving substrate at moderate speed ($\beta=1$), Fig. 8 shows that the primary wave becomes more significant than in the case of $\beta=0$. There is a noticeable reduction in the amplitude of the wave, and the front advancement of the wave is also faster than in case of high-amplitude substrate (compare with Fig. 6), but the leading edge of the secondary wave is not as steep. The demarcation between the primary and the secondary waves is also less pronounced. Also there is no sharp discontinuity (shocklike structure). For $\beta=2$, the free surface behaves in more or less the same way as in the case of high-amplitude substrate, except that the amplitudes of the wave train are smaller.

3.5 Numerical Assessment for Transient Flow. The assessment of numerical accuracy and convergence has so far been carried out for steady flow. In this case, the accuracy of the transient formulation is addressed for high-inertia flow over a substrate with high amplitude of modulation, thus under significant nonlinear effects. The calculations were repeated for various values of the time increment, Δt, and the number of modes, M. The influence of Δt is examined by monitoring the maximum height, $\eta_{\max}(t)$, for $0.1 \geq t \geq 0.025$ ($M=4$). Generally, it has not been difficult to avoid numerical instability by varying the time increment and monitoring its effect on the evolution of the flow. In fact, convergence is essentially achieved for $\Delta t \leq 0.04$. This is also confirmed through additional calculations carried out for different inertia levels and substrate velocity. The influence of the number of modes is an important issue . The number of modes M was varied ranging from $M=1$ to $M=4$, at different values of β. Figure 9 shows variation in free-surface height with time at a fixed location $x=5$, for different levels of truncation. For a stationary substrate ($\beta=0$), there is some difference between the free-surface height based on the $M=1$ and that based on $M=2$, which grows

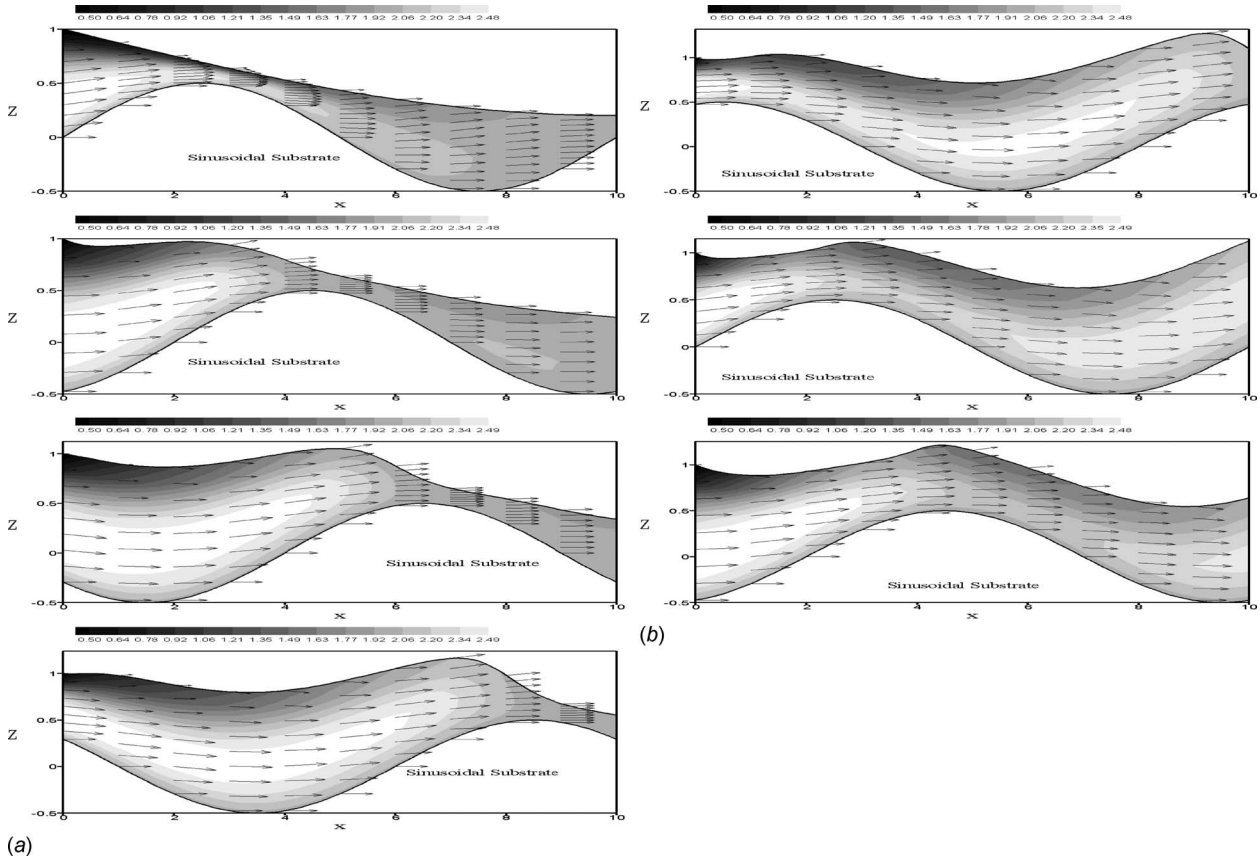

Fig. 7 Flow field and contours of velocity magnitude at different times for a sinusoidal substrate with $A=0.5$ and $\omega=1$. The velocity of the substrate is $\beta=2$.

with time and becomes constant after some time $t\approx 1$. Nevertheless, there is not much difference between the free surface based on $M=2$ and those based on $M=3$ and 4. This agreement occurs over the whole time period, which means that convergence is essentially achieved for $M>3$. For a moving substrate ($\beta=2$), the figure shows variation in free-surface height over a period of 3 time units, at different levels of truncation. It is evident that all the modes are essentially coincident over a period of $t\approx 2$ time units. Thereafter, the free surface based on $M=1$ exhibits a significant deviation from the other solutions. The free surface does not change noticeably in transition from $M=3$ to $M=4$. Thus, convergence is achieved at $M>3$. In summary, all the results presented in this study are based on $M=4$, and $\Delta t=0.04$. Additional calculations show that this level of truncation ($M=4$) appears to be independent of substrate geometry.

3.6 Flow Over a Flat Substrate With a Bump. It is appropriate to analyze a substrate with a different geometry, given the fact that the flow response is strongly affected by substrate topography. The analysis so far has focused on a continuous substrate topography. A discontinuous variation in substrate geometry is taken here to correspond to a flat substrate with a bump near the channel exit. The bump serves as a moving obstacle in the flow, and is thus interesting to analyze. The substrate topography is given by

$$h(x,t)=\begin{cases} A\sin\left[\dfrac{\pi}{4}(x-\beta t)\right], & \beta t\le x<\beta t+\pi \\ 0, & x\ge \beta t+\pi \end{cases} \tag{27}$$

A represents the maximum height of the bump. The presence of a discontinuity in the substrate topography violates in principle one of the basic assumptions for thin-film flow, namely, that related to small curvature. However, in their study on thin film over variable topography, Kalliadasis et al. [4] examined the flow over square ridges and bumps. The presence of sharp corners does not seem to lead to significant inaccuracies. The absence of inertia in their study allowed Kalliadasis et al. to confirm this conclusion by comparing their thin-film formulation with the boundary element method.

The bump is near the channel exit initially, but moves downstream with time. Again, the initial conditions corresponding to Eq. (21) will be used in this case. It is important to note that, in this case, and in contrast to the case of undulated substrate, the steady state exists for all values of β. An interesting question arises as to whether the steady state in the case of a moving bump is stable. The evolution of the flow is shown in Fig. 10 for moderately high inertia, $\mathrm{Re}=100$ and for a substrate with $A=0.5$. For a stationary substrate ($\beta=0$), the primary wave increases in amplitude with time, exhibiting a parabolic shape that reflects the shape of the bump, and eventually embracing the steady state. Because of the presence of the bump, the flow exhibits a secondary and a tertiary wave, the amplitude of the latter being smaller than the former (as in the case of the continuous sinusoidal substrate). However, in this case, the depression between the primary and the secondary waves is quite significant, and that between the secondary and the tertiary waves is even more significant than in the case of the sinusoidal substrate. It is once again important to notice the steepness in the secondary wave, which eventually results in a sharp discontinuity.

The influence of substrate movement is depicted also in Fig. 10 for $\beta=1$ and 2. The steady state in these cases corresponds to that of a film over a straight substrate, long after the bump has moved downstream. The steady state thus prevails after the bump has

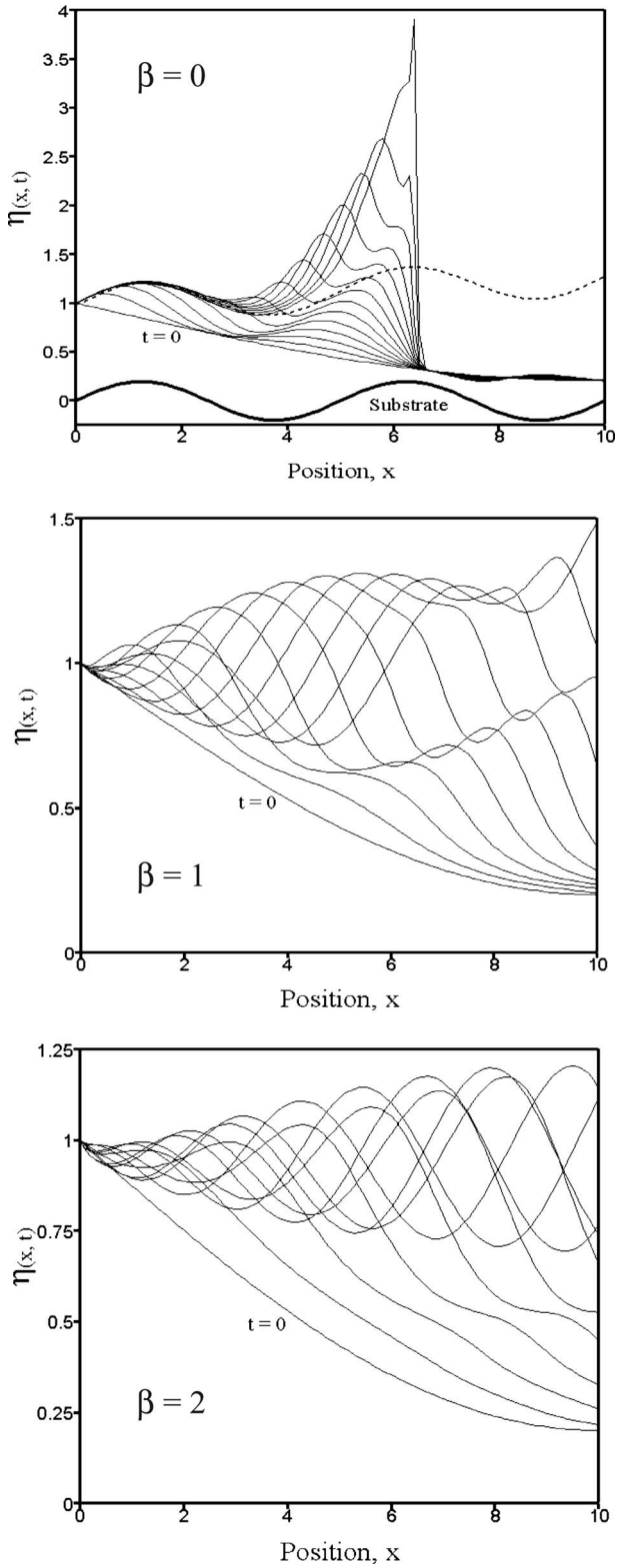

Fig. 8 Evolution of free surface at moderately high inertia (Re=100) at equal intervals of 0.4 time units over a period of 5.2 time units, including initial (t=0) profiles, for mildly undulated substrate at different speeds (β=0,1,2). Here A=0.2 and ω=2. Also shown are the steady state (dashed) and substrate topography (thick solid) lines for the case β=0.

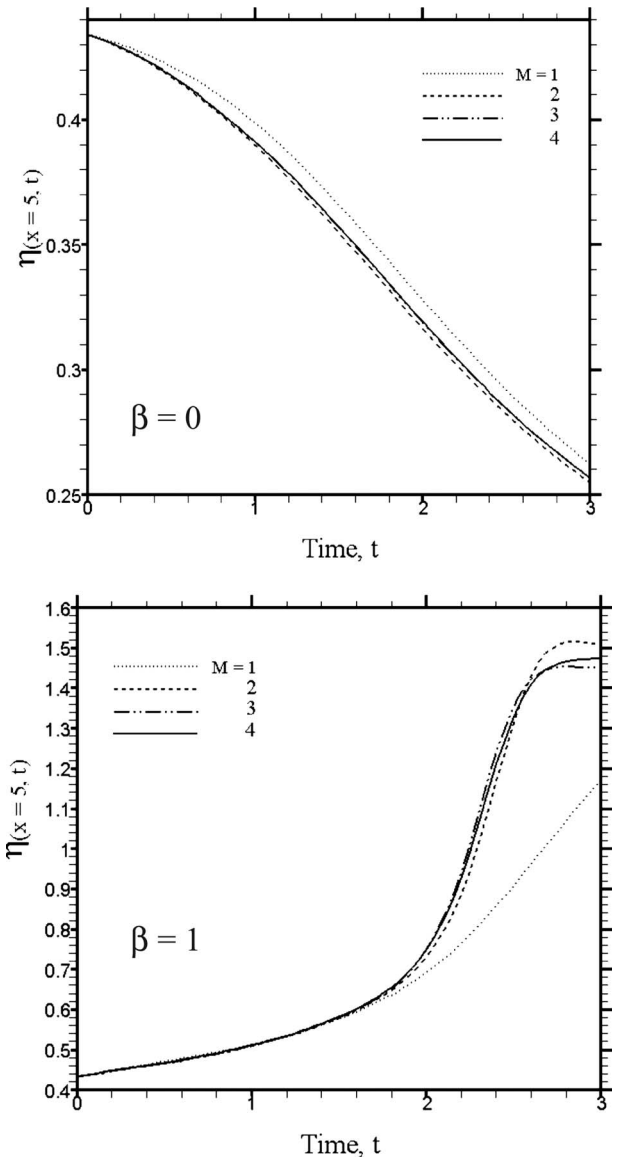

Fig. 9 Influence of higher-order modes at β=0 and β=1, for high-inertial flow, Re=100, in the absence of gravity, and for a sinusoidal substrate with A=0.5 and ω=1. The figure shows variation in free-surface profiles (at fixed location, x=5) when different numbers of modes are retained.

moved completely out of the computational domain. Figure 10 shows that for β=1, the primary wave moves downstream while being in phase with the bump. It is evident that the growth rate of the secondary wave, which also moves downstream, is slower than in the case of stationary substrate, eventually resulting in delaying the formation of shock. The trailing edge of the primary wave already attains steady state over more than half of the computational domain ($x \approx 6$, compared with $x \approx 4$ in case of β=0). Thus the effect of substrate movement is to stabilize the flow. The flow exhibits remarkably different response if the value of β is further increased. For β=2, there is no distinction between the primary and secondary waves among the several waves that are present. Also, shock formation appears to be prohibited by substrate movement. This is simultaneously reflected in the relatively small deviation of the film height from the steady state, as well as in the diffusion of the wave tail, which embraces the steady state over most of the computational domain.

Finally, the flow details for the case of β=2 are further appre-

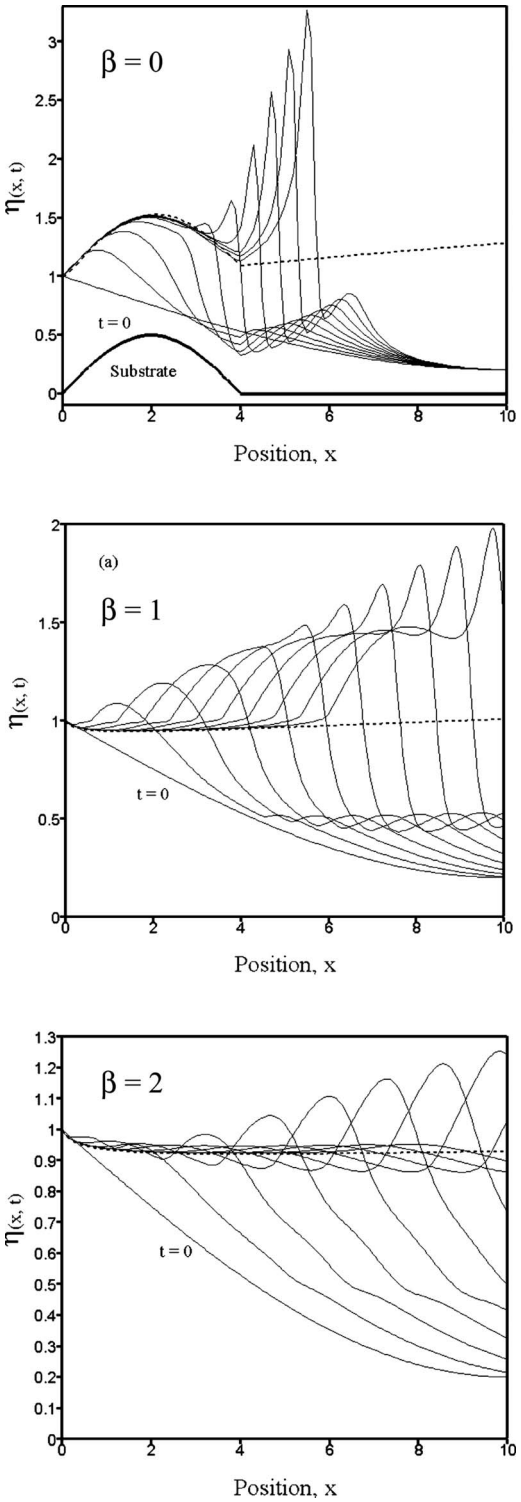

Fig. 10 Evolution of free surface at moderately high inertia (Re=100) at equal intervals of 0.6 time units over a period of 5.4 time units, including initial (t=0) profiles, for a substrate with a bump at different speeds (β=0,1,2). Here A=0.5. Also shown are the steady state (dashed) and substrate topography (thick solid) lines for the case β=0.

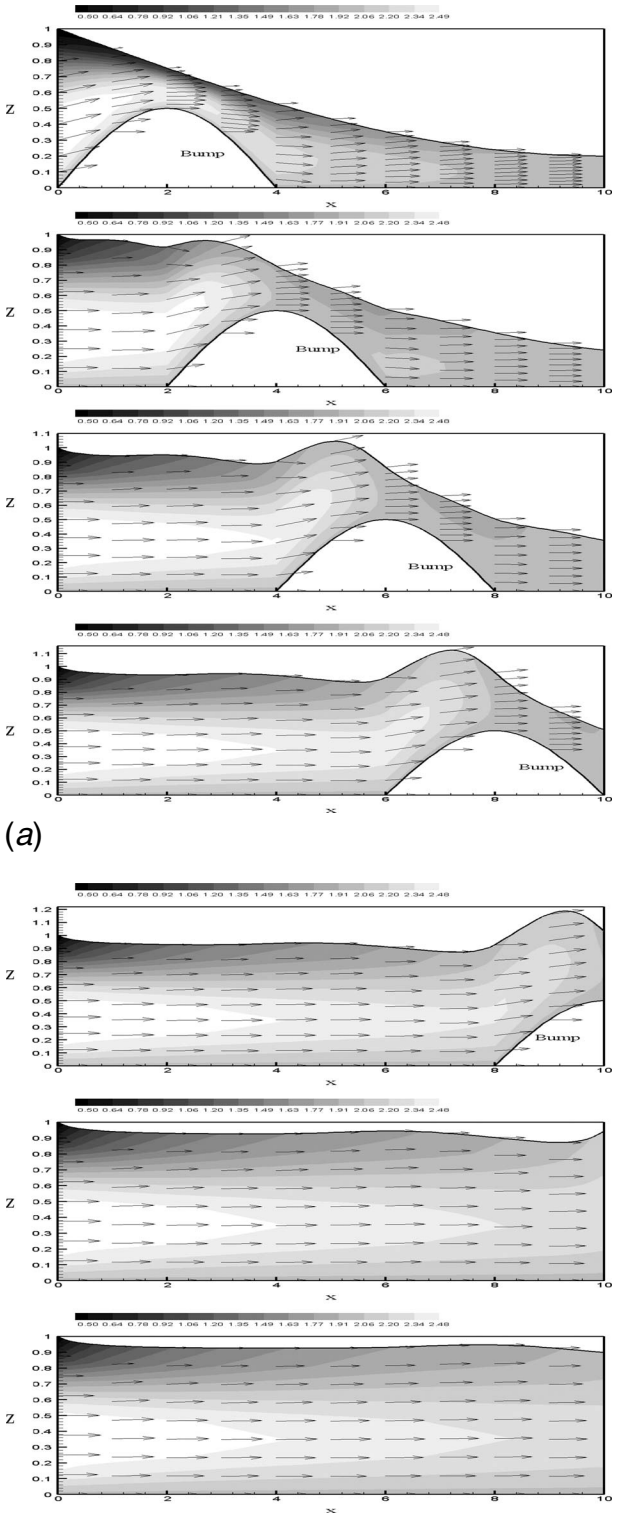

Fig. 11 Flow field and contours of velocity magnitude at different times for a substrate with a bump with A=0.5. The velocity of the substrate is β=2.

ciated from Fig. 11, which shows the flow field and contours of velocity magnitude at different time units over a period of 6 time units. The initial flow field and the substrate geometry are also shown.

4 Conclusion

The effect of substrate topography and its movement on the transient two-dimensional pressure-driven Newtonian coating flow, with inertia, is examined in this study. The fluid emerges from a channel, wherein Couette–Poiseuille conditions are assumed to prevail, and flows over a moving substrate of arbitrary

topography. The boundary-layer equations for thin-film flow are solved by expanding the flow field in orthonormal modes over the depth. The Galerkin projection method is applied to generate the equations governing the expansion coefficients. A time-marching implicit finite-difference discretization, together with a spatial Runge–Kutta integration scheme, is implemented to obtain the spatiotemporal behavior of the free-surface shape and the flow field.

Substrate topography is found to have a significant effect on the flow response. It is found that the movement of a continuous sinusoidal substrate gives rise to the formation of a secondary wave, following the primary wave that propagates downstream, with continuous steepening and after some time results in a sharp discontinuity (gradient catastrophe). A standing or tertiary wave following the secondary wave also forms. The effect of substrate movement is to delay and eventually to remove the discontinuity induced by the secondary wave. Another substrate geometry examined in this study, is a flat substrate with a bump over its surface. In this case there exists a stable steady state. The primary wave moves with the substrate in phase with the bump.

Appendix: Shape Functions

In this appendix, the first five shape functions are listed, namely,

$$\Phi_1(\xi) = -1.369306393\xi^2 + 2.738612788\xi$$

$$\Phi_2(\xi) = 14.37947255\xi^3 - 27.41086955\xi^2 + 11.68332144\xi$$

$$\Phi_3(\xi) = -80.71414203\xi^4 + 183.7798927\xi^3 - 126.9252058\xi^2 + 25.36730180\xi$$

$$\Phi_4(\xi) = 389.9538429\xi^5 - 1057.971363\xi^4 + 994.0868796\xi^3 - 372.4133056\xi^2 + 44.68221123\xi$$

$$\Phi_5(\xi) = -1763.606622\xi^6 + 5597.733212\xi^5 - 6635.908240\xi^4 + 3599.673097\xi^3 - 866.3257670\xi^2 + 70.23887810\xi$$

Note that these functions satisfy conditions (11).

References

[1] Cheng, H. C., and Demekhin, E. A., 2002, *Complex Wave Dynamics on Thin Films*, Elsevier, New York.

[2] Khayat, R. E., and Welke, S., 2001, "Influence of Inertia, Gravity and Substrate Topography on the Two-Dimensional Transient Coating Flow of a Thin Newtonian Fluid Film," Phys. Fluids, **13**(2), pp. 355–367.

[3] Ruschak, K. J., and Weinstein, S. J., 1999, "Viscous Thin-Film Flow Over a Rounded Crested Weir," ASME J. Fluids Eng., **121**, pp. 673–677.

[4] Kalliadasis, S., Bielarz, C., and Homsy, G. M., 2000, "Steady Free-Surface Thin Film Flows Over Topography," Phys. Fluids, **12**(8), pp. 1889–1898.

[5] Stillwagon, L. E., and Larson, R. G., 1988, "Fundamentals of Topographic Substrate Leveling," J. Appl. Phys., **63**(11), pp. 5251–5258.

[6] Stillwagon, L. E., and Larson, R. G., 1990, "Leveling of Thin Films Over Uneven Substrates During Spin Coating," Phys. Fluids A, **2**(11), pp. 1937–1944.

[7] Spaid, M. A., and Homsy, G. M., 1994, "Viscoelastic Free Surface Flows: Spin Coating and Dynamic Contact Lines," J. Non-Newtonian Fluid Mech., **55**, pp. 249–281.

[8] Johnson, M. W., and Mangkoesoebroto, S., 1993, "Analysis of Lubrication Theory for the Power-Law Fluid," Trans. ASME, J. Tribol., **115**(1), pp. 71–77.

[9] Tichy, J. A., 1996, "Non-Newtonian Lubrication With the Convected Maxwell Model," Trans. ASME, J. Tribol., **118**, pp. 344–348.

[10] Ross, A. B., Wilson, S. K., and Duffy, B. R., 1999, "Blade Coating of a Power-Law Fluid," Phys. Fluids, **11**(5), pp. 958–970.

[11] Khayat, R. E., and Kim, K., 2002, "Influence of Initial Conditions on Transient Two-Dimensional Thin Film Flow," Phys. Fluids, **14**(12), pp. 4448–4451.

[12] Khayat, R. E., 2000, "Transient Two-Dimensional Coating Flow of a Viscoelastic Fluid Film on a Substrate of Arbitrary Shape," J. Non-Newtonian Fluid Mech., **95**, pp. 199–233.

[13] Kim, K., and Khayat, R. E., 2002, "Transient Coating Flow of a Thin Non-Newtonian Fluid Film," Phys. Fluids, **14**(7), pp. 2202–2215.

[14] Meyers, T. G., 1998, "Thin Films With High Surface Tension," SIAM Rev., **40**(3), pp. 441–462.

[15] Kriegsmann, J. J., Miksis, M. J., and Vanden-Broeck, J. M., 1998, "Pressure-Driven Disturbances on a Thin Viscous Film," Phys. Fluids, **10**(6), pp. 1249–1255.

[16] Hamrock, B. J., 1994, *Fundamentals of Fluid Flow Lubrication*, McGraw-Hill, New York.

[17] Lee, J., and Mei, C. C., 1996, "Stationary Waves on an Inclined Sheet of Viscous Fluid at High Reynolds and Moderate Weber Numbers," J. Fluid Mech., **307**, pp. 191–229.

[18] Omodei, B. J., 1979, "Computer Solutions of a Plane Newtonian Jet With Surface Tension," Comput. Fluids, **7**, pp. 79–96.

[19] Goren, S. L., and Wronski, S., 1966, "The Shape of Low-Speed Capillary Jets of Newtonian Liquids," J. Fluid Mech., **25**, pp. 185–198.

[20] Tillett, J. P. K., 1968, "On the Laminar Flow in a Free Jet of Liquid at High Reynolds Numbers," J. Fluid Mech., **32**, pp. 273–292.

[21] Zienkiewicz, O. C., and Heinrich, J. C., 1979, "A Unified Treatment of Steady-State Shallow Water and Two-Dimensional Navier-Stokes Equations—Finite Element Penalty Function Approach," Comput. Methods Appl. Mech. Eng., **17-18**, pp. 673–698.

[22] Watson, E. J., 1964, "The Radial Spreading of a Radial Jet Over a Horizontal Plane," J. Fluid Mech., **20**, pp. 481–499.

[23] Middleman, S., 1995, *Modeling Axisymmetric Flows, Dynamics of Films, Jets, and Drops*, Academic, San Diego, CA.

[24] Chang, H. C., 1994, "Wave Evolution on a Falling Film," Annu. Rev. Fluid Mech., **26**, pp. 103–136.

[25] Logan, J. D., 1994, *An Introduction to Nonlinear Partial Differential Equations*, Wiley Interscience, New York.

Weakly Nonlinear Stability Analysis of a Thin Liquid Film With Condensation Effects During Spin Coating

C. K. Chen[1]
e-mail: ckchen@mail.ncku.edu.tw

M. C. Lin

Department of Mechanical Engineering,
National Cheng Kung University,
No. 1 Ta-Hsueh Road,
Tainan, Taiwan 701, R.O.C.

This paper investigates the stability of a thin liquid film with condensation effects during spin coating. A generalized nonlinear kinematic model is derived by the long-wave perturbation method to represent the physical system. The weakly nonlinear dynamics of a film flow are studied by the multiple scales method. The Ginzburg–Landau equation is determined to discuss the necessary conditions of the various states of the critical flow states, namely, subcritical stability, subcritical instability, supercritical stability, and supercritical explosion. The study reveals that decreasing the rotation number and the radius of the rotating circular disk generally stabilizes the flow.
[DOI: 10.1115/1.3222907]

Keywords: spin coating, stability analysis, rotation number

1 Introduction

Spin coating is a process for coating the surface of a spinning substrate, wherein a liquid coating material is dispensed radially from the center to the edge or from the edge to the center of the substrate, after which the coating material is cured. The spin coating process is one of the fundamental fabrication methods found in integrated circuit (IC) chip manufacturing processes such as wafer manufacturing, photolithography and sputtering deposition. For example, photolithography [1] is a patterning process that transfers a designed pattern from a mask to a photoresist on a wafer surface. The photolithography process can be subdivided into three main operations: photoresist coating, alignment and exposure, and photoresist developing. In fact, photoresist coating is the most important process in photolithography since macroscopic instability can cause detrimental conditions to occur in film flows, with very harmful consequences to the quality of the final product. Therefore it is highly desirable to develop suitable working techniques for homogeneous film growth, techniques that are able to adapt to various flow configurations and associated time-dependent properties. For these reasons, the ability to control and maintain uniform and stable thin films is an important research topic with regard to spin coating [2,3].

Linear stability theories for various film flows have been presented by Chandrasekhar and Lin using the long-wave perturbation method to study condensate flow linear instability problems. Benney [4] studied the nonlinear evolution equation for film flow free surfaces using the small parameter method. The solutions thus obtained can be used to predict nonlinear instability conditions. However, the solutions cannot be used to predict supercritical stability since the influence of surface tension is neglected in the modeling process of the small parameter method. The effect of surface tension was studied by Lin [5], Nakaya [6], and Krishna and Lin [7], who considered that it was one of the necessary conditions, treating it as zeroth order terms. Atherton and Homsy [8] discussed the derivation of complicated nonlinear partial equations, evolution equations that describe the movement of a fluid-fluid interface. Ünsal and Thomas [9] investigated the nonlinear stability of vertical condensate film flow by using perturbation methods. Marschall and Lee [10] accounted the disturbances in the temperature field and predicted the existence of a critical Reynolds number below which the condensate film flow is stable. They concluded that condensation will stabilize the film flow and evaporation will destabilize the flow.

Extensive studies on the hydrodynamic stability problems regarding rotating-disk flow have already been investigated by several researchers. Emslie et al. [11] were the pioneers who analyzed a Newtonian liquid flowing on rotating disk. The flow is governed by a balance between the centrifugal force and the viscous resisting force. It was shown that the nonuniform distribution in the initial film profile tends to become uniform during spinning. This model has been widely employed in the subsequent investigations. Higgins [12] analyzed the flow of a Newtonian liquid placed on an impulsively started rotating disk. In this work, a uniform film thickness is assumed and the method of matched asymptotic expansions is adopted. It is showed that for films that maintain a planar interface there exists a self-similar form for the velocity field that allows the radial dependence to be factored out of the Navier–Stokes equations and boundary conditions. Kitamura et al. [13] solved the unsteady thin liquid film flow of nonuniform thickness on a rotating disk by asymptotic methods.

In the present study, the authors present a weakly nonlinear stability analysis of a thin liquid film with condensation effects during spin coating. The authors consider condensation effects because a significant amount of vapor condenses due to cooling during spin coating, making the presented results more compatible with practical situations. The influence of the rotational motion and the disk size on the equilibrium finite amplitude is studied and characterized mathematically. In an attempt to verify the computational results and to illustrate the effectiveness of the proposed modeling approach, several numerical examples are presented.

2 Mathematical Formulation

Figure 1 shows the appropriate physical configuration for axisymmetric flow of a liquid film with condensation effects flowing on a rotating circular disk which rotates with constant velocity Ω^*. A variable with a superscript "$*$" represents a dimensional quantity. Here the cylindrical polar coordinate axes r^*, θ^*, z^* are chosen as the radial direction, the circumferential direction, and the axial

[1]Corresponding author.

Contributed by the Fluids Engineering Division of ASME for publication in the JOURNAL OF FLUIDS ENGINEERING. Manuscript received August 7, 2008; final manuscript received August 3, 2009; published online September 24, 2009. Assoc. Editor: Joseph Katz.

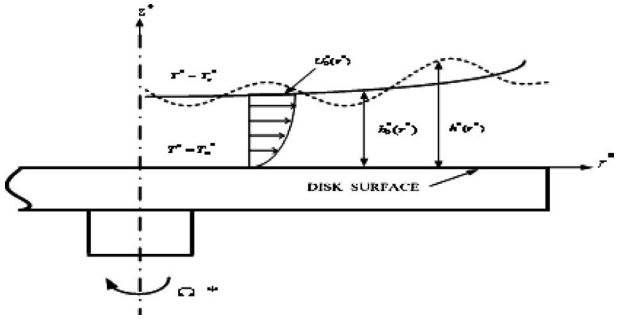

Fig. 1 Schematic diagram of a thin condensate film flowing on a rotating disk

direction, respectively. All associated physical properties and the rate of film flow are assumed to be constant (i.e., time-invariant). Let u^* and w^* be the velocity components in the radial direction r^* and the perpendicular direction z^* of the disk, respectively. The governing equations of continuity, motion, and energy can be expressed as

$$\frac{1}{r^*}\frac{\partial(r^*u^*)}{\partial r^*}+\frac{\partial w^*}{\partial z^*}=0 \tag{1}$$

$$\frac{\partial u^*}{\partial t^*}+u^*\frac{\partial u^*}{\partial r^*}+w^*\frac{\partial u^*}{\partial z^*}-\frac{v^{*2}}{r^*}=-\frac{1}{\rho}\frac{\partial p^*}{\partial z^*}\frac{\mu}{\rho}\left(\frac{1}{r^*}\frac{\partial}{\partial r^*}\left(r^*\frac{\partial u^*}{\partial r^*}\right)-\frac{u^*}{r^{*2}}+\frac{\partial^2 u^*}{\partial z^{*2}}\right) \tag{2}$$

$$\frac{\partial w^*}{\partial t^*}+u^*\frac{\partial w^*}{\partial r^*}+w^*\frac{\partial w^*}{\partial z^*}=-\frac{1}{\rho}\frac{\partial p^*}{\partial z^*}-g+\frac{\mu}{\rho}\left(\frac{1}{r^*}\frac{\partial}{\partial r^*}\left(r^*\frac{\partial w^*}{\partial r^*}\right)+\frac{\partial^2 w^*}{\partial z^{*2}}\right) \tag{3}$$

$$\frac{\partial T^*}{\partial t^*}+u^*\frac{\partial T^*}{\partial r^*}+w^*\frac{\partial T^*}{\partial z^*}=\frac{K}{\rho C_p}\left(\frac{1}{r^*}\frac{\partial}{\partial r^*}\left(r^*\frac{\partial T^*}{\partial r^*}\right)+\frac{\partial^2 T^*}{\partial z^{*2}}\right) \tag{4}$$

where v^* is tangential velocity, ρ is constant fluid density, p^* is fluid pressure, g is acceleration due to gravity, μ is fluid dynamic viscosity, T^* is fluid temperature, C_p is fluid specific heat and K is fluid thermal conductivity.

On the disk surface $z^*=0$. The boundary conditions are treated as nonslip as follows:

$$u^*=0 \tag{5}$$

$$w^*=0 \tag{6}$$

$$T^*=T_w^* \tag{7}$$

The boundary conditions for the free surface at $z^*=h^*$ are derived based on the results given by Edwards et al. [14]. The boundary condition approximated by the vanishing of shear stress is expressed as

$$\left(\frac{\partial u^*}{\partial z^*}+\frac{\partial w^*}{\partial r^*}\right)\left(1-\left(\frac{\partial h^*}{\partial r^*}\right)^2\right)-2\left(\frac{\partial u^*}{\partial r^*}-\frac{\partial w^*}{\partial z^*}\right)\left(\frac{\partial h^*}{\partial r^*}\right)=0 \tag{8}$$

The normal stress condition obtained by solving the balance equation in the direction normal to the free surface is given as

$$p^*+\frac{k^2(\beta-1)}{h_{fg}^2\rho\beta}\left(\frac{\partial T^*}{\partial z^*}-\frac{\partial h^*}{\partial r^*}\frac{\partial T^*}{\partial r^*}\right)^2\left[1+\left(\frac{\partial h^*}{\partial r^*}\right)^2\right]^{-1}-2\rho\nu\left[\frac{\partial u^*}{\partial r^*}-\left(\frac{\partial w^*}{\partial r^*}+\frac{\partial u^*}{\partial z^*}\right)\frac{\partial h^*}{\partial r^*}+\frac{\partial w^*}{\partial z^*}\left(\frac{\partial h^*}{\partial r^*}\right)^2\right]\times\left[1+\left(\frac{\partial h^*}{\partial r^*}\right)^2\right]^{-1}+S^*\left\{\frac{\partial^2 h^*}{\partial r^{*2}}\left[1+\left(\frac{\partial h^*}{\partial r^*}\right)^2\right]^{-3/2}\right\}=p_g^* \tag{9}$$

$$T^*=T_s^* \tag{10}$$

The kinematic condition that ensures the flow does not travel across a free surface can be given as

$$K\left(\frac{\partial T^*}{\partial z^*}-\frac{\partial T^*}{\partial r^*}\frac{\partial h^*}{\partial r^*}\right)-\rho h_{fg}\left(\frac{\partial h^*}{\partial t^*}+u^*\frac{\partial h^*}{\partial r^*}-w^*\right)=0 \tag{11}$$

where T_s^* is vapor saturation temperature, T_w^* is wall temperature, P_g^* is vapor pressure, h^* is the local film thickness, h_{fg} is the latent heat of phase change, and S^* is surface tension. By introducing a stream function φ^*, the dimensional velocity components can be expressed as

$$u^*=\frac{1}{r^*}\frac{\partial\varphi^*}{\partial z^*},\quad w^*=-\frac{1}{r^*}\frac{\partial\varphi^*}{\partial r^*} \tag{12}$$

The following variables are used to form the dimensionless governing equations and boundary conditions

$$z=\frac{z^*}{h_0^*}\quad r=\frac{\alpha r^*}{h_0^*}\quad t=\frac{\alpha t^* u_0^*}{h_0^*}\quad h=\frac{h^*}{h_0^*}\quad \varphi=\frac{\alpha\phi^*}{u_0^* h_0^{*2}}\quad \mathrm{Re}=\frac{u_0^* h_0^*}{\nu}$$

$$p=\frac{p^*-p_g^*}{\rho u_0^{*2}}\quad \mathrm{Pr}=\frac{\rho\nu C_p}{K}\quad \mathrm{Pe}=\mathrm{Pr}\,\mathrm{Re},\quad \mathrm{Nd}=\frac{(1-\beta)\xi^2}{\beta\,\mathrm{Pr}^2},$$

$$\mathrm{Fr}=\frac{gh_0^*}{u_0^{*2}},\quad S=\frac{S^*}{\rho u_0^{*2}h_0^*},\quad \alpha=\frac{2\pi h_0^*}{\lambda},\quad \theta=\frac{T^*-T_w^*}{T_s^*-T_w^*} \tag{13}$$

where h_0^* is the average film thickness, α is the dimensionless wave number, u_0^* is the scale of velocity, ν is the kinematic viscosity, Re is the Reynolds number, Pr is the Prandtl number, Fr is the Froude number, Pe is the Peclet number, ξ is the Jakob number, β is density ratio, θ is dimensionless temperature, and λ is the wavelength.

For simplification it is assumed that the liquid film is very thin ($h^*\ll r^*$). In consequence, it is reasonable to assume that the tangential velocity is constant throughout the radial direction in the thin film, i.e., $v^*=r^*\Omega^*$. In order to investigate the effect of angular velocity, Ω^*, on the stability of the flow field, the dimensionless parameter Ro (rotation number) is defined as

$$\mathrm{Ro}=\frac{\Omega^* h_0^*}{u_0^*} \tag{14}$$

In terms of these nondimensional variables, the equations of motion and energy can be expressed as

$$r^{-1}\varphi_{zzz}=-\mathrm{Re}\ \ r\mathrm{Ro}^2+\ \alpha\ \mathrm{Re}(p_r+r^{-1}\varphi_{tz}+r^{-2}\varphi_z\varphi_{rz}-r^{-3}\varphi_z^2-r^{-2}\varphi_r\varphi_{zz})]+O(\alpha^2) \tag{15}$$

$$p_z=-\mathrm{Fr}+\alpha(-\mathrm{Re}^{-1}\ \ r^{-1}\varphi_{rzz})+O(\alpha^2) \tag{16}$$

$$\theta_{zz}=\alpha\ \ \mathrm{Pe}(r^{-1}\varphi_z\theta_r-r^{-1}\varphi_r\theta_z+\theta_t)+O(\alpha^2) \tag{17}$$

Using nondimensional variables, the boundary conditions at the surface of disk $z=0$ reduce to

$$\varphi=\varphi_r=\varphi_z=0 \tag{18}$$

and the boundary conditions at the free surface of disk $z=h$ become

$$r^{-1}\varphi_{zz} = \alpha^2[r^{-1}\varphi_{rr} - r^{-2}\varphi_r + 2h_r(1-\alpha^2 h_r^2)^{-1}(2r^{-1}\varphi_{rz} - r^{-2}\varphi_z)] \tag{19}$$

$$p = -S\alpha^2 h_{rr}(1+\alpha^2 h_r^2)^{-3/2} + \alpha[-2\ \mathrm{Re}^{-1}(1+\alpha^2 h_r^2)^{-1}(r^{-1}\varphi_{rz} + r^{-1}\varphi_{zz}h_r)] - \mathrm{Nd}\cdot\mathrm{Re}^{-2}\ \theta_z^2 + O(\alpha^2) \tag{20}$$

$$\xi(\theta_z - \alpha^2 h_r\theta_r) - \alpha\ \mathrm{Pe}(h_t + r^{-1}h_r\varphi_z + r^{-1}\varphi_r) = 0 \tag{21}$$

Hence the term $\alpha^2 S$ can be treated as a quantity of zeroth order [15]. Since the long-wavelength modes that give the smallest wave number are most likely to induce flow instability for the film flow, the above equations can be computed by expanding the stream function, flow pressure, and temperature in terms of some small wave number ($\alpha \ll 1$) as

$$\varphi = \varphi_0 + \alpha\varphi_1 + o(\alpha^2) \tag{22}$$

$$p = p_0 + \alpha p_1 + o(\alpha^2) \tag{23}$$

$$\theta = \theta_0 + \alpha\theta_1 + o(\alpha^2) \tag{24}$$

The flow conditions of the thin film can be obtained by inserting the above expressions into Eqs. (15)–(20) and then solving systematically the resulting equations. By collecting all terms of zeroth order α^0 and first order α^1 in the above governing equations and boundary conditions, the solutions of the zeroth order and first order equations were obtained and are given in the Appendix.

The zeroth and first order solutions are inserted into the dimensionless free surface kinematic equation to yield the following generalized nonlinear kinematic equation

$$h_t + X(h) + A(h)h_r + B(h)h_{rr} + C(h)h_{rrr} + D(h)h_{rrrr} + E(h)h_r^2 + F(h)h_r h_{rrr} = 0 \tag{25}$$

where

$$X(h) = -\frac{\xi}{h\cdot\mathrm{Pe}\cdot\alpha} + \frac{h^3\cdot\mathrm{Re}\cdot\mathrm{Ro}^2(8\mathrm{Pe} - 5\ \mathrm{Re}\cdot\xi)}{12\mathrm{Pe}} \tag{26}$$

$$A(h) = -\frac{2\mathrm{Nd}\cdot\alpha}{3r\cdot\mathrm{Re}} - \frac{\mathrm{Fr}\cdot h^3\cdot\mathrm{Re}\cdot\alpha}{3r} + \frac{h^2\cdot r\cdot\mathrm{Re}\cdot\mathrm{Ro}^2(8\mathrm{Pe} - 5\ \mathrm{Re}\cdot\xi)}{8\mathrm{Pe}} \tag{27}$$

$$B(h) = -\frac{2\mathrm{Nd}\cdot\alpha}{3\ \mathrm{Re}} - \frac{1}{3}\mathrm{Fr}\cdot h^3\cdot\mathrm{Re}\cdot\alpha + \frac{2}{15}h^6\cdot r^2\cdot\mathrm{Re}^3\cdot\mathrm{Ro}^4\cdot\alpha \tag{28}$$

$$C(h) = \frac{h^3\cdot\mathrm{Re}\cdot S\cdot\alpha^3}{3r} \tag{29}$$

$$D(h) = \frac{h^3\cdot\mathrm{Re}\cdot S\cdot\alpha^3}{3} \tag{30}$$

$$E(h) = -\mathrm{Re}\cdot\mathrm{Fr}\cdot h^2\cdot\alpha + \frac{4}{5}h^5\cdot r^2\cdot\mathrm{Re}^3\cdot\mathrm{Ro}^4\cdot\alpha \tag{31}$$

$$F(h) = \mathrm{Re}\cdot S\cdot h^2\cdot\alpha^3 \tag{32}$$

3 Stability Analysis

The dimensionless film thickness when expressed in perturbed state can be given as

$$h(r,t) = 1 + \eta(r,t) \tag{33}$$

where η is a perturbed quantity of the stationary film thickness. Substituting the value of $h(r,t)$ into the evolution Eq. (25) and all terms up to the order of η^3 are collected, the evolution equation of η becomes

$$\eta_t + X'\eta + A\eta_r + B\eta_{rr} + C\eta_{rrr} + D\eta_{rrrr} + E\eta_r^2 + F\eta_r\eta_{rrr} = -\left[\frac{X''}{2}\eta^2 + \frac{X'''}{6}\eta^3 + \left(A'\eta + \frac{A''}{2}\eta^2\right)\eta_r + \left(B'\eta + \frac{B''}{2}\eta^2\right)\eta_{rr} + \left(C'\eta + \frac{C''}{2}\eta^2\right)\eta_{rrr} + \left(D'\eta + \frac{D''}{2}\eta^2\right)\eta_{rrrr} + (E + E'\eta)\eta_r^2 + (F + F'\eta)\eta_r\eta_{rrr}\right] + O(\eta^4) \tag{34}$$

where the values of X, A, B, C, D, E, F and their derivatives are all evaluated at the dimensionless height of the film $h=1$.

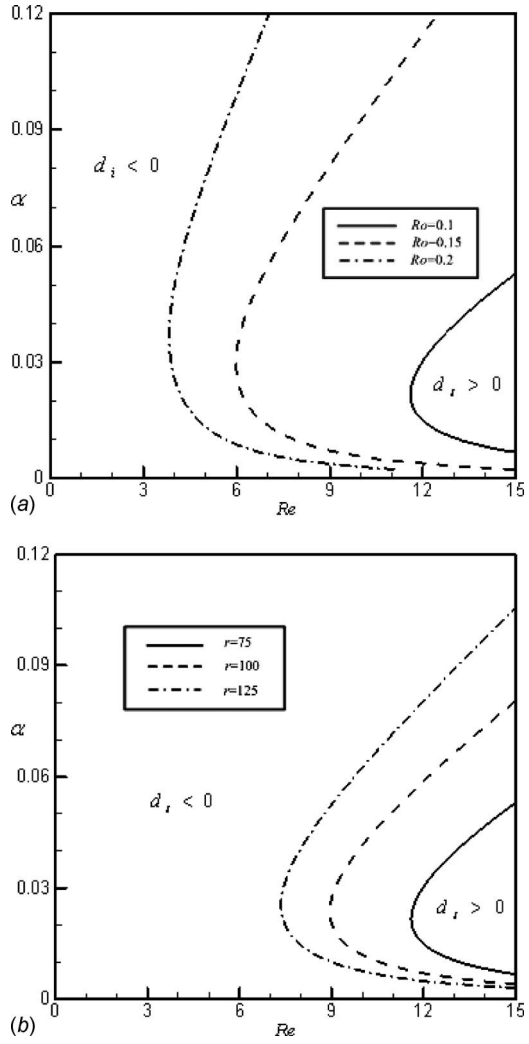

Fig. 2 (*a*) **Linear neutral stability curves for three different Ro values at *r*=75 and (*b*) linear neutral stability curves for three different *r* values at Ro=0.1**

3.1 Linear Stability Analysis. When the nonlinear terms of Eq. (34) are neglected, the linearized equation is given as

$$\eta_t + X'\eta + A\eta_r + B\eta_{rr} + C\eta_{rrr} + D\eta_{rrrr} = 0 \tag{35}$$

In order to use normal mode analysis we assume that

$$\eta = a\ \exp[i(r - dt)] + \mathrm{cc} \tag{36}$$

where a is the perturbation amplitude and cc is the complex conjugate counterpart. The complex wave celerity, d, is given as

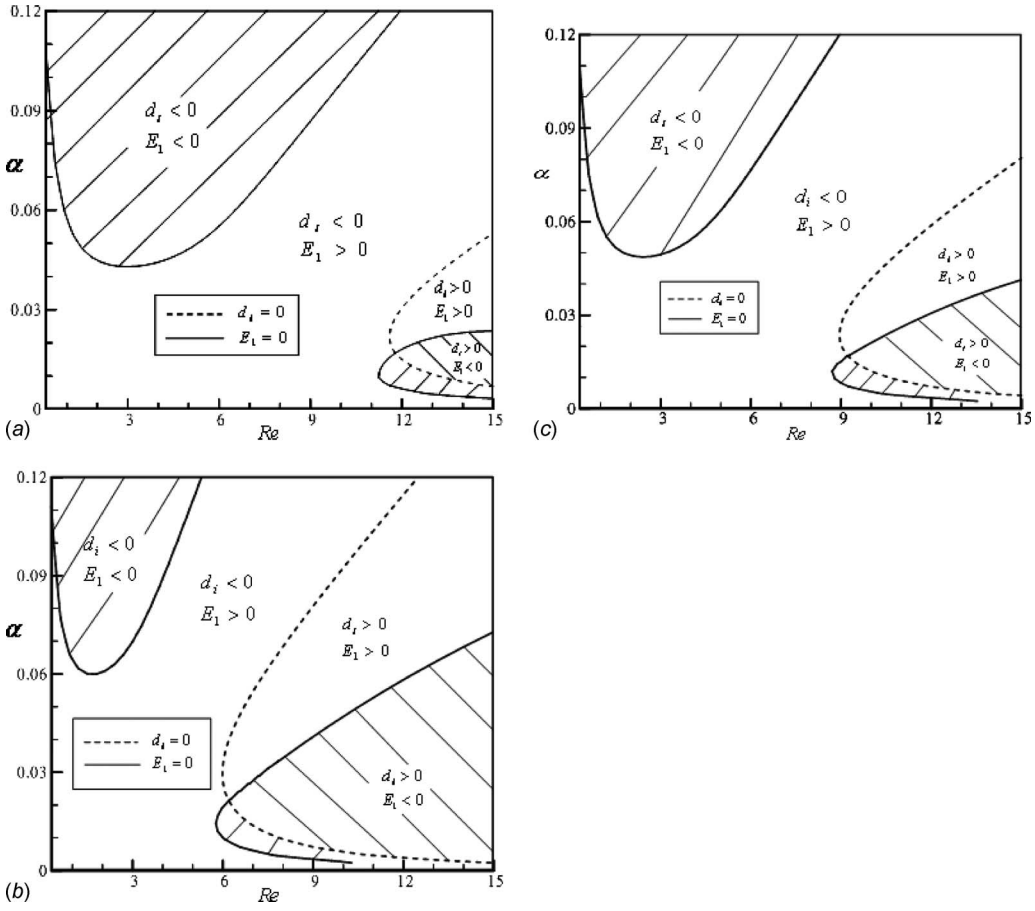

Fig. 3 (*a*) **Neutral stability curves of condensate film flows for Ro=0.1 and *r*=75,** (*b*) **neutral stability curves of condensate film flows for Ro=0.15 and *r*=75, and** (*c*) **neutral stability curves of condensate film flows for Ro=0.1 and *r*=100**

$$d = d_r + id_i = (A - C) + i(B - D - X') \tag{37}$$

where d_r and d_i are regarded as the linear wave speed and linear growth rate of the disturbance, respectively. The solution of the disturbance about $h(r,t)=1$ is asymptotically stable or unstable according as $d_i<0$ or $d_i>0$.

3.2 Weakly Nonlinear Stability Analysis. Nonlinear effects, when they are weak enough, do not fundamentally alter the nature of the motion. A weakly nonlinear solution can still be usefully expressed as a superposition of plane waves, but the amplitudes of these waves do not remain constant: they are modulated by nonlinear interactions. In order to characterize the nonlinear behavior of thin film flow, the method of multiple scales [7] is employed here and the resulting Ginburg–Landau equation [16] can be derived following the same procedure as Chen et al. [17], and Cheng and Lai [18].

$$\frac{\partial a}{\partial t_2} + D_1\frac{\partial^2 a}{\partial r_1^2} - \varepsilon^{-2}d_i a + (E_1 + iF_1)a^2\bar{a} = 0 \tag{38}$$

where

$$e = e_r + ie_i = \frac{\left(-\frac{X''}{2} + B' - D' + E - F\right)(16D - 4B + X') + 6C(A' - C')}{(16D - 4B - X')^2 + 36C^2} + i\frac{6C\left(-\frac{X''}{2} + B' - D' + E - F\right) - (A' - C')(16D - 4B + X')}{(16D - 4B + X')^2 + 36C^2} \tag{39}$$

$$D_1 = [(B - 6D) + i(3C)] \tag{40}$$

$$E_1 = (X'' - 5B' + 17D' + 4E - 10F)e_r - (A' - 7C')e_i + \left(\frac{X'''}{2} - \frac{3}{2}B'' + \frac{3}{2}D'' + E' - F'\right) \tag{41}$$

$$F_1 = (X'' - 5B' + 17D' + 4E - 10F)e_i + (A' - 7C')e_r + \frac{1}{2}(A'' - C'') \tag{42}$$

The overhead bar appearing in Eq. (38) stands for the complex conjugate of the same variable. Equation (38) can be used to investigate the weak nonlinear behavior of the fluid film flow. In order to solve for Eq. (38), we assume a filtered wave with no

spatial modulation, so the filtered wave can be expressed as

$$a = a_0 \exp[-ib(t_2)t_2] \tag{43}$$

After substituting Eq. (43) into Eq. (38), one can obtain

$$\frac{\partial a_0}{\partial t_2} = (\varepsilon^{-2} d_i - E_1 a_0^2) a_0 \tag{44}$$

$$\frac{\partial [b(t_2)t_2]}{\partial t_2} = F_1 a_0^2 \tag{45}$$

The associated wave amplitude εa_0 in the supercritical stable region and the nonlinear wave speed Nc_r are then derived and given as

$$\varepsilon a_0 = \sqrt{\frac{d_i}{E_1}} \tag{46}$$

$$\mathrm{Nc}_r = d_r + d_i \left(\frac{F_1}{E_1} \right) \tag{47}$$

If $E_1 = 0$, then Eq. (44) is reduced to a linear equation. The second term on the right-hand side of Eq. (44) is due to nonlinearity and may moderate or accelerate the exponential growth of the linear disturbance according to the signs of d_i and E_1. Equation (45) is used to modify the perturbed wave speed caused by infinitesimal disturbances appearing in the nonlinear system. The Ginzburg–Landau equation can be used to characterize various flow states, with the results summarized and presented as a Landau table [19].

4 Numerical Illustration and Discussions

In order to numerically demonstrate our theoretical modeling, we selected randomly but within specified ranges physical parameters for numerical experiment. The ranges for these parameters are based on published reasonable ranges for these parameters [17,20]. More specifically, these parameters and their values include: (1) Reynolds number (range from 0 to 15), (2) dimensionless perturbation wave numbers (range from 0 to 0.12), (3) rotation number (any one of the three values 0.1, 0.15, and 0.2), (4) dimensionless radius (any one of the three values 75, 100, and 125). Other of our parameters are treated as constants for all numerical computations since we are considering practical spin coating systems in which these variables are not expected to undergo significant variation. The Re, Pe, Fr, and α^2 S are taken to be of the same order (O(1)) [17,20], so the values of dimensional quantities are taken as a constant dimensionless surface tension $S = 6173.5$ [17,20,21] and Fr=9.8. Other dimensionless parameters related to fluid properties are also selected as constants: the Jakob number $\xi = 0.0872$, Prandtl number Pr=2.62, and density ratio $\beta = 0.000611$. These last three physical quantities are taken from the characteristics of condensate water at the temperature of $T_w^* + \Delta T/3$, except for surface tension at 373 °K. The pressure of the system is set to 1 atm [20].

4.1 Linear Stability Analysis. By setting $d_i = 0$ in the linear stability analysis, the neutral stability curve can be determined easily from Eq. (37). The α-Re plane is divided into two different characteristic regions by the neutral stability curve. One is the linearly stable region, where small disturbances decay with time and the other is the linearly unstable region, where small perturbations grow as time increases. Figure 2(*a*) shows that the stable region decreases and unstable region increases with an increase in rotation number. Figure 2(*b*) shows that the stable region decreases and the unstable region increases with increasing radius of the circular disk. Hence one can say that with regard to linear stability analysis, the rotation number and the radius of circular disk generate similar destabilizing effects.

4.2 Weakly Nonlinear Stability Analysis. Figures 3(*a*)–3(*c*) show the neutral stability curves for subcritical instability, ($d_i < 0, E_1 < 0$); subcritical stability, ($d_i < 0, E_1 > 0$); supercritical stability, ($d_i > 0, E_1 > 0$); and the supercritical explosion, ($d_i > 0, E_1 < 0$). Figure 4(*a*) shows the threshold amplitude in the subcritical instability region for various wave numbers with different Ro values at Re=3 and $r = 75$. The results indicate that the threshold amplitude εa_0 becomes smaller as the value of rotation number (Ro) increases. Figure 4(*b*) shows the threshold amplitude in the subcritical instability region for various wave numbers with different values of radius (r) at Re=3 and Ro=0.1. The results indicate that the threshold amplitude εa_0 becomes smaller as the value of radius (r) changes from 75, 100, and 125. The reason for this phenomenon is the existence of the centrifugal force term, which is a radius-related force in the governing equation. Increasing the radius and the rotation number results in accelerated growth of the linear disturbance due to the centrifugal force. The film flow, which has the higher threshold amplitude value, will become more stable than those that have smaller ones. If the initial finite-amplitude disturbance is less than the threshold amplitude, the system will become conditionally stable.

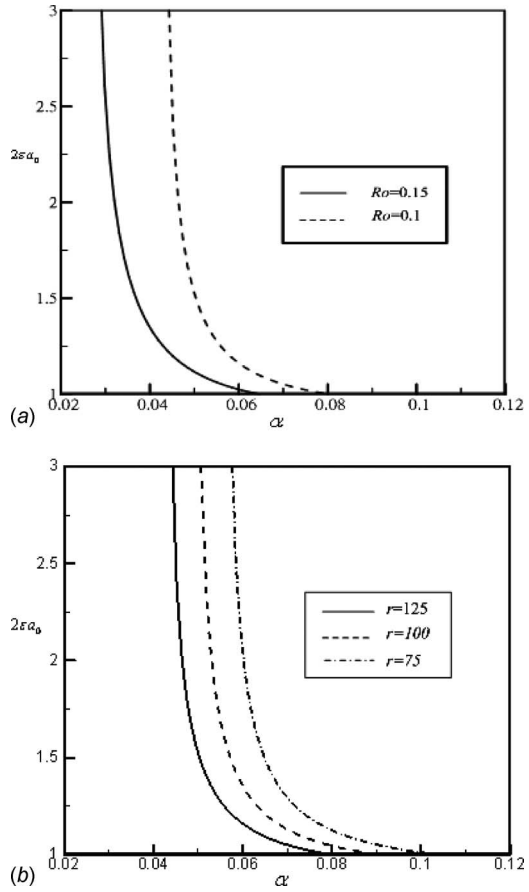

Fig. 4 (*a*) Threshold amplitude in subcritical instability region for three different Ro values at Re=3 and *r*=75 and (*b*) threshold amplitude in subcritical instability region for three different *r* values at Re=3 and Ro=0.1

Figure 5(*a*) shows the threshold amplitude in the supercritical stability region for various wave numbers with different Ro values at Re=9 and $r = 100$. It is found that decreasing the rotation number will lower the threshold amplitude, whereupon the flow becomes relatively more stable. Figure 5(*b*) shows the threshold amplitude in the supercritical stability region for various wave numbers with different r values at Re=9 and Ro=0.1. It is also found that decreasing of the radius of the circular disk will lower the threshold amplitude.

The wave speed of Eq. (37) predicted by linear theory is a

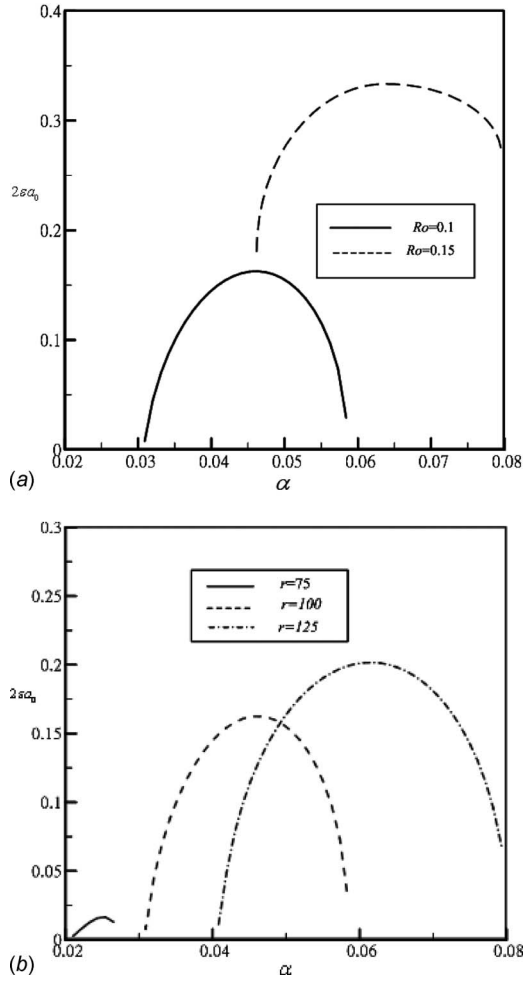

Fig. 5 (*a*) Threshold amplitude in supercritical stability region for two different Ro values at Re=9 and *r*=100 and (*b*) threshold amplitude in supercritical stability region for three different *r* values at Re=9 and Ro=0.1

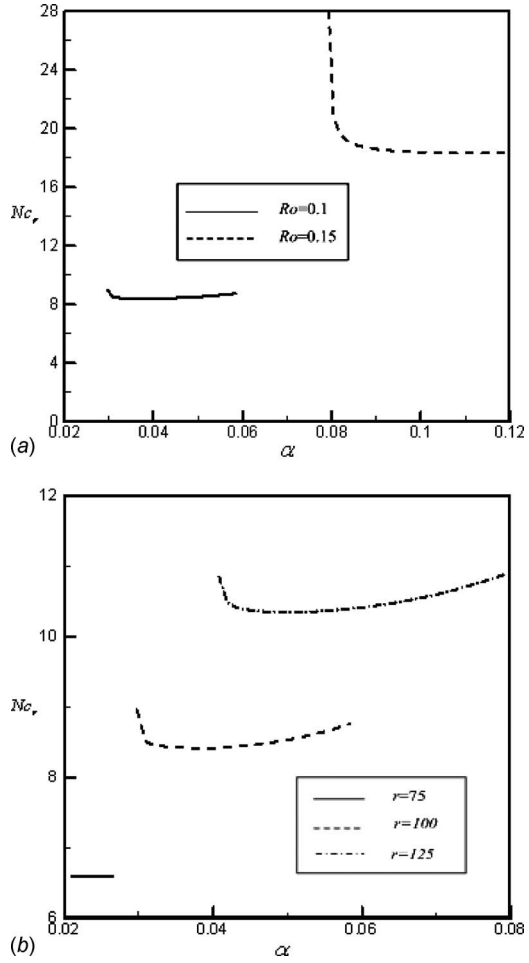

Fig. 6 (*a*) Nonlinear wave speed in supercritical stability region for two different Ro values at Re=9 and *r*=100 and (*b*) nonlinear wave speed in supercritical stability region for three different *r* values at Re=9 and Ro=0.1

constant value for all wave numbers and rotation numbers. However, the wave speed of Eq. (47) predicted by nonlinear theory is no longer a constant. It is actually a function of the wave number, Reynolds number, rotation number, and the radius of disk. Figure 6(*a*) shows the nonlinear wave speed in the supercritical stability region for various perturbed wave numbers and different Ro values at Re=9 and $r=100$. Figure 6(*b*) shows the nonlinear wave speed in the supercritical stability region for various perturbed wave numbers and different r values at Re=9 and Ro=0.1. It is found that the nonlinear wave speed increases as the rotation number or the radius of the disk increase.

5 Concluding Remarks

The stability of a thin liquid film with condensation effects during spin coating is investigated using the method of long-wave perturbation. On the basis of the results of numerical modeling, two conclusions can be drawn:

1. The modeling results indicate that the region of linear stability becomes smaller for increasing rotation number or increasing radius. Hence one can say that in linear stability analysis, the rotation number and the radius of a circular disk give similar destabilizing effects.
2. Weakly nonlinear stability analysis has successfully revealed the subcritical stability, subcritical instability, supercritical stability, and supercritical explosion regions for the flow patterns of a thin film on a rotating disk with condensation effects. It is found that in subcritical instability region, the threshold amplitude εa_0 becomes smaller as the value of the rotation number or the radius of circular disk become larger. When the initial finite-amplitude disturbance is less than the threshold amplitude, the flow will be conditionally stable.

Acknowledgment

The authors sincerely thank the reviewers for their very useful comments and suggestions which have helped in improving the quality of this manuscript.

Nomenclature

C_p = specific heat of fluid
D = complex wave celerity=d_r+id_i
Fr = Prandtl number=gh_0^*/u_o^{*2}
g = acceleration due to gravity
h^* = the local film thickness
h_0^* = the average film thickness
h_{fg} = latent heat
K = fluid thermal conductivity
Nd = dimensionless parameter=$(1-\beta)\xi^2/\beta\,\mathrm{Pr}^2$
Nc_r = nonlinear wave speed
P^* = fluid pressure
P_g^* = vapor pressure
Pe = local Peclet number=Pr Re

Pr = Prandtl number$=\rho\nu$
Re = Reynolds number$=u_0^* h_0^*/\nu$
Ro = rotation number$=\Omega^* h_0^*/u_0^*$
S = surface tension
T^* = fluid temperature
T_s^* = vapor saturation temperature
T_w^* = wall temperature
u_0^* = the scale of velocity
h_{fg} = latent heat

Greek symbols

α = dimensionless wave number
β = density ratio
ε = small perturbation parameter
εa_0 = wave amplitude
ζ = Jakob number
Ω^* = angular velocity
η = dimensionless perturbed film thickness
λ = perturbed wavelength
v^* = tangential velocity
ν = kinematic viscosity of the fluid
μ = fluid dynamic viscosity
ρ = constant fluid density
φ = stream function
θ = dimensionless temperature

Appendix

Zeroth order solution can be given as

The solutions for the equations of order can be given as

$$\varphi_0 = \tfrac{1}{6} r^2 \cdot \mathrm{Re} \cdot \mathrm{Ro}^2 (3h - z) z^2$$

$$p_0 = \mathrm{Fr}(h - z) - S\alpha^2 h_{rr} - \mathrm{Nd} \cdot \mathrm{Re}^{-2}\, h^{-2}$$

$$\theta_0 = \tfrac{z}{h}$$

First order solution can be given as

$$p_1 = \mathrm{Ro}^2 (3z^2 - 6z \cdot h + h^2 - r(z + h)) h_r$$

$$\varphi_1 = k_1 z^8 + k_2 z^7 + k_3 z^6 + k_4 z^5 + k_5 z^4 + k_6 z^3 + k_7 z^2 + k_8 z + k_9$$

$$\theta_1 = C_1 z^6 + 3_2 z^5 + C_3 z^4 + C_4 z^3 + C_5 z^2 + C_6 z + C_7$$

where

$$k_1 = -\frac{r^2 \cdot \mathrm{Re}^3 \cdot \mathrm{Ro}^4}{2016}$$

$$k_2 = \frac{(3 + 5h) r^2 \cdot \mathrm{Re}^3 \cdot \mathrm{Ro}^4}{1260}$$

$$k_3 = -\frac{h(5 + 3h) r^2 \cdot \mathrm{Re}^3 \cdot \mathrm{Ro}^4}{360}$$

$$k_4 = \frac{r^2 \cdot \mathrm{Re}^2 \cdot \mathrm{Ro}^2 (2h^4 \cdot \mathrm{Pe} \cdot \mathrm{Re} \cdot \mathrm{Ro}^2 - h^3 \cdot \mathrm{Pe} \cdot r \cdot \mathrm{Re} \cdot \mathrm{Ro}^2 \cdot h_r + 2\alpha \cdot \xi \cdot h_r^2)}{120 h^2 \cdot \mathrm{Pe}}$$

$$k_5 = -\frac{r^2 \cdot \mathrm{Re}^2 \cdot \mathrm{Ro}^2 \cdot \xi}{24h \cdot \mathrm{Pe} \cdot \alpha}$$

$$k_6 = \frac{r\left(\left(\frac{2\mathrm{Nd}}{h^3} + \mathrm{Fr} \cdot \mathrm{Re}^2\right) h_r - \mathrm{Re}^2 \cdot S \cdot \alpha^2 \cdot h_{rrr}\right)}{6\ \mathrm{Re}}$$

$$k_7 = \frac{1}{360 h^2 \cdot \mathrm{Re} \cdot \mathrm{Pe} \cdot \alpha} (r(h^3 \cdot r \cdot \mathrm{Re}^3 \cdot \mathrm{Ro}^2 (h^4 (-3 + 20h) \mathrm{Pe} \cdot \mathrm{Re} \cdot \mathrm{Ro}^2 \cdot \alpha - 90\xi) - 30\alpha \cdot h_r (\mathrm{Pe}(12\mathrm{Nd} + 6\mathrm{Fr} \cdot h^3 \cdot \mathrm{Re}^2 - h^6 \cdot r^2 \cdot \mathrm{Re}^4 \cdot \mathrm{Ro}^4) + 2h^3 \cdot r \cdot \mathrm{Re}^3 \cdot \mathrm{Ro}^2 \cdot \alpha \cdot \xi \cdot h_r) + 180 h^3 \cdot \mathrm{Pe} \cdot \mathrm{Re}^2 S \cdot \alpha^3 \cdot h_{rrr}))$$

$$k_8 = k_9 = 0$$

$$C_1 = -\frac{\mathrm{Pe} \cdot \mathrm{Re} \cdot \mathrm{Ro}^2}{90h^2}$$

$$C_2 = \frac{\mathrm{Pe} \cdot \mathrm{Re} \cdot \mathrm{Ro}^2}{20h}$$

$$C_3 = \frac{\mathrm{Pe} \cdot r \cdot \mathrm{Re} \cdot \mathrm{Ro}^2 \cdot h_r}{12h}$$

$$C_4 = -\frac{\xi}{6h^3 \cdot \alpha}$$

$$C_5 = 0$$

$$C_6 = -\frac{11}{60} h^3 \cdot \mathrm{Pe} \cdot \mathrm{Re} \cdot \mathrm{Ro}^2 + \frac{\xi}{2h \cdot \alpha} - \frac{1}{3} h^2 \cdot \mathrm{Pe} \cdot r \cdot \mathrm{Re} \cdot \mathrm{Ro}^2 \cdot h_r$$

$$C_7 = 0$$

References

[1] Xiao, H., 2001, *Introduction to Semiconductor Manufacturing Technology*, Prentice-Hall, Englewood Cliffs, NJ.
[2] Yang, Y. K., and Chang, T. C., 2006, "Experimental Analysis and Optimization of a Photo Resist Coating Process for Photolithography in Wafer Fabrication," Microelectron. J., **37**, pp. 746–751.
[3] Kuo, Y. K., and Chao, C. G., 2006, "Control Ability of Spin Coating Planarization of Resist Film and Optimal of Developers," Microelectron. J., **37**, pp. 759–764.
[4] Benney, D. J., 1996, "Long Waves on Liquid Film," J. Math. Phys. (Cambridge, Mass.), **45**, pp. 150–155.
[5] Lin, S. P., 1974, "Finite Amplitude Side-Band Stability of a Viscous Film," J. Fluid Mech., **63**, pp. 417–429.
[6] Nakaya, C., 1974, "Equilibrium State of Periodic Waves on the Fluid Film Down a Vertical Wall," J. Phys. Soc. Jpn., **36**, pp. 921–926.
[7] Krishna, M. V. G., and Lin, S. P., 1977, "Nonlinear Stability of a Viscous Film With Respect to Three-Dimensional Side-Band Disturbance," Phys. Fluids, **20**, pp. 1039–1044.
[8] Atherton, R. W., and Homsy, G. M., 1976, "On the Derivation of Evolution Equations for Interfacial Waves," Chem. Eng. Commun., **2**, pp. 57–77.
[9] Ünsal, M., and Thomas, W. C., 1980, "Nonlinear Stability of Film Condensation," ASME J. Heat Transfer, **102**, pp. 483–488.

[10] Marschall, E., and Lee, C. Y., 1973, "Stability of Condensate Flow Down a Vertical Wall," Int. J. Heat Mass Transfer, **16**, pp. 41–48.
[11] Emslie, A. G., Bonner, F. T., and Peck, L. G., 1958, "Flow of a Viscous Liquid on a Rotating Disk," J. Appl. Phys., **29**, pp. 858–862.
[12] Higgins, B. G., 1986, "Film Flow on a Rotating Disk," Phys. Fluids, **29**, pp. 3522–3529.
[13] Kitamura, A., Hasegawa, E., and Yoshizawa, M., 2002, "Asymptotic Analysis of the Formation of Thin Liquid Film in Spin Coating," Fluid Dyn. Res., **30**, pp. 107–125.
[14] Edwards, D. A., Brenner, H., and Wasan, D. T., 1991, *Interfacial Transport Processes and Rheology*, Butterworth-Heinemann, Boston, MA.
[15] Rosenau, P., and Oron, A., 1989, "Evolution and Breaking of Liquid Film Flowing on a Vertical Cylinder," Phys. Fluids A, **1**, pp. 1763–1766.
[16] Ginzburg, V. L., and Landau, L. D., 1950, "Theory of Superconductivity," J. of Experiential Theoretic Physics (USSR), **20**, pp. 1064–1082.
[17] Chen, C. I., Chen, C. K., and Yang, Y. T., 2004, "Perturbation Analysis to the Nonlinear Stability Characterization of the Thin Condensate Falling Film on the Outer Surface of a Rotating Vertical Cylinder," Int. J. Heat Mass Transfer, **47**, pp. 1937–1951.
[18] Cheng, P. J., and Lai, H. Y., 2006, "Nonlinear Stability Analysis of Thin Film Flow From a Liquid Jet Impinging on a Circular Concentric Disk," J. Mech., **22**, pp. 115–124.
[19] Eckhaus, W., 1965, *Studies in Nonlinear Stability*, Springer, Berlin.
[20] Chen, C. I., Chen, C. K., and Yang, Y. T., 2006, "Nonlinear Stability Analysis of Thin Condensate Falling Film Inside a Rotating Vertical Cylinder," Int. J. Heat Mass Transfer, **49**, pp. 707–717.
[21] Hung, C. I., Chen, C. K., and Tsai, J. S., 1996, "Weakly Nonlinear Stability Analysis of Condensate Film Flow Down a Vertical Cylinder," Int. J. Heat Mass Transfer, **39**, pp. 2821–2829.

A Device for Measuring Thin Fluid Flow Depth Over an Inclined Open Rectangular Channel

A. K. Majumder
Advanced Materials and Processes Research Institute,
Hoshangabad Road,
Bhopal 462026, India
e-mail: arunmajumder@hotmail.com

Accurate knowledge of the fluid flow depth over an inclined rectangular open channel is of obvious value in the modeling of flow characteristics over that channel. Understanding of this type of fluid flow behavior is of immense importance to the mineral processing fraternity as a large number of separators work on this principle. Therefore, a multiple point computer-controlled depth gauge was developed to measure water flow depths at various flow rates ranging from 0.81 l/s to 2.26 l/s over an inclined (17.5 deg) rectangular channel (2400 mm long and 370 mm wide). This paper describes the details about the device and the data acquisition procedure. An attempt has also been made to predict the measured flow depths at various operating conditions by using a modified form of the conventional law of the wall model. An overall relative error of 4.23% between the measured and the predicted flow depths at various flow rates establishes the validity of the model. [DOI: 10.1115/1.3153362]

Keywords: open channel flow, surface waves, laminar boundary layer, turbulent boundary layer

1 Introduction

Modeling of fluid flow behavior through open channels is an established subject in the field of fluid mechanics, hydraulics engineering, chemical engineering, etc. Most particle separators in mineral processing involve particle motion through water and separation between particles of differing size, and density takes place as a result of the interplay of body forces (gravitation or centrifugal), drag forces, and particle inertia. An inclined rectangular open channel is the simplest form of these separators in which particle separation takes place in a flowing film of a few millimeters thick. Therefore, the flow conditions in mineral separators are different in terms of the size of the channel and the operating flow depth to that of rivers and other devices used by the chemical engineers. For this reason, a project was formulated to model the particle separation characteristics in a thin flowing stream of slurry using established theories in fluid mechanics. The details of this work may be found elsewhere [1].

The basic assumption made during modeling was that the flow was fully developed, which means that the depth of flow remained unchanged at any location along the length. Experimental verification of this basic assumption was, therefore, essential.

It was also necessary to identify any effects of the sidewalls across the entire width of the channel. Measuring of flow depth, a few millimeters thick, over the entire width and length of the channel with reasonable accuracy is not simple because of the presence of random surface waves.

Holtham [2] developed a multiple point computer-controlled depth gauge for studying the fluid flow depth profiles across a spiral concentrator, and it was claimed that the accuracy of measurement was within 0.25 mm. For this reason, a multipoint computer-controlled depth gauge has been developed based on Holtham's [2] approach for the present study. The detailed description of this depth gauge is the subject matter of this paper. An attempt has also been made to predict the water flow depth at various flow rates using a modified form of the conventional law of the wall.

2 The Experimental Rig

A closed-circuit test rig consisting of an open inclined rectangular channel (sluice) was constructed for the experimental work (Fig. 1). The channel was made from a 6 mm thick plate glass, 2400 mm long, and 370 mm wide, stiffened with aluminum angles. The 60 mm high sidewalls were made of 6 mm Perspex. Water was pumped to the channel through a distribution box from a 260 l sump by a centrifugal pump fitted with a variable speed drive. Several deflective vanes were placed inside the distribution box for uniform distribution of fluid over the channel. A specially designed splitter was fitted at the discharge end to split the flow at different flow heights. The flow thus split into underflow, and overflow was collected through two Vezin type samplers so that the exact flow rate could be back calculated accurately.

3 Description of the Device

Figure 2 shows the depth gauge mounted across the channel width. A Perspex bar carrying 16 probes made of 2 mm diameter stainless steel rod was raised or lowered by means of two ball screws. The ball screws were connected through a drive belt and were driven by a small computer-controlled stepper motor.

To minimize the surface tension effect holding water to probes, the tip of each probe was tapered and silver grease was applied. The individual probes were located in a manner such that their distances from the two side walls of the channel remained identical (5 mm, 15 mm, 25 mm, 35 mm, 45 mm, 85 mm, 125 mm, and 155 mm, respectively). An additional probe had also been mounted to provide a position feedback signal to compensate for any slip in the stepper motor.

The circuit diagram of each probe is shown in Fig. 3. The circuit consists of an operational amplifier (op-amp) to detect contact with the fluid, and a Schmitt trigger to condition the signal to the logic levels of the 486 PC to carry out the measurements. The signals from the 16 probes and the signal from the feedback probe were interfaced via a digital input/output (I/O) card to the personal computer. The stepper motor was driven by the computer through this card too. The metallic frame of the channel (termed as launder electrode) was connected to a 5 V dc power supply so that the depth probes when in contact with the fluid (termed as pulp contact) flowing down the channel could get that voltage. The interface card registered the signals from each probe through the electronics circuit and recorded 5 V (logic 1) indicating fluid contact, or 0 V (logic 0) indicating no contact. The LABVIEW programming language was used to drive the stepper motor as well as to interrogate the probes.

3.1 Operation. Small holes were drilled through the channel frame so that the gauge could be bolted at any chosen distance from the discharge end of the channel. Prior to starting each experimental run, the Perspex bar carrying the probes was driven down until the feedback probe contacted a reference position. At this position all the 16 probes were adjusted to be in contact with the channel floor. Once steady-state flow conditions were achieved in the channel, the measurement program was started, and the bar was driven upward in one step increments at an interval of 1 s. The LABVIEW software interrogated each probe for a contact/no-contact signal with water, and the data were collected by continuous sampling at 500 Hz. Interrogation took place every time the probes were moved by one step by the stepper motor. The data thus collected were recorded in separate files for each step of

Contributed by the Fluids Engineering Division of ASME for publication in the JOURNAL OF FLUIDS ENGINEERING. Manuscript received June 9, 2005; final manuscript received July 20, 2007; published online August 25, 2009. Assoc. Editor: Timothy J. O'Hern.

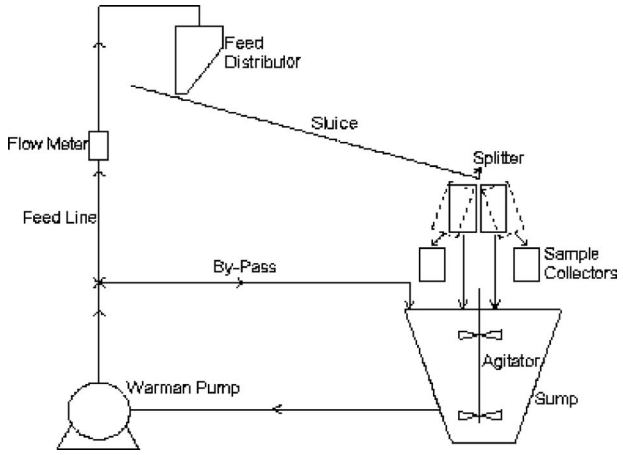

Fig. 1 Schematic of the experimental rig

each probe for later analysis.

The data files were analyzed to determine the number of times each probe was in contact with the water at each step. The fractional number of contacts was then plotted against the number of steps the probes had been lifted. For clarity a sample plot with samples from only two probes, at distances of 5 mm (probe 1) and 155 mm (probe 2) from the side walls, is shown in Fig. 4. The noise due to wave action is clearly visible.

To eliminate the wave effect and determine a consistent flow depth, the C_{50}, the point where the fractional contact is 50%, was found by fitting the individual plots in Fig. 4 with a sigmoid curve. The number of steps the probes stepped up in order to reach the C_{50} point was then considered to be the real depth and was converted to a depth in millimeters (48 steps equals 1 mm, i.e., each step equals 20.8 μm).

3.2 Calibration. Calibration of the gauge was carried out as follows. All the probes were first put in contact with the channel surface and then they were lifted up 400 steps. A small rectangular metal piece of known thickness was held to the channel surface under the probe being checked. Then the probes were driven down until the contact was sensed through the metal piece and the number of steps was noted. The metal piece was provided with 5 V for electronics to sense its contact. Then the noted increments were subtracted from the prefixed 400 steps to calculate the actual measured thickness of the metal piece. This procedure was repeated several times for all the 16 probes, and it was found that the measured and the actual thickness of the metal plate agree with an error of 2.8%. This suggested that the depth gauge was accurate enough to measure the fluid flow depth at any operating condition.

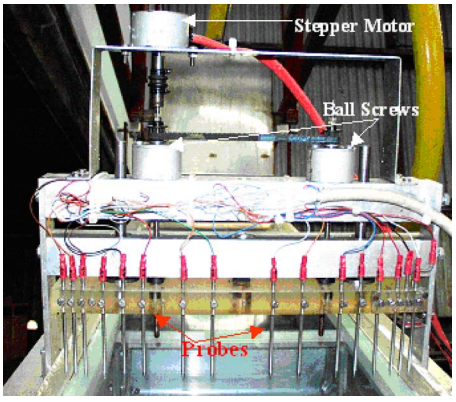

Fig. 2 Depth gauge mounted on the channel

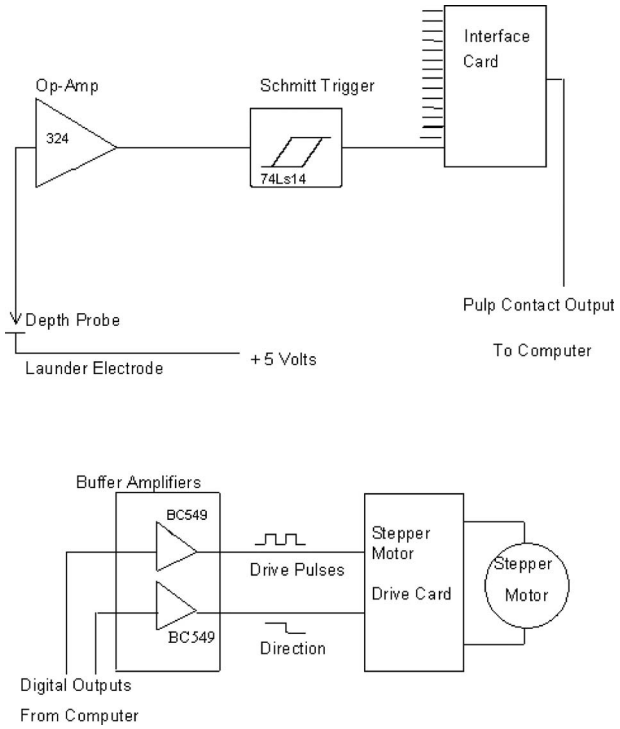

Fig. 3 Schematic diagram of electronic circuit

3.3 Measured Depths. Following the aforementioned procedures, the water flow depths at 16 different locations across the width of the channel at various flow rates (ranging from 0.81 l/s to 2.26 l/s) and a fixed channel inclination of 17.5 deg were then measured. The depth measurement at each operating condition was repeated five times to calculate the average flow depth at a particular location and to calculate the measurement errors. The depth profiles across the width of the channel at different flow rates are shown with error bars (two standard deviations) in Fig. 5.

From Fig. 5 it can be observed that there is slight increase in flow depth close to the side walls as expected, but the depth remains almost constant in the middle portions. However, the very low ratio of the measured average flow depth (approximately 4 mm maximum) at the maximum operating flow rate and the width of the channel (370 mm) suggest that the channel may be considered as a wide open channel. This means that the effects of the side walls on the principal nature of flow may safely be ignored. Several measurements were made 500 mm from the inlet all the way to the outlet following the similar methodology. It was found that the average measured depth at any point remained constant

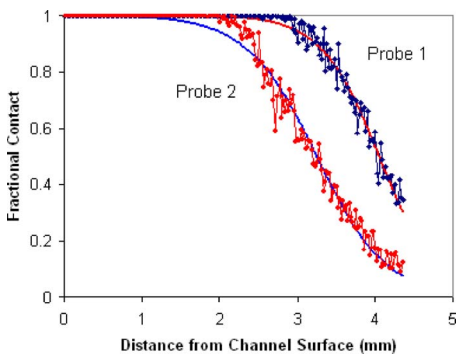

Fig. 4 Fractional contacts of probes with water

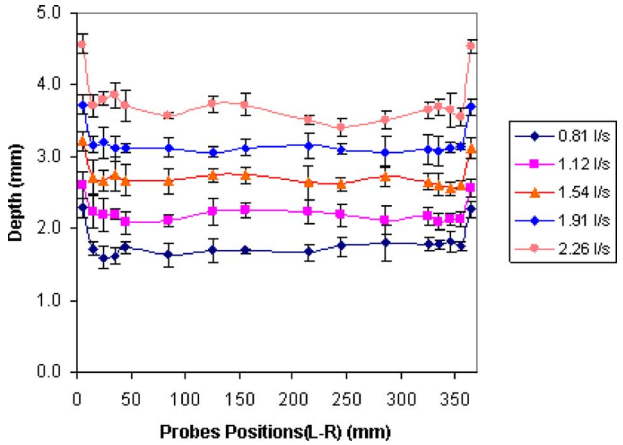

Fig. 5 Measured flow depth profiles at a distance of 1500 mm from the inlet

(within 0.05 mm) along the length of the channel, which justifies the assumption of fully developed flow over the channel.

4 Modeling

Ignoring the influence of the sidewalls, the flow is essentially one dimensional where any variable is a function only of the coordinate normal to the channel floor (the y direction).

A simple force balance on an element of fluid permits calculation of the shear stress at the bottom surface

$$\tau_0 = \rho g h_f \sin\theta \tag{1}$$

where ρ is the fluid density, g the acceleration due to gravity, h_f the depth of the flow, and θ the channel inclination.

The Reynolds numbers at the lowest and the highest flow rates used (0.81 l/s and 2.26 l/s) were calculated to be 2189 and 6108, respectively, using the following formula:

$$\mathrm{Re} = (\rho Q/\mu W)$$

where ρ is the water density, Q is the total volumetric flow, μ is the viscosity of water, and W is the channel width.

The critical Reynolds number for this type of flow lies between 250 and 600 [3] and therefore, the flow is considered to be turbulent. In such a hydrodynamic regime, a typical thick boundary layer flow consisting of a viscous sublayer on the bottom of the channel followed by a transition zone to a turbulent boundary layer is expected to be observed. If the flow depth is sufficient, a region of more or less fully developed turbulent flow should exist beyond the turbulent boundary layer.

Within an inner region the time-averaged flow velocity, μ_x, is dependent only on the shear stress at the wall, τ_0, the distance from the channel bed, y, and the kinematic viscosity, ν. Using the "law of the wall," the equation for this region is

$$\frac{\mu_x}{\mu^*} = \frac{1}{k}\ln\left(\frac{\mu^* y}{\nu}\right) + B \tag{2}$$

where $\mu^* = \sqrt{\tau_0/\rho}$ is the shear or friction velocity, k (approximately 0.41) is known as the von Karman constant, and $B \approx 5.0$ is a dimensionless constant [4].

This profile should predict the velocity profile up to a dimensionless distance [5] of

$$y^+ = \frac{\mu^* y}{\nu} \approx 750 \tag{3}$$

Considering a fixed channel inclination of 17.5 deg, this dimensionless depth is equivalent to a flow depth of approximately 5.35 mm. The actual flow depth at the operating conditions prevailing in the channel may be expected to be less than 5.35 mm, so Eq. (2) for the velocity profile may well be applicable to the entire region of the flow.

In the viscous sublayer, the time-averaged flow velocity, μ_x, can be written as

$$\mu_x = \mu^{*2} y/\nu \tag{4}$$

This is a linear profile dominated by viscous forces, and its thickness is given by

$$\delta_v \cong 6\nu/\mu^* \tag{5}$$

The transition region occurs approximately in the region between $6 < \mu^* y/\nu < 30$, beyond which the boundary layer flow is deemed turbulent [5].

Now if the linear and logarithmic profiles are matched at $y = h_m$, then from Eqs. (2) and (4) it can be written that

$$\frac{\mu^* h_m}{\nu} = \frac{1}{k}\ln\left(\frac{\mu^* h_m}{\nu}\right) + B \tag{6}$$

or

$$B = \frac{\mu^* h_m}{\nu} - \frac{1}{k}\ln\left(\frac{\mu^* h_m}{\nu}\right) \tag{7}$$

In Eq. (7), substituting the previously mentioned approximate values of k and B, the dimensionless matching height, $y_m^+ = \mu^* h_m/\nu$, becomes approximately 10.8.

The volumetric flow per unit width of the channel, q, can then be determined from

$$q(y) = \int_0^y \mu_x(y)dy \tag{8}$$

or

$$q(y) = \nu\int_0^{h_m} \frac{\mu^{*2}}{\nu^2} y dy + \nu\int_{h_m}^{y}\left[\frac{\mu^*}{\nu}\left\{\frac{1}{k}\ln\left(\frac{\mu^* y}{\nu}\right)\right\} + B\right]dy \tag{9}$$

After integration, Eq. (9) may be written in terms of the dimensionless distance, $y^+ = \mu^* y/\nu$, and dimensionless matching height, y_m^+, as

$$q(y) = \nu\left[y^+\left(y_m^+ - \frac{1}{k}\ln y_m^+\right) + \frac{1}{k}y^+(\ln y^+ - 1) + \frac{1}{k}y_m^+ - \frac{y_m^{+2}}{2}\right] \tag{10}$$

The flow depth can now be calculated from a known value of total flow rate, Q, by solving Eq. (10) numerically.

While solving Eq. (10) numerically, the density of water was taken to be 997.1 $\mathrm{kg/m^3}$ and the kinematic viscosity 0.897×10^{-6} $\mathrm{m^2/s}$. For comparison purposes, the measured flow depth data close to the side walls have been ignored by ignoring the data recorded by the first and the 16th probes while calculating the average flow depth at a given flow rate. The comparison of the measured depth (average) and the predicted depth data at different flow rates is shown in Fig. 6.

The overall percent difference between the measured and the predicted depth data is calculated to be 4.23%. However, the following facts may be considered.

(1) Only the widely accepted values of von Karman's constant and the dimensionless constant in Eq. (2) are used here, but these values may differ as they are mainly empirically determined values for other flow conditions
(2) The errors associated with the average flow rate, the uncertainty in measurement with the device (2.8%), and the measurement reproducibility (two standard deviations) are neglected while calculating the overall error.

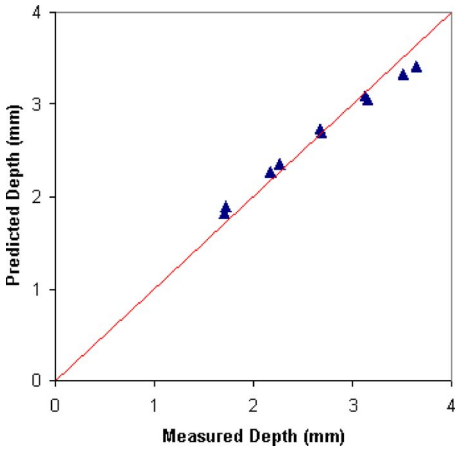

Fig. 6 Comparisons of measured and predicted flow depths

The conclusion may now be drawn that this model is adequate to explain the thin water flow depth over an open inclined rectangular channel.

5 Conclusions

Based on the above discussions, the following conclusions may be drawn.

(1) The developed device can measure the thin fluid flow depth of a few millimeters thick across the entire width of an inclined channel with a precision of around 20 μm (1/48 mm).
(2) The proposed data acquisition methodology can provide statistically acceptable depth profile across the width of the channel bypassing the effects of random surface waves.
(3) A modified form of the law of the wall can predict the flow depth data with an overall relative error of 4.23% for a fluid flowing over an inclined open rectangular channel.

Acknowledgment

The author gratefully acknowledges the kind support provided by Dr. P. N. Holtham, Dr. G. J. Lyman, and Dr. V. Subramanian of JKMRC, University of Queensland, Australia at the various stages of this work.

References

[1] Majumder, A. K., 2002, "Modelling of Flowing Film Concentrators," Ph.D. thesis, The University of Queensland, Australia.
[2] Holtham, P. N., 1990, "The Fluid Flow Pattern and Particle Motion on Spiral Separators," Ph.D. thesis, University of New South Wales, Australia.
[3] Schubert, H., 1979, *Aufbereitung Fester Mineralischer Rohstoffe*, VEB, Leipzig, in German.
[4] Wilcox, D. C., 1993, *Turbulence Modeling For CFD*, DCW Industries, Inc., Glendale, CA.
[5] Hunt, J. N., 1964, *Incompressible Fluid Dynamics*, Longmans, Green, London.